REPORT DOCUMENTATION PAGE

Form Approved
OMB NO. 0704-0188

Public Reporting burden for this collection of information is estimated to average 1 hour per response, including the time for reviewing instructions, searching existing data sources, gathering and maintaining the data needed, and completing and reviewing the collection of information. Send comment regarding this burden estimates or any other aspect of this collection of information, including suggestions for reducing this burden, to Washington Headquarters Services, Directorate for information Operations and Reports, 1215 Jefferson Davis Highway, Suite 1204, Arlington, VA 22202-4302, and to the Office of Management and Budget, Paperwork Reduction Project (0704-0188,) Washington, DC 20503.

1. AGENCY USE ONLY (Leave Blank)

2. REPORT DATE
April 30, 2008

3. REPORT TYPE AND DATES COVERED
Final (03/01/05 - 12/31/07)

4. TITLE AND SUBTITLE
Numerical Investigation of Transition in Supersonic Boundary Layers Using DNS and LES

5. FUNDING NUMBERS
FA9550-05-1-0170

6. AUTHOR(S)
Dr Hermann F. Fasel

7. PERFORMING ORGANIZATION NAME(S) AND ADDRESS(ES)
Dept. of Aerospace and Mechanical Engineering, University of Arizona,
Tucson, AZ 85721

8. PERFORMING ORGANIZATION REPORT NUMBER

9. SPONSORING / MONITORING AGENCY NAME(S) AND ADDRESS(ES)
Air Force Office of Scientific Research
875 N. Randolph St. Room 3112
Arlington, VA 22203
Dr John Schmisseur/NA

10. SPONSORING / MONITORING AGENCY REPORT NUMBER
AFRL-SR-AR-TR-08-0297

11. SUPPLEMENTARY NOTES

12 a. DISTRIBUTION / AVAILABILITY STATEMENT
Approved for public release; distribution unlimited.

12 b. DISTRIBUTION CODE

13. ABSTRACT (Maximum 200 words)

High-speed boundary-layer transition is still not fully understood. To investigate physical mechanisms leading to breakdown to turbulence supersonic transition investigations at Mach 2 and hypersonic transition investigations at Mach 8 are performed using Direct Numerical Simulations (DNS). The flat-plate experiments of Kosinov at al. (1994) and Ermolaev et al. (1996) at Mach 2 discovered subharmonic resonance triads (oblique subharmonic resonance) in the weakly nonlinear regions of transition. Our DNS reveal the possible existence of an oblique breakdown based on detailed comparisons with experimental data. Therefore, both mechanisms, the oblique subharmonic resonance and the oblique breakdown, are thoroughly investigated.Comparison of the results of the flat-plate, cylindrical, and conical geometries allow for conclusions on the influences of spanwise curvature. Because spanwise curvature is stabilizing the hypersonic boundary layer, the circular cone becomes increasingly more unstable in downstream direction.Depending on the nose radius under investigation the stability behavior of high-speed boundary-layer flows over circular cones is greatly altered. Stetson et al. (1984) reported that small nose radii are stabilizing while large nose radii are destabilizing the flow. A conclusive explanation of this so-called transition reversal could not be provided so far and therefore predictions of the critical nose radius could not be made. Our DNS link this change in critical Reynolds number to an instability of acoustic waves traveling faster than the free stream. These waves do not require the existence of a generalized inflection point so that the critical nose radius can be linked to base-flow properties.

14. SUBJECT TERMS

15. NUMBER OF PAGES
231

16. PRICE CODE

17. SECURITY CLASSIFICATION OR REPORT UNCLASSIFIED	18. SECURITY CLASSIFICATION ON THIS PAGE UNCLASSIFIED	19. SECURITY CLASSIFICATION OF ABSTRACT UNCLASSIFIED	20. LIMITATION OF ABSTRACT UL

NSN 7540-01-280-5500

Standard Form 298 (Rev.2-89)
Prescribed by ANSI Std. 239-18
298-102

Enclosure 1

NUMERICAL INVESTIGATION OF TRANSITION IN SUPERSONIC BOUNDARY LAYERS USING DNS AND LES

Final Report
FA9550-05-1-0170

Hermann F. Fasel
Frank Husmeier
Christian S. J. Mayer
Department of Aerospace and Mechanical Engineering
The University of Arizona
Tucson, AZ 85721

Submitted to
Dr. John Schmisseur, Program Manager
The Air Force Office of Scientific Research

March 31, 2008

20080610 118

Table of Contents

List of Figures **7**

List of Tables **26**

Nomenclature **28**

Nomenclature **28**

Abstract **31**

1. Introduction **33**

1.1 Motivation 33

1.2 Transition Process and Breakdown Scenarios 34

1.3 Common Methods for Stability Investigations 38

1.3.1 Linear Stability Theory 38

1.3.1.1 Inviscid Theory 38

1.3.1.2 Viscous Theory 41

1.3.2 Parabolized Stability Equations 42

1.3.3 Temporal Direct Numerical Simulations 43

1.4 Earlier Investigations of High-Speed Boundary-Layer Stability 44

1.4.1 Experimental Efforts 44

1.4.1.1 Flat-Plate and Swept-Wing Geometry 44

1.4.1.2 Cone Geometries 45

1.4.2 Computational Efforts 49

1.4.2.1 Flat-Plate and Swept-Wing Geometry 49

1.4.2.2 Cone Geometries 51

1.5 Objectives and Overview 54

Table of Contents—*Continued*

2. Governing Equations **56**
2.1 Viscosity 56
2.2 Non-dimensional Equations 57

3. Numerical Method and Simulation Setup **60**
3.1 Initial Condition 60
3.2 Computational Domain 61
3.3 Inflow Boundary Condition 62
3.4 Free-Stream Boundary Condition 62
3.4.1 For the Base Flow 62
3.4.2 For the Disturbance Flow 63
3.5 Outflow Boundary Condition 64
3.6 Wall Boundary Condition 64
3.6.1 For the Base Flow 64
3.6.2 For the Disturbance Flow 65
3.7 Disturbance Generation 65

4. Code Validation **67**
4.1 Flat Plate 67
4.2 Sharp Cone 68
4.3 Blunt Cone ($R_N = 0.15$") 71

5. Transition Investigations of a Boundary Layer on a Flat Plate . . **74**
5.1 Supersonic Flow at Mach 2 74
5.2 Physical Problem and Computational Setup 75
5.3 Identification of oblique breakdown 78
5.3.1 Receptivity Study 80
5.3.2 Linear Behavior 84

Table of Contents—*Continued*

- 5.3.3 Nonlinear Behavior 88
- 5.4 Asymmetric Subharmonic Resonance 96
  - 5.4.1 Linear Stability Considerations 96
  - 5.4.2 DNS Results 103
    - 5.4.2.1 Linear Behavior 104
    - 5.4.2.2 Simulation of Asymmetric Subharmonic Resonance . 107
- 5.5 Summary 117
- 5.6 Hypersonic Flow 119
  - 5.6.1 Oblique Breakdown 121
  - 5.6.2 Oblique Subharmonic Resonance 122
  - 5.6.3 Oblique Fundamental Resonance 123
  - 5.6.4 Fundamental Breakdown (K-Type) 124
  - 5.6.5 Subharmonic Breakdown (N-/H-Type) 127
- 5.7 Summary 128

6. Transition Investigations of a Boundary Layer on a Cylinder . . 130

- 6.1 Oblique Breakdown 132
- 6.2 Oblique Subharmonic Resonance 133
- 6.3 Oblique Fundamental Resonance 134
- 6.4 Fundamental Breakdown (K-Type) 135
- 6.5 Subharmonic Breakdown (N-/H-Type) 136
- 6.6 Summary 137

7. Transition Investigations of a Boundary Layer on a Sharp Cone . 138

- 7.1 Pulsed Disturbance 139
- 7.2 Oblique Breakdown 142
- 7.3 Oblique Subharmonic Resonance 147

Table of Contents—*Continued*

7.4 Oblique Fundamental Resonance 150

7.5 Breakdown Mechanisms involving steady vortices 153

7.6 Fundamental Breakdown (K-type) 155

7.7 Subharmonic Breakdown (N-/H-type) 160

7.8 Summary 164

8. Transition Investigations of a Boundary Layer on a Blunt Cone ($R_N = 0.15$") 166

8.1 Pulsed Disturbance 168

8.2 Oblique Breakdown 170

8.3 Oblique Subharmonic Resonance 172

8.4 Oblique Fundamental Resonance 176

8.5 Fundamental Breakdown (K-type) 178

8.6 Subharmonic Breakdown (N-/H-type) 180

8.7 Summary 181

9. Transition Investigations of a Boundary Layer on a Blunt Cone ($R_N = 0.7$") 182

9.1 Pulsed Disturbance 185

9.2 Breakdown Mechanisms of Slow Subsonic Disturbance Waves 186

  9.2.1 Oblique Breakdown 186

  9.2.2 Oblique Fundamental Resonance 188

9.3 Breakdown Mechanisms of Regular Disturbance Waves 189

9.4 Summary 191

10. Conclusions 192

10.1 Supersonic Flow at Mach 2 192

10.2 Hypersonic Flow at Mach 8 193

Table of Contents—*Continued*

Appendix A List of Vectors and Coefficients in the Governing Equations . . . 197

Appendix B Postprocessing of Simulation Results . . . 200

B.1 Amplitude Distribution Plots . . . 200

B.2 Vorticity . . . 201

B.3 Q-criterion . . . 201

B.4 Displacement thickness . . . 204

Appendix C Computational Parameters . . . 205

References . . . 225

List of Figures

1.1 Stages of the transition process (side and top view). 35

1.2 Computational domain for temporal DNS (taken from Balzer (2003)). . 43

2.1 Sharp Cone. $Ma = 7.95$, $Re = 3,333,333$, $T_\infty = 53.35K$. 57

2.2 Curvilinear coordinate transformation. 59

3.1 Initial condition. 61

3.2 Schematic of transferring data from the precursor simulation to the computational domain for transition investigations. 61

3.3 Computational domain. 62

4.1 (a) Linear stability diagram for two-dimensional waves at $Ma = 6.8$, $T_\infty = 71K$, adiabatic wall. (b) Amplification rate comparison of DNS with LST at $F = 8 \cdot 10^{-5}$. 68

4.2 Base-flow comparison. $Ma = 7.95$, $Re = 3,333,333$, $T_\infty = 53.35K$. . . . 69

4.3 Two-dimensional amplification rate compared with results from Fezer & Kloker (2004) and Chang & Malik (1993*a*). $Ma = 7.95$, $Re = 3,333,333$, $T_\infty = 53.35K$, $F = 1.17 \cdot 10^{-4}$, $A_{1,0} = 0.001\%$. 70

4.4 Wall pressure distribution in downstream direction of different disturbance waves. $Ma = 7.95$, $Re = 3,333,333$, $T_\infty = 53.35K$, $F = 1.17 \cdot 10^{-4}$. 70

4.5 Base-flow profiles of streamwise velocity at different downstream locations. Comparison of experimental measurements and numerical simulations. $Ma = 7.99$, $Re = 8,566,826$, $T_\infty = 54.47K$. 71

4.6 Boundary-layer thickness. Comparison of experimental measurements and numerical simulations. $Ma = 7.99$, $Re = 8,566,826$, $T_\infty = 54.47K$. . 71

4.7 Simplified generalized inflection point. Comparison of experimental data and numerical simulations. $Ma = 7.99$, $Re = 8,566,826$, $T_\infty = 54.47K$. . 72

List of Figures—*Continued*

4.8 Comparison of base-flow profiles with numerical efforts by Rosenboom *et al.* (1999) for two downstream locations. $Ma = 7.99$, $Re = 8,566,826$, $T_\infty = 54.47K$. 73

5.1 Comparison of experimental flat-plate model (H×L×W = $10 \times 450 \times 200mm$) with the computational domain. 76

5.2 Computational setup: (*a*) Contours of disturbance pressure ($20kHz$) with the spanwise wave number $\beta = 0.1mm^{-1}$ indicating that reflections from the free-stream boundary reach the near wall region inside the buffer domain downstream of the region of interest, (*b*) contours of disturbance pressure ($20kHz$) at the wall showing that the disturbances do not reach the spanwise boundaries. 77

5.3 Computational setup: (*a*) Grid in streamwise direction for a simulation with equidistant grid (–) (CFUND 1-4 and CSUB 1-10) and a simulation with increased resolution near the outflow (- -) (CFUND 5), grid in wall-normal direction for all simulations (...) discussed here, (*b*) symbols indicate grid locations used to resolve the second maximum of the wall-normal amplitude distribution for the u-velocity disturbance with $20kHz$ (■–■) and its corresponding wall-normal phase distribution (•- -•) at the spanwise wave number $\beta = 0.5mm^{-1}$ and the streamwise position $x^* = 0.06m$. 78

5.4 Spanwise amplitude (*a*) and phase (*b*) distribution ($20kHz$) of normalized output signal $(e^*)'/E^*$ (disturbance voltage over mean voltage) measured by a hot-wire anemometer in the experiment at streamwise location $x^* = 0.06m$ and wall-normal location $y^*/\delta^* = 0.53$: (□) experiment (Kosinov, 2006), (–) interpolated by a cubic spline. 80

List of Figures—*Continued*

5.5 Spanwise amplitude (*a*) and phase (*b*) distribution ($20kHz$) of normalized output signal $(e^*)'/E^*$ from figure 5.4 transformed into Fourier space using a symmetric FFT: (–) output signal of hotwire, (- -) mass-flux disturbance non-dimensionalized by mean values measured at $y^*/\delta^* = 0.53$, (■) mass-flux disturbance non-dimensionalized by mean values measured in the free stream. 83

5.6 Spanwise amplitude (*a*) and phase (*b*) distributions ($20kHz$) of mass-flux disturbance (ρu)' at wall-normal location $y^*/\delta^* = 0.53$ and streamwise location $x^* = 0.06m$: (...) Forcing (v-velocity over the disturbance slot) applied in the DNS, (–) response of mass-flux disturbance due to the forcing in the DNS, (■) experimental data, (*) calculated using equation (5.2) and (5.3). 83

5.7 Spanwise amplitude (*a*) and phase (*b*) distributions ($20kHz$) of mass-flux disturbance (ρu)' at wall-normal location $y^*/\delta^* = 0.53$ and streamwise location $x^* = 0.06m$ of the DNS (–) and the experiment (■ FFT by Kosinov, □ symmetric FFT) for the new amplitude and phase distributions of the v-velocity over the disturbance slot (...). 85

5.8 Isosurface of constant v-velocity disturbance over the disturbance slot for three different time instants. The v-velocity at the wall is disturbed by the dotted amplitude and phase distribution in figure 5.7 (CFUND 2). The dark bar indicates the disturbance slot. 85

5.9 Wall-normal amplitude and phase distribution of streamwise velocity disturbance and density disturbance for three different spanwise wave numbers for the fundamental frequency $20kHz$ at $x^* = 0.06m$. *Symbols* represent results obtained from LST (($\star$): amplitude, ($\times$): phase) and *lines* represent DNS results ((–): amplitude, (- -): phase). 87

List of Figures—*Continued*

5.10 Downstream development of complex streamwise wave number predicted by LST and by DNS (obtained from wall-pressure disturbance) for three different spanwise wave numbers and the fundamental frequency $20kHz$. 88

5.11 Temporal evolution of the mass-flux disturbance $(\rho u)'$ for the fundamental frequency ($20kHz$) at the wall-normal position $y^*/\delta^* = 0.53$ and the streamwise position $x^* = 0.06m$ for the experiment (*a*) (Kosinov, 2006) and the DNS (*b*) (CFUND 2): (–) positive disturbance amplitude, (...) negative disturbance amplitude. 89

5.12 Contour levels of the Fourier amplitude (*a*, *c*) and the phase (*b*, *d*) for the mass-flux disturbance $(\rho u)'$ with frequency $20kHz$ at wall-normal location $y^*/\delta^* = 0.53$ for different streamwise and spanwise locations: (*a*, *b*) DNS with low forcing amplitude (CFUND 2), (*c*, *d*) DNS with high forcing amplitude (CFUND 4). 91

5.13 Spanwise amplitude (*a*, *c*, *e*) and phase (*b*, *d*, *f*) distribution of the mass-flux disturbance $(\rho u)'$ ($20kHz$) at wall-normal location $y^*/\delta^* = 0.53$ for the streamwise positions $x^* = 0.11m$ (*a*, *b*), $x^* = 0.12m$ (*c*, *d*) and $x^* = 0.13m$ (*e*, *f*): (–) low forcing amplitude (CFUND 2), (*) medium forcing amplitude (CFUND 3), (- -) largest forcing amplitude (CFUND 4), (□) experiment (Kosinov, 2006). 93

5.14 Temporal evolution of the mass-flux disturbance $(\rho u)'$ for the fundamental frequency ($20kHz$) at the wall-normal position $y^*/\delta^* = 0.53$ and the streamwise position $x^* = 0.13m$ for the experiment (*a*) (Kosinov, 2006) and the DNS (*b*) (CFUND 4): (–) positive disturbance amplitude, (...) negative disturbance amplitude. 94

List of Figures—*Continued*

5.15 Contour levels of the Fourier amplitude for the mass flux disturbance (ρu)' at wall-normal location $y^*/\delta^* = 0.53$ for different streamwise and spanwise locations of the DNS. 95

5.16 *LINES*: Spanwise distribution of amplification rate α_i and streamwise wave number α_r at the positions $x^* = 0.06m$ and $x^* = 0.13m$. (—) $20kHz$, (−−) $10kHz$. *SYMBOLS*: Spanwise distribution of normalized amplitude N ($x_{ref} = 0.038$). (■) $20kHz$, (▼) $10kHz$. 98

5.17 Illustration of the procedure used to determine a particular asymmetric, subharmonic resonance triad using LST results. 102

5.18 Dependency of the spanwise wave number of both subharmonic waves (β^*_{10kHz}) included in the triad on the spanwise wave number of the primary wave (β^*_{20kHz}). 104

5.19 Downstream development of the streamwise wave number α^*_r for all three wave components of two asymmetric, subharmonic resonance triads from the first group. 104

5.20 Contour levels of Fourier amplitude (a,c) and phase (b,d) for the mass-flux disturbance (ρu)' at wall-normal location $y^*/\delta^* = 0.53$ for different streamwise and spanwise locations: (a,b) fundamental frequency, (c,d) subharmonic frequency. Note, the phase in figure 5.20b,d is plotted downstream of $x^* \simeq 0.04m$ marked by vertical dashed lines. 106

5.21 Spanwise amplitude (a) and phase (b) distribution for the mass-flux disturbance (ρu)' at wall-normal location $y^*/\delta^* = 0.53$ for two different streamwise positions. 107

List of Figures—*Continued*

5.22 Contour levels of Fourier amplitude (a) and phase (b) of the mass-flux disturbance (ρu)' for the subharmonic frequency $(10kHz)$ at wall-normal location $y^*/\delta^* = 0.53$ for different streamwise and spanwise locations (CSUB 1). 109

5.23 Spanwise amplitude distribution for CSUB 1 (a), CSUB 2 (b) and CSUB 3 (c) of the mass-flux disturbance (ρu)' for the subharmonic frequency $(10kHz)$ at wall-normal location $y^*/\delta^* = 0.53$. 110

5.24 Effect of phase difference $\Delta\theta_p^{2D}/\pi$ (phase difference between 2D fundamental waves and 2D subharmonic waves) on the contour levels of Fourier amplitude of the mass-flux disturbance (ρu)' for the subharmonic frequency $(10kHz)$ at wall-normal location $y^*/\delta^* = 0.53$ for different streamwise and spanwise locations. *(a)* $\Delta\theta_p^{2D}/\pi \simeq -0.15$ (CSUB 4), *(b)* $\Delta\theta_p^{2D}/\pi \simeq -0.30$ (CSUB 5), *(c)* $\Delta\theta_p^{2D}/\pi \simeq -0.45$ (CSUB 6), *(d)* $\Delta\theta_p^{2D}/\pi \simeq -0.60$ (CSUB 7), *(e)* $\Delta\theta_p^{2D}/\pi \simeq -0.75$ (CSUB 8), *(f)* $\Delta\theta_p^{2D}/\pi \simeq -0.90$ (CSUB 9) . . . 112

5.25 Spanwise wave number and amplitude value of first and second maximum in (ρu)' at $y^*/\delta^* = 0.53$ vs. phase difference $\Delta\theta_p^{2D}/\pi$ between subharmonic and fundamental forcing. For (b) and (d) the amplitudes are normalized by the forcing amplitude $\tilde{A}(\beta) = A$ (see also table 5.3). . . . 113

5.26 Spanwise amplitude distribution of the mass-flux disturbance (ρu)' for the subharmonic frequency $(10kHz)$: (a) experiment (Kosinov *et al.*, 1994), (b) theory (Tumin, 1996) and (c) DNS (CSUB 10) with $\Delta\theta_p^{2D}/\pi = -0.30$. Note the amplitudes of of all plots are arbitrarily scaled. 115

List of Figures—*Continued*

5.27 Contour levels of Fourier amplitude (a,c) and phase (b,d) of the mass-flux disturbance (ρu)' for the fundamental frequency ($20kHz$) and the subharmonic frequency ($10kHz$) at wall-normal location $y^*/\delta^* = 0.53$ for different streamwise and spanwise locations (CSUB 10, with $\Delta\theta_p^{2D}/\pi = -0.30$). 116

5.28 Spanwise amplitude (a) and phase (b) distribution for the mass-flux disturbance (ρu)' at wall-normal location $y^*/\delta^* = 0.53$ for two different streamwise positions. Comparison between DNS of the "entire" experiment including the subharmonic resonance and results from a simulation of the nonlinear disturbance development for the fundamental frequency only (see figures 5.13 and 5.7). 117

5.29 Boundary-layer properties. $Ma = 6.8$, $Re = 4,790,000$, $T_\infty = 71K$. . . . 119

5.30 Boundary-layer properties (normalized with boundary layer thickness). $Ma = 6.8$, $Re = 4,790,000$, $T_\infty = 71K$. 119

5.31 Linear amplification rates. *Sharp cone:* $Ma = 8$, $Re = 3,333,333$, $T_\infty = 53.35K$, $F_{1,0} = 1.17 \cdot 10^{-4}$, $A_{1,0} = 1 \cdot 10^{-3}\%$, $F_{1,1} = 5.85 \cdot 10^{-5}$, $A_{1,1} = 1 \cdot 10^{-3}\%$, $\Psi_{1,1} = 60°$. *Flat plate:* $Ma = 6.8$, $Re = 4,790,000$, $T_\infty = 71K$, $F_{1,0} = 8 \cdot 10^{-5}$, $A_{1,0} = 1 \cdot 10^{-3}\%$, $F_{1,1} = 4 \cdot 10^{-5}$, $A_{1,1} = 1 \cdot 10^{-3}\%$, $\Psi_{1,1} = 60°$. 120

5.32 Oblique breakdown. $Ma = 6.8$, $Re = 4,790,000$, $T_\infty = 71K$, $F = 8 \cdot 10^{-5}$, $A_{1,1} = 1\%$, $\Psi = 20°$. 121

5.33 Oblique breakdown. $Ma = 6.8$, $Re = 4,790,000$, $T_\infty = 71K$, $F = 8 \cdot 10^{-5}$, $A_{1,1} = 5\%$, $\Psi = 20°$. 121

5.34 Oblique subharmonic resonance. $Ma = 6.8$, $Re = 4,790,000$, $T_\infty = 71K$, $F = 8 \cdot 10^{-5}$, $A_{2,1} = 5\%$, $A_{1,1} = 5\%$, $\Psi_{2,1} = 20°$. 123

5.35 Oblique subharmonic resonance. $Ma = 6.8$, $Re = 4,790,000$, $T_\infty = 71K$, $F = 8 \cdot 10^{-5}$, $A_{2,1} = 2\%$, $A_{1,1} = 2\%$, $A_{0,1} = 1\%$, $\Psi_{2,1} = 20°$. 123

List of Figures—*Continued*

5.36 Oblique fundamental resonance. $Ma = 6.8$, $Re = 4,790,000$, $T_\infty = 71K$, $F = 8 \cdot 10^{-5}$, $A_{1,1} = 5\%$, $A_{1,2} = 5\%$, $\Psi_{1,1} = 20°$. 123

5.37 Oblique fundamental resonance. $Ma = 6.8$, $Re = 4,790,000$, $T_\infty = 71K$, $F = 8 \cdot 10^{-5}$, $A_{1,1} = 1\%$, $A_{1,2} = 1\%$, $A_{0,1} = 1\%$, $\Psi_{1,1} = 20°$. 124

5.38 Oblique fundamental resonance. $Ma = 6.8$, $Re = 4,790,000$, $T_\infty = 71K$, $F = 8 \cdot 10^{-5}$, $A_{1,1} = 1\%$, $A_{1,2} = 1\%$, $\Psi_{1,1} = 20°$. 124

5.39 Fundamental breakdown. $Ma = 6.8$, $Re = 4,790,000$, $T_\infty = 71K$, $F = 8 \cdot 10^{-5}$, $A_{1,0} = 5\%$, $A_{1,1} = 1 \cdot 10^{-3}\%$, $\Psi_{1,1} = 60°$. 125

5.40 Fundamental breakdown. $Ma = 6.8$, $Re = 4,790,000$, $T_\infty = 71K$, $F = 8 \cdot 10^{-5}$, $A_{1,0} = 5\%$, $A_{1,1} = 1 \cdot 10^{-3}\%$, $A_{0,1} = 1\%$, $\Psi_{1,1} = 60°$. 126

5.41 Fundamental breakdown. $Ma = 6.8$, $Re = 4,790,000$, $T_\infty = 71K$, $F = 8 \cdot 10^{-5}$, $A_{1,0} = 5\%$, $A_{1,1} = 1 \cdot 10^{-3}\%$, $A_{0,1} = 5\%$, $\Psi_{1,1} = 60°$. 126

5.42 Subharmonic breakdown. $Ma = 6.8$, $Re = 4,790,000$, $T_\infty = 71K$, $F_{2,0} = 8 \cdot 10^{-5}$, $A_{2,0} = 5\%$, $A_{1,1} = 1 \cdot 10^{-2}\%$, $\Psi_{1,1} = 60°$. 127

5.43 Subharmonic breakdown. $Ma = 6.8$, $Re = 4,790,000$, $T_\infty = 71K$, $F_{2,0} = 8 \cdot 10^{-5}$, $A_{2,0} = 5\%$, $A_{1,1} = 1 \cdot 10^{-2}\%$, $A_{0,1} = 1\%$, $\Psi_{1,1} = 60°$. 127

6.1 Numerical set-up for the cylindrical investigations in comparison to the sharp cone set-up. 131

6.2 Boundary-layer thickness ratio based on radius for the cone and the cylinder. *Cone:* $Ma = 8$, $Re = 3,333,333$, $T_\infty = 53.35K$. *Cylinder:* $Ma = 6.8$, $Re = 4,790,000$, $T_\infty = 71K$. 131

6.3 Boundary-layer properties for the flat plate, cylinder, and cone. *Flat Plate/Cylinder:* $Ma = 6.8$, $Re = 4,790,000$, $T_\infty = 71K$. *Cone:* $Ma = 8$, $Re = 3,333,333$, $T_\infty = 53.35K$. 131

List of Figures—*Continued*

6.4 Comparison of linear amplification rate for the flat plate and the cylinder. $Ma = 6.8$, $Re = 4,790,000$, $T_\infty = 71K$, $F_{1,0} = 8 \cdot 10^{-5}$, $F_{1,1} = 4 \cdot 10^{-5}$, $\Psi_{1,1} = 60°$. 131

6.5 Oblique breakdown. $Ma = 6.8$, $Re = 4,790,000$, $T_\infty = 71K$, $F = 8 \cdot 10^{-5}$, $A_{1,1} = 1\%$, $\Psi = 20°$. 132

6.6 Oblique breakdown. $Ma = 6.8$, $Re = 4,790,000$, $T_\infty = 71K$, $F = 8 \cdot 10^{-5}$, $A_{1,1} = 5\%$, $\Psi = 20°$. 133

6.7 Oblique breakdown. $Ma = 6.8$, $Re = 4,790,000$, $T_\infty = 71K$, $F = 8 \cdot 10^{-5}$, $A_{1,1} = 5\%$, $\Psi = 20°$. 133

6.8 Oblique subharmonic resonance. $Ma = 6.8$, $Re = 4,790,000$, $T_\infty = 71K$, $F = 8 \cdot 10^{-5}$, $A_{2,1} = 2\%$, $A_{1,1} = 2\%$, $\Psi_{2,1} = 20°$. 134

6.9 Oblique subharmonic resonance. $Ma = 6.8$, $Re = 4,790,000$, $T_\infty = 71K$, $F = 8 \cdot 10^{-5}$, $A_{2,1} = 2\%$, $A_{1,1} = 2\%$, $A_{0,1} = 1\%$, $\Psi_{2,1} = 20°$. 134

6.10 Oblique fundamental resonance. $Ma = 6.8$, $Re = 4,790,000$, $T_\infty = 71K$, $F_{1,1} = 8 \cdot 10^{-5}$, $A_{1,1} = 2\%$, $A_{1,2} = 2\%$, $\Psi_{1,1} = 20°$. 134

6.11 Oblique fundamental resonance. $Ma = 6.8$, $Re = 4,790,000$, $T_\infty = 71K$, $F_{1,1} = 8 \cdot 10^{-5}$, $A_{1,1} = 2\%$, $A_{1,2} = 2\%$, $A_{0,1} = 1\%$, $\Psi_{1,1} = 20°$. 134

6.12 Fundamental breakdown. $Ma = 6.8$, $Re = 4,790,000$, $T_\infty = 71K$, $F = 8 \cdot 10^{-5}$, $A_{1,0} = 5\%$, $A_{1,1} = 1 \cdot 10^{-3}\%$, $\Psi_{1,1} = 60°$. 135

6.13 Fundamental breakdown. $Ma = 6.8$, $Re = 4,790,000$, $T_\infty = 71K$, $F = 8 \cdot 10^{-5}$, $A_{1,0} = 5\%$, $A_{1,1} = 1 \cdot 10^{-3}\%$, $A_{0,1} = 1\%$, $\Psi_{1,1} = 60°$. 135

6.14 Subharmonic breakdown. $Ma = 6.8$, $Re = 4,790,000$, $T_\infty = 71K$, $F_{2,0} = 8 \cdot 10^{-5}$, $A_{2,0} = 5\%$, $A_{1,1} = 1 \cdot 10^{-3}\%$, $\Psi_{1,1} = 60°$. 136

6.15 Subharmonic breakdown. $Ma = 6.8$, $Re = 4,790,000$, $T_\infty = 71K$, $F_{2,0} = 8 \cdot 10^{-5}$, $A_{2,0} = 5\%$, $A_{1,1} = 1 \cdot 10^{-3}\%$, $A_{0,1} = 1\%$, $\Psi_{1,1} = 60°$. 137

List of Figures—*Continued*

6.16 Subharmonic breakdown. $Ma = 6.8$, $Re = 4,790,000$, $T_\infty = 71K$, $F_{2,0} = 8 \cdot 10^{-5}$, $A_{2,0} = 5\%$, $A_{1,1} = 1 \cdot 10^{-3}\%$, $A_{0,2} = 1\%$, $\Psi_{1,1} = 60°$. 137

7.1 Comparison of amplification rates at $\Psi = 0°$ and $\Psi = 20°$. $Ma = 7.95$, $Re = 3,333,333$, $T_\infty = 53.35K$, $F = 1.17 \cdot 10^{-4}$. 138

7.2 Wall-pressure distribution in downstream direction of different disturbance waves. $Ma = 7.95$, $Re = 3,333,333$, $T_\infty = 53.35K$, $F = 1.17 \cdot 10^{-4}$. 139

7.3 Wall-pressure distribution in downstream direction of different disturbance waves and their higher harmonics. $Ma = 7.95$, $Re = 3,333,333$, $T_\infty = 53.35K$, $F = 1.17 \cdot 10^{-4}$. 139

7.4 Spectral input signal of pulsed disturbance. $Ma = 7.95$, $Re = 3,333,333$, $T_\infty = 53.35K$, $\Psi = 20°$. 141

7.5 Linear amplification rate for selected frequencies. $Ma = 7.95$, $Re = 3,333,333$, $T_\infty = 53.35K$, $\Psi = 20°$. 141

7.6 Amplitude distribution based on wall pressure for selected frequencies. $Ma = 7.95$, $Re = 3,333,333$, $T_\infty = 53.35K$, $\Psi = 20°$. 141

7.7 Linear amplification rate plotted over frequency at different downstream locations. $Ma = 7.95$, $Re = 3,333,333$, $T_\infty = 53.35K$, $\Psi = 20°$. 141

7.8 Oblique breakdown. ρ'-amplitude distribution. $Ma = 7.95$, $Re = 3,333,333$, $T_\infty = 53.35K$, $F = 4.9 \cdot 10^{-5}$, $A_{1,1} = 1\%$, $\Psi = 60°$. 142

7.9 Oblique breakdown. ρ'-amplitude distribution. $Ma = 7.95$, $Re = 3,333,333$, $T_\infty = 53.35K$, $F = 1.17 \cdot 10^{-4}$, $A_{1,1} = 1\%$, $\Psi = 20°$. 142

7.10 Oblique breakdown. Vortical structures identified by the Q-criterion (Q = 500). $Ma = 7.95$, $Re = 3,333,333$, $T_\infty = 53.35K$, $F = 1.17 \cdot 10^{-4}$, $A_{1,1} = 1\%$, $\Psi = 20°$. 143

List of Figures—*Continued*

7.11 Oblique breakdown. Steady vortical structures identified by the Q-criterion (Q = 100). $Ma = 7.95$, $Re = 3,333,333$, $T_\infty = 53.35K$, $F = 1.17 \cdot 10^{-4}$, $A_{1,1} = 1\%$, $\Psi = 20°$. 144

7.12 Oblique breakdown. ρ'-amplitude distribution. $Ma = 7.95$, $Re = 3,333,333$, $T_\infty = 53.35K$, $F = 9.8 \cdot 10^{-5}$, $A_{1,1} = 1\%$, $\Psi = 26°$. 145

7.13 Oblique breakdown. Vortical structures identified by the Q-criterion (Q = 500). $Ma = 7.95$, $Re = 3,333,333$, $T_\infty = 53.35K$, $F = 9.8 \cdot 10^{-5}$, $A_{1,1} = 1\%$, $\Psi = 26°$. 145

7.14 Oblique breakdown. Vortical structures identified by the Q-criterion (Q = 1,500). $Ma = 7.95$, $Re = 3,333,333$, $T_\infty = 53.35K$, $F = 9.8 \cdot 10^{-5}$, $A_{1,1} = 1\%$, $\Psi = 26°$. 146

7.15 Oblique breakdown. Wall-normal heat flux. a) at the wall. b) at the boundary-layer edge. $Ma = 7.95$, $Re = 3,333,333$, $T_\infty = 53.35K$, $F = 9.8 \cdot 10^{-5}$, $A_{1,1} = 1\%$, $\Psi = 26°$. 146

7.16 Oblique breakdown. Flat Plate. ρ'-amplitude distribution. $Ma = 6.8$, $Re = 4,790,000$, $T_\infty = 71K$, $F = 8 \cdot 10^{-5}$, $A_{1,1} = 2\%$, $\Psi = 20°$. 146

7.17 Oblique breakdown. Flat Plate. Vortical structures identified by the Q-criterion (Q = 500). $Ma = 6.8$, $Re = 4,790,000$, $T_\infty = 71K$, $F = 8 \cdot 10^{-5}$, $A_{1,1} = 2\%$, $\Psi = 20°$. 146

7.18 Oblique subharmonic resonance. ρ'-amplitude distribution. $Ma = 7.95$, $Re = 3,333,333$, $T_\infty = 53.35K$, $F_{2,1} = 1.17 \cdot 10^{-4}$, $A_{2,1} = 1\%$, $\Psi_{2,1} = 20°$, $F_{1,1} = 5.85 \cdot 10^{-5}$, $A_{1,1} = 1\%$, $\Psi_{1,1} = 36°$. 147

7.19 Oblique subharmonic resonance. Streamwise wave number and phase velocity. $Ma = 7.95$, $Re = 3,333,333$, $T_\infty = 53.35K$, $F_{2,1} = 1.17 \cdot 10^{-4}$, $A_{2,1} = 1\%$, $\Psi_{2,1} = 20°$, $F_{1,1} = 5.85 \cdot 10^{-5}$, $A_{1,1} = 1\%$, $\Psi_{1,1} = 36°$. 149

List of Figures—*Continued*

7.20 Oblique subharmonic resonance. ρ'-amplitude distribution. $Ma = 7.95$, $Re = 3,333,333$, $T_\infty = 53.35K$, $F_{2,1} = 9.8 \cdot 10^{-5}$, $A_{2,1} = 1\%$, $\Psi_{2,1} = 20°$, $F_{1,1} = 4.9 \cdot 10^{-5}$, $A_{1,1} = 1\%$, $A_{0,1} = 1\%$, $\Psi_{1,1} = 36°$. 149

7.21 Oblique subharmonic resonance. Vortical structures identified by the Q-criterion (Q = 500). $Ma = 7.95$, $Re = 3,333,333$, $T_\infty = 53.35K$, $F_{2,1} = 9.8 \cdot 10^{-5}$, $A_{2,1} = 1\%$, $\Psi_{2,1} = 20°$, $F_{1,1} = 4.9 \cdot 10^{-5}$, $A_{1,1} = 1\%$, $A_{0,1} = 1\%$, $\Psi_{1,1} = 36°$. 149

7.22 Oblique fundamental resonance. ρ'-amplitude distribution. $Ma = 7.95$, $Re = 3,333,333$, $T_\infty = 53.35K$, $F = 1.17 \cdot 10^{-4}$, $A_{1,1} = 1\%$, $\Psi_{1,1} = 20°$, $\Psi_{1,2} = 36°$. 150

7.23 Oblique fundamental resonance. ρ'-amplitude distribution. $Ma = 7.95$, $Re = 3,333,333$, $T_\infty = 53.35K$, $F_{1,1} = 9.8 \cdot 10^{-5}$, $A_{1,1} = 1\%$, $A_{1,2} = 1\%$, $A_{0,1} = 1\%$, $\Psi_{1,1} = 20°$, $\Psi_{1,2} = 36°$. 152

7.24 Oblique fundamental resonance. Phase speed. $Ma = 7.95$, $Re = 3,333,333$, $T_\infty = 53.35K$, $F_{1,1} = 9.8 \cdot 10^{-5}$, $A_{1,1} = 1\%$, $A_{1,2} = 1\%$, $A_{0,1} = 1\%$, $\Psi_{1,1} = 20°$, $\Psi_{1,2} = 36°$. 152

7.25 Oblique fundamental resonance. Vortical structures identified by the Q-criterion (Q = 500). $Ma = 7.95$, $Re = 3,333,333$, $T_\infty = 53.35K$, $F_{1,1} = 9.8 \cdot 10^{-5}$, $A_{1,1} = 1\%$, $A_{1,2} = 1\%$, $A_{0,1} = 1\%$, $\Psi_{1,1} = 20°$, $\Psi_{1,2} = 36°$. . . . 152

7.26 Steady vortex mode. ρ'-amplitude distribution. $Ma = 7.95$, $Re = 3,333,333$, $T_\infty = 53.35K$, $F = 1.17 \cdot 10^{-4}$, $A_{1,0} = 1\%$, $\Psi_{0,1} = 20°$. 154

7.27 Steady vortex mode. ρ'-amplitude distribution. $Ma = 7.95$, $Re = 3,333,333$, $T_\infty = 53.35K$, $F = 1.17 \cdot 10^{-4}$, $A_{1,0} = 1\%$, $\Psi_{0,1} = 60°$. 154

7.28 Fundamental breakdown. ρ'-amplitude distribution. $Ma = 7.95$, $Re = 3,333,333$, $T_\infty = 53.35K$, $F = 9.8 \cdot 10^{-5}$, $A_{1,0} = 1\%$, $A_{1,1} = 0.001\%$, $\Psi_{1,1} = 60°$. 155

List of Figures—*Continued*

7.29 Fundamental breakdown. ρ'-amplitude distribution. $Ma = 7.95$, $Re = 3,333,333$, $T_\infty = 53.35K$, $F = 9.8 \cdot 10^{-5}$, $A_{1,0} = 1\%$, $A_{1,1} = 0.001\%$, $A_{0,1} = 1\%$, $\Psi_{1,1} = 60°$. 155

7.30 Fundamental breakdown. Phase speed. $Ma = 7.95$, $Re = 3,333,333$, $T_\infty = 53.35K$, $F = 9.8 \cdot 10^{-5}$, $A_{1,0} = 1\%$, $A_{1,1} = 0.001\%$, $\Psi_{1,1} = 60°$. . . 156

7.31 Fundamental breakdown. Wall-normal phase distribution. $Ma = 7.95$, $Re = 3,333,333$, $T_\infty = 53.35K$, $F = 9.8 \cdot 10^{-5}$, $A_{1,0} = 1\%$, $A_{1,1} = 0.001\%$, $\Psi_{1,1} = 60°$. 157

7.32 Fundamental breakdown. ρ'-amplitude distribution. $Ma = 7.95$, $Re = 3,333,333$, $T_\infty = 53.35K$, $F = 9.8 \cdot 10^{-5}$, $A_{1,0} = 1\%$, $A_{1,1} = 0.001\%$, $\Psi_{1,1} = 20°$. 158

7.33 Fundamental breakdown. ρ'-amplitude distribution. $Ma = 7.95$, $Re = 3,333,333$, $T_\infty = 53.35K$, $F = 9.8 \cdot 10^{-5}$, $A_{1,0} = 1\%$, $A_{1,1} = 0.001\%$, $\Psi_{1,1} = 60°$, $\Delta\phi = 1.93511$. 158

7.34 Fundamental breakdown. ρ'-amplitude distribution. $Ma = 7.95$, $Re = 3,333,333$, $T_\infty = 53.35K$, $F = 9.8 \cdot 10^{-5}$, $A_{1,0} = 5\%$, $A_{1,1} = 0.001\%$, $A_{0,1} = 1\%$, $\Psi_{1,1} = 60°$. 159

7.35 Fundamental breakdown. Vortical structures identified by the Q-criterion (Q = 500). $Ma = 7.95$, $Re = 3,333,333$, $T_\infty = 53.35K$, $F = 9.8 \cdot 10^{-5}$, $A_{1,0} = 1\%$, $A_{1,1} = 0.001\%$, $\Psi_{1,1} = 60°$. 159

7.36 Fundamental breakdown. Temporal *DNS*. ρ'-amplitude development in time. $Ma = 7.95$, $Re = 3,333,333$, $T_\infty = 53.35K$, $F = 9.8 \cdot 10^{-5}$, $A_{1,0} = 1\%$, $A_{1,1} = 0.001\%$, $\Psi_{1,1} = 60°$. 159

7.37 Fundamental breakdown. Temporal *DNS*. ρ'-base-flow profiles at different times. $Ma = 7.95$, $Re = 3,333,333$, $T_\infty = 53.35K$, $F = 9.8 \cdot 10^{-5}$, $A_{1,0} = 1\%$, $A_{1,1} = 0.001\%$, $\Psi_{1,1} = 60°$. 159

List of Figures—*Continued*

7.38 Subharmonic breakdown. Phase speed. $Ma = 7.95$, $Re = 3,333,333$, $T_\infty = 53.35K$, $F = 9.8 \cdot 10^{-5}$, $A_{2,0} = 1\%$, $A_{1,1} = 0.001\%, \Psi_{1,1} = 60°$. . . . 160

7.39 Subharmonic breakdown. ρ'-amplitude distribution. $Ma = 7.95$, $Re = 3,333,333$, $T_\infty = 53.35K$, $F = 9.8 \cdot 10^{-5}$, $A_{2,0} = 1\%$, $A_{1,1} = 0.001\%, \Psi_{1,1} = 60°$. . . . 161

7.40 Subharmonic breakdown. ρ'-amplitude distribution. $Ma = 7.95$, $Re = 3,333,333$, $T_\infty = 53.35K$, $F = 9.8 \cdot 10^{-5}$, $A_{2,0} = 1\%$, $A_{1,1} = 0.001\%$, $A_{0,1} = 1\%$, $\Psi_{1,1} = 60°$. . . . 161

7.41 Comparison of mean-flow profiles with and without steady vortex mode. $Ma = 7.95$, $Re = 3,333,333$, $T_\infty = 53.35K$, $F = 1.17 \cdot 10^{-4}$. . . . 161

7.42 Subharmonic breakdown. Phase speed. $Ma = 7.95$, $Re = 3,333,333$, $T_\infty = 53.35K$, $F = 9.8 \cdot 10^{-5}$, $A_{2,0} = 1\%$, $A_{1,1} = 0.001\%$, $A_{0,1} = 1\%$, $\Psi_{1,1} = 60°$. . . . 162

7.43 Comparison of subharmonic breakdown with fundamental breakdown. ρ'-amplitude distribution. $Ma = 7.95$, $Re = 3,333,333$, $T_\infty = 53.35K$, $F = 9.8 \cdot 10^{-5}$, $A_{primary} = 1\%$, $A_{secondary} = 0.001\%, \Psi_{secondary} = 60°$. . . . 162

7.44 Subharmonic breakdown. Temporal DNS. ρ'-amplitude development in time. $Ma = 7.95$, $Re = 3,333,333$, $T_\infty = 53.35K$, $F = 9.8 \cdot 10^{-5}$, $A_{2,0} = 1\%$, $A_{1,1} = 0.001\%$, $\Psi_{1,1} = 60°$. . . . 164

7.45 Subharmonic breakdown. ρ'-amplitude distribution. ρ'-amplitude development in time. $Ma = 7.95$, $Re = 3,333,333$, $T_\infty = 53.35K$, $F = 1.96 \cdot 10^{-4}$, $A_{2,0} = 1\%$, $A_{1,1} = 0.001\%, \Psi_{1,1} = 60°$. . . . 164

8.1 Base-flow profiles. Comparison of blunt cone with sharp cone for three different downstream locations. $Ma = 7.95$, $Re = 3,333,333$, $T_\infty = 53.35K$. 167

List of Figures—*Continued*

8.2 Simplified generalized inflection point criterion for three different location in comparison with sharp cone results. $Ma = 7.95$, $Re = 3,333,333$, $T_\infty = 53.35K$. 168
8.3 Linear amplification rate for different frequencies. $Ma = 7.95$, $Re = 3,333,333$, $T_\infty = 53.35K$, $\Psi = 20°$. 168
8.4 Spectral input signal of pulsed disturbance. $Ma = 7.95$, $Re = 3,333,333$, $T_\infty = 53.35K$, $\Psi = 20°$. 169
8.5 Linear amplification rate for selected frequencies. $Ma = 7.95$, $Re = 3,333,333$, $T_\infty = 53.35K$, $\Psi = 20°$. 169
8.9 Comparison of T'-amplitude distribution. $Ma = 7.95$, $Re = 3,333,333$, $T_\infty = 53.35K$, $F = 9.8 \cdot 10^{-5}$, $\Psi = 0°$. 169
8.6 Amplitude distribution based on wall pressure for different frequencies. $Ma = 7.95$, $Re = 3,333,333$, $T_\infty = 53.35K$, $\Psi = 20°$. 170
8.7 Base-flow properties of the blunt cone (dashed) compared to the sharp cone (solid). 170
8.8 Linear amplification rate plotted over frequency for different downstream locations. $Ma = 7.95$, $Re = 3,333,333$, $T_\infty = 53.35K$, $\Psi = 20°$. 171
8.10 Oblique breakdown. ρ'-amplitude distribution. $Ma = 7.95$, $Re = 3,333,333$, $T_\infty = 53.35K$, $F = 4.9 \cdot 10^{-5}$, $A_{1,1} = 1\%$, $\Psi = 70°$. 172
8.11 Oblique breakdown. ρ'-amplitude distribution. $Ma = 7.95$, $Re = 3,333,333$, $T_\infty = 53.35K$, $F = 1.17 \cdot 10^{-4}$, $A_{1,1} = 1\%$, $\Psi = 20°$. 172
8.12 Oblique subharmonic resonance. ρ'-amplitude distribution. $Ma = 7.95$, $Re = 3,333,333$, $T_\infty = 53.35K$, $F = 4.9 \cdot 10^{-5}$, $A_{2,1} = 1\%$, $A_{1,1} = 1\%$, $\Psi_{2,1} = 70°$, $\Psi_{1,1} = 80°$. 173

List of Figures—*Continued*

8.13 Oblique subharmonic resonance. ρ'-amplitude distribution. $Ma = 7.95$, $Re = 3,333,333$, $T_\infty = 53.35K$, $F = 4.9 \cdot 10^{-5}$, $A_{2,1} = 1\%$, $A_{1,1} = 1\%$, $A_{0,1} = 1\%$, $\Psi_{2,1} = 70°$, $\Psi_{1,1} = 80°$. 173

8.14 Oblique subharmonic resonance. ρ'-amplitude distribution. $Ma = 7.95$, $Re = 3,333,333$, $T_\infty = 53.35K$, $F = 9.8 \cdot 10^{-5}$, $A_{2,1} = 1\%$, $A_{1,1} = 1\%$, $\Psi_{2,1} = 20°$, $\Psi_{1,1} = 36°$. 174

8.15 Oblique subharmonic resonance. ρ'-amplitude distribution. $Ma = 7.95$, $Re = 3,333,333$, $T_\infty = 53.35K$, $F = 9.8 \cdot 10^{-5}$, $A_{2,1} = 1\%$, $A_{1,1} = 1\%$, $A_{0,1} = 1\%$, $\Psi_{2,1} = 20°$, $\Psi_{1,1} = 36°$. 174

8.16 Oblique subharmonic resonance. Phase velocity. $Ma = 7.95$, $Re = 3,333,333$, $T_\infty = 53.35K$, $F = 9.8 \cdot 10^{-5}$, $A_{2,1} = 1\%$, $A_{1,1} = 1\%$, $\Psi_{2,1} = 20°$, $\Psi_{1,1} = 36°$. 174

8.17 Oblique subharmonic resonance. Phase velocity. $Ma = 7.95$, $Re = 3,333,333$, $T_\infty = 53.35K$, $F = 9.8 \cdot 10^{-5}$, $A_{2,1} = 1\%$, $A_{1,1} = 1\%$, $A_{0,1} = 1\%$, $\Psi_{2,1} = 20°$, $\Psi_{1,1} = 36°$. 174

8.18 Oblique subharmonic resonance. Vortical structures identified by the Q-criterion (Q = 500). $Ma = 7.95$, $Re = 3,333,333$, $T_\infty = 53.35K$, $F_{2,1} = 9.8 \cdot 10^{-5}$, $A_{2,1} = 1\%$, $\Psi_{2,1} = 20°$, $F_{1,1} = 4.9 \cdot 10^{-5}$, $A_{1,1} = 1\%$, $\Psi_{1,1} = 36°$. 175

8.19 Oblique subharmonic resonance. Vortical structures identified by the Q-criterion (Q = 500). $Ma = 7.95$, $Re = 3,333,333$, $T_\infty = 53.35K$, $F_{2,1} = 9.8 \cdot 10^{-5}$, $A_{2,1} = 1\%$, $\Psi_{2,1} = 20°$, $F_{1,1} = 4.9 \cdot 10^{-5}$, $A_{1,1} = 1\%$, $A_{0,1} = 1\%$, $\Psi_{1,1} = 36°$. 175

8.20 Oblique fundamental resonance. ρ'-amplitude distribution. $Ma = 7.95$, $Re = 3,333,333$, $T_\infty = 53.35K$, $F = 4.9 \cdot 10^{-5}$, $A_{1,1} = 1\%$, $A_{1,2} = 1\%$, $\Psi_{1,1} = 70°$, $\Psi_{1,2} = 80°$. 176

List of Figures—*Continued*

8.21 Oblique fundamental resonance. ρ'-amplitude distribution. $Ma = 7.95$, $Re = 3,333,333$, $T_\infty = 53.35K$, $F = 4.9 \cdot 10^{-5}$, $A_{1,1} = 1\%$, $A_{1,2} = 1\%$, $A_{0,1} = 1\%$, $\Psi_{1,1} = 70°$, $\Psi_{1,2} = 80°$. 176

8.22 Oblique fundamental resonance. Phase velocity. $Ma = 7.95$, $Re = 3,333,333$, $T_\infty = 53.35K$, $F = 9.8 \cdot 10^{-5}$, $A_{1,1} = 1\%$, $A_{1,2} = 1\%$, $\Psi_{1,1} = 20°$, $\Psi_{1,2} = 36°$. 177

8.23 Oblique fundamental resonance. ρ'-amplitude. $Ma = 7.95$, $Re = 3,333,333$, $T_\infty = 53.35K$, $F = 9.8 \cdot 10^{-5}$, $A_{1,1} = 1\%$, $A_{1,2} = 1\%$, $A_{0,1} = 1\%$, $\Psi_{1,1} = 20°$, $\Psi_{1,2} = 36°$. 177

8.24 Oblique fundamental resonance. Phase velocity. $Ma = 7.95$, $Re = 3,333,333$, $T_\infty = 53.35K$, $F = 9.8 \cdot 10^{-5}$, $A_{1,1} = 1\%$, $A_{1,2} = 1\%$, $A_{0,1} = 1\%$, $\Psi_{1,1} = 20°$, $\Psi_{1,2} = 36°$. 177

8.25 Oblique fundamental resonance. ρ'-amplitude. $Ma = 7.95$, $Re = 3,333,333$, $T_\infty = 53.35K$, $F = 9.8 \cdot 10^{-5}$, $A_{1,1} = 1\%$, $A_{1,2} = 1\%$, $A_{0,1} = 1\%$, $\Psi_{1,1} = 20°$, $\Psi_{1,2} = 36°$. 177

8.26 Fundamental breakdown. ρ'-amplitude distribution. $Ma = 7.95$, $Re = 3,333,333$, $T_\infty = 53.35K$, $F = 9.8 \cdot 10^{-5}$, $A_{1,0} = 1\%$, $A_{1,1} = 1 \cdot 10^{-3}\%$, $\Psi = 41°$. 179

8.27 Fundamental breakdown. ρ'-amplitude distribution. $Ma = 7.95$, $Re = 3,333,333$, $T_\infty = 53.35K$, $F = 9.8 \cdot 10^{-5}$, $A_{1,0} = 1\%$, $A_{1,1} = 1 \cdot 10^{-3}\%$, $A_{0,1} = 1\%$, $\Psi = 41°$. 179

8.28 Fundamental breakdown. ρ'-amplitude distribution. $Ma = 7.95$, $Re = 3,333,333$, $T_\infty = 53.35K$, $F = 9.8 \cdot 10^{-5}$, $A_{1,0} = 1\%$, $A_{1,1} = 1 \cdot 10^{-3}\%$, $\Psi = 60°$. 179

List of Figures—*Continued*

8.29 Fundamental breakdown. ρ'-amplitude distribution. $Ma = 7.95$, $Re = 3,333,333$, $T_\infty = 53.35K$, $F = 9.8 \cdot 10^{-5}$, $A_{1,0} = 1\%$, $A_{1,1} = 1 \cdot 10^{-3}\%$, $A_{0,1} = 1\%$, $\Psi = 60°$. 179

8.30 Subharmonic breakdown. ρ'-amplitude distribution. $Ma = 7.95$, $Re = 3,333,333$, $T_\infty = 53.35K$, $F = 9.8 \cdot 10^{-5}$, $A_{2,0} = 1\%$, $A_{1,1} = 1 \cdot 10^{-3}\%$, $\Psi = 60°$. 180

8.31 Subharmonic breakdown. ρ'-amplitude distribution. $Ma = 7.95$, $Re = 3,333,333$, $T_\infty = 53.35K$, $F = 9.8 \cdot 10^{-5}$, $A_{2,0} = 1\%$, $A_{1,1} = 1 \cdot 10^{-3}\%$, $A_{0,1} = 1\%$, $\Psi = 60°$. 180

9.1 Edge Mach number comparison. $Ma = 7.95$, $Re = 3,333,333$, $T_\infty = 53.35K$. 183

9.2 Comparison of boundary-layer thickness and displacement thickness for different nose radii. $Ma = 7.95$, $Re = 3,333,333$, $T_\infty = 53.35K$. 183

9.3 Flow field around the blunt cone with a nose radius of $R_N = 0.7"$. $Ma = 7.95$, $Re = 3,333,333$, $T_\infty = 53.35K$. 184

9.4 Wall-temperature distribution for different nose radii. $Ma = 7.95$, $Re = 3,333,333$, $T_\infty = 53.35K$. 186

9.5 Wall-normal location of the generalized inflection point and the critical layer. $Ma = 7.95$, $Re = 3,333,333$, $T_\infty = 53.35K$. 186

9.6 Oblique breakdown. ρ'-amplitude distribution. $Ma = 7.95$, $Re = 3,333,333$, $T_\infty = 53.35K$, $F = 8.7 \cdot 10^{-5}$, $A_{1,1} = 5\%$, $\Psi = 55°$. 187

9.7 Oblique breakdown. ρ'-amplitude distribution. $Ma = 7.95$, $Re = 3,333,333$, $T_\infty = 53.35K$, $F = 3.625 \cdot 10^{-5}$, $A_{1,1} = 5\%$, $\Psi = 20°$. 187

9.8 Oblique fundamental resonance. ρ'-amplitude distribution. $Ma = 7.95$, $Re = 3,333,333$, $T_\infty = 53.35K$, $F = 3.625 \cdot 10^{-5}$, $A_{1,1} = 5\%$, $A_{1,2} = 5\%$, $\Psi_{1,1} = 20°$. 188

List of Figures—*Continued*

9.9 Oblique fundamental resonance. ρ'-amplitude distribution. $Ma = 7.95$, $Re = 3,333,333$, $T_\infty = 53.35K$, $F = 3.625 \cdot 10^{-5}$, $A_{1,1} = 4\%$, $A_{1,2} = 4\%$, $A_{0,1} = 2\%$, $\Psi_{1,1} = 20°$. 188

9.10 Schematic of introducing free-stream disturbances. 189

9.11 Regular disturbance. ρ'-amplitude distribution for two different heights. $Ma = 7.95$, $Re = 3,333,333$, $T_\infty = 53.35K$, $F = 3.625 \cdot 10^{-5}$, $A_{1,1} = 0.01\%$, $\Psi_{1,1} = 20°$. 189

9.12 Oblique breakdown. ρ'-amplitude. $Ma = 7.95$, $Re = 3,333,333$, $T_\infty = 53.35K$, $F = 3.625 \cdot 10^{-5}$, $A_{1,1} = 1\%$, $\Psi_{1,1} = 20°$. 190

9.13 Oblique breakdown. ρ'-amplitude. $Ma = 7.95$, $Re = 3,333,333$, $T_\infty = 53.35K$, $F = 3.625 \cdot 10^{-5}$, $A_{1,1} = 3\%$, $\Psi_{1,1} = 20°$. 190

B.1 Two-dimensional amplification rate based on various flow quantities. $Ma = 7.95$, $Re = 3,333,333$, $T_\infty = 53.35K$, $F = 1.17 \cdot 10^{-4}$, $A_{1,0} = 0.001\%$. . . 200

B.2 Example of flow structures identified by the Q-criterion for flow over a cone. $Ma = 7.95$, $Re = 3,333,333$, $T_\infty = 53.35K$. 203

B.3 Comparison of flow structures identified by the Q-criterion ($Q = 10$) and by vorticity ($\omega_i = 10$). $Ma = 7.95$, $Re = 3,333,333$, $T_\infty = 53.35K$. . . . 204

List of Tables

5.1 Reduced frequencies used for the linear stability analysis. 96
5.2 Amplitude study: forcing amplitude and phase (of the v-velocity at the wall) for the subharmonic frequency. 109
5.3 Phase study: forcing amplitude and phase (of the v-velocity at the wall) for the subharmonic frequency. 111

7.1 Flow parameters before and after the shock. 138

8.1 Flow parameters before and after the shock. 166

9.1 Flow parameters before and after the shock. 182

C.1 Acronyms. 205
C.2 Computational parameter. Flat plate. 206
C.3 Computational parameter. Flat plate. 207
C.4 Computational parameter. Flat plate. 208
C.5 Computational parameter. Cylinder. 209
C.6 Computational parameter. Cylinder. 210
C.7 Computational parameter. Cylinder. 211
C.8 Computational parameter. Sharp cone. 212
C.9 Computational parameter. Sharp cone. 213
C.10 Computational parameter. Sharp cone. 214
C.11 Computational parameter. Sharp cone. 215
C.12 Computational parameter. Blunt cone ($R_N = 0.15$"). 216
C.13 Computational parameter. Blunt cone ($R_N = 0.15$"). 217
C.14 Computational parameter. Blunt cone ($R_N = 0.15$"). 218
C.15 Computational parameter. Blunt cone ($R_N = 0.15$"). 219
C.16 Computational parameter. Blunt cone ($R_N = 0.7$"). 220
C.17 Computational parameter. Blunt cone ($R_N = 0.7$"). 221

List of Tables—*Continued*

C.18 Parameters used for simulations of a flat-plate boundary layer at Mach 2. 222

C.19 Parameters used for simulations of a flat-plate boundary layer at Mach 2. 223

C.20 Parameters used for simulations of a flat-plate boundary layer at Mach 2. See table 5.2 and table 5.3 for CSUB 2-9. 224

Nomenclature

Latin Characters

a	speed of sound
	minor axis of ellipse
b	major axis of ellipse
c	phase speed
$A_{i,j}$	forcing amplitude in jth z-mode with frequency $i \cdot \omega$
e	eccentricity
E	energy
h_i	weight factors
$\bar{M}$	relative Mach number
Ma	Mach number
p	pressure
q	heat flux
Q	vortex identification variable
R	radius
R_N	nose (tip) radius
Re	global Reynolds number
R_x	square root of local Reynolds number based on x
R_δ	Reynolds number based on boundary-layer thickness δ
t	time
T	temperature
u, v, w	velocity in the (x, y, z) directions
U, V, W	base-flow velocity in the (x, y, z) directions
v_p	disturbance profile velocity
x, y, z	streamwise, wall-normal, spanwise directions (Cartesian grid)

Nomenclature—*Continued*

Greek Characters

α	wave number in the x-direction
	half-cone opening angle
α_i	growth rate
β	wave number in the spanwise direction
	shock wave angle
Δ	entropy-layer thickness
δ	boundary-layer thickness
δ^*	displacement thickness
γ	ratio of specific heats
λ	wavelength
μ	kinematic viscosity
Φ	phase shift
ϕ	arbitrary variable
Ψ	wave angle
ρ	density
τ	viscous stress
Θ	momentum thickness
ω	angular frequency
	vorticity
ξ, η, φ	streamwise, wall-normal, spanwise directions (curvilinear coordinates)

Nomenclature—*Continued*

Modifiers

ϕ	vector
$\lvert\phi\rvert$	absolute value
ϕ'	disturbance quantity
ϕ^*	dimensional variable
$\hat{\phi}$	magnitude
ϕ_∞	reference state of variable (free-stream value)
ϕ_0	critical layer
ϕ_{in}	inflow value
ϕ_e	boundary layer edge values
ϕ_{out}	outflow value
ϕ_s	generalized inflection points values
ϕ_t	total value
ϕ_{wall}	value at the wall
ϕ_x,ϕ_y,ϕ_z	with reference to the (x, y, z) direction

Frequent Abbreviations

BC	**B**oundary **C**ondition
DNS	**D**irect **N**umerical **S**imulation
LST	**L**inear **S**tability **T**heory
ODE	**O**rdinary **D**ifferential **E**quation
PSE	**P**arabolized **S**tability **E**quations
TDNS	**T**emporal **D**irect **N**umerical **S**imulation
TPS	**T**hermal **P**rotection **S**ystem
TS	**T**ollmin **S**chlichting
TVD	**T**otal **V**ariation **D**iminishing

Abstract

This work focuses on instability mechanisms of high-speed boundary layers over flat plates and cones with a circular cross section. Supersonic transition investigations at Mach 2 and hypersonic transition investigations at Mach 8 are performed using Direct Numerical Simulations (DNS). At wind-tunnel conditions, these simulations allow for comparison with experimental measurements to verify fundamental stability characteristics. For the DNS of boundary-layer transition at Mach 2, the experimental studies by Kosinov *et al.* (1994) and Ermolaev *et al.* (1996) for a flat plate serve as reference and provide the physical conditions for the numerical setup. In these experiments, the weakly nonlinear regime of transition was studied resulting in the discovery of asymmetric subharmonic resonance triads. Scrutinizing the experimental data, reveals however the presence of another, possibly competing breakdown mechanism, in the experiments. Both mechanisms were addressed in detail in this work.

To better understand geometrical influences, flat-plate and cylindrical geometries are studied under after-shock conditions of the conical investigations (experiments). This allows for a direct comparison with the results of the sharp cone to evaluate the influence of spanwise curvature and cone opening angle. The ratio of the boundary layer thickness to the spanwise radius is used to determine the importance of spanwise curvature effects. For a cone, in downstream direction the radius increases linearly while the boundary layer thickness stays almost constant. Hence, spanwise curvature effects are strongest close to the nose tip and decrease in downstream direction. Their influences on the secondary instability mechanisms provide some preliminary guidance in the design for future high-speed air vehicles.

In experiments, blunting of the nose tip of the circular cone results in an increase in critical Reynolds number (c.f. Stetson *et al.* (1984)). However, once a certain threshold is exceeded, the critical Reynolds number decreases even to lower values than for the sharp cone. Conclusive answers could not be obtained based on the

available experimental data. Therefore, DNS are used to study the effect of nose bluntness on secondary instability mechanisms to shed light on the underlying flow physics. To this end, three different nose radii are considered – a sharp cone, a small nose radius and a large nose radius. A small nose radius moves the transition on-set downstream, while for a large nose radius the so-called transition reversal is observed. Experimentalists link the different stability behavior resulting from the different nose radii to the entropy layer. Detailed numerical studies allow for an alternate conclusion.

1. Introduction

1.1 Motivation

The sonic boom is a firm indicator for the change in flow physics when passing $Ma = 1$. With that, the design concepts of air vehicles change drastically at supersonic speeds. Aircrafts traveling at low supersonic speeds have sharp edges and noses in order to reduce the wave drag of shocks. Advancing to hypersonic speeds, thermal loads become increasingly dominant over the wave drag. Since the heat transfer is inverse proportional to the radius ($q_{wall} = \frac{1}{\sqrt{R_{nose}}}$), air vehicles are designed with large radii to protect the fuselage from over-heating.

In principal, transition to turbulence plays a key factor of the aerodynamic performance of a vehicle. For supersonic and hypersonic flows, transition is additionally associated with an increasing heat transfer to the vehicle. Usually the heat loads during transition exceed the heat transfer of even fully turbulent flows. Therefore, understanding the stability behavior of high-speed boundary layers is essential for the design of the vehicle and the successful operation during its missions. The exploitation of instability mechanisms can delay the transition process and reduce associated heat loads, therefore enhancing the performance of the vehicle and reduce weight penalties for the thermal protection system (TPS). Especially at high Mach numbers, the reduction of the aerothermal loads may result in a significant weight reduction, thus increasing the payload of the air vehicle.

The flow over cones with circular and elliptical cross-sections is an important step towards the modeling of real vehicle geometries. Nose sections of vehicles traveling at supersonic speeds are similar in shape to circular cones. Thus understanding the governing flow physics for this geometry helps improve real-scale vehicle performance.

Although significant progress has been made in recent years, crucial aspects of transition physics are still not well understood. The lack of insight into the physical mechanisms of the transition processes in supersonic and hypersonic boundary-layer flows is a major obstruction in developing reliable transition prediction methods. In this study, Direct Numerical Simulations (*DNS*) are used to elaborate the influences of nose radii and spanwise curvature on the hypersonic transition process. These simulations have the advantages of being highly accurate and cost efficient compared with experiments. Despite the fact that the complex flow structure of compressible boundary-layer flows still challenges today's supercomputers, *DNS* help identify viable paths to transition and will narrow the gap between simulations and real-life applications.

For comparison and validation purposes, other approaches to stability investigations are introduced in the next two sections before secondary instabilities are discussed and experimental and computational efforts are summarized.

1.2 Transition Process and Breakdown Scenarios

Classically, the transition process depicted in Figure 1.1 can be divided into five stages:

I. Receptivity:

- Disturbances from surroundings penetrate the boundary layer.

II. Linear region:

- Amplitudes of these disturbances grow exponentially.

III. Secondary instability:

- Once finite amplitude are reached, higher modes are generated nonlinearly and flow becomes increasingly three-dimensional.
- Lambda vortices with peak and valley stations are formed through streamwise vortices with higher amplification at the peak station.

IV. Tertiary instability:

- Hairpin vortices evolve from the lambda vortices whose heads start to break up into smaller structures.
- Turbulent spots are generated.

V. Turbulent region:

- Agglomeration/Merging of turbulent spots form fully turbulent region.

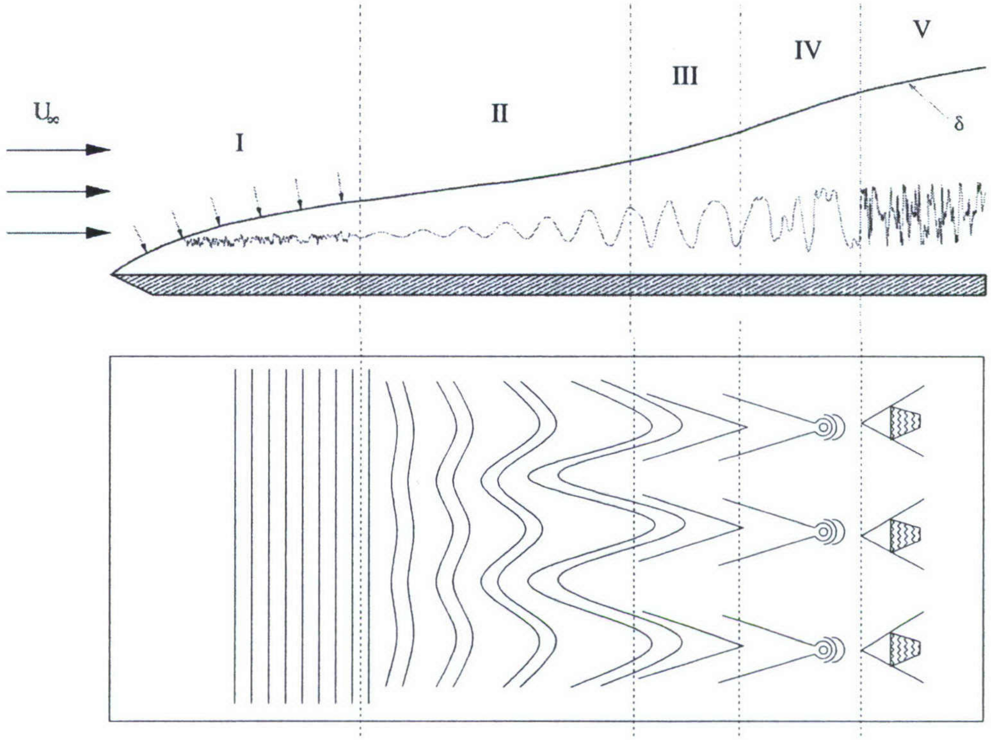

Figure 1.1: Stages of the transition process (side and top view).

The transition process is non-unique and does not necessarily involve all of the above mentioned stages (bypass transition). Because Mach number has stabilizing effects, hypersonic boundary layers are very stable. This work concentrates on the nonlinear regime of transition to identify scenarios which cause the final breakdown. Therefore, a composition of known (secondary) instability mechanisms follows. Herbert (1988) summarizes the secondary instabilities of incompressible boundary layers— K-type, C-type and N-/H-type. He investigated secondary instabilities by the Floquet analysis and compared his findings with experiments.

Secondary instabilities occur when waves travel at the same phase speeds thus enabling energy transfer from the primary to the secondary waves which results in rapid growth of the secondary waves and eventually in breakdown to turbulence.

The different scenarios are:

K-type: Klebanoff *et al.* (1962) discovered this instability in their flat-plate experiments. A finite amplitude two-dimensional Tollmien-Schlichting (TS) wave interacts with a steady streamwise vortex generated by spanwise spacers. Small (linear) amplitude three-dimensional waves at the same frequency as the primary wave (fundamental breakdown) emerge through nonlinear interactions. The finite amplitude of the primary wave is responsible for a phase locking with the secondary (generated) waves and therefore enabling this resonance. This breakdown results in aligned streamwise Λ-vortices producing a peak-valley formation in spanwise direction with similar wavelength than the two-dimensional fundamental wave $\lambda_z \approx \lambda_x$.

C-type: Craik (1971) investigated a resonant triad where all three waves involved travel at the same phase speed. The two-dimensional fundamental wave has twice the frequency of the two secondary oblique (subharmonic) waves. To achieve equality of the phase speed the oblique waves travel at a specific wave angle ($\lambda_{z,subh} = 2\lambda_{x,fund}$). It is not necessary for the two-dimensional fundamental waves to reach finite amplitudes in order to transfer energy to the oblique waves, thus causing early rapid amplification. Because there exists only one specific wave triad for each frequency of the primary waves, this resonance is not as robust as the N-/H-type breakdown.

N-type or H-type: In a subharmonic breakdown, a finite amplitude two-dimensional wave leads to a resonance with a small (linear) amplitude three-dimensional wave with half the frequency of the two-dimensional (primary) wave. These secondary oblique waves travel at different wave angles as in a C-type breakdown making the C-type a special case of the N-/H-type secondary instability. The flow field shows staggered streamwise Λ-vortices with a spanwise wavelength half of the streamwise wavelength of the fundamental wave ($2\lambda_z = \lambda_x$). Experiments by Kachanov & Levchenko (1984) and theoretical work by Herbert (1984) revealed the associated spanwise variations of the subharmonic disturbance waves. For an incompressible flat-plate boundary layer, the subharmonic breakdown is usually a stronger mechanism than a fundamental (K-type) breakdown, despite the fact that it has been discovered over 20 years later.

Oblique Breakdown: In his numerical investigations of supersonic flows, Thumm (1991) first discovered this mechanism which is not a secondary instability in the common sense. A pair of oblique waves traveling with the same wave angle in opposite directions relative to the flow ($\pm\Psi$) generate a pair of steady streamwise vortices. These vortices interact with the primary disturbance waves again causing rapid amplification of nonlinearly generated waves. The oblique breakdown works especially well when three-dimensional waves are more unstable than two-dimensional waves which is the case at low supersonic Mach numbers ($Ma \lesssim 4$).

Oblique Subharmonic Resonance: This secondary instability is a generalization of a C-type breakdown where the fundamental waves are also oblique. Therefore, the primary and the two subharmonic waves all travel at different wave angles in order to form a wave triad. This breakdown was observed in experiments performed by Kosinov *et al.* (1994). As for the oblique breakdown, this resonance works best at low supersonic Mach numbers since the eigenbehavior of the waves further support this breakdown.

Oblique Fundamental Resonance: Just as the oblique subharmonic resonance is a generalization of a C-type breakdown, the oblique fundamental resonance is a generalization of a K-type resonance where the primary and the secondary waves are three-dimensional. Both waves involved possess the same frequency but travel at different wave angles. As for the K-type, steady streamwise vortices are generated through first-order interactions. So far, only minor attention was drawn to this kind of breakdown.

1.3 Common Methods for Stability Investigations

1.3.1 Linear Stability Theory

For his extensive numerical investigations, Mack (1984) split the total flow into a steady (base) flow and an unsteady disturbance flow. He then linearized the equations and applied the normal-mode approach for disturbance waves which assumes the amplitude to only vary in wall-normal direction:

$$\phi = \hat{\phi}(y)e^{i(\alpha x+\beta z-\omega t)} \,. \tag{1.1}$$

Because the amplitude is not allowed to vary in x-direction, a so-called local flow analysis (parallel-flow assumption) is accomplished. Further simplification of the governing equations is possible if one of the dissipation terms of the energy equation[1] is set to zero thus decoupling the energy equation from the z-momentum equation. The result is a system of six (instead of eight) first order ODEs. He justified this step by comparison of the results obtained with both eighth order and sixth order systems and concluded that the error of the sixth order system of about 14% is acceptable due to a tremendous reduction in computation time when compared with results of the eighth order system.

1.3.1.1 Inviscid Theory

In contrast to incompressible flow, the compressible boundary layer may be unstable to inviscid disturbances due to a generalized inflection point where

---

[1] $\frac{2\mu}{\alpha^2+\beta^2}\left(\alpha\frac{dw}{dy}-\beta\frac{du}{dy}\right)\tilde{\alpha}\frac{d\bar{w}'}{dy}=0$

$$\frac{d}{dy}\left(\rho\frac{du}{dy}\right) = 0$$

within the boundary layer. The distance from the wall of the generalized inflection point is denoted y_s and the local speed of the fluid is labelled c_s.

When the velocity of the flow within the boundary layer is the speed of sound slower than the free-stream velocity, the derived equations become singular. This so-called critical layer appears at the wall-normal location y_0 where the speed of the flow is $c_0 = 1 - 1/Ma$ (*Note:* y_0 and c_0 are both functions of the downstream direction). Whenever $y_s > y_0$, the supersonic boundary layer flow is unstable to inviscid (subsonic) disturbances. This inviscid instability becomes stronger with increasing Mach number.

According to Lees and Lin (c.f. Mack (1984), page 3-35), disturbance waves are classified by their speed relative to the free-stream velocity:

increase in speed	▶ supersonic disturbance	$c < 1 - \frac{1}{Ma}$	generalized inflection point profiles
	▶ sonic disturbance	$c = 1 - \frac{1}{Ma}$	
	▶ subsonic disturbance	$c > 1 - \frac{1}{Ma}$	
	▶ regular disturbance	$1 < c < 1 + \frac{1}{Ma}$	no inflection point

It should be noted that generally the most important waves with respect to the stability of a compressible boundary layer are subsonic disturbances. Exceptions, e.g. in the presence of strong wall cooling where amplified disturbance waves are found in the regular disturbance family, are discussed later in this section.

When a *relative* Mach number $\left(\bar{M} = (\alpha U + \beta W - \omega)\, Ma / \left(\sqrt{(\alpha^2 + \beta^2)\,T}\right)\right)$ is introduced and large wave numbers considered the simplified compressible Rayleigh equation

$$\frac{d^2\hat{p}}{dy^2} - \left(\alpha^2 + \beta^2\right)\left(1 - \bar{M}\right)\hat{p} = 0$$

shows that an infinite number of solutions exist if $\bar{M} > 1$. The only requirements for these higher modes to exist is a relative supersonic flow region within the boundary layer. This relative supersonic flow appears when $Ma > 2.2$ in the inviscid theory ($Re \rightarrow \infty$). The higher modes are also called *Mack modes* because Mack (1965) was the first to discover their importance in the stability behavior of supersonic flows, although Lees & Reshotko (1962) mention their possible existence earlier. The most important Mack mode for Mach number up to ten is the second mode. First and higher modes can be best distinguished by the number of phase shifts of their pressure eigenfunction (number of zero crossings in their amplitude distribution). The mode under consideration shows one null less than its mode number—so the pressure amplitude eigenfunction of a first-mode disturbance wave has no zeros and the second mode has one.

For an insulated wall, amplified first modes travel with a phase velocity between c_0 and c_s. For three-dimensional (first-mode) waves traveling with a wave angle Ψ, the flow properties in direction of the wave are important—thus $c_{s3D} = c_{s2D}\ cos\Psi$ and $c_{03D} = (cos\Psi - 1/Ma)$. Therefore, larger wave angles Ψ increase the difference between c_s and c_0 up to an optimum, and three-dimensional first-mode waves are destabilized (*Note:* the optimal wave angle is a function of Mach number). Three-dimensional higher mode waves are more stable than two-dimensional higher mode waves so that at low supersonic speeds three-dimensional first-mode waves are most unstable while, at higher Mach numbers, two-dimensional second-mode waves are most amplified. This statement is generally valid although exceptions are possible in both cases.

When the wall is moderately cooled, a second inflection point appears below the critical layer and does therefore not introduce an additional instability. With increased cooling the second inflection point is moving upward, cancelling the generalized inflection point and thus totally stabilizing first-mode waves. At the same time higher modes which travel with a higher velocity than the free stream (regular disturbance waves) are destabilized. No general stability tendency of wall cooling can therefore be observed and its effect on the transition process has to be examined for each case separately.

1.3.1.2 Viscous Theory

Going to finite Reynolds numbers, i.e. accounting for viscous effects, increases the Mach number when higher modes first appear. Typically, the second mode emerges at $Ma \sim 4$ under wind-tunnel conditions. Another important difference to the inviscid theory is that the first and higher mode waves are not distinguished waves any longer. In the viscous theory, all waves traveling with $c < 1$, i.e. supersonic, sonic, and subsonic disturbances are linear independent to the regular disturbance waves traveling at $c > 1$. Nonetheless, the viscous stability behavior of a compressible boundary layer is basically governed by subsonic waves as in inviscid theory. Within that category, waves behave like first-mode or higher-mode waves depending on the flow parameters. Mack (1984) calls these waves "the viscous counterpart of an inviscid first mode wave" (or inviscid higher mode). In order not to unnecessarily complicate the manner, the viscous counterparts are still called first mode or higher modes in this report–knowing that it is the same wave with different characteristics.

For an insulated wall, first-mode waves of low supersonic Mach numbers ($Ma < 2$) experience a viscous instability, i.e. waves are more amplified than according to the inviscid theory. But with increasing Mach number, viscosity only acts to damp the inviscid instability of waves (caused by the generalized inflection point). Viscous dissipation increases with increasing wave number α and decreasing local Reynolds number R_x. Therefore, all higher modes are stabilized by viscous effects.

The effects of wall cooling for finite Reynolds numbers show similar behavior as in the inviscid theory. Thus, first modes are fully stabilized by eliminating the inflection point through strong wall cooling.

1.3.2 Parabolized Stability Equations

Since computations and experiments are compared to results obtained by the Parabolized Stability Equations (*PSE*), a brief overview is given here. For a more detailed description, the reader is referred to Chang & Malik (1993*a*). First, one distinguishes between linear and nonlinear *PSE*. In comparison to *LST*, linear and also non-linear *PSE* has the major advantage that influences of the growing boundary layer are considered (no parallel-flow assumption). Additionally for nonlinear *PSE*, a limited amount of nonlinear interactions of waves are allowed.

In order to include non-parallel and nonlinear effects, *PSE* uses a multiple-scale approach to decompose a disturbance in streamwise direction into a wave-like part (varying wave number) and a shape function (varying amplitude function $\hat{\phi}(x, y)$).

$$\phi = \sum_{m=-M}^{M} \sum_{n=-N}^{N} \hat{\phi}_{mn}(x, y) e^{i\left(\int \alpha_{mn} dx + n\beta z - m\omega t\right)}$$

Plugging this approach into the governing equations, with neglecting second-order derivatives (e.g. $\frac{\partial^2 v}{\partial x^2}$) and multiplications of first-order derivatives (e.g. $\frac{\partial \alpha}{\partial x} \frac{\partial u}{\partial x}$) in the streamwise direction, eliminates the elliptic nature of the equations— they are *parabolized*. By eliminating the elliptic character no information can be passed upstream anymore and these equations are therefore only capable of calculating convective instabilities. Because non-parallel and nonlinear effects are not neglected, transition on-set and the early stages of transition can be computed in very good agreement with experimental results. Hence, *PSE* is a powerful tool for investigating the early stages of transition but performs less good in predicting flow behaviors in the later stages of the breakdown process.

1.3.3 Temporal Direct Numerical Simulations

In the wave equation (eq 1.1), α and ω are generally complex. The real parts α_r and ω_r are the wave number and frequency, respectively. The imaginary parts both describe the amplification of the wave, i.e. α_i is the spatial while ω_i is the temporal amplification. For the *spatial* approach, which is mainly used in this work, α is complex and ω is real. To discuss possible resonances of disturbance waves, investigations are also performed with a *temporal* DNS. In the temporal simulations, only one streamwise wavelength is computed. The resulting computational domain is graphed in Figure 1.2. Because of its small streamwise extent the flow variables are assumed to be constant in that direction. Hence, the base-flow profile and with that the boundary-layer thickness, does not change and periodicity is assumed (parallel flow assumption, as in *LST*). The computational domain travels with the wave speed and therefore, the wave becomes stationary within the reference frame. Based on this approach, temporal amplification can be computed and related to spatial amplification rates with the transformation by Gaster (1962). For a more detailed description of the temporal approach, please refer to Marxen (1998). Balzer (2003) describes the temporal code used for the investigations of conical geometries.

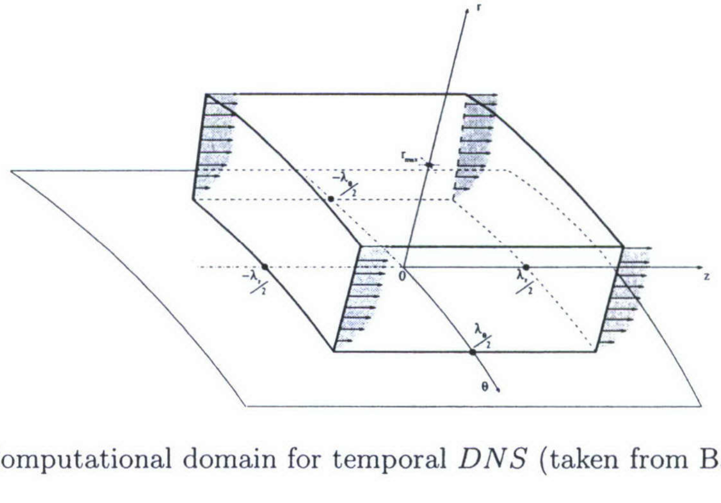

Figure 1.2: Computational domain for temporal *DNS* (taken from Balzer (2003)).

1.4 Earlier Investigations of High-Speed Boundary-Layer Stability

1.4.1 Experimental Efforts

1.4.1.1 Flat-Plate and Swept-Wing Geometry

At the Institute of Theoretical and Applied Mechanics in Novosibirsk, Russia, controlled experiments of flow over a flat plate at $Ma = 2$ were investigated. These controlled experiments, meaning that disturbances are introduced by a generator at specific frequencies (here via a spark discharge), were performed by Kosinov *et al.* (1994). Their main finding is that a resonance of oblique subharmonic waves exists. Theoretical work of Kosinov & Tumin (1996) confirmed this result. Ermolaev *et al.* (1996) used a larger subharmonic amplitude than Kosinov *et al.* (1994) resulting in a slightly different wave triad—possibly not caused by the amplitude but by a phase difference in their disturbance signal (c.f. Mayer & Fasel (2008)). They measured an asymmetric spectra in spanwise direction which could not be theoretically verified. So Ermolaev *et al.* (1996) speculated that this asymmetry is connected to the generation of subharmonic two-dimensional sound waves.

Brown & Graziosi (2002) investigated the disturbance development within a flat-plate boundary layer at Mach 3. They elaborated only the linear stages of transition caused by natural disturbances, i.e. noise radiated from the free stream into the boundary layer. The initial stages of transition were generally confirmed by *LST*. Graziosi (1999) claimed that first-mode unstable waves are sonic wave disturbances and play therefore a main role in the transition process. Therefore, follow-up experiments (Brown & Fan (2003)) with controlled disturbances which are introduced through a loudspeaker upstream of the wind-tunnel nozzle are used to investigate the receptivity of the boundary layer to sound-wave disturbances. The experiments revealed that disturbance waves in the free stream travel initially in phase with the generated disturbance waves in the boundary layer. At a later time (at the same location), a phase shift between waves in the free stream and in the boundary layer became apparent.

When three-dimensional boundary layers are considered, so-called cross-flow instabilities govern the stability of the flow. To investigate these cross-flow instabilities, swept-wings, rotating disks, and elliptical cones are common geometries. In the facility in Novosibirsk, Levchenko *et al.* (1996) found formations of steady streamwise vortices caused by the cross-flow instability of an infinite swept wing at $Ma = 2$. Saric & Reed (2002) investigated the cross-flow instability of a swept wing at Mach 2.4. They were successful in delaying transition by placing distributed roughnesses close to the leading edges in order to weaken the cross-flow instability. Therefore, it is concluded that steady vortices are an efficient mechanism in controlling cross-flow instabilities.

1.4.1.2 Cone Geometries

Circular Cone

Most experiments of conical geometries are performed in the hypersonic Mach number range of $Ma = 6$ to $Ma = 8$ before the shock. An exemption are the experiments of Corke *et al.* (2002) who also found an oblique subharmonic resonance, as Kosinov *et al.* (1994) did for a flat plate at $Ma = 2$, for a slender cone at Mach 3.5. Laddon & Schneider (1998) analyzed the stability behavior of controlled disturbances (introduced via a glow discharge) in a flow over a circular cone for small angles of attack at $Ma = 4$. They measured a phase speed of 0.9 times the free-stream velocity and saw the maximum rms-amplitude values built up at the outer part of the boundary layer— both indications that a second-mode instability is present. They speculated that although amplitude growth was significant the disturbance amplitude of the glow discharge was too small in order to cause transition.

The best documented and most detailed experiments of a circular cone geometry are probably those of Stetson *et al.* (1983) and Stetson & Kimmel (1992). They investigated the influences of nose radius, wall temperature, angle of attack, unit Reynolds number, Mach number, and transverse curvature. Independent of these factors, higher harmonics of the most amplified wave developed. In their early experiments, Stetson *et al.* (1983) focused on the sharp cone at Mach 8 at one unit Reynolds number. The principle instability was identified as a two-dimensional second-mode wave which is selective to a specific disturbance frequency. The wavelength of this frequency relates to the boundary-layer thickness ($\lambda_x \approx 2 \cdot \delta$). Since the boundary-layer thickness is almost constant for this cone configuration, the most amplified frequency does not vary as much in downstream direction as it does e.g. for the flat plate. Measured rms-amplitudes grow close to the boundary layer edge and stay at about noise level at the inner part of the boundary layer close to the wall. Far downstream these second-mode disturbance waves decay and first-mode waves grow again leading to the conclusion that transition on-set has occurred.

Nose Bluntness: In later experiments, Stetson *et al.* (1984) showed that a small nose-tip bluntness can completely control the stability behavior of the hypersonic boundary layer, i.e. a small bluntness delays transition while larger nose radii enhance transition compared to the sharp cone. So he hypothesized that the stability behavior at the frustum of the cone is governed by the entropy layer and the boundary-layer edge properties because once the entropy layer was "swallowed" by the boundary layer, disturbances rapidly amplified again. Stetson (1979) named the reduction in unit Reynolds number due to total pressure losses over the normal-shock region the main reason for the downstream movement of the transition location for a small to moderate nose bluntness. For larger nose radii transition occurred in the subsonic region of the boundary layer and transition moved forward again.

Wall Temperature: Because second-mode disturbance waves are dominant, a decrease in wall temperature increases the amplification of these waves and reduces the critical Reynolds number.

Angle of Attack: The transition point on the windward site of the cone was found to move rearward and forward on the leeward site. The forward movement of the transition on-set can be explained by a cross-flow instability. However, the major effect of an angle of attack was on the location of the amplification of a second-mode disturbance but not on the amplification rate itself.

Unit Reynolds number: The experimental data revealed a linear correlation of unit Reynolds number and the amplification rate of a second-mode disturbance. Thus, for a particular downstream location based on local Reynolds number, the amplification rate was twice as high if the unit Reynolds number was doubled.

Mach number: Comparison of the collected data at Mach 8 with data at Mach 6 showed basically the same stability behavior in both cases.

Transverse curvature: Quiet wind-tunnel data support the numerical results of *LST* that the location of a second-mode disturbance is somewhat farther upstream but the amplification rate is lower for a compressible flat-plate boundary layer compared to conical flows. The reason for such a behavior lies in the above mentioned selectivity of the frequency of the conical boundary layer so that overall a second-mode instability is emphasized for flow over cones.

Bountin *et al.* (2004) and Shiplyuk *et al.* (2003) analyzed the flow around a circular cone with a porous wall. They concentrated their work on mode interactions through the bispectral method and found that a subharmonic resonance of two-dimensional waves with three-dimensional waves is possible. In addition, they emphasized the importance of first-mode oblique waves alone in the breakdown process— like breakdown scenarios with oblique primary waves.

Flared Cone

On a flared cone the radius increases quadratically in the downstream direction, usually after a linear portion along the nose section of the cone (as on a conventional cone). Associated with the resulting concave curvature are Görtler vortices and adverse pressure gradients.

At the NASA Langley Research Center, the flared cone at $Ma = 6$ was analyzed by a group of researchers around Chokani. Lachowicz *et al.* (1996) found that second-mode two-dimensional waves dominate the transition process while higher harmonics are unrelated to the free-stream disturbance levels— further undermining the results of Stetson *et al.* (1983). Doggett *et al.* (1997) saw the same trends for a flared cone at an angle of attack as for the conventional cone, i.e. the leeward side became more unstable and the windward side was stabilized compared to a cone at a zero degree angle of attack. From 1999 through 2002, Chokani (1999), Chokani (2000*a*), Chokani (2000*b*), Norris & Chokani (2001), and Norris & Chokani (2002) emphasized their experimental efforts on the identification of nonlinear interactions leading to transition. They claimed a subharmonic resonance of a two-dimensional second-mode wave with three-dimensional first-mode waves responsible for boundary layer transition.

Horvath (2002) investigated both cone geometries, the conventional slender cone and a flared cone. He postulated that the adverse pressure gradient instead of Görtler vortices is the main driving force for higher amplification rates of second-mode disturbances over the flared cone. Hence, the breakdown mechanisms involving two-dimensional waves are emphasized for the flared cone compared to flow over cones without streamwise curvature.

Elliptical Cone

Kimmel *et al.* (1999) investigated the three-dimensional boundary-layer flow over a cone with elliptical cross-section (ratio 2:1) at Mach 8. Their measurements revealed that inflection-point profiles are present close to the centerline where the boundary layer is also significantly thicker than away from the centerline. With the laminar state of the flow already very complex, they could only speculate that transition at the centerline is caused by the inflection point while close to the shoulder of the cone transition is induced by cross-flow instabilities. The instability of the inflectional boundary layer seemed to be stronger than the instability of the cross flow so that transition occurred first at the centerline and farther downstream at the shoulder of the cone. Continuing work of Poggie *et al.* (2000) revealed second-mode disturbance waves close to the centerline of the elliptical cone. It remained unclear if disturbances caused by cross flow or first-mode waves are present at the shoulder of the cone. According to Poggie *et al.* (2000), a minor identification which favors the presence of cross-flow instabilities is that the measured wavelength was rather short. Because the group velocity vector of leading-edge disturbances did not deviate more than 1 degree off the edge velocity vector, they hypothesized that oblique leading edge disturbances do not play an important role in the stability behavior at the shoulder of the cone. Although the amplitudes under investigation were too high for a receptivity study, Schmisseur *et al.* (2002) saw a response to thermal disturbances generated by a laser placed in the free stream close to the shoulder of their 4:1 elliptic cone at $Ma = 4$. Future research remains to clarify more specific issue of their stability experiments.

1.4.2 Computational Efforts

1.4.2.1 Flat-Plate and Swept-Wing Geometry

Since the early 90's, when Thumm (1991) discovered the oblique breakdown for a supersonic boundary layer at Mach 1.6, simulations performed by several investigators, see for example Bestek & Eißler (1996), Chang & Malik (1994), Fasel *et al.* (1993) or Mayer (2004), also showed that this breakdown of two oblique waves with the same wave angle ($\pm\Psi$) is a strong mechanism in the on-set of transition for various Mach numbers and flow parameters. Unfortunately, this breakdown lacks experimental verification so far, although Mayer *et al.* (2007) has strong indications of a possible oblique breakdown in the experimental measurements of Ermolaev *et al.* (1996).

Eißler (1995) performed computations under wind-tunnel, so-called "cold", conditions and free-flight, so-called "hot", conditions with an adiabatic, isothermal, and radiation-cooled wall and was therefore capable of determining realistic heat loads on the wall during transition. His simulations with an adiabatic and radiation-cooled wall revealed that the oblique breakdown is the strongest mechanism for "cold" conditions at $Ma = 4.8$. With the same wall behaviors but under atmospheric ("hot") conditions, two-dimensional second-mode waves were strongly amplified. For a fundamental breakdown (K-type) secondary three-dimensional waves showed relevant amplitudes level only far downstream and a N-/H-type subharmonic resonance could not be found. Due to the computer power at that time, he was unable to simulate K-type or N-/H-type breakdown scenarios with an isothermal wall. It is our hypothesis that the second-mode waves were highly destabilized (as predicted by *LST*) and early transition occurred. Therefore, he summarized that the oblique breakdown for an adiabatic flat-plate boundary layer is the strongest mechanism within his investigated scope of parameters—despite the strong amplification of two-dimensional second-mode waves.

Theoretical work of Tumin (1996) and Terekhova (2003) analyzed the experiments of the oblique subharmonic breakdown by Kosinov *et al.* (1994). Tumin (1996) used 50 wave packets in a locally parallel flow uniformly spaced in spanwise direction and found good qualitative agreement to the experiments. Based on his findings, he concluded that a subharmonic resonance is responsible for the stability behavior of the flow. Terekhova (2003) investigated the nonlinear interactions with seven waves—only considering first-order interactions. She found that there are strong interactions between the fundamental waves (traveling at $\pm\Psi$) generating a two-dimensional wave (*Remark:* as in the oblique breakdown), but also stated that the first-order interactions are not the main process in the energy re-distribution among waves. Husmeier *et al.* (2005) transferred the subharmonic oblique breakdown to Mach 3 flow conditions matching the experimental setup of Brown & Graziosi (2002). But due to the arising flow structures and instability mode behavior, they concluded that, although possible, an oblique breakdown was overlaying the subharmonic resonance. They also investigated K- and N-/H-type breakdown scenarios but because of the high disturbance amplitudes necessary at the disturbance slot, their conclusion was that the oblique breakdown is the strongest mechanism under those conditions. With his numerical efforts, Zengl (2005) focused on the oblique subharmonic resonance of Kosinov *et al.* (1994) under the conditions of Brown & Graziosi (2002). His simulations showed that only two waves, i.e. one primary and one secondary wave pair, need to be disturbed while the third wave closing the triad is automatically generated and amplified through nonlinear interactions. Therefore, the oblique subharmonic instability is strongest when both, primary and secondary, waves are perturbed with equal amplitudes. In this case, the oblique subharmonic breakdown shows competitive performance to the oblique breakdown.

Chang *et al.* (1995) investigated the stability behavior of a three-dimensional boundary layer by performing a PSE analysis of flow over a swept cylinder at $Ma = 3.5$. Stationary cross-flow vortices evolved with unsteady (high-frequency) cross-flow disturbances residing on top of these structures. Because of the very high frequency of these disturbances they speculated that traveling cross-flow instabilities rather than an instability of the steady vortices are more likely to govern the stability behavior. Similar results saw Kloker (2002) for an incompressible swept-wing geometry. He related the unsteady cross-flow disturbances to the free-stream turbulence level. At low free-stream turbulence levels stationary cross-flow vortices prevailed.

1.4.2.2 Cone Geometries

Circular Cone

Theoretical work by Seddougui & Bassom (1997) who investigated the linear stability behavior of flow over cones following the triple-deck-formulation, revealed the importance of the shock location relative to the cone radius. Only looking at viscous modes they stated that inviscid instabilities might alter their findings. Seddougui & Bassom (1997) revealed that with increasing radius, i.e. moving in downstream direction, first-mode waves are higher amplified than higher-mode waves— a phenomenon already observed by Stetson *et al.* (1983) in their experiments. Additionally, Seddougui & Bassom (1997) stated that with the shock moving away from the cone surface amplification rates generally drop and axisymmetric waves are more unstable than oblique waves.

Using DNS and PSE, Pruett *et al.* (1995) investigated a second-mode three- dimensional linear disturbance under the conditions of Stetson *et al.* (1983). Comparing DNS with PSE results showed good agreement. Pruett *et al.* (1995) recognized an extreme sensitivity of the stability behavior of high-speed boundary layer flows to changes in the base-flow profiles. Therefore, Pruett (1993) concentrated on the influence of the wall-normal gradients of the flow variables within the boundary layer. In a second part, Pruett & Chang (1995) investigated breakdown scenarios in more detail. They found that subharmonic resonances (N-/H-type) are an unlikely path to turbulence since the downstream extent of the instability region of two-dimensional waves is too short. Instead, they claimed a second-mode oblique breakdown with arising steady vortices responsible for transition. These structures having a significant impact on the stability behavior formed closed to the critical layer. Robarge & Schneider (2005) linked the sensitivity of the stability behavior of the boundary layer, as seen by Pruett *et al.* (1995), to changes in the viscosity. Thus, they observed a large scatter in computed amplification rates although the location of the instability region was in good agreement when compared with PSE results. Fezer & Kloker (2004) also investigated the same cone geometry as used in the experiments by Stetson *et al.* (1983) but under atmospheric conditions, i.e. a "hot" approach flow, and with a radiation-cooled wall. A fundamental resonance (K-type) with accompanying hot streaks along the wall initiated transition in that case. The high temperature streaks along the wall resulted from vortex structures which built up during this breakdown. Zhong (2005) analyzed three different nose radii under Stetson's experimental conditions (c.f. Stetson *et al.* (1984)). Zhong (2005) observed a shift to lower dominant frequencies with increasing bluntness due to a thickening boundary layer. But as reported by Stetson & Kimmel (1992), Zhong (2005) was unable to find an instability reversal, i.e. in his simulations the critical Reynolds number increased monotonically with increasing nose radius. In the experiments of Stetson & Kimmel (1992) a decrease in critical Reynolds number followed the initial increase so that there was an optimal nose radius regarding transition delay in the their experiments.

In all cases mentioned above, the authors were unable to draw conclusions on why the observed instabilities prevailed over other mechanisms and what role the boundary and flow conditions play in influencing these scenarios.

Flared Cone

Pruett & Chang (1998) continued their transition investigation by analyzing the flared cone geometry at $Ma = 6$. Due to the flared region on the cone, the boundary layer thickness decreases and the dominating disturbance frequencies increase. As observed by Stetson *et al.* (1983), they were able to link the wavelength of the most important frequency to about twice the boundary-layer thickness. For a flared cone, flow structures developed close to the wall and upstream of those on the circular cone (c.f. Pruett & Chang (1995)). Generally, Pruett & Chang (1998) saw the transition on-set appearing earlier but developing more gradually in downstream direction in comparison to the development on the circular cone. But if Mach number, adverse pressure gradient, streamwise wall curvature, or unstable Görtler vortices are responsible for this behavior is unclear.

Elliptical Cone

Kimmel *et al.* (1997) performed precursor simulation of flows over cones with three different elliptical cross sections before starting their experiments (c.f. Kimmel *et al.* (1999)). Their eccentricities were $1.5 : 1$, $2 : 1$, and $4 : 1$. Due to the large amplitude growth on the centerline close to the nose of the cone with the $4 : 1$-cross section, early transition on-set was observed influencing transition on the shoulder of the cone. Because breakdown mechanisms cannot be easily distinguished for this configuration

(4 : 1), they excluded this geometry from their experimental investigations (c.f. Kimmel *et al.* (1999)). Martin *et al.* (2000) tested the subgrid-scale turbulence model in comparison with DNS results. Follow-up simulations performed by Martin *et al.* (2001) demonstrated grid resolution requirements but no stability investigations were performed.

1.5 Objectives and Overview

Because of the aforementioned difficulties from which experimental investigations of hypersonic boundary layer transition suffer, many questions are left unanswered. Especially the absence of controlled disturbance input makes it harder to single out specific wave interactions and therefore it is very difficult if not almost impossible to draw conclusions on the physical mechanisms of the relevant breakdown scenarios. Therefore, DNS are employed to identify and investigate breakdown scenarios for high-speed boundary-layer flows over circular cones. To get an as complete picture as possible on how transition is initiated breakdown scenarios of first-mode and second-mode waves, two-dimensional and three-dimensional (primary) waves and the influence of steady streamwise vortex modes are studied for each geometry. How geometrical parameters, with special focus on spanwise curvature and nose radius, influence the stability behavior is elaborated.

To give confidence into the simulations and to assure the correct implementation of the governing equations and numerical procedure, presented in chapter 2 and 3 respectively, a summary of performed validation cases is composed in chapter 4. The diameter of the cone varies in downstream direction. To discuss the effects of spanwise curvature on the hypersonic boundary layer transition and create a data base for later comparison with the circular cone results of the investigated breakdown scenarios, results for the flat-pate and cylinder geometry are presented in chapter 5 and chapter 6. Experimental investigations by Stetson *et al.* (1984) have revealed a critical nose radius. Numerical efforts by Rosenboom *et al.* (1999) and Zhong (2005) were unable to confirm this stability feature. To further elaborate the influences of the nose radius breakdown scenarios for the sharp cone (chapter 7), for a small (chapter 8), and a large nose radius (chapter 9) are discussed and compared with each other. Main discoveries are concluded in chapter 10.

2. Governing Equations

The Navier-Stokes equations consisting of conservation of mass (continuity equation), conservation of momentum, and conservation of total energy form the set of governing equations for the high-speed transition investigations. Air as thermally and calorically ideal gas is assumed so that the equation of state is used to close the set of equations. This assumption limits the temperature within the flow field to below $2,000K$, because, above that temperature, dissociation sets in voiding the ideal gas assumption. Hence, the investigations are based on "cold" wind-tunnel conditions where the adiabatic wall temperature does not exceed $1,000K$. Because no further assumptions are incorporated all non-parallel and nonlinear effects are included.

2.1 Viscosity

The fluid is assumed to obey the Newtonian viscosity law governed by the local temperature T^*. Note, that for investigations over the cone, the viscosity is computed with the local temperature T^* *after* the shock. The viscosity, depending on the temperature T^*, is constant, shows linear behavior or is obtained by Sutherland's Law,

$$\mu^*(T^*) = \begin{cases} C_1 T_1^* & , \quad T^* < T_1^* \\ C_1 T^* & , \quad T_1^* < T^* < T_2^* \\ C_2 \frac{T^{*3/2}}{T^* + T_2^*} & , \quad T^* > T_2^* \end{cases} \qquad (2.1)$$

with

$$\begin{array}{ll} T_1^* = 40.0K & C_1 = 6.8070 \times 10^{-8} Ns/m^2K \\ T_2^* = 110.4K & C_2 = 1.4458 \times 10^{-6} Ns/m^2K^{1/2} \, . \end{array}$$

For the investigations presented in this work, the temperature ranges from below $110.4K$ to above $110.4K$ so that the viscosity is computed linearly in the free stream and with Sutherland's Law in the boundary layer. This switching of viscosity laws causes a small discontinuity (see Figure 2.1a). Figure 2.1b shows the wall-normal distance where the discontinuity occurs in comparison with the boundary layer thickness, the location of the generalized inflection point y_s and the location of the critical layer y_0. Because the maximum amplitude of amplified disturbance waves is located between y_s and y_0, the discontinuity does not influence the stability behavior (see also chapter 4 (Code Validation)). To eliminate this discontinuity, the functions have to be continuous and smooth, i.e. function values and their derivative at the interface have to match. Both conditions result in the same relationship between C_1 and C_2

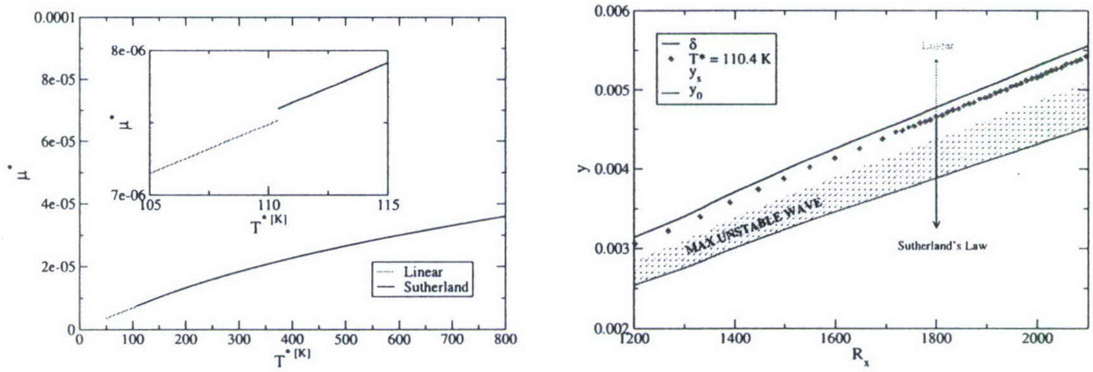

(a) Viscosity with respect to fluid temperature.

(b) Wall-normal location of discontinuity in relation to base-flow properties.

Figure 2.1: Sharp Cone. $Ma = 7.95$, $Re = 3,333,333$, $T_\infty = 53.35K$.

$$C_2 = 2\sqrt{T_2^*}\,C_1 \tag{2.2}$$

so that one of the coefficients C_1 or C_2 is still arbitrary.

2.2 Non-dimensional Equations

Non-dimensionalization of the governing equations is carried out by using a length scale (the length of the test article in the experiments L_∞^*) and free-stream values of velocity, temperature, density, and specific heat (U_∞^*, T_∞^*, ρ_∞^* and $C_{p\infty}^*$, respectively). For investigations of flows over cones, free-stream values *before* the shock are used for non-dimensionalization. The non-dimensionalization removes all explicit dependence on these parameters with the exception of the temperature T^*, since it is used to calculate the viscosity (see preceding section 2.1).

To allow for the simulation of cones with circular and elliptical cross section, an orthogonal curvilinear coordinate transformation is introduced (see Tannehill *et al.* (1997)). The rectangular Cartesian coordinates (of the computational domain) are related to the curvilinear coordinates by

$$\begin{aligned} x &= x(\xi,\eta,\varphi) \\ y &= y(\xi,\eta,\varphi) \\ z &= z(\xi,\eta,\varphi)\,. \end{aligned} \tag{2.3}$$

The differential arc length ds can be represented in both coordinate systems— in Cartesian coordinates simply through Pythagoras in three dimensions

$$ds^2 = dx^2 + dy^2 + dz^2 \tag{2.4}$$

and in curvilinear coordinates with

$$ds^2 = (h_1\,d\xi)^2 + (h_2\,d\eta)^2 + (h_3\,d\varphi)^2\,. \tag{2.5}$$

The resulting h_i-factors are listed in appendix A. Figure 2.2 illustrates the Cartesian and the resulting curvilinear (body-fitted) coordinate systems for the cone geometry. With the help of equation 2.5, gradient, divergence and product of vectors can be defined and substituted into the governing equations. This transformation causes (additional) source terms in the ξ-, η- and φ-momentum equations, and therefore the governing equations are not strongly conservative. But the computational effort is greatly reduced compared to a (strongly conservative) generalized coordinate transformation and therefore chosen for this investigation.

For further simplification, the Mach number *Ma* and the Reynolds number *Re* are introduced as

$$Ma = \frac{U^*_\infty}{a^*_\infty} = \frac{U^*_\infty}{\sqrt{(\gamma-1)C^*_{p\infty}T^*_\infty}} \quad , \quad Re = \frac{\rho^*_\infty U^*_\infty L^*_\infty}{\mu^*_\infty}\,.$$

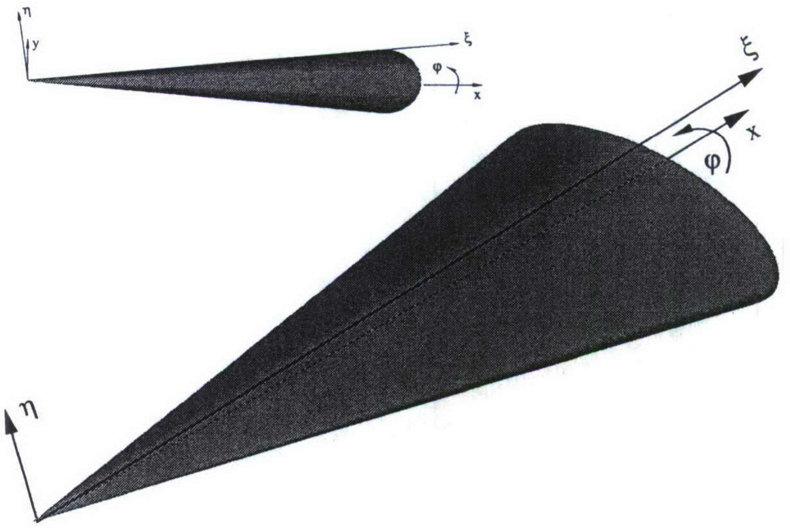

Figure 2.2: Curvilinear coordinate transformation.

With the help of these derivations the governing equations can be sorted by their derivatives along the coordinate axes and the so-called vector form is obtained:

$$\frac{\partial \mathbf{U}}{\partial t} + \frac{1}{h_1 h_2 h_3} \left[\frac{\partial h_2 h_3 \mathbf{E}}{\partial \xi} + \frac{\partial h_1 h_3 \mathbf{F}}{\partial \eta} + \frac{\partial h_1 h_2 \mathbf{G}}{\partial \varphi} + \mathbf{H} \right] = 0 \,. \tag{2.6}$$

All vectors and coefficients for the different geometries under investigation can be found in appendix A.

3. Numerical Method and Simulation Setup

A spatial DNS model is used with a fourth-order Runge-Kutta method for time-advancement and "fourth-order" split finite differences in the x- and y-directions. However, an analysis of the modified equation indicates that this spatial discretization is formally only third-order accurate (see Harris (1997)). In the z-direction, a periodic solution is assumed and, consequently, a Fourier transformation is applied. Variables are symmetric over one-half of the spanwise wavelength (except for w, which is antisymmetric over this distance), thus only half a wavelength in the z-direction needs to be computed. For the conical/cylindrical geometries, the "wavelength" is the azimuthal angle φ, which has to be an integer fraction of a full circle. For the cylinder and circular cone, different sizes of the cross-sectional wedge can be computed (for this work the wedge ranges from $2\pi/8$ to $2\pi/24$). But for simulations of an elliptical cone, half the cross section ($\varphi = \pi$) has to be chosen because only two symmetry planes, i.e. one along the vertical and the second one along the horizontal centerline are present. The numerical method is explained in detail in the dissertation of Harris (1997).

3.1 Initial Condition

To obtain an initial condition (IC) precursor simulations are performed with a formally second-order accurate Total Variation Diminishing (TVD)-upwind scheme. In these simulations the entire flow field including the conical shock wave is computed (as can be seen in Figure 3.1). Thus exact consistency with the experimental set-up, e.g. influences of the nose radius, is achieved. Because the TVD-upwind scheme is very robust, so it is capable of capturing the shock, it is for the same reason not suitable for boundary-layer transition simulations. Hence, a two-step procedure is employed where the domain of interest is extracted from the precursor simulation

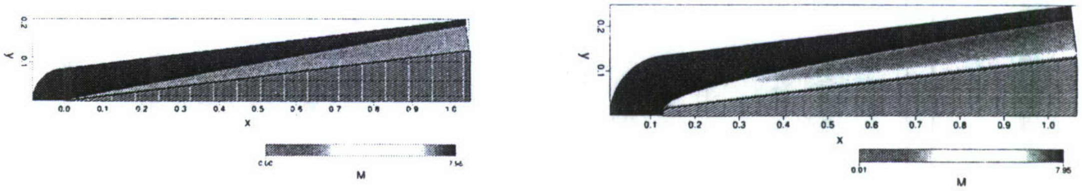

(a) $R_N = 3.81 \cdot 10^{-5}$m.

(b) $R_N = 1.78 \cdot 10^{-2}$m.

Figure 3.1: Initial condition.

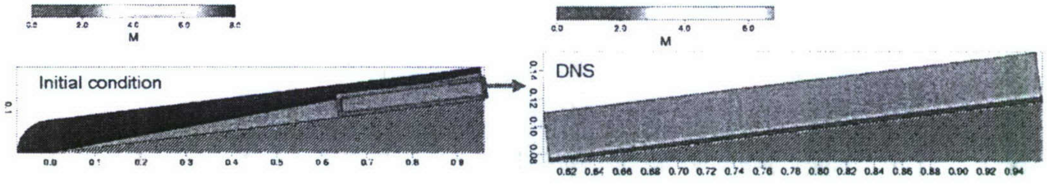

Figure 3.2: Schematic of transferring data from the precursor simulation to the computational domain for transition investigations.

and serves as an initial condition for the investigations of stability and transition. This procedure is schematically depicted in Figure 3.1. Because the domain of interest is a smaller sub-domain of the entire flow field, high resolution can be achieved for accurate investigations of stability and transition.

3.2 Computational Domain

The domain, on which the boundary-layer transition simulations are performed, is illustrated in Figure 3.3. The domain starts at x_{in} and ends at x_{out} covering the region of interest from a transitional point of view. The upper limit of the domain remains below the shock allowing the usage of more accurate and efficient numerical schemes. Disturbances are introduced through a slot located between x_1 and x_2. A more detailed description of the disturbance generation can be found in section 3.7.

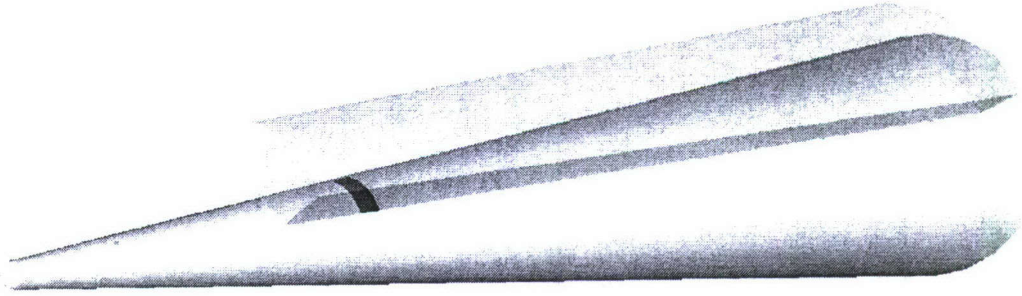

Figure 3.3: Computational domain.

3.3 Inflow Boundary Condition

At the inflow boundary, all values are fixed using the initial solution (from the precursor simulation or from the similarity solution for flat-plate and cylinder investigations) with the exception in the subsonic region close to the wall where the pressure is computed by

$$\frac{\partial p}{\partial \xi} = 0 \,. \tag{3.1}$$

Because the temperature T and the density ρ are fixed, the equation of state is violated in this subsonic region. However, upstream-traveling sound waves are allowed to pass through the boundary with only weak reflections. This allows the disturbance slot to be located close to the inflow.

3.4 Free-Stream Boundary Condition

3.4.1 For the Base Flow

A boundary condition based on characteristics after Thompson (1987) is implemented with an additional term which determines the reflectivity of the boundary condition after Kim & Duck (2000). Thompson (1987) assumed an inviscid flow at the boundary of the domain which can be diagonalized in wall-normal direction. The governing equations (2.6) with $\mu = 0$ are translated to primitive variables ρ, u, v, w, p and eigenvalues λ_i with related eigenvectors of the matrix $\mathbf{Q}$ in equation (3.2) are found.

$$\frac{\partial \mathbf{U}}{\partial t} + \mathbf{Q}\frac{\partial \mathbf{F}}{\partial \eta} + \mathbf{C} = 0\,, \tag{3.2}$$

where $\mathbf{C}$ contains the summation of the source terms, ξ-, and φ-derivatives. If $\lambda < 0$, the wave is incoming and $\lambda > 0$ represent outgoing waves. For the slender cone geometries under investigation the free stream is a subsonic inflow with only one of the five waves traveling outward. For the outgoing wave, properties can be computed from grid nodes within the domain while for the incoming waves boundary conditions have to be modeled. Therefore, an ambient state from the initial condition is stored and used to extrapolate properties for the incoming waves with regard to the surroundings. This is a valid approach because the correct streamwise and wall-normal gradients are already known from the initial condition (precursor simulation). Hence, no further models are needed to simulate the boundary condition. The scheme to compute the free-stream boundary condition is so far second order accurate. A more detailed mathematical derivation and description can be found in the literature of Thompson (1990) and Kim & Duck (2000).

3.4.2 For the Disturbance Flow

An exponential decay condition is applied when disturbances are introduced. The total flow approaching the free-stream boundary is split into a steady (base flow) and an unsteady part (disturbances). While the steady part is fixed, disturbances are assumed to decay exponentially in wall-normal direction. Although the Mach wave emanating from the disturbance slot and hitting the free-stream boundary travels along a characteristic, the exponential decay condition results in lower domain heights without influencing the disturbance waves inside the boundary layer. Therefore, the computational domain for the transition investigations can be placed closer to the nose of the cone using this boundary condition. Further discussion is provided in Thumm (1991) and Terzi (2004).

3.5 Outflow Boundary Condition

Assuming that a small-amplitude sinusoidal wave hits the outflow, the condition

$$\frac{\partial^2 \phi'}{\partial \xi^2} = -\alpha^2 \phi' \tag{3.3}$$

allows the disturbance waves to pass the boundary with minimal reflections. Experience has shown that treating the outflow boundary by applying

$$\frac{\partial^2 \phi}{\partial \xi^2} = 0 \tag{3.4}$$

to all conservative variables works equally well unless $\phi \leq 0$, or if $|\phi|$ is near zero. Therefore, a buffer domain is used for nonlinear disturbance calculations where disturbances are ramped down and the base flow is recovered. The length of the outflow ramp should be about two wavelengths of the largest high-amplitude wave under consideration in order to minimize upstream effects of this boundary condition.

3.6 Wall Boundary Condition

3.6.1 For the Base Flow

An adiabatic, no-slip, no-penetration wall boundary condition is applied. Hence, all velocity components are zero at the wall. In order to simulate a wall without heat transfer a Neumann condition is applied to the temperature:

$$\frac{\partial T}{\partial \eta} = 0\,. \tag{3.5}$$

The wall pressure p_{wall} is calculated from the wall-normal momentum equation. This equation, as derived from equation (2.6), in the y-direction is

$$\begin{gathered}\tfrac{\partial}{\partial \eta}(h_1 h_3 p) - p\tfrac{\partial h_1 h_3}{\partial \eta} = -h_1 h_2 h_3 \tfrac{\partial \rho v}{\partial t} + \tfrac{\partial}{\partial \xi}(h_2 h_3 \tau_{\xi\eta}) - \tfrac{\partial}{\partial \eta}[h_1 h_3\,(\rho v^2 - \tau_{\eta\eta})] + \tfrac{\partial}{\partial \varphi}(h_1 h_2 \tau_{\eta\varphi}) \\ +h_3 \tau_{\xi\eta} \tfrac{\partial h_2}{\partial \xi} + h_1 \tau_{\eta\varphi} \tfrac{\partial h_2}{\partial \varphi} - h_3 \tau_{\xi\xi} \tfrac{\partial h_1}{\partial \eta} - h_1 \tau_{\varphi\varphi} \tfrac{\partial h_3}{\partial \eta}\end{gathered} \tag{3.6}$$

Since the base flow is steady, the time derivative term in the momentum equation is zero.

3.6.2 For the Disturbance Flow

All velocities are still zero except for the v-velocity in the region where disturbances are introduced through the blowing and suction slot (see Figure 3.3). The time derivative in the momentum equation for the perturbed flow cannot be neglected over the disturbance slot. Instead is computed with

$$\frac{\partial \rho v}{\partial t} = v\frac{\partial \rho}{\partial t} + \rho\frac{\partial v}{\partial t}\,. \tag{3.7}$$

The term $\partial\rho/\partial t$ is computed with the continuity equation and the term $\partial v/\partial t$ is analytically computed from equation (3.8). The wall BC for the temperature switches from adiabatic to isothermal because the temperature fluctuations are too "fast" to influence the wall temperature. This way, the physics of a wind-tunnel flow are best captured due to the inertia of the wall regarding high-frequency disturbances.

3.7 Disturbance Generation

Harmonic disturbances are introduced by periodic blowing and suction through a slot in the wall, located about one TS wavelength downstream of the inflow (see Figure 3.3). All other boundary conditions are not affected. Note, that the pressure boundary condition (equation (3.6)) is valid for a non-zero wall-normal velocity. The perturbed velocity v is given as

$$v(\xi, t) = A(t)v_p(\xi)\sin(\omega t - \Phi)\,, \tag{3.8}$$

which is a harmonic function with (disturbance) frequency ω and time-dependent amplitude $A(t)$. In this study, the amplitude is ramped up over the first period beginning at $t = 0$ with and held constant subsequently. In addition, no mass flux is going into the flow due to the prescribed spatial disturbance profile $v_p(x)$ which is a fifth order polynomial simulating a dipole so that predominantly vorticity modes are excited. For generating steady longitudinal vortices, steady forcing through a monopole after Meitz (1996) is applied in the v-velocity over the same disturbance slot as used for the harmonic forcing. Although no mass flux is globally introduced into the flow, the base-flow profiles change locally depending on the disturbance profile.

4. Code Validation

4.1 Flat Plate

The code originally developed by Harris (1995) to investigate plane supersonic wakes has been intensively tested for various applications over the past years. Terzi (2004) investigated subsonic backward-facing steps and implemented to that end several turbulent models. Husmeier (2002) investigated the non-parallel effects of a supersonic boundary layer at Mach 3, while Mayer (2004) studied the effects of adverse streamwise pressure gradients at $Ma = 3$. Zengl (2005) concentrated on the oblique subharmonic resonance at Mach 3 as discovered in the Mach 2 experiments by Kosinov *et al.* (1994). Mayer *et al.* (2007) performed in-depth comparison with experimental measurements by Kosinov (2006), further validating the accuracy of the code and its capability to capture flow conditions and instabilities present under wind-tunnel conditions. Please refer to the latter references for validation cases with LST and experimental data at moderate supersonic speeds. Based on its excellent performance, this code was chosen for the numerical investigations of transition at hypersonic speeds. Because no validation at hypersonic speeds was performed in our group so far, a brief comparison of a flat-plate boundary layer at Mach 6.8 is presented before further validation cases are discussed for conical geometries in the following section.

To this end, the stability behavior of a small-amplitude two-dimensional second-mode wave is compared with LST. The physical parameters for the computational setup are chosen to match "cold" wind-tunnel conditions (c.f. Stetson *et al.* (1983)), i.e. the Mach number is 6.8, free-stream temperature and pressure are $71K$ and $415.56Pa$, respectively. The wall is assumed to be adiabatic with isothermal disturbances. The domain of interest (red line) is graphed in the stability diagram (see Figure 4.1a) at a frequency of $F = 8 \cdot 10^{-5}$, which is chosen because a region of highest amplification is passed. The amplitude is chosen to be $A_{1,0} = 0.01\%$ in order to exclude nonlinear effects and therefore better compare with *LST*. Effects of the growing boundary layer (non-parallel effects) are still simulated in the *DNS* which are also neglected for the *LST* (c.f. section 1.3.1). Across the unstable region, Figure 4.1b shows good agreement of the amplification rates obtained by *DNS* with *LST* once the wave has developed downstream of $R_x = 1,400$. The deviation of the *DNS* from *LST* is small and within the margin of other publications (c.f. e.g Thumm (1991) or Eißler (1995)). Therefore it is believed that the correct stability behavior is simulated.

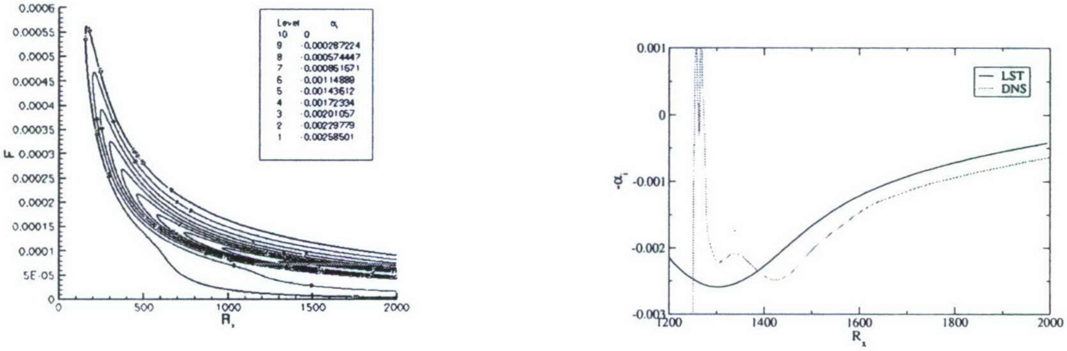

(a) Linear Stability Diagram.

(b) Amplification rate plot.

Figure 4.1: (a) Linear stability diagram for two-dimensional waves at $Ma = 6.8$, $T_\infty = 71K$, adiabatic wall. (b) Amplification rate comparison of *DNS* with *LST* at $F = 8 \cdot 10^{-5}$.

4.2 Sharp Cone

To verify the implemented coordinate transformation, numerical results are compared with experimental measurements and other numerical investigations. The comparison of base-flow profiles with experimental measurements (c.f. Stetson *et al.* (1983)) in Figure 4.2a shows an overall close agreement. The insert in Figure 4.2a compares experimentally measured and computed boundary-layer thickness δ because it is used to normalize the ordinates in the graphs of Figure 4.2. The discrepancies with the experimental data might be due to the uncertainties in the measurements considering the excellent agreement between the base-flow profiles from our simulations and from those performed by Pruett *et al.* (1995) and Fezer & Kloker (2004) (c.f. Figure 4.2b). As seen from Figure 4.3, good agreement is also achieved for the growth rates of small-amplitude disturbance waves. The amplification rate based on maximal temperature disturbances of a second-mode two-dimensional wave lies within a few percent of the *PSE* results by Chang & Malik (1993*b*) and the *DNS* results by Fezer & Kloker (2004) validating our numerical simulations. It is hypothesized that the two *DNS* do not match each other exactly because of the different methods of how the base-flow quantities are derived. Fezer & Kloker (2004) use a Mangler transformation of a flat-plate similarity profile, which neglects spanwise curvature effects, and superpose an Euler solution to obtain the streamwise gradients. As stated in section 3.1 the whole flow field is simulated without those assumptions for the current investigations. For a further validation the wall pressure distribution for second-mode two-dimensional waves is compared with experimental measurements in Figure 4.4, including different

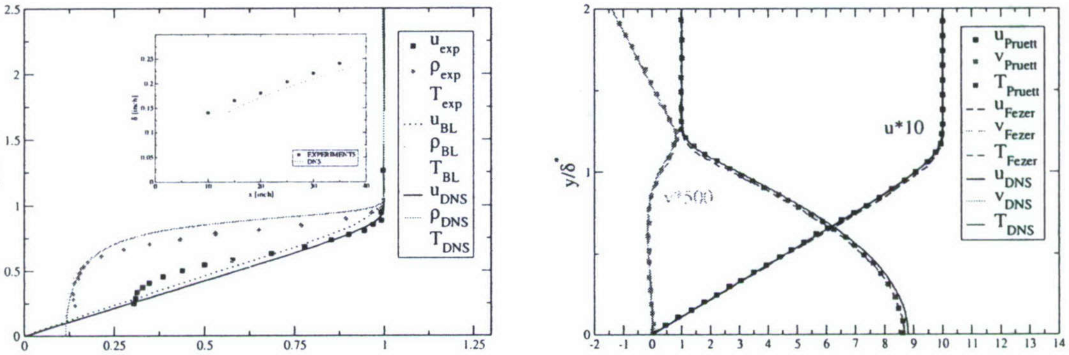

(a) Experiments (c.f. Stetson *et al.* (1983)) at $R_x = 2048$.

(b) Simulations (c.f. Pruett *et al.* (1995); Fezer & Kloker (2004)) at $R_x = 1742$.

Figure 4.2: Base-flow comparison. $Ma = 7.95$, $Re = 3,333,333$, $T_\infty = 53.35K$.

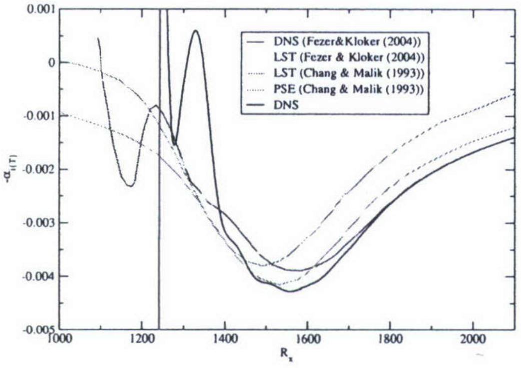

Figure 4.3: Two-dimensional amplification rate compared with results from Fezer & Kloker (2004) and Chang & Malik (1993*a*). $Ma = 7.95$, $Re = 3,333,333$, $T_\infty = 53.35K$, $F = 1.17 \cdot 10^{-4}$, $A_{1,0} = 0.001\%$.

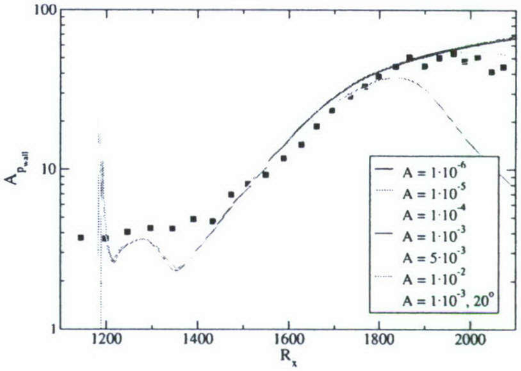

Figure 4.4: Wall pressure distribution in downstream direction of different disturbance waves. $Ma = 7.95$, $Re = 3,333,333$, $T_\infty = 53.35K$, $F = 1.17 \cdot 10^{-4}$.

disturbance amplitude levels of two-dimensional waves and a second-mode oblique wave at a small wave angle. Comparing the two-dimensional waves, amplitudes levels up to 0.1% overlap each other, matching the experimental measurements up to $R_x = 1,900$. When the disturbance amplitude level is further increased higher harmonics of the disturbance waves cause the amplitude levels of the fundamental waves to decrease. To this end, a disturbance amplitude of 0.5% matches the experimental data best leading to the conclusion that moderate nonlinear amplitude levels are present in the natural transition process of the experiments by Stetson *et al.* (1983). The three-dimensional wave plotted in Figure 4.4 outlines the possibility that, instead of the assumed two-dimensional waves, second-mode oblique waves at small wave angles might also be present in the experiments. This fact underlines the practical significance of the breakdown scenarios with oblique primary waves discussed in chapter 7 and chapter 8.

4.3 Blunt Cone ($R_N = 0.15"$)

Stetson *et al.* (1984) increased the unit Reynolds number of the experiments for cones with different nose radii. To exclude possible Reynolds number effects, DNS are therefore performed with a Reynolds number of $Re = 8,566,826$ in order to match the unit Reynolds number of the experiments ($Re/ft = 2,500,000$). Results for the nose radius $R_N = 0.15"$ are chosen for validation. For that case, base-flow velocity profiles of different downstream locations are graphed in Figure 4.5. Because these base-flow profiles have a positive $du/d\eta$ even in the free stream it is numerically hard to determine the boundary layer edge values and with that the boundary layer thickness. This stands in contrast to the sharp cone where the streamwise velocity is decreasing outside of the boundary layer in wall-normal direction, i.e. there is a maximum velocity in wall-normal direction for the sharp cone. Figure 4.6 shows how sensible the boundary layer thickness reacts to different percentages of boundary-layer edge velocity. Because the boundary-layer thickness based on 99.5% of the edge velocity matches best the experimental measurements, those values are used for normalization

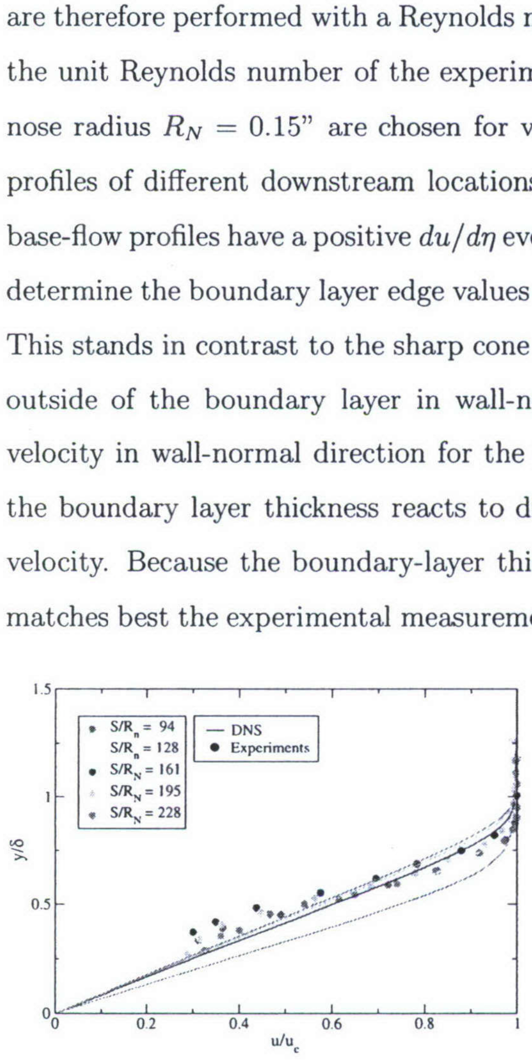

Figure 4.5: Base-flow profiles of streamwise velocity at different downstream locations. Comparison of experimental measurements and numerical simulations. $Ma = 7.99$, $Re = 8,566,826$, $T_\infty = 54.47K$.

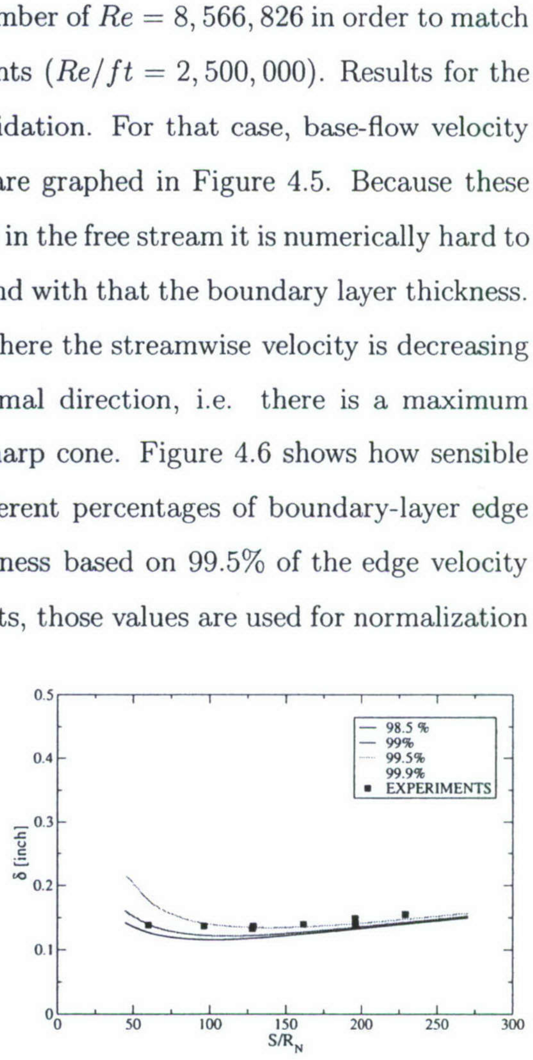

Figure 4.6: Boundary-layer thickness. Comparison of experimental measurements and numerical simulations. $Ma = 7.99$, $Re = 8,566,826$, $T_\infty = 54.47K$.

in Figure 4.5. Within the experimental uncertainties, Figure 4.5 and Figure 4.6 agree well. Even better confirmation of capturing the correct instability behavior of the hypersonic flow is achieved when looking at a simplified general inflection point criterion for different downstream locations (Figure 4.7). The numerical results and experimental data agree very well except for the most upstream location. This can be linked to the difficulties in defining the boundary-layer thickness in presence of an entropy layer. Close to the nose, when the entropy layer has not been swallowed yet by the boundary layer, it is hard to distinguish between entropy layer and boundary-

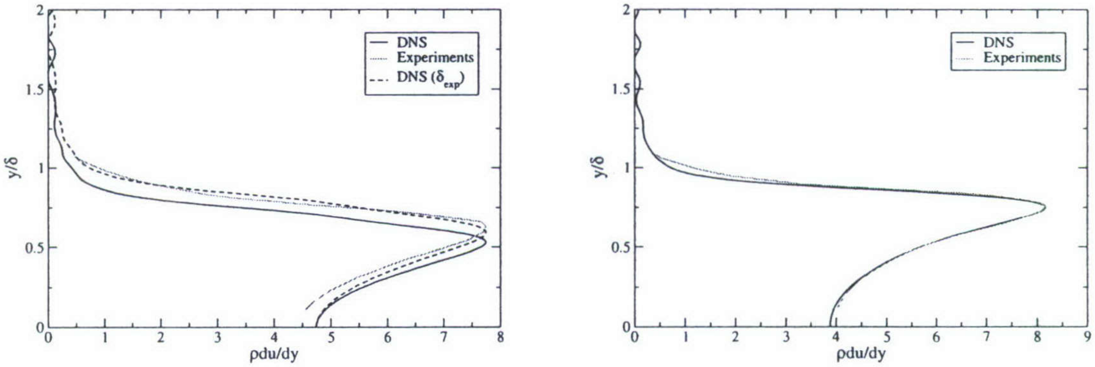

(a) $S/R_N = 80.9$.

(b) $S/R_N = 128.6$.

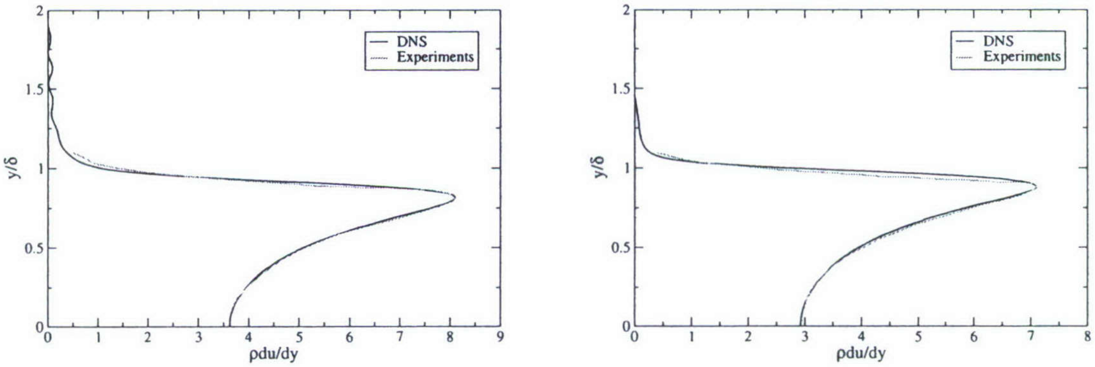

(c) $S/R_N = 158.5$.

(d) $S/R_N = 265.0$.

Figure 4.7: Simplified generalized inflection point. Comparison of experimental data and numerical simulations. $Ma = 7.99$, $Re = 8,566,826$, $T_\infty = 54.47K$.

layer thickness. In Figure 4.6, the boundary-layer thickness computed with 99.5% of edge velocity incorporates the entropy layer and is therefore over-estimated resulting in the discrepancies in the wall-normal direction for the most upstream location in Figure 4.7. When the experimentally determined boundary layer thickness is used for normalization, the profile agree as well as the farther downstream locations. In order to eliminate the uncertainty if the correct boundary-layer thickness is captured, results are compared with numerical simulations performed by Rosenboom *et al.* (1999). They analyzed the effect of nose bluntness under the experimental condition of Stetson *et al.* (1984) through local and non-local linear instability theory. A comparison with their dimensional velocity and temperature base-flow profiles are graphed in Figure 4.8. Both profiles for the two downstream locations match—giving confidence in the numerical results. The small differences may be due to a coarser resolution in their simulations of Rosenboom *et al.* (1999). Zhong (2005), also performed numerical investigation of the effect of nose radius on the receptivity behavior of the conical boundary layer. Unfortunately, results are only plotted for one downstream location which exceeds the experimental test model length (and also the computational domain used for this validation) so that a comparison is not possible.

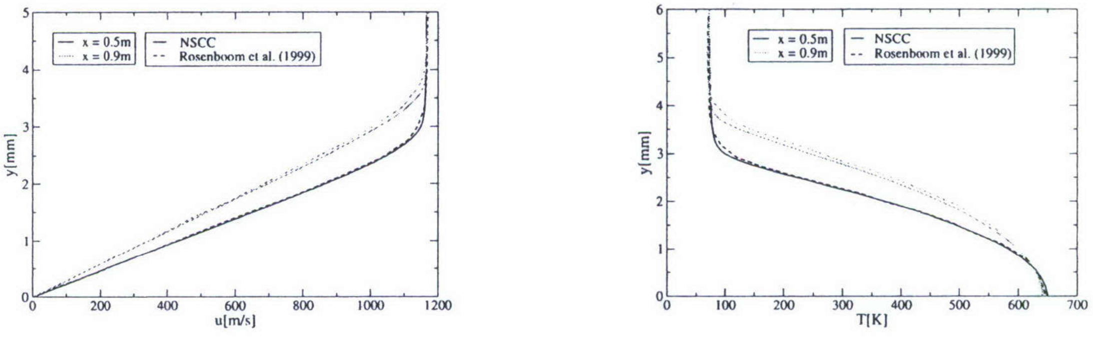

(a) Streamwise velocity.

(b) Temperature.

Figure 4.8: Comparison of base-flow profiles with numerical efforts by Rosenboom *et al.* (1999) for two downstream locations. $Ma = 7.99$, $Re = 8,566,826$, $T_\infty = 54.47K$.

5. Transition Investigations of a Boundary Layer on a Flat Plate

5.1 Supersonic Flow at Mach 2

The early nonlinear stages of transition in a supersonic boundary layer at Mach 2.0 were investigated using spatial Direct Numerical Simulations (DNS). The computational setup matches earlier experimental studies by Kosinov *et al.* (1994) and Ermolaev *et al.* (1996), where transition was triggered by localized forcing leading to the development of a wedge-shaped wave train. While the focus of these experiments had been on a new breakdown mechanism, called asymmetric subharmonic resonance, the experimental data indicates the presence of another, possibly competing mechanism. With the simulations presented here, two fundamental questions were addressed. First, does this new breakdown mechanism, visible in the experimental data set from Ermolaev *et al.* (1996), has any characteristics of oblique breakdown (Fasel *et al.*, 1993), a mechanism never observed in any experimental investigation before? And second, if oblique breakdown indeed occurs in these experiments, what role does it play for supersonic boundary-layer transition at Mach 2 when compared to asymmetric subharmonic resonance, the mechanism that was considered by Ermolaev *et al.* (1996) to be dominant? In order to answer the last question the subharmonic transition route was studied in detail. A similar subharmonic resonance mechanism as observed in the experiments was also visible in the present work. Additionally, several other resonance triads can be identified using Linear Stability Theory (LST) and DNS. The selection process for a specific triad is not influenced by the amplitude ratio of fundamental and subharmonic disturbances as proposed by the experimentalists (Ermolaev *et al.*, 1996), but by the phase relation between disturbances of both frequencies.

5.2 Physical Problem and Computational Setup

Supersonic flow at Ma = 2.0 over a flat plate is investigated numerically using spatial DNS. The computational setup is designed to allow for a direct comparison of the DNS results with the experimental measurements by Ermolaev *et al.* (1996). The unit Reynolds number is $Re = 6.6 \times 10^6 m^{-1}$ and the free-stream temperature is $T^*_\infty = 160K$. The mean flow in the DNS is very close to the compressible similarity solution for Ma = 2.0. In earlier investigations by Kosinov *et al.* (1990), the mean flow profile in their experiment also matches the similarity solution for a Ma = 2.0 boundary layer. Therefore, it can be assumed that the experiment (Ermolaev *et al.*, 1996) and the DNS presented here are performed under the same mean flow conditions.

As illustrated in figure 5.1, the flat-plate model used by Ermolaev *et al.* (1996) had a length of $0.45m$ and a width of $0.2m$. Disturbances were generated by a glow discharge (harmonic point source) in an electrical discharge chamber placed inside the flat plate and penetrated the flow through a hole with a diameter of $0.42mm$ at $x^* \simeq 0.038m$. In order to minimize computational cost, the extent of the computational domain for the DNS discussed here covers only a portion of the experimental setup, as indicated by the box placed on top of the flat plate in figure 5.1. The inflow of the domain is located $0.02m$ downstream of the leading edge of the plate ($x^*_0 = 0.02m$), while the outflow is placed at $x^*_L \simeq 0.11m$ or $x^*_L \simeq 0.18m$, depending on the purpose of the simulation (parameter study or final simulation). The domain height of $y^*_H \simeq 0.035m \sim 34\delta$ (at the outflow) or $y^*_H \simeq 0.02m \sim 24\delta$ (according to the domain length) has been sized such that disturbance reflections from the free-stream boundary into the domain of interest are prevented (figure 5.2a). A spectral discretization is employed in the spanwise direction of the computations and, as a result, the single disturbance generated by the glow discharge in the experiments is replaced by a periodic series of localized disturbances spaced one fundamental wave length apart, $\lambda^*_z = z^*_W = 0.063m$. This wave length corresponds to a fundamental spanwise wave number of $\beta^* = 2\pi/z_W^* = 0.1mm^{-1}$. The domain width z_w has been chosen large enough that adjacent disturbances do not interact with each other inside the computational domain (figure 5.2b). In fact, computational cost is reduced even further by enforcing symmetry with respect to the $z^* = 0.0$ plane; thus, in effect, restricting the simulation to the interval $[0, z_W^*/2 = \lambda_z^*/2]$.

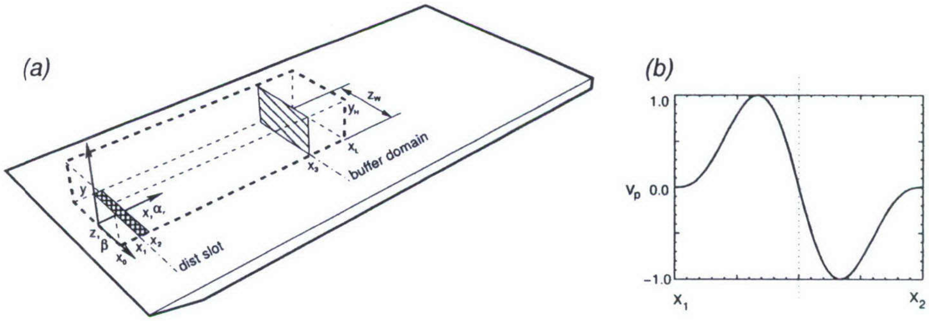

Figure 5.1: Comparison of experimental flat-plate model (H×L×W $= 10 \times 450 \times 200mm$) with the computational domain.

As indicated in figure 5.1, time-harmonic disturbances with the fundamental frequency of $20kHz$ and the subharmonic frequency of $10kHz$ are introduced through a blowing and suction slot located between $x_1^* \simeq 0.029m \leq x^* \leq x_2^* \simeq 0.038m$ ($x_2^* - x_1^* \simeq 0.7\lambda_x^{2D}$ of the fundamental frequency). The subharmonic frequency and therefore, the subharmonic resonance triad investigated by Kosinov *et al.* (1994) and Ermolaev *et al.* (1996) has been deliberately excluded in some DNS (CFUND 1-5) in order to focus only on the nonlinear wave interactions at $20kHz$. With these simulations, the question whether oblique breakdown appears in the experiments could be addressed. For simulations of the subharmonic resonance triad (CSUB 1-10), the flow was also perturbed with the subharmonic frequency. Since the forcing method in the simulations differs from the experiment, a calibration procedure is required for adjusting the spanwise distribution of the disturbance input in the DNS such that the flow response downstream of the forcing location closely matches that from the experiment. A detailed description of this procedure is provided in section 5.3.1.

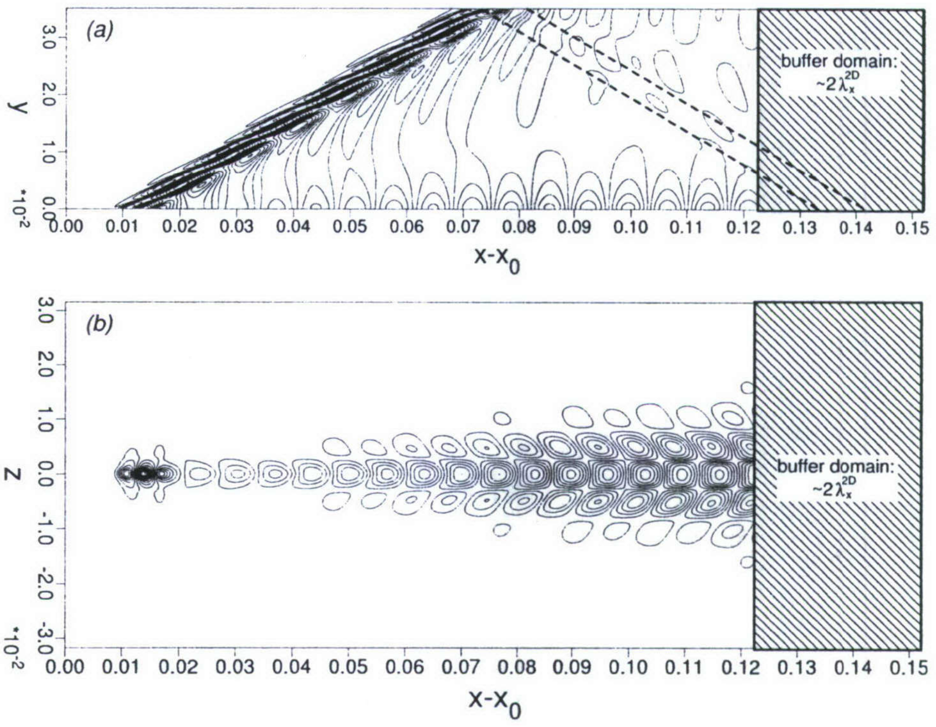

Figure 5.2: Computational setup: (*a*) Contours of disturbance pressure ($20kHz$) with the spanwise wave number $\beta = 0.1mm^{-1}$ indicating that reflections from the free-stream boundary reach the near wall region inside the buffer domain downstream of the region of interest, (*b*) contours of disturbance pressure ($20kHz$) at the wall showing that the disturbances do not reach the spanwise boundaries.

The computational grid for all simulations has been stretched in wall-normal direction and for certain simulations the mesh size in streamwise direction was reduced near the outflow (figure 5.3a). Only weak grid stretching has been employed in order to avoid any grid dependence of the numerical solution. The number of grid points required in streamwise direction is determined by the domain length and the streamwise wave length of the evolving instability waves. The streamwise domain extends across 12 wave lengths of a two-dimensional instability wave with frequency $20kHz$ (in the linear stage). One wave length is resolved with about 27 points inside the equidistant grid region before the resolution is increased towards the outflow. The wall-normal grid resolution has been determined using as a guideline the shape of the wall-normal amplitude distribution for the u-velocity disturbance in the linear stage. As an example, a small portion of this wall-normal distribution is illustrated in figure 5.3b for the case of frequency $20kHz$, spanwise wave number $\beta = 0.5mm^{-1}$ and the streamwise position $x^* = 0.06m$. For spanwise wave numbers close to $\beta = 0.5mm^{-1}$, a small second amplitude maximum appears near the wall, which, in this case, is resolved by 6 points. Disturbances with the subharmonic frequency do not exhibit such a behavior in the linear stage.

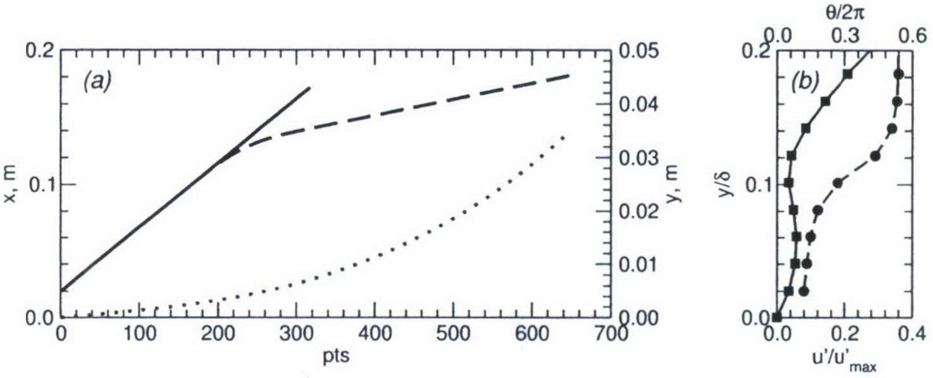

Figure 5.3: Computational setup: (*a*) Grid in streamwise direction for a simulation with equidistant grid (–) (CFUND 1-4 and CSUB 1-10) and a simulation with increased resolution near the outflow (- -) (CFUND 5), grid in wall-normal direction for all simulations (...) discussed here, (*b*) symbols indicate grid locations used to resolve the second maximum of the wall-normal amplitude distribution for the u-velocity disturbance with $20kHz$ (■–■) and its corresponding wall-normal phase distribution (●- -●) at the spanwise wave number $\beta = 0.5mm^{-1}$ and the streamwise position $x^* = 0.06m$.

5.3 Identification of oblique breakdown

A difficulty that arises when setting up simulations to match the experiment by Ermolaev *et al.* (1996) is the implementation of the disturbance generation into the Navier-Stokes solver. The diameter ($0.42mm$) of the hole in the plate model used in the experiment is far too small for being properly resolved in a DNS. In the present numerical simulations, the disturbances are therefore introduced into the computational domain by forcing the v-velocity through a blowing and suction slot at the wall. The application of this very different disturbance generation can be justified if the evolving instability waves are in the linear regime since their eigenbehavior does not depend on the details of the wave generation. Important are only the resulting amplitude and phase of the different spanwise Fourier modes contained within the disturbance developing immediately downstream of the disturbance slot. Therefore, a receptivity study has been performed in order to determine what spanwise amplitude and phase distribution of the v-velocity over the disturbance slot produces the same flow response as the localized forcing technique used in the experiment. Since the experimental data are not known at the forcing location, a position nearby ($x^* = 0.06m$) serves as a reference location for the receptivity study. The modeling of the harmonic point source with the blowing and suction slot leads to a broad spanwise forcing spectrum. This forcing method differs from previous investigations of the oblique breakdown by Thumm (1991), Fezer & Kloker (1999) and Husmeier *et al.* (2005), where only one discrete wave pair was forced and only the higher-harmonic spanwise modes of this waves were included in the simulations.

The results of the receptivity study are presented in the next section. Following the receptivity study, DNS results for the linear regime (low disturbance amplitude) are compared to data obtained from LST and experimental data by Kosinov (2006) at $x^* = 0.06m$ in order to verify the validity of the numerical setup and the application of the different disturbance generation. Results of the early nonlinear regime are discussed in the succeeding sections. Here, the focus is on answering the two previously raised questions: Can oblique breakdown be identified in the experiments and if oblique breakdown indeed occurs, what role does it play when compared to asymmetric subharmonic resonance. To answer the first question, DNS have been performed, where only the fundamental frequency was perturbed, resulting in a deliberate exclusion of the subharmonic resonance triad.

5.3.1 Receptivity Study

A receptivity study has been performed for the fundamental frequency ($20kHz$). Disturbances of this frequency still exhibit a linear behavior up to the streamwise position $x^* = 0.06m$ in both, the experiment and the DNS. The experimental data employed as a reference for the receptivity study have been provided by Kosinov (2006) and were obtained using hot-wire measurements at the wall-normal location $y^*/\delta^* = 0.53$. The raw measurement data consist of the disturbance voltage over the mean voltage $(e^*)'/E^*$ measured at various spanwise locations extending from $z^* = -11.2mm$ to $z^* = 7.3mm$. The experimental data exhibit a slight asymmetry with respect to $z^* = 0.0$. Since the computational setup is symmetric with respect to $z^* = 0.0$, only half of the experimental data points have been considered as a reference for the receptivity study (from $z^* = 0.0$ to $z^* = 11.2mm$ in figure 5.4). The measurement data have been extended up to $z^* = z^*_W/2 \simeq 0.0315$ using additional data points with zero amplitude and zero phase, then interpolated onto an equidistant grid with

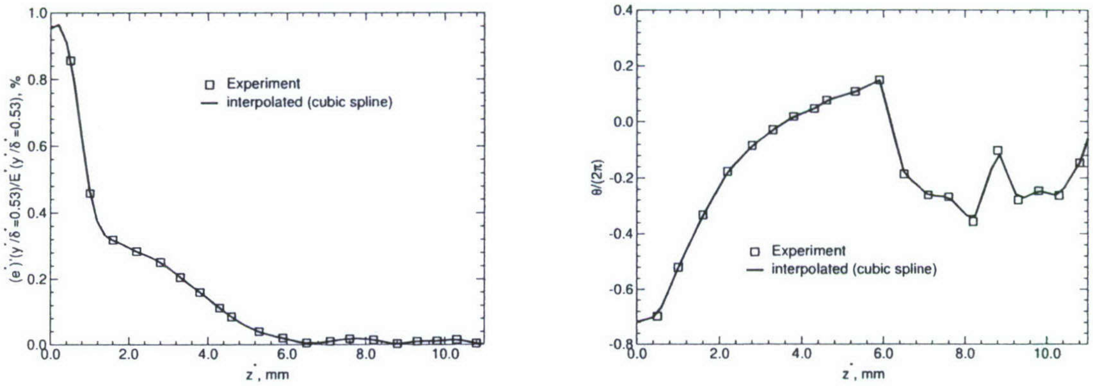

(a) Spanwise amplitude distribution.

(b) Spanwise phase distribution.

Figure 5.4: Spanwise amplitude (a) and phase (b) distribution ($20kHz$) of normalized output signal $(e^*)'/E^*$ (disturbance voltage over mean voltage) measured by a hot-wire anemometer in the experiment at streamwise location $x^* = 0.06m$ and wall-normal location $y^*/\delta^* = 0.53$: (□) experiment (Kosinov, 2006), (–) interpolated by a cubic spline.

$n_z = 161$ points, and finally transformed into Fourier space using a symmetric FFT (figure 5.5).

The raw hot-wire output signal can be related to mass-flux and temperature fluctuations in the flow. The temperature fluctuations are assumed to be small (Kosinov, 2006) and therefore, the mass-flux disturbance can be directly calculated according to

$$\frac{(\rho^* u^*)'}{(\rho^* U^*)} = K \frac{(e^*)'}{E^*} \tag{5.1}$$

(figure 5.5a). Here, the calibration factor K depends on many parameters, e.g. the temperature loading factor of the hot-wire. For the present experimental data, its value is approximately 1/0.27 (Kosinov, 2006). In the hot-wire measurements, the mass-flux disturbance (figure 5.5a) is measured relative to the local mean mass flux $(\rho^* U^*)$ at the measurement location $(x^*, y^*) = (0.06m, 0.53\delta^*)$. The DNS data, on the other hand, are normalized by the free-stream value at the inflow boundary, $(\rho^* U^*)_\infty$. Therefore, as a final step, the measured mass-flux disturbance has been rescaled by $(\rho^* U^*)/(\rho^* U^*)_\infty \simeq 0.5$ so that the resulting amplitude distribution (figure 5.5a) can now be compared directly to the DNS data. As seen from figure 5.5a, the absolute disturbance amplitude at the reference location $x^* = 0.06m$ is small enough that the disturbance development from the forcing location up to $x^* = 0.06m$ is assured to be linear. This is necessary for the justification of the very different disturbance method (blowing and suction slot) employed in the simulations.

Having established the spectral composition of the disturbance at $x^* = 0.06m$ measured in the experiment, the receptivity study for matching up the DNS with this data proceeds as follows. In a first simulation (CFUND 1), disturbances with the same fundamental frequency of $20kHz$ as in the experiment are introduced by time-harmonic blowing and suction with a very low (linear) amplitude. At this point, the proper spectral distribution of the forcing amplitude $\tilde{A}(\beta)$ and phase $\theta(\beta)$ for the v-velocity that would lead to a match with the experimental data is still unknown.

Therefore, as a first guess, both $\tilde{A}(\beta)$ and $\theta(\beta)$ are kept constant over all spanwise Fourier modes, as indicated by the dotted lines in the amplitude and phase distribution plots of figure 5.6. The amplitude and phase distribution at the reference location $x^* = 0.06m$ of the disturbance that is generated by this type of forcing are also plotted in figure 5.6 as solid lines. Clearly, the DNS data do not match the corresponding experimental data points. However, considering that the disturbance development is linear, the appropriate forcing amplitude $\tilde{A}(\beta)^{new}$ for the v-velocity can now be calculated from the ratio of the amplitude distributions from experiment and DNS in figure 5.6a

$$\tilde{A}(\beta)^{new} = \frac{\frac{(e^*)'}{E^*}(\beta)}{\frac{(e^*)'}{E^*}(\beta = 0.0)}|^{exp} \cdot \frac{(\rho u)'(\beta = 0.0)}{(\rho u)'(\beta)}|^{DNS}, \tag{5.2}$$

and the appropriate phase $\theta(\beta)^{new}$ from the difference of the corresponding phase distributions in figure 5.6b

$$\theta(\beta)^{new} = \theta(\beta)|^{exp} - \theta(\beta)|^{DNS}. \tag{5.3}$$

The new forcing amplitude and phase distribution are plotted in figure 5.6 as the curves marked by stars and also in figure 5.7 as dotted lines. When using this adjusted forcing in a second DNS (CFUND 2, low forcing amplitude), the new simulation results match the experimental data almost exactly, as seen from figure 5.7. Note, the data in figure 5.7a are normalized by the amplitude value of the mass-flux disturbance at $\beta^* = 0.0$

The experimental data in figure 5.7 (Kosinov, 2006) have been transformed into Fourier space by a full Fourier series expansion specified in Ermolaev *et al.* (1996). Therefore, the experimental data are not entirely symmetric with respect to $\beta^* = 0.0$. The difference in the Fourier series expansion is also responsible for the small discrepancy between the phase distributions in figure 5.7(*b*). The experimental data,

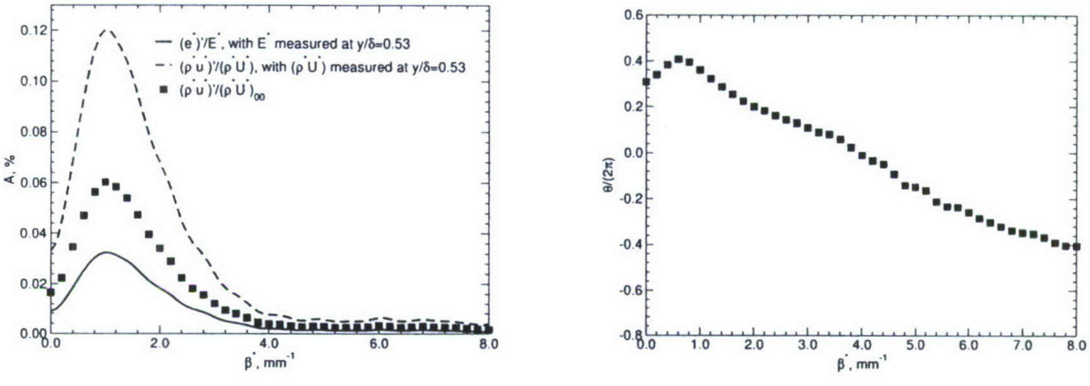

(a) Spanwise amplitude distribution.

(b) Spanwise phase distribution.

Figure 5.5: Spanwise amplitude (a) and phase (b) distribution ($20kHz$) of normalized output signal $(e^*)'/E^*$ from figure 5.4 transformed into Fourier space using a symmetric FFT: (–) output signal of hotwire, (- -) mass-flux disturbance non-dimensionalized by mean values measured at $y^*/\delta^* = 0.53$, (■) mass-flux disturbance non-dimensionalized by mean values measured in the free stream.

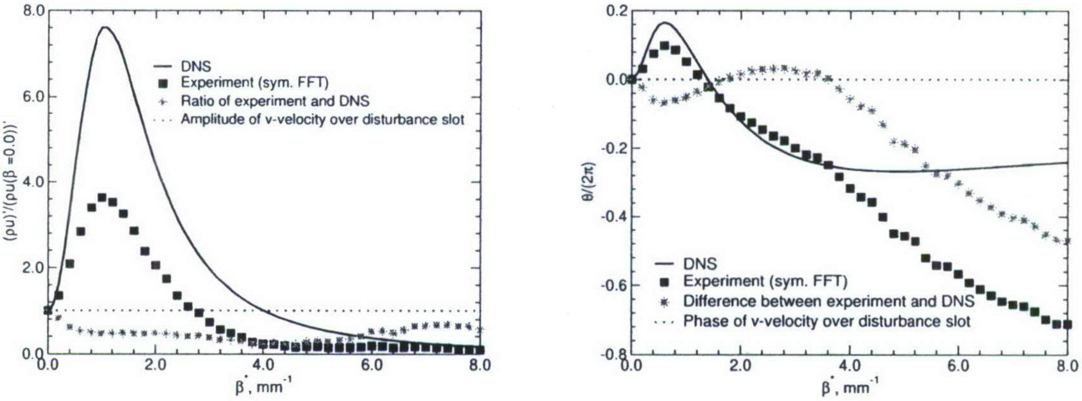

(a) Spanwise amplitude distribution.

(b) Spanwise phase distribution.

Figure 5.6: Spanwise amplitude (a) and phase (b) distributions ($20kHz$) of mass-flux disturbance (ρu)' at wall-normal location $y^*/\delta^* = 0.53$ and streamwise location $x^* = 0.06m$: (...) Forcing (v-velocity over the disturbance slot) applied in the DNS, (–) response of mass-flux disturbance due to the forcing in the DNS, (■) experimental data, (*) calculated using equation (5.2) and (5.3).

when transformed by a symmetric FFT in figure 5.5, match the numerical results in figure 5.7b exactly.

We close this section by providing an impression of the flow structures that develop over the disturbance slot in response to the blowing and suction at the wall with the amplitude and phase distribution shown in figure 5.7 as dotted lines. In figure 5.8, the flow response to this disturbance method is illustrated by isosurfaces of the v-velocity disturbance for different time instants. It is clearly visible that the resulting disturbance over the blowing and suction slot (indicated as a dark bar in figure 5.8) is highly localized in the DNS, just as the glow discharge in the experiment. The two different shades for the isosurfaces distinguish between the sign of the v-velocity. The larger structures travel along the Mach wave towards the free stream whereas smaller downstream travelling structures develop close to the surface.

5.3.2 Linear Behavior

The receptivity study from the previous section provides a tool for matching the flow response to the localized forcing technique applied in the experiments for the fundamental frequency ($20kHz$). This matching procedure however is based on a single quantity, $(\rho^* u^*)'$ and location $(x^*, y^*) = (0.06m, 0.53\delta^*)$ within the entire flow field. In order to verify that near the forcing location the disturbance development is indeed linear, the simulation results have been compared to results from Linear Stability Theory. Shown in figure 5.9 for selected spanwise wave numbers are the wall-normal amplitude and phase distributions for the streamwise velocity and the density from the DNS (CFUND 2, low forcing amplitude) and the corresponding eigenfunctions from LST. The amplitude distributions from both, linear theory and DNS, are normalized by their respective maximum value within the boundary layer. The excellent agreement between LST and DNS indicates that the linear eigenbehavior of the disturbances is correctly reproduced in the DNS. Furthermore, this

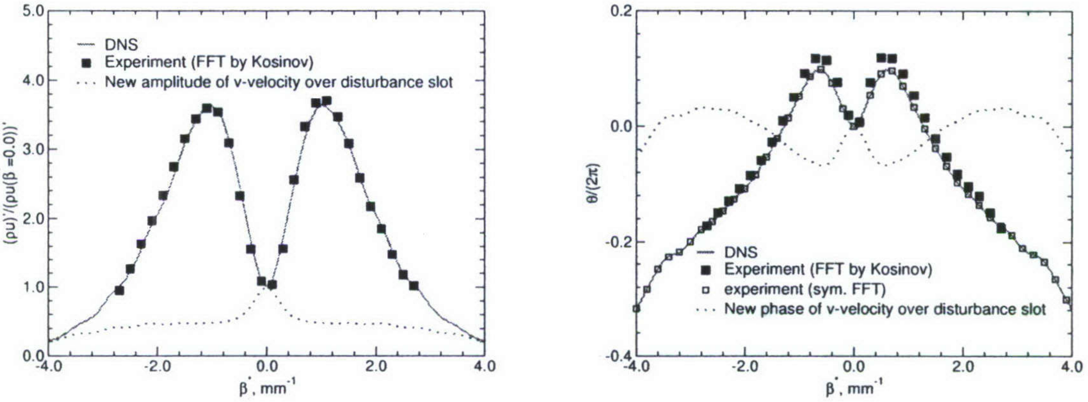

(a) Spanwise amplitude distribution.

(b) Spanwise phase distribution.

Figure 5.7: Spanwise amplitude (a) and phase (b) distributions ($20kHz$) of mass-flux disturbance (ρu)' at wall-normal location $y^*/\delta^* = 0.53$ and streamwise location $x^* = 0.06m$ of the DNS (−) and the experiment (■ FFT by Kosinov, □ symmetric FFT) for the new amplitude and phase distributions of the v-velocity over the disturbance slot (...).

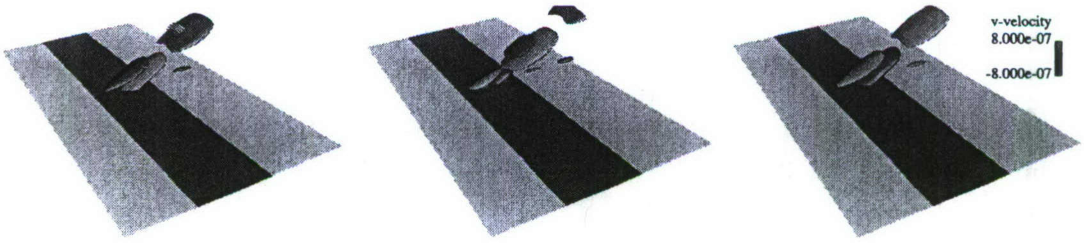

(a) $t = \frac{T}{4}$.

(b) $t = \frac{T}{2}$.

(c) $t = \frac{3T}{4}$.

Figure 5.8: Isosurface of constant v-velocity disturbance over the disturbance slot for three different time instants. The v-velocity at the wall is disturbed by the dotted amplitude and phase distribution in figure 5.7 (CFUND 2). The dark bar indicates the disturbance slot.

agreement emphasises that the DNS would match the mass-flux disturbance $(\rho^* u^*)'$ in the experiments throughout the linear regime if experimental data from different streamwise and wall-normal positions were available for comparison.

Figure 5.10 provides another indication that the disturbances in the DNS develop linearly, according to their eigenbehavior. The streamwise amplification rate α_i and the wave number α_r from LST, are compared to α_i and α_r from the DNS, which are computed from the wall-pressure disturbance. In figure 5.10a, the amplification rate from the DNS is most likely modulated by acoustic waves generated by the forcing. The amplification of disturbances in the DNS is somewhat stronger than predicted by LST. This difference between LST and DNS has also been observed in previous investigations (Thumm *et al.* 1989, Thumm 1991, Husmeier *et al.* 2005) and has been attributed to non-parallel effects resulting from the growth of the boundary layer. For the streamwise wave number α_r (figure 5.10b), which is less sensitive to non-parallel effects, the agreement between DNS and LST is nearly perfect.

In summary, the focus of this section has been on the linear behavior of disturbances with the fundamental frequency of $20kHz$. It was shown that the DNS can reproduce the results predicted by linear theory for the wall-normal shape of the eigenfunctions and the downstream disturbance growth. In the experiment, the disturbance development up to $x^* = 0.06m$ is assumed to be linear. Therefore, the receptivity study from section 5.3.1 can be employed to match the development of the mass-flux disturbance $(\rho u)'$ from the DNS and the experiment throughout the entire linear regime. The temporal evolution of the mass-flux disturbance $(\rho u)'$ at $y^*/\delta^* = 0.53$ and $x^* = 0.06m$ in figure 5.11 illustrates this agreement between the experiment and the DNS.

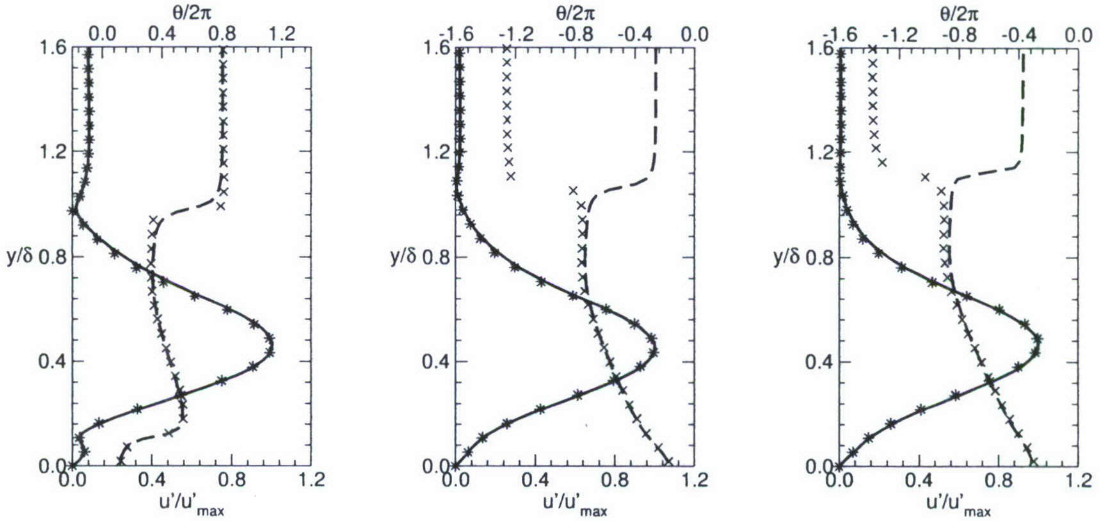

(a) u', $\beta^* = 0.5mm^{-1}$ (b) u', $\beta^* = 1.0mm^{-1}$ (c) u', $\beta^* = 1.5mm^{-1}$

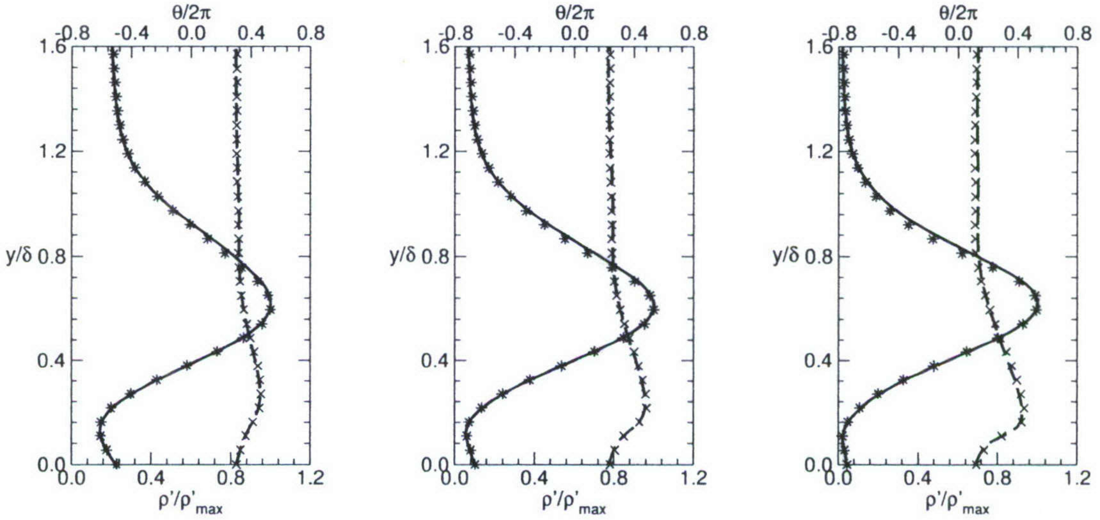

(d) ρ', $\beta^* = 0.5mm^{-1}$ (e) ρ', $\beta^* = 1.0mm^{-1}$ (f) ρ', $\beta^* = 1.5mm^{-1}$

Figure 5.9: Wall-normal amplitude and phase distribution of streamwise velocity disturbance and density disturbance for three different spanwise wave numbers for the fundamental frequency $20kHz$ at $x^* = 0.06m$. *Symbols* represent results obtained from LST (($\star$): amplitude, ($\times$): phase) and *lines* represent DNS results ((–): amplitude, (- -): phase).

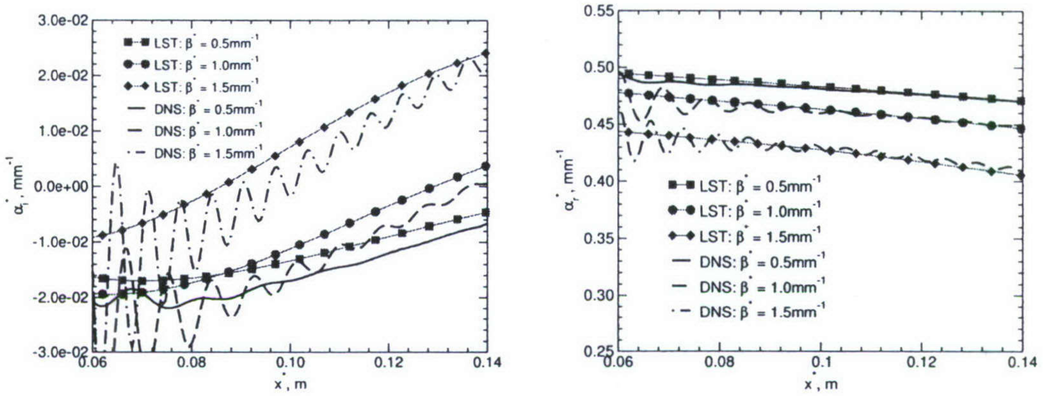

(a) streamwise amplification rate α_i (b) streamwise wave number α_r

Figure 5.10: Downstream development of complex streamwise wave number predicted by LST and by DNS (obtained from wall-pressure disturbance) for three different spanwise wave numbers and the fundamental frequency $20kHz$.

5.3.3 Nonlinear Behavior

Before trying to identify the oblique breakdown mechanism in the simulations, a short summary of the most important characteristics of oblique breakdown is presented. In many previous numerical investigations (Thumm *et al.* 1990, Adams & Sandham 1993, Fezer & Kloker 1999), the authors concluded that oblique breakdown is a very dominant mechanism. For the computational setup of these simulations, oblique breakdown produced the highest growth rates for the nonlinearly generated modes. In all these previous simulations, oblique breakdown was triggered by forcing two oblique instability waves with equal but opposite wave angle. The wave angle of this wave pair was determined by forcing discretely at the most unstable spanwise wave number according to linear theory. This chosen spanwise wave number also defined the domain size in spanwise direction $z_W = 2\pi/\beta$ (Thumm *et al.* 1990, Adams & Sandham 1993, Fezer & Kloker 1999, Husmeier *et al.* 2005). All waves with smaller spanwise wave numbers were therefore excluded from the simulations.

One of the most important features of oblique breakdown, observed in these earlier

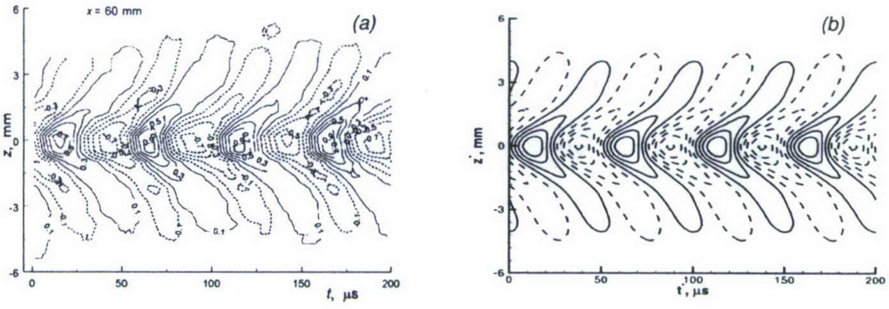

Figure 5.11: Temporal evolution of the mass-flux disturbance $(\rho u)'$ for the fundamental frequency ($20kHz$) at the wall-normal position $y^*/\delta^* = 0.53$ and the streamwise position $x^* = 0.06m$ for the experiment (a) (Kosinov, 2006) and the DNS (b) (CFUND 2): (–) positive disturbance amplitude, (...) negative disturbance amplitude.

investigations, is the generation of steady longitudinal modes, which grow strongly in the streamwise direction. As oblique breakdown sets in, the steady modes (denoted by $[0, \pm 2]$) start to play a dominant role, since they are directly generated by the forced wave pair $[1, \pm 1]$. The notation $[h, k]$ is used to identify a particular wave according to its frequency h and its spanwise wave number k. h denotes multiples of the fundamental frequency and k multiples of the smallest spanwise wave number. The $[0, \pm 2]$ modes are responsible for the generation of various other modes, as for example the wave pair $[1, \pm 3]$ or the steady longitudinal modes $[0, \pm 4]$. A detailed description of the nonlinear wave interactions in the early nonlinear stages of oblique breakdown can be found in Thumm (1991). Thumm *et al.* (1990) and Fasel *et al.* (1993) also stated a particular characteristic of the nonlinear wave interactions in oblique breakdown: Modes with odd spanwise wave numbers k are only generated for odd harmonic frequencies h, and modes with even spanwise wave numbers are generated only for even frequencies h.

Having discussed the main characteristics of oblique breakdown enables one to analyze the following numerical results and to identify this mechanism in the experiments. Four DNS of the early nonlinear stages of transition have been performed and are partially compared to the experimental findings in the succeeding paragraphs. The flow is perturbed by the method outlined in section 5.3.1 with the single frequency of $20kHz$. The four simulations differ in the absolute value of the forcing amplitude (v-velocity over disturbance slot). For the first simulation (CFUND 2), the forcing amplitude is small enough for the developing disturbances to be in the linear regime throughout the entire computational domain. The second simulation (CFUND 3) has a forcing amplitude for which the absolute spanwise amplitude of the mass-flux disturbance (ρu)' at the streamwise location $x^* = 0.06m$ in the experiment is matched exactly (figure 5.5). For the last simulation (CFUND 4), the forcing amplitude is again increased and differs from CFUND 3 by a factor of ~ 1.36. Note that even for this forcing amplitude, the disturbance behavior is still linear at $x^* = 0.06m$. In first three simulations, the computational domain ranges in downstream direction from $x_0^* = 0.02m$ to $x_L^* \simeq 0.17m$ so that the numerical results can be compared to the reported experimental data at locations $x^* = 0.11m$, $x^* = 0.12m$, and $x^* = 0.13m$. The final simulation (CFUND 5) has the highest forcing amplitude. For this simulation, also the number of spanwise Fourier modes and the streamwise extend ($x_L^* \simeq 0.18m$) of the computational domain are increased. Therefore, this simulation covers a wider range of the transition process than the other simulations.

The streamwise development of the disturbance generated by the localized forcing at $x^* = 0.038m$ is illustrated in spectral space by figure 5.12 for CFUND 2 and CFUND 4. CFUND 3 exhibits a similar behavior as CFUND 4 and is therefore not presented in figure 5.12. In figures 5.12a,c, the Fourier amplitudes for the mass-flux disturbance (ρu)' at the wall-normal location $y^*/\delta^* = 0.53$ are plotted versus the streamwise direction x and the spanwise wave number β. Only one half of the spanwise domain extent is shown since all simulations are symmetric to $\beta^* = 0.0mm^{-1}$. Initially both, the small-amplitude disturbances (figure 5.12a) and the large-amplitude disturbances (figure 5.12c), experience exponential amplitude growth resulting in a maximum near $\beta^* = 0.8mm^{-1}$. For the large-amplitude disturbances in figure 5.12c,

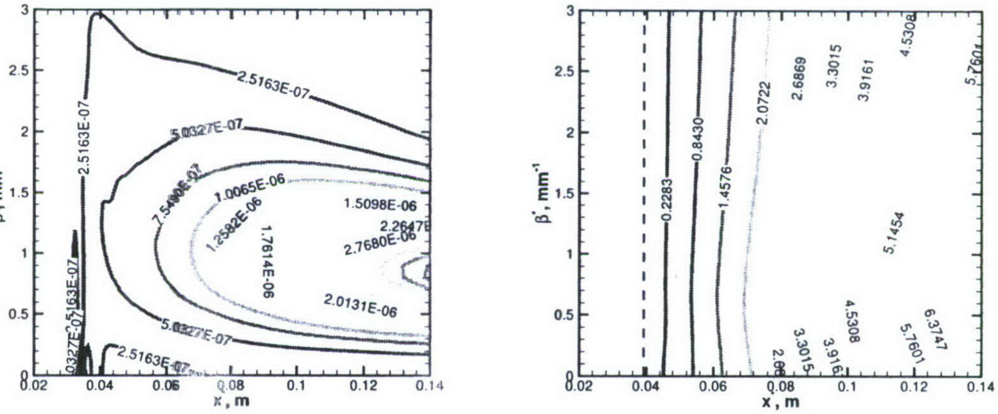

(a) amplitude distribution (b) phase distribution

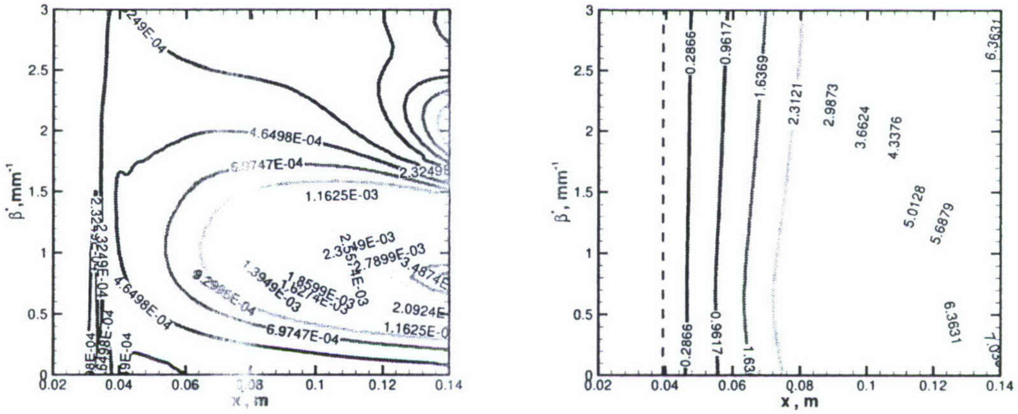

(c) amplitude distribution (d) phase distribution

Figure 5.12: Contour levels of the Fourier amplitude (a, c) and the phase (b, d) for the mass-flux disturbance $(\rho u)'$ with frequency $20kHz$ at wall-normal location $y^*/\delta^* = 0.53$ for different streamwise and spanwise locations: (a, b) DNS with low forcing amplitude (CFUND 2), (c, d) DNS with high forcing amplitude (CFUND 4).

however, a second maximum forms near $\beta^* = 2mm^{-1}$ downstream of $x^* = 0.1m$ as a result of nonlinear wave interactions. These nonlinear wave interactions are also visible in the phase development for the mass-flux disturbance (ρu)' at the same wall-normal position (figure 5.12d). In figure 5.12c,d, the near-field of the disturbance slot is excluded and the start position for the post-processing is indicated by the horizontal dashed line.

At $x^* = 0.11m$, $x^* = 0.12m$, and $x^* = 0.13m$ downstream of the leading edge of the flat plate, experimental data are compared to the numerical results in figure 5.13. In this figure, the amplitude and phase distribution of the mass-flux disturbance $(\rho u)'$ are plotted for the first three DNS over a wider range of spanwise wave numbers. Noted as primary peaks and secondary peaks, the same maxima as in figure 5.12 also appear in figure 5.13 for both DNS with a large forcing amplitude (CFUND 3 and CFUND 4). The absolute values of the mass-flux disturbance of the DNS in this figure are rescaled by a single, constant factor A_{ref} (CFUND 3: $\simeq 3.008 \cdot 10^{-4}$, CFUND 4: $\simeq 4.794 \cdot 10^{-4}$) to match the experimental data. The experimental results are again provided by Kosinov (2006) and are transformed into spectral space using a full (asymmetric) Fourier series expansion (Ermolaev *et al.* 1996). The streamwise development of the primary maxima in CFUND 4 matches the behavior observed in the experiment perfectly. This is not the case for the streamwise development of the nonlinearly generated secondary maxima. In CFUND 3, these maxima are not as pronounced as in CFUND 4, although the absolute disturbance amplitudes from CFUND 3 at position $x^* = 0.06m$ match the estimated values from the experiments (figure 5.5). To achieve a comparable nonlinear behavior as in the experiments, the forcing amplitude of CFUND 3 had to be increased (factor 1.36) to the forcing amplitude of CFUND 4.

The temporal evolution of the disturbances at the streamwise location $x^* = 0.13m$ from the experiment and the DNS (CFUND 4) is illustrated in figure 5.14. In the experiments, the subharmonic frequency is strongly visible. Structures close to the

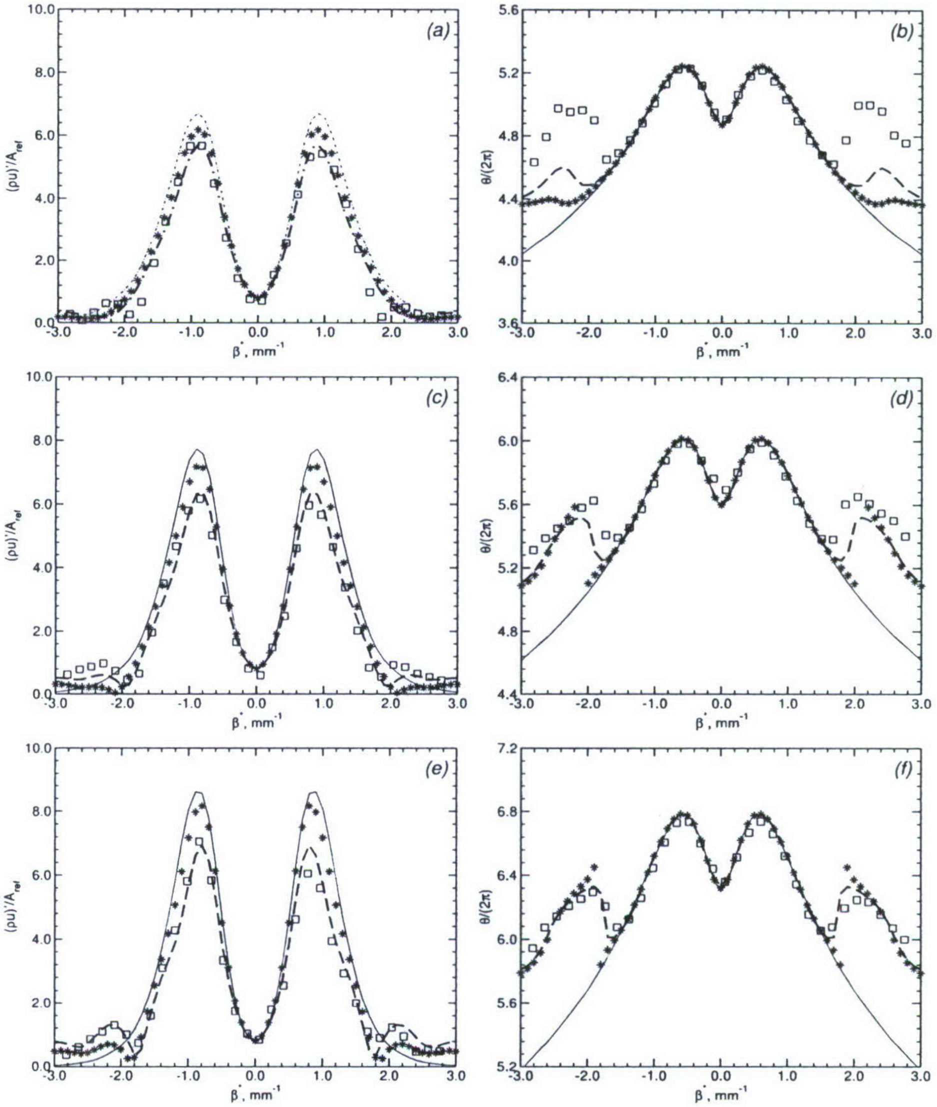

Figure 5.13: Spanwise amplitude (*a*, *c*, *e*) and phase (*b*, *d*, *f*) distribution of the mass-flux disturbance $(\rho u)'$ ($20kHz$) at wall-normal location $y^*/\delta^* = 0.53$ for the streamwise positions $x^* = 0.11m$ (*a*, *b*), $x^* = 0.12m$ (*c*, *d*) and $x^* = 0.13m$ (*e*, *f*): (–) low forcing amplitude (CFUND 2), (*) medium forcing amplitude (CFUND 3), (- -) largest forcing amplitude (CFUND 4), (□) experiment (Kosinov, 2006).

centerline ($z^* = 0.0m$) repeat every second period of the fundamental frequency. For the DNS, the temporal evolution of the structures close to the centerline exhibits one great difference to the experiment: Not surprisingly, the influence of the subharmonic frequency does not appear since this frequency is not disturbed. Instead, steady modes modulate the disturbance signal between $z^* = -0.004m$ and $z^* = 0.004m$ shifting the disturbance amplitude to purely positive or negative values.

The overall excellent agreement between the numerical results of the DNS and the experimental data in figure 5.13 indicates that even with the (deliberate) suppression of a subharmonic development (present in the experiment) the simulations capture the development of the fundamental frequency correctly. The results from the DNS therefore suggest that in the experiments another mechanism coexists with the subharmonic resonance triad. The generation of steady modes in figure 5.14 and the development of secondary peaks in figure 5.13 at a spanwise wave number that is a higher harmonic of the spanwise wave number of the primary peaks are an indication for the presence of an oblique breakdown mechanism.

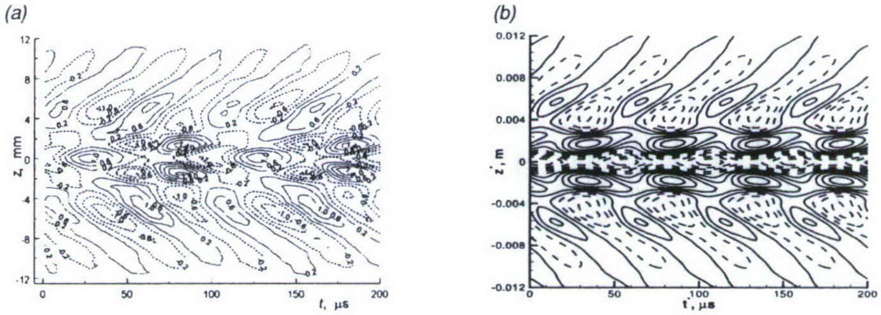

Figure 5.14: Temporal evolution of the mass-flux disturbance $(\rho u)'$ for the fundamental frequency ($20kHz$) at the wall-normal position $y^*/\delta^* = 0.53$ and the streamwise position $x^* = 0.13m$ for the experiment (*a*) (Kosinov, 2006) and the DNS (*b*) (CFUND 4): (–) positive disturbance amplitude, (...) negative disturbance amplitude.

The DNS with the highest forcing amplitude (CFUND 5) reveals stronger nonlinear wave interactions and therefore also a more pronounced secondary maximum.

Shown in figure 5.15 is the nonlinear development of the mass-flux disturbance (ρu)' at $y^*/\delta^* = 0.53$ in response to the high forcing. Clearly, many additional maxima at equally spaced spanwise wave numbers are visible for the fundamental frequency in figure 5.15b. The steady part in figure 5.15a exhibits also several maxima equally spaced in spanwise direction. The dashed lines indicate the spanwise wave number of the maxima for the steady modes near the outflow. These dashed lines are also plotted in figure 5.15b to illustrate that the maxima of the steady modes are located in between the maxima for the fundamental frequency. Oblique breakdown predicts exactly this behavior. The first maximum in figure 5.15b represents mode $[1,1]$, the additional maxima at higher spanwise wave numbers represent mode $[1,3]$, $[1,5]$ etc. Similarly, the maximum at $\beta \simeq 1.4mm^{-1}$ in figure 5.15a corresponds to mode $[0,2]$ and the additional maxima to the modes $[0,4]$, $[0,6]$ etc.

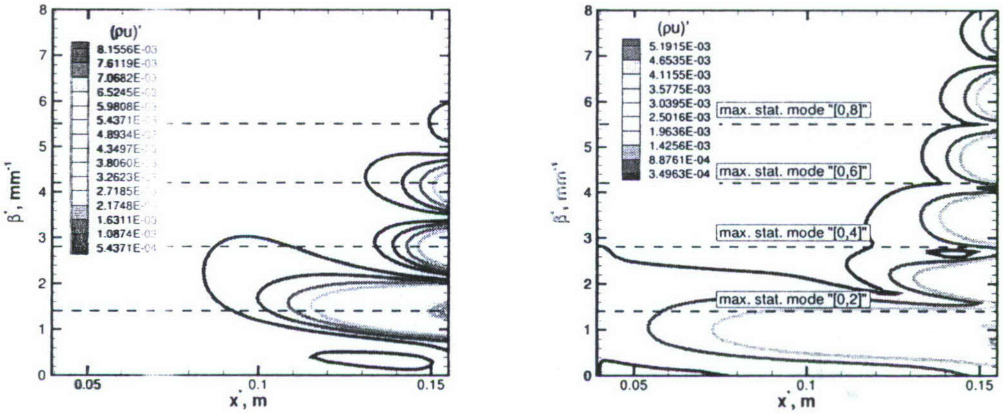

(a) steady modes (CFUND 5)

(b) fundamental frequency (CFUND 5)

Figure 5.15: Contour levels of the Fourier amplitude for the mass flux disturbance (ρu)' at wall-normal location $y^*/\delta^* = 0.53$ for different streamwise and spanwise locations of the DNS.

5.4 Asymmetric Subharmonic Resonance

After identifying oblique breakdown in the experiments by Ermolaev *et al.* (1996), asymmetric subharmonic resonance was studied to clarify its role in supersonic boundary-layer transition when compared to oblique breakdown. Towards this end, both disturbance frequencies ($20kHz$ and $10kHz$) were considered and therefore, the "entire" experiment was simulated. Before any DNS results are discussed, the linear behavior of instability waves with both frequencies obtained using linear stability theory (LST) are presented to determine the spanwise wave numbers of highly unstable waves at both frequencies. For these waves, possible resonance triads according to LST are determined. Furthermore, DNS results for the linear regime are compared to results obtained from LST in order to identify the influence of nonparallel effects resulting from the boundary layer growth on these triads. Following the study of the linear disturbance behavior, the early nonlinear stages of transition caused by a subharmonic route are discussed with the main focus on the selection process for a particular subharmonic resonance triad.

5.4.1 Linear Stability Considerations

For the linear stability analysis, the dimensional fundamental and subharmonic frequencies f^* are scaled using the streamwise velocity u^*_∞ and the kinematic viscosity ν^*_∞ at the free-stream in order to obtain their corresponding reduced frequencies

$$F = \frac{2\pi f^* \nu^*_\infty}{{u^*_\infty}^2} \tag{5.4}$$

listed in Table 5.1. The reduced frequency is required as input for the linear stability

Table 5.1: Reduced frequencies used for the linear stability analysis.

f^* (kHz)	F [-]
10	$1.9 \cdot 10^{-5}$
20	$3.8 \cdot 10^{-5}$

solver of Mack (1965). For a given frequency, Reynolds number and spanwise wave number, this tool solves the eigenvalue problem posed by spatial LST and returns the complex wave number

$$\alpha = \alpha_r + i\,\alpha_i, \tag{5.5}$$

as its solution. Here, α_r is the streamwise wave number and α_i is the streamwise amplification rate. Negative values of α_i indicate amplification and positive values damping of the eigensolution.

According to LST, waves observed in the experiments with the fundamental frequency of $20kHz$ and in the spanwise wave number range of $\beta^* = 0.5mm^{-1}$ to $\beta^* = 1.0mm^{-1}$ are in the vicinity of the maximum amplification rate α_i, at both locations $x = 0.06m$ and $0.13m$ as shown in figures 5.16a,b. For the subharmonic frequency $10kHz$, figures 5.16a,b indicate that the range of maximum amplification rate is slightly shifted to lower spanwise wave numbers at $x^* = 0.13m$. A better criterion for identification of instability waves reaching the highest amplitudes within the domain of interest is the normalized amplitude N. It is obtained by integration of α_i between two streamwise locations or, equivalently, by taking the logarithm of the ratio of the disturbance amplitudes at these two locations:

$$N = \int_{x_{ref}}^{x} -\alpha_i(\hat{x})\,d\hat{x} = ln(\frac{A(x)}{A(x_{ref})}), \tag{5.6}$$

where x_{ref} is the start location for the integration, i.e., the reference location for the amplitude ratio. At location $x^* = 0.13$ in Figure 5.16b the normalized amplitudes (N) are shown for both frequencies (symbols) at different spanwise wave numbers. They were obtained by integrating the amplification rates α_i predicted by LST with x_{ref} being equal to the location where the disturbances were introduced in the experiments by Kosinov *et al.* (1994) ($x^*_{ref} = 0.038m$). For the fundamental frequency, waves with a spanwise wave number β between $0.7mm^{-1}$ and $0.8mm^{-1}$ reach the highest normalized amplitudes, whereas for the subharmonic frequency, waves with a spanwise wave number $\beta^* = 0.6mm^{-1}$ have the highest normalized amplitude.

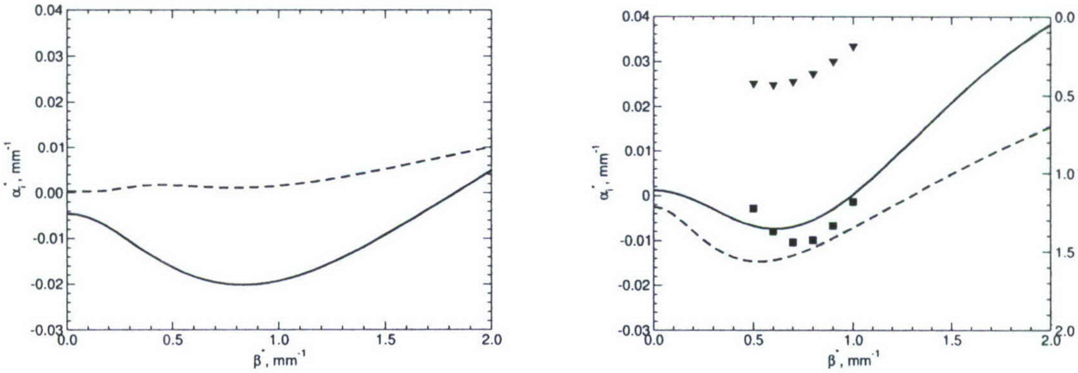

(a) α_i^*, $x^* = 0.06m$

(b) α_i^*, $x^* = 0.13m$

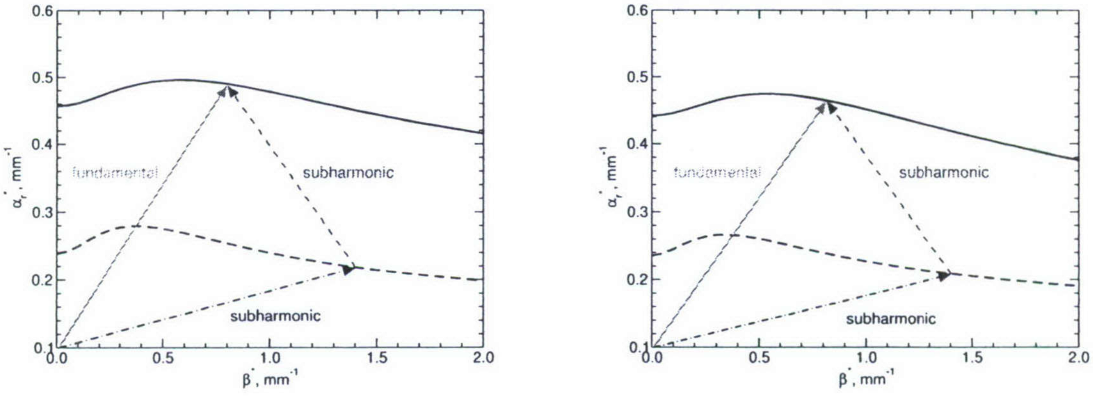

(c) α_r^*, $x^* = 0.06m$

(d) α_r^*, $x^* = 0.13m$

Figure 5.16: *LINES*: Spanwise distribution of amplification rate α_i and streamwise wave number α_r at the positions $x^* = 0.06m$ and $x^* = 0.13m$. (—) $20kHz$, (– –) $10kHz$. *SYMBOLS*: Spanwise distribution of normalized amplitude N ($x_{ref} = 0.038$). (■) $20kHz$, (▼) $10kHz$.

Before the different three-wave resonance triads are determined using LST, a short introduction to the resonance conditions is given below. Generally, the resonance condition for a three-wave triad is a phase synchronization of all three instability waves (Kachanov & Levchenko, 1984):

$$\theta^1 = \theta^2 + \theta^3 , \quad \theta^n(x, z, t) = \alpha_r^n x + \beta^n z - \omega^n t. \tag{5.7}$$

Here, θ symbolizes the phase, ω the angular frequency, α_r and β the streamwise and spanwise wave number, respectively. By comparing the coefficients in front of the independent variables x, z, t the following three conditions can be derived:

$$\omega^1 = \omega^2 + \omega^3 , \quad \alpha_r^1 = \alpha_r^2 + \alpha_r^3 , \quad \beta^1 = \beta^2 + \beta^3. \tag{5.8}$$

For the special case of a symmetric, subharmonic resonance triad with one primary 2D wave (ω^1, β^1) and two symmetric, subharmonic oblique waves ($\omega^{\frac{1}{2}}, \beta^{\frac{1}{2}}$), equation (5.8) reduces to the well-known conditions for incompressible boundary layers (Kachanov & Levchenko, 1984)

$$\omega^1 = 2\omega^{\frac{1}{2}} , \quad \alpha_r^1 = 2\alpha_r^{\frac{1}{2}} , \quad \beta^2 = -\beta^3. \tag{5.9}$$

Equation (5.9) can be further utilized to derive an expression for the phase velocity c_x^1 of the 2D instability wave

$$c_x^1 = v_x^{\frac{1}{2}} , \quad c_x^1 = \frac{\omega^1}{\alpha_r^1} , \quad v_x^{\frac{1}{2}} = \frac{\omega^{\frac{1}{2}}}{\alpha_r^{\frac{1}{2}}}, \tag{5.10}$$

where $v_x^{\frac{1}{2}}$ is the velocity of the two oblique waves "with which it is necessary to move along the x-axis in order that the subharmonic phase should not depend on the time" (Kachanov & Levchenko, 1984). It is important to note that $v_x^{\frac{1}{2}}$ is not the phase speed of the oblique waves since their phase speed is defined as

$$c_x^{\frac{1}{2}} = \frac{\omega^{\frac{1}{2}} \alpha_r^{\frac{1}{2}}}{(\alpha_r^{\frac{1}{2}})^2 + (\beta^{\frac{1}{2}})^2}. \tag{5.11}$$

Since symmetric, subharmonic resonance triads do not play an important role in the transition process of a Mach 2 boundary layer, the resonance conditions for Kosinov's asymmetric, subharmonic resonance triad are more complicated. For this case, equation (5.8) simplifies to

$$\omega^1 = 2\omega^{2,3}, \quad \alpha_r^1 = \alpha_r^2 + \alpha_r^3, \quad \beta^1 = \beta^2 + \beta^3. \tag{5.12}$$

Equation (5.12) is illustrated as an addition of three wave vectors in figures 5.16c,d for $x^* = 0.06m$ and $x^* = 0.13m$ forming a triad that was also observed by Kosinov *et al.* (1994) in his early experiment in 1994. The primary wave of this triad has the fundamental frequency of $20kHz$ and a spanwise wave number of $\beta^* = 0.8mm^{-1}$. The two subharmonic waves that close the triad have a spanwise wave number of $\beta^* = -0.6mm^{-1}$ and $\beta^* = 1.4mm^{-1}$.

In the following, the procedure used to locate a resonance triad using LST results is explained (Zengl, 2005). Figure 5.17a shows the spanwise distribution of the streamwise wave number α_r for both frequencies at $x^* = 0.06m$ (for reference see figure 5.16c). In order to satisfy the resonance condition for the spanwise wave number in equation (5.12) both subharmonic waves of the triad need to have a difference in their spanwise wave number that has the value of the spanwise wave number of the primary, fundamental wave

$$\beta^2 + \beta^3 = \Delta\beta = \beta^1. \tag{5.13}$$

Therefore, the spanwise distribution of α_r for the subharmonic frequency in figure 5.17a is shifted by $\Delta\beta$ as defined in equation (5.13) (blue dashed line in figure 5.17a). In this example, $\Delta\beta^*$ is equal to $0.5mm^{-1}$, which implies that we are looking for a triad with $\beta^* = 0.5mm^{-1}$ as the spanwise wave number for the primary wave. To satisfy the resonance condition for the streamwise wave number in equation (5.12) both graphs of the streamwise wave number for the subharmonic frequency in figure 5.17a are added (red dashed line). The resulting graph exhibits the value of the streamwise wave number of the fundamental primary wave with $\beta^* = 0.5mm^{-1}$

at only one single point indicated by a black dot. The spanwise wave number at this position is about $\beta^* = 1.16mm^{-1}$. The black dot in figure 5.17a suggests the existence of a resonance triad, which is composed of one primary wave with fundamental frequency of $20kHz$ and spanwise wave number of $\beta^* = 0.5mm^{-1}$ and two subharmonic waves with $\beta^* = -0.66mm^{-1}$ and $\beta^* = 1.16mm^{-1}$. The same triad can be found at $x^* = 0.13mm^{-1}$ (figure 5.17b). Note that this triad was not reported by Kosinov and his co-workers.

In figure 5.17c,d the black dot with the largest spanwise wave number ($\beta^* = 1.4mm^{-1}$) represents the asymmetric subharmonic resonance triad discovered by Kosinov *et al.* (1994). Furthermore, figure 5.17c exhibits two other dots, which are related to one new triad (spanwise wave number of the primary wave: $\beta^* = 0.8mm^{-1}$ and of the two subharmonic waves: $\beta^* \simeq 0.0mm^{-1}$ and $\beta^* \simeq 0.8mm^{-1}$). Note that for this case, the resonance conditions are not exactly fullfilled at $x^* = 0.06m$. This triad cannot be identified farther downstream at $x^* = 0.13m$. It, however, might still play an important role since it could explain the development of a peak near $\beta^* = 0.0mm^{-1}$ in the subharmonic disturbance signal of the mass flux from the experiments (Kosinov *et al.*, 1994). More details on this topic can be found in section 5.4.2.2.

Using this method, various asymmetric, subharmonic resonance triads can be determined for a Mach 2 boundary layer. The spanwise wave number of both subharmonic waves is fixed by the value of the spanwise wave number for the primary wave with the fundamental frequency. This dependency is illustrated in figure 5.18 for $x^* = 0.06m$ and $x^* = 0.13m$. It is clearly visible that at least one resonance triad exists for every spanwise wave number of the primary wave between $\beta^* = 0.5mm^{-1}$ and $\beta^* = 1.0mm^{-1}$. For one group of triads, the subharmonic wave that initially experiences mainly linear growth (blue symbols) has a spanwise wave number close to the one connected to the maximum amplitude growth as shown in figure 5.16b ($\beta^* \simeq 0.6mm^{-1}$). These triads are denoted as triads of the first group. Triads with one subharmonic wave close to $\beta^* \simeq 0.0mm^{-1}$ are called triads of the second group

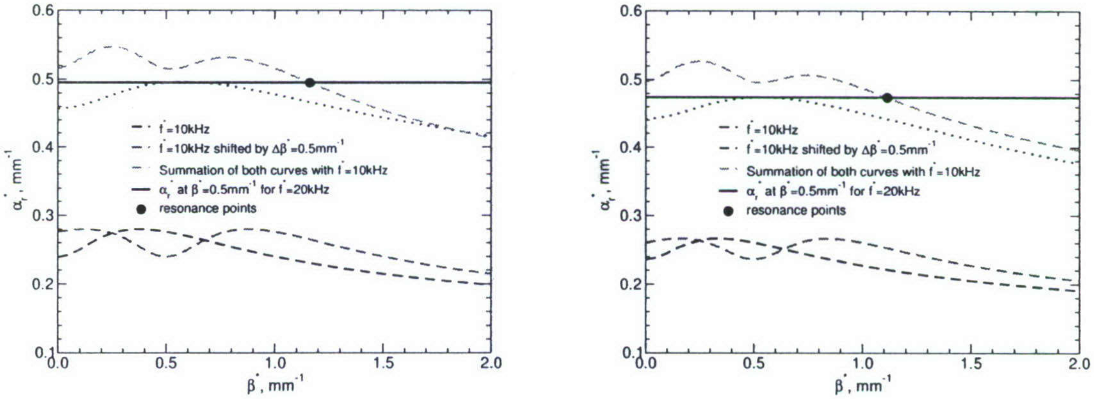

(a) $\Delta\beta = 0.5mm^{-1}$, $x^* = 0.06m$ (b) $\Delta\beta = 0.5mm^{-1}$, $x^* = 0.13m$

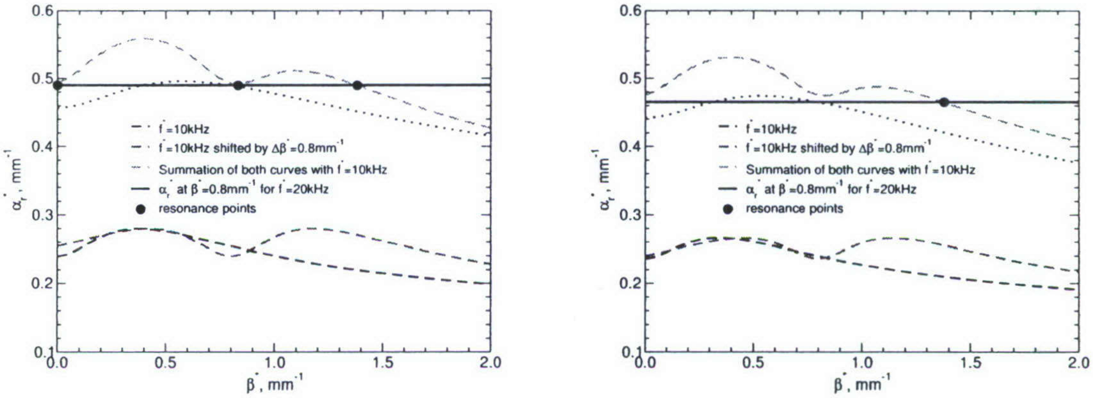

(c) $\Delta\beta = 0.8mm^{-1}$, $x^* = 0.06m$ (d) $\Delta\beta = 0.8mm^{-1}$, $x^* = 0.13m$

Figure 5.17: Illustration of the procedure used to determine a particular asymmetric, subharmonic resonance triad using LST results.

throughout this document.

For the resonance triads discussed so far, the resonance conditions formulated in equation (5.12) have only been verified at two different streamwise locations ($x^* = 0.06m$ and $x^* = 0.13m$). Two triads from the first group have been chosen for figure 5.19 to confirm whether these conditions are also satisfied for other streamwise locations. In figure 5.19, the downstream development of the streamwise wave number α_r^* for all three waves participating in both triads are plotted (lines). The symbols represent the sum of the streamwise wave number from both subharmonic waves. The values of this sum are very close to the spanwise wave number of the primary wave as required by equation (5.12) for all streamwise positions.

To this end, it can be summarized that LST predicts various asymmetric, subharmonic resonance triads for the physical flow conditions of Kosinov's experiments. Most likely, there is a mechanism that is responsible for the selection process of a specific triad since Kosinov reported only one triad. Furthermore, Kosinov might also have observed the second group of triads indicated in figure 5.18 since these triads could explain the development of a peak near $\beta^* = 0.0mm^{-1}$ in the subharmonic disturbance signal of the mass flux from the experiments (Kosinov *et al.*, 1994).

5.4.2 DNS Results

The linear behavior of disturbances for both frequencies is discussed in the next section. These results are obtained from DNS with very small forcing amplitudes and can be used as a reference to identify a deviation from the linear behavior in simulations with larger forcing amplitudes. Following the study of the linear disturbance behavior, DNS results of the "entire" experiment, including the asymmetric subharmonic resonance, are discussed.

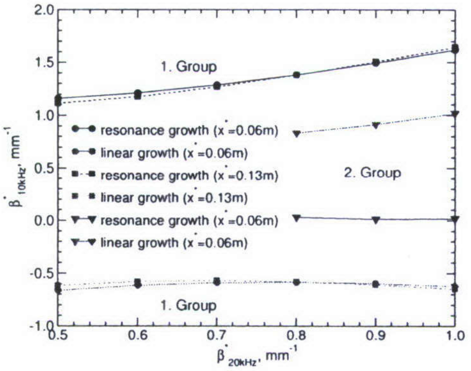

Figure 5.18: Dependency of the spanwise wave number of both subharmonic waves (β^*_{10kHz}) included in the triad on the spanwise wave number of the primary wave (β^*_{20kHz}).

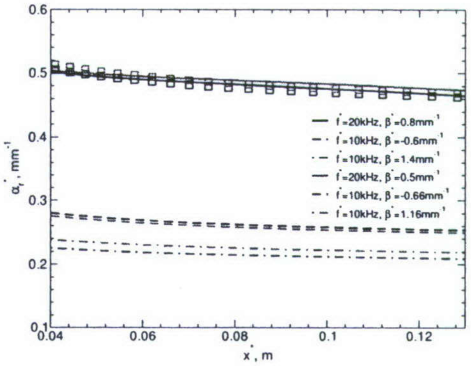

Figure 5.19: Downstream development of the streamwise wave number α^*_r for all three wave components of two asymmetric, subharmonic resonance triads from the first group.

5.4.2.1 Linear Behavior

Two DNS with a very small forcing amplitude have been conducted in order to investigate the linear disturbance development. In one DNS, only the fundamental frequency is forced as already explained in section 5.3.1 (CFUND 1) and in the other DNS, only the subharmonic frequency is perturbed. Note, for the subharmonic frequency (10 kHz), the calibration procedure in section 5.3.1 cannot be applied since it is based on the assumption of initially linear disturbance development. Through the resonance interaction of disturbances with both frequencies, an initially linear disturbance development for subharmonic disturbances cannot be guarantied in our simulations with high (fundamental) forcing amplitudes. Therefore, disturbances with subharmonic frequency were excited by forcing each spanwise Fourier mode with the same amplitude $\tilde{A}(\beta) = A$ and phase $\theta_p(\beta) = \theta$ resulting in a finite approximation of the delta function. Results from both simulations are shown in figure 5.20. The streamwise and spanwise amplitude and phase distributions of the mass-flux disturbance $(\rho u)'$ at wall-normal location $y^*/\delta^* = 0.53$ is illustrated in figure 5.20a,b for the fundamental frequency and in figure 5.20c,d for the subharmonic frequency. (Note, this wall-normal position ($y^*/\delta^* = 0.53$) is chosen since in the experiments, data were measured at the same position.) Both cases show similar trends. The maximum in the amplitude distribution in both figures is caused by the exponential growth according to linear theory. For the fundamental frequency, the maximum is located near $\beta^* = 0.8mm^{-1}$ (close to the outflow) and for the subharmonic frequency, the maximum is near $\beta^* = 0.6mm^{-1}$ as predicted by LST in figure 5.16b. Two-dimensional disturbances and disturbances with a small wave angle do not experience any streamwise growth for the subharmonic frequency and only a very weak growth for the fundamental frequency (figure 5.21).

Figure 5.21 illustrates an important aspect for the setup of the asymmetric subharmonic resonance in the experiments. As for the "classical" symmetric subharmonic resonance for incompressible flow, where the primary wave of the resonance triad is a highly amplified two-dimensional wave, the oblique, primary waves of the asymmetric, subharmonic resonance triads found in figure 5.18 also experience a high streamwise amplitude growth.

In order to study the influence of nonparallel effects resulting from boundary layer growth on the resonance triads, the complex streamwise wave number obtained from LST has to be compared to the corresponding result from the DNS. For the fundamental frequency $20kHz$, this result has already been shown in figure 5.10. As mentioned in section 5.3.2, the amplification of disturbances in the DNS is somewhat stronger than predicted by LST (figure 5.10a). This fact is attributed to nonparallel effects. Note that the streamwise amplification rate α_i obtained from the DNS is dependent on the "criterion" used for its calculation (here, wall-pressure disturbance) and that nonparallel effects might have a different influence on different criteria. For the streamwise wave number α_r, the agreement between DNS and LST is nearly perfect (figure 5.10b) confirming that this quantity is less sensitive to nonparallel effects (connected to the criterion). A very similar observation can also be made for the subharmonic frequency implying that the resonance triads are only weakly

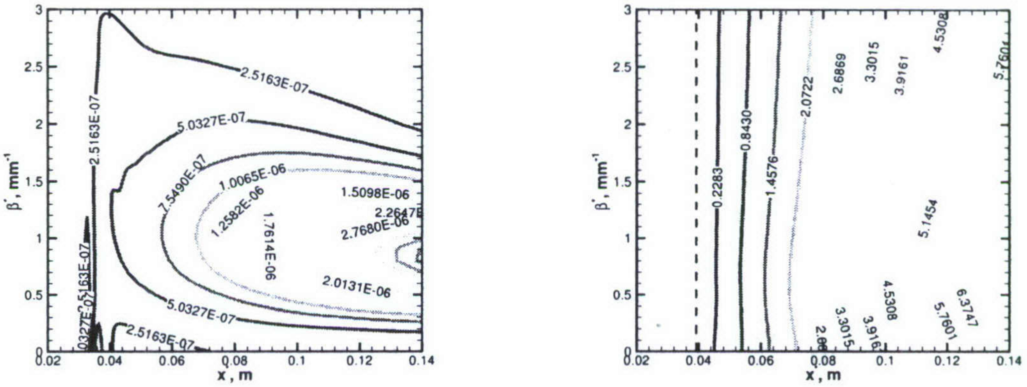

(a) amplitude distribution, $f^* = 20kHz$

(b) phase distribution $(\theta/(2\pi))$, $f^* = 20kHz$

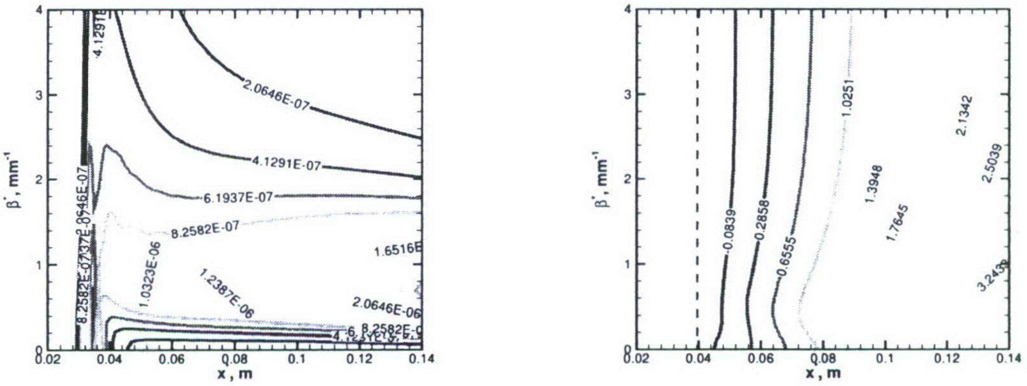

(c) amplitude distribution, $f^* = 10kHz$

(d) phase distribution $(\theta/(2\pi))$, $f^* = 10kHz$

Figure 5.20: Contour levels of Fourier amplitude (a,c) and phase (b,d) for the mass-flux disturbance $(\rho u)'$ at wall-normal location $y^*/\delta^* = 0.53$ for different streamwise and spanwise locations: (a,b) fundamental frequency, (c,d) subharmonic frequency. Note, the phase in figure 5.20b,d is plotted downstream of $x^* \simeq 0.04m$ marked by vertical dashed lines.

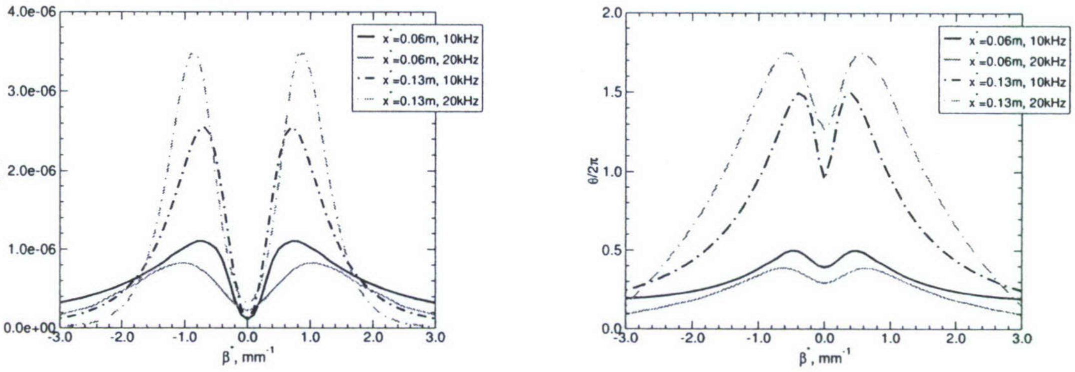

(a) spanwise amplitude distribution

(b) spanwise phase distribution

Figure 5.21: Spanwise amplitude (a) and phase (b) distribution for the mass-flux disturbance (ρu)' at wall-normal location $y^*/\delta^* = 0.53$ for two different streamwise positions.

affected by the growth of the boundary layer. Therefore, it can be assumed that the same resonance triads as identified using LST will also be present in all DNS with high forcing amplitudes.

As a preliminary summary, the results in this section show that Kosinov did setup his experiments similarly to a classical subharmonic resonance triad for incompressible boundary layers. The primary waves in each of the subharmonic resonance triads identified by LST experience strong exponential amplitude growth as the 2D primary wave for the incompressible case. The resonance triads are only weakly affected by the streamwise growth of the boundary layer. Hence, the same resonance triads discovered using LST will also be present in the following simulations with high forcing amplitudes.

5.4.2.2 Simulation of Asymmetric Subharmonic Resonance

In order to investigate the dependency of the asymmetric subharmonic resonance on the relationship between fundamental and subharmonic disturbances, several numerical studies have been performed and are discussed in the following. First, the influence of the amplitude ratio between disturbances of both frequencies and then, the influence of the phase relation is studied. For all simulations presented in this section, the forcing amplitudes for disturbances with the fundamental frequency have been increased in order to see the imprint of the resonance triads in the subharmonic disturbance field. Both, the absolute value of the forcing amplitude and the spanwise forcing profile over the disturbance slot inside the flat plate are identical to CFUND 4. As before, disturbances with subharmonic frequency are excited by forcing each spanwise Fourier mode with the same amplitude $\tilde{A}(\beta) = A$ and phase $\theta_p(\beta) = \theta$. To save computational costs, the DNS for both parametric studies have smaller computational domains in both the streamwise and wall-normal direction than illustrated in figures 5.2a and 5.2b.

Figure 5.22 shows results from one DNS (CSUB 1) that will serve as a reference for all other cases discussed in this section. The amplitude and phase of the forcing for subharmonic disturbances is listed in column one of table 5.2. The flow response to this type of forcing is illustrated in figure 5.22 for the subharmonic frequency. This figure shows contour levels versus streamwise direction and spanwise wave number of the Fourier amplitude and phase of the mass-flux disturbance $(\rho u)'$ at wall-normal location $y^*/\delta^* = 0.53$. It is clearly visible that at higher spanwise wave numbers a second maximum appears near $\beta^* = 1.7mm^{-1}$ close to the outflow (figure 5.22a). The nonlinear wave interactions caused by the resonance triads alter the flow field immediately downstream of the disturbance generation (compare figure 5.22a with 5.20c). Note, this is the reason why the calibration procedure (section 5.3.1) applied for the fundamental frequency cannot be used for the subharmonic frequency. The phase is also significantly changed by nonlinear effects leading to two phase jumps close to $\beta^* = 1.2mm^{-1}$ and $\beta^* = 0.0mm^{-1}$ in figure 5.22. The phase jump at $\beta^* = 0.0mm^{-1}$ supports the previously stated possibility (section 5.4.1) of additional triads from the second group in figure 5.18.

CSUB 2 and CSUB 3 in table 5.2 differ from CSUB 1 in the absolute value of the

Table 5.2: Amplitude study: forcing amplitude and phase (of the v-velocity at the wall) for the subharmonic frequency.

	CSUB 1	CSUB 2	CSUB 3
$\tilde{A}(\beta)$ [-]	$5 \cdot 10^{-6}$	$1 \cdot 10^{-5}$	$3 \cdot 10^{-5}$
$\theta_p(\beta)$ [-]	0.0	0.0	0.0

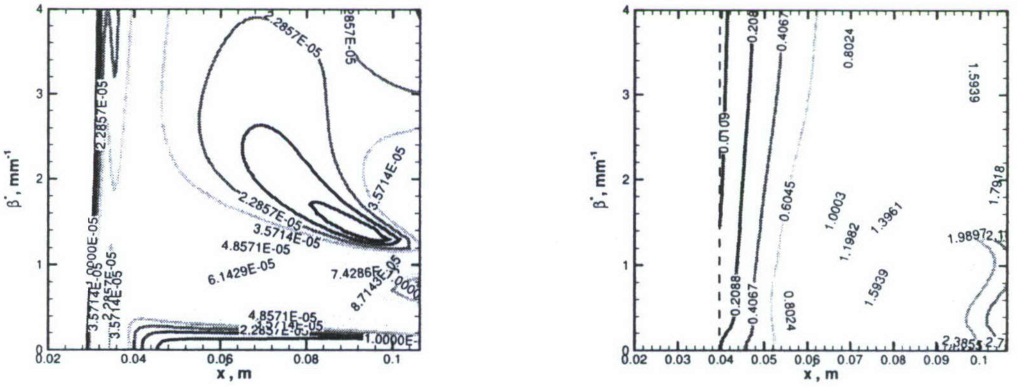

(a) amplitude distribution, CSUB 1

(b) phase distribution ($\theta/(2\pi)$), CSUB 1

Figure 5.22: Contour levels of Fourier amplitude (a) and phase (b) of the mass-flux disturbance (ρu)' for the subharmonic frequency ($10kHz$) at wall-normal location $y^*/\delta^* = 0.53$ for different streamwise and spanwise locations (CSUB 1).

forcing amplitude for the subharmonic frequency. In CSUB 2, the forcing amplitude is two times larger than for CSUB 1. For CSUB 3, the forcing amplitude of the subharmonic frequency is further increased by a factor of three when compared to CSUB 2. A similar disturbance development as for CSUB 1 in figure 5.22 is also found for CSUB 2 and CSUB 3. Figure 5.23 provides a more detailed comparison between all three cases (CSUB 1, 2 and 3). Here, the spanwise amplitude distribution of (ρu)' at $y^*/\delta^* = 0.53$ for several streamwise positions are compared and do not show any noticeable differences between all three cases. This is a clear indication that the nonlinear resonant growth of subharmonic disturbances does not depend on the forcing amplitude for this frequency and that the amplitude ratio for disturbances of both frequencies does not determine a specific resonance triad in the simulations. This is in contrast to the experimental findings (Kosinov *et al.* 1994, Ermolaev *et al.* 1996) where an influence of the forcing amplitude on the nonlinear wave development was reported.

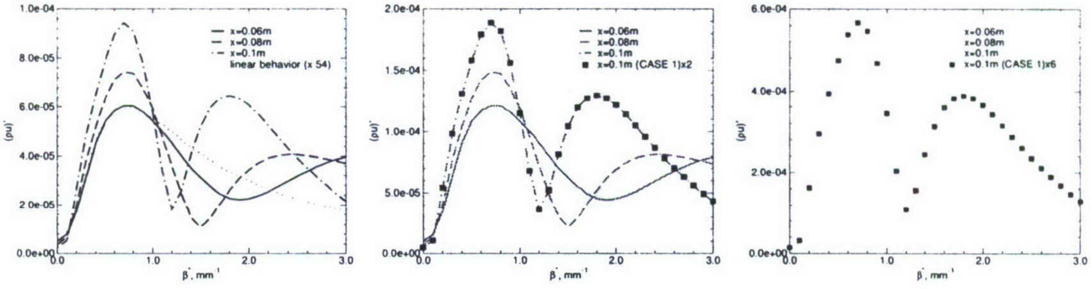

(a) CSUB 1 (b) CSUB 2 (c) CSUB 3

Figure 5.23: Spanwise amplitude distribution for CSUB 1 (a), CSUB 2 (b) and CSUB 3 (c) of the mass-flux disturbance (ρu)' for the subharmonic frequency $(10kHz)$ at wall-normal location $y^*/\delta^* = 0.53$.

In the simulations, however, the asymmetric subharmonic resonance can be strongly influenced by changing the phase relation between fundamental and subharmonic disturbances. The influence of the phase relation on the resonance mechanism of one particular triad was previously studied for incompressible boundary layers by Zelman & Maslennikova (1993) and for a Mach 3 boundary layer by Zengl (2005). In both investigations, it was possible to delay transition by changing the phase to a specific value. Several simulations have been performed in order to investigate the importance of the phase relation on the resonance mechanism. Some of these simulations are listed in table 5.3. For these DNS, the phase of subharmonic disturbances has been altered with respect to the phase of fundamental disturbances in the forcing slot by introducing a phase shift $\theta_p(\beta)$. This phase shift is quantified in table 5.3 as a phase difference $(\Delta\theta_p^{2D}/\pi)$ between 2D fundamental waves and 2D subharmonic waves. Note that only for the subharmonic frequency the phase of the forcing signal is constant over the spanwise wave numbers. The spanwise phase distribution for the fundamental frequency is taken from CFUND 4 in section 5.3.1, therefore, $\Delta\theta_p^{2D}/\pi$ varies with β.

Table 5.3: Phase study: forcing amplitude and phase (of the v-velocity at the wall) for the subharmonic frequency.

	CSUB 4	CSUB 5	CSUB 6	CSUB 7	CSUB 8	CSUB 9
$\tilde{A}(\beta)$ [-]	$5 \cdot 10^{-6}$	$5 \cdot 10^{-6}$	$5 \cdot 10^{-6}$	$5 \cdot 10^{-6}$	$5 \cdot 10^{-6}$	$5 \cdot 10^{-6}$
$\Delta\theta_p^{2D}/\pi$ [-]	-0.15	-0.30	-0.45	-0.60	-0.75	-0.90

For all six cases summarized in table 5.3 the phase difference $\Delta\theta_p^{2D}/\pi$ between 2D fundamental waves and 2D subharmonic waves was changed. Figure 5.24 displays the contour levels of the Fourier amplitude of the mass-flux disturbance (ρu)' for the subharmonic frequency $(10kHz)$ of different streamwise locations and spanwise wave numbers. The first two figures (CSUB 4 and 5) exhibit similar trends as already discussed for CSUB 1 in figure 5.22a. As before, the first maximum at small spanwise wave numbers results from the exponential growth according to linear theory, whereas the second maximum at higher wave numbers develops due to the resonance. For both DNS, this second maximum is, however, shifted towards smaller spanwise wave numbers when compared to CSUB 1. Moreover, it is more pronounced for CSUB 5 (figure 5.24b) than for CSUB 1 and CSUB 4 (figure 5.22a) and close to the outflow, reaches higher amplitude levels than the first maximum. With increasing absolute value of $\Delta\theta_p^{2D}/\pi$, the second maximum moves even closer to the first resulting in a merging of both maxima and in an increase of its absolute amplitude (CSUB 7 and 8 in figures 5.24d,e).

Figure 5.25 provides further details of the simulation results from figure 5.24 and of results from additional simulations. A tool was developed that tracks the spanwise wave number and the amplitude value of both maxima in figure 5.24 and these values are plotted versus $\Delta\theta_p^{2D}/\pi$ in figure 5.25 for three different streamwise positions. The spanwise wave number of the first maximum (figure 5.25a), which is generated

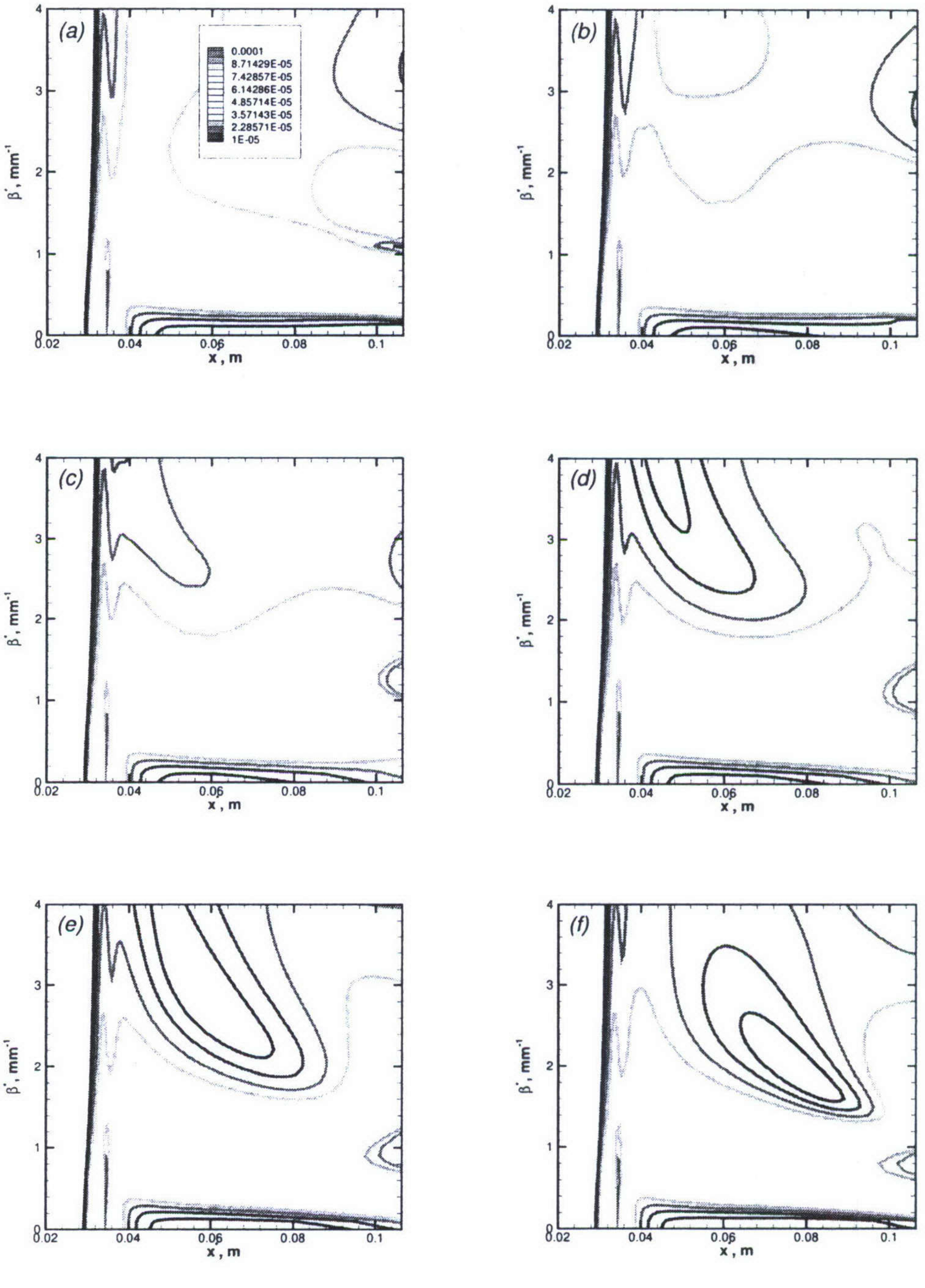

Figure 5.24: Effect of phase difference $\Delta\theta_p^{2D}/\pi$ (phase difference between 2D fundamental waves and 2D subharmonic waves) on the contour levels of Fourier amplitude of the mass-flux disturbance (ρu)' for the subharmonic frequency ($10kHz$) at wall-normal location $y^*/\delta^* = 0.53$ for different streamwise and spanwise locations. (*a*) $\Delta\theta_p^{2D}/\pi \simeq -0.15$ (CSUB 4), (*b*) $\Delta\theta_p^{2D}/\pi \simeq -0.30$ (CSUB 5), (*c*) $\Delta\theta_p^{2D}/\pi \simeq -0.45$ (CSUB 6), (*d*) $\Delta\theta_p^{2D}/\pi \simeq -0.60$ (CSUB 7), (*e*) $\Delta\theta_p^{2D}/\pi \simeq -0.75$ (CSUB 8), (*f*) $\Delta\theta_p^{2D}/\pi \simeq -0.90$ (CSUB 9)

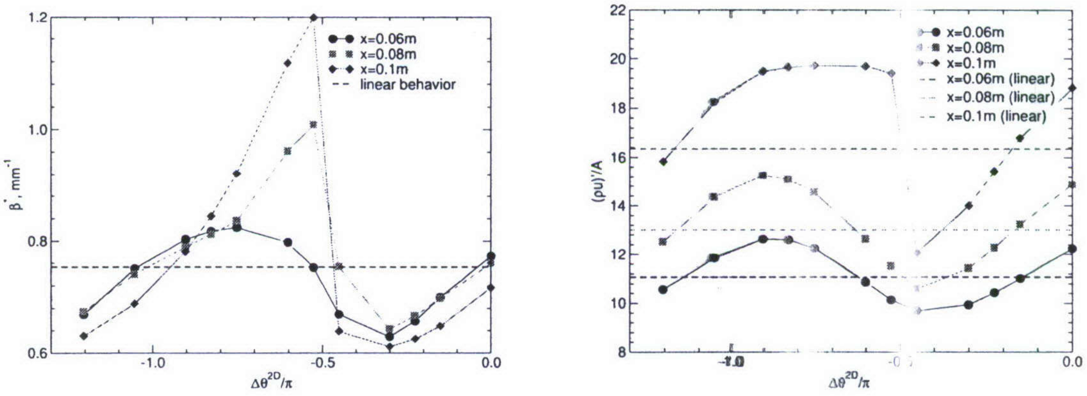

(a) spanwise wave number of first maximum

(b) amplitude value of first maximum

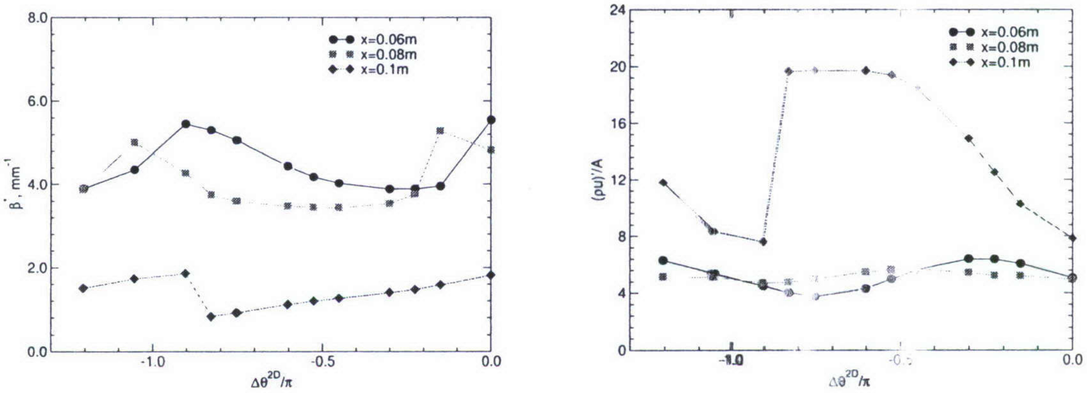

(c) spanwise wave number of second maximum

(d) amplitude value of second maximum

Figure 5.25: Spanwise wave number and amplitude value of first and second maximum in $(\rho u)'$ at $y^*/\delta^* = 0.53$ vs. phase difference $\Delta\theta_p^{2D}/\pi$ between subharmonic and fundamental forcing. For (b) and (d) the amplitudes are normalized by the forcing amplitude $\tilde{A}(\beta) = A$ (see also table 5.3).

according to linear theory, does not match the spanwise wave number from the DNS with small forcing amplitude (figure 5.20c) indicating that nonlinear wave interactions have already altered the subharmonic disturbance field. At positions $x^* = 0.08m$ and $x^* = 0.1m$ and for a phase difference of $\Delta\theta_p^{2D}/\pi \simeq -0.53$, the spanwise wave number experiences a sudden increase in its value to $\beta^* \simeq 1.0mm^{-1}$ and $\beta^* \simeq 1.2mm^{-1}$, respectively. This sudden increase is due to the merging of the amplitude maxima seen in figures 5.24e,d. The plots for the second maximum (figures 5.25c,d) show a general trend that can also be observed in the contour plots in figure 5.22 and figure 5.24 and in the amplitude plots in figure 5.23: The spanwise wave number of a maximum decreases with increasing streamwise position. The graph for $x^* = 0.1m$ in figure 5.25c also confirms that we were able to shift the second maximum within a certain interval of the spanwise wave number ranging from $\beta^* \simeq 1.0mm^{-1}$ to $\beta^* \simeq 1.9mm^{-1}$. A similar range for triads from the first group was also obtained using the results from LST in figure 5.18. Another important finding in figure 5.25 is indicated by the green symbols. All graphs in figure 5.25 have a periodicity of $\Delta\theta_p^{2D} = \pi$. The green symbols result from a simulation with $\Delta\theta_p^{2D}/\pi = -1.60$. These results match exactly the DNS with $\Delta\theta_p^{2D}/\pi = -0.60$.

The study in figure 5.25 can also be employed to determine the optimum $\Delta\theta_p^{2D}$ for which the DNS results exhibit the similar characteristics in the spanwise mass-flux distribution for the subharmonic frequency as obtained from the experiments by Kosinov *et al.* (1994) and from theory by Tumin (1996). Figure 5.26 provides a quantitative comparison of these results (from a DNS with a larger computational domain) for different streamwise positions with $\Delta\theta_p^{2D}/\pi = -0.30$ (CSUB 10 in the appendix). All three results show a small first peak around $\beta^* \simeq \pm 0.6mm^{-1}$ and a strong second peak at $\beta^* \simeq \pm 1.4mm^{-1}$ generated by two resonance triads from the first group with two primary waves at $\beta^* = \pm 0.8$ and four subharmonic waves at $\beta^* = \mp 0.6$ and $\beta^* = \pm 1.4$. Note that figures 5.26a,c also have a very small peak at $\beta^* = 0.0mm^{-1}$ which might be generated by triads of the second group

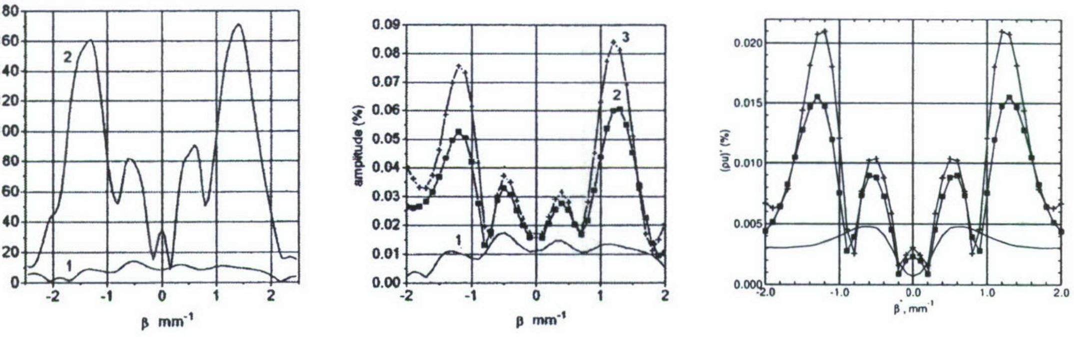

(a) Experiment (Kosinov et al., 1994)

(b) Theory (Tumin, 1996)

(c) DNS ($\Delta\theta_p^{2D}/\pi = -0.30$)

Figure 5.26: Spanwise amplitude distribution of the mass-flux disturbance (ρu)' for the subharmonic frequency ($10kHz$): (a) experiment (Kosinov *et al.*, 1994), (b) theory (Tumin, 1996) and (c) DNS (CSUB 10) with $\Delta\theta_p^{2D}/\pi = -0.30$. Note the amplitudes of of all plots are arbitrarily scaled.

(section 5.4.1). Ermolaev *et al.* (1996), however, attributed these peaks to acoustic disturbances radiating form the supersonic boundary layer.

This section is closed by discussing figure 5.27, which illustrates contour levels of Fourier amplitude and phase of the mass-flux disturbance (ρu)' for both, the fundamental frequency and the subharmonic frequency, with $\Delta\theta_p^{2D}/\pi = -0.30$. The disturbance development for the fundamental frequency is of great interest. Section 5.3.3 suggests that the nonlinear wave interactions for this frequency might be due to the oblique breakdown mechanism involving only the fundamental disturbances with frequency $20kHz$. The results in figure 5.27 are obtained from case CSUB 10. Nevertheless, the disturbance development for the fundamental frequency in figures 5.27a,b matches exactly the earlier findings (see also figure 5.28) confirming the concept of two co-existing transition mechanisms in the experiments by Kosinov *et al.* (1994).

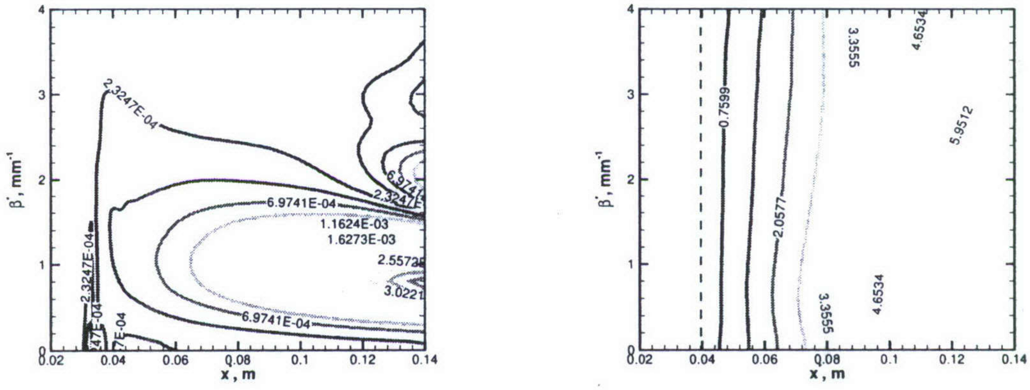

(a) amplitude distribution, $f^* = 20kHz$

(b) phase distribution $(\theta/(2\pi))$, $f^* = 20kHz$

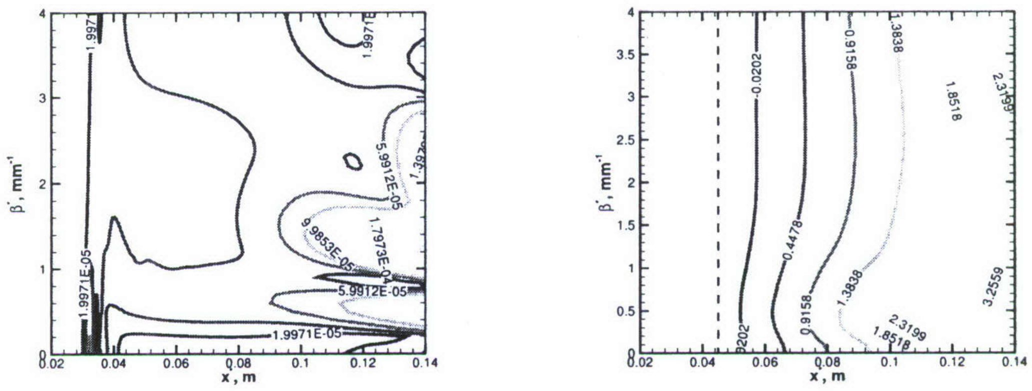

(c) amplitude distribution, $f^* = 10kHz$

(d) phase distribution $(\theta/(2\pi))$, $f^* = 10kHz$

Figure 5.27: Contour levels of Fourier amplitude (a,c) and phase (b,d) of the mass-flux disturbance $(\rho u)'$ for the fundamental frequency ($20kHz$) and the subharmonic frequency ($10kHz$) at wall-normal location $y^*/\delta^* = 0.53$ for different streamwise and spanwise locations (CSUB 10, with $\Delta\theta_p^{2D}/\pi = -0.30$).

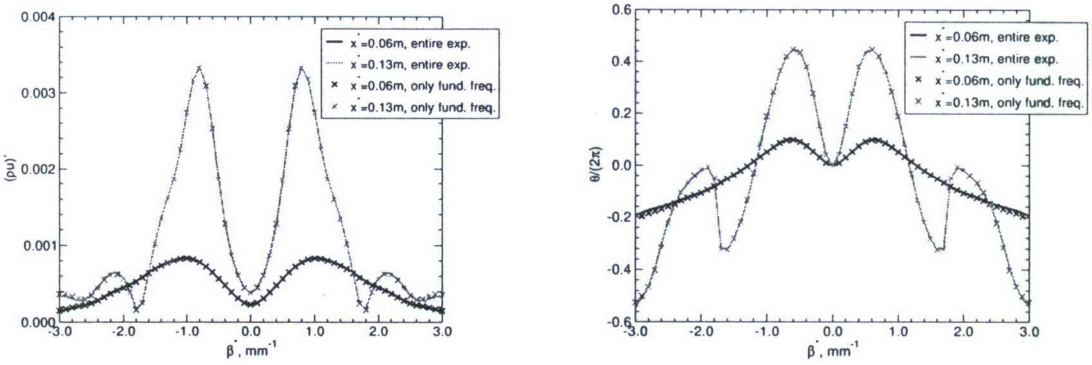

(a) spanwise amplitude distribution

(b) spanwise phase distribution

Figure 5.28: Spanwise amplitude (a) and phase (b) distribution for the mass-flux disturbance (ρu)' at wall-normal location $y^*/\delta^* = 0.53$ for two different streamwise positions. Comparison between DNS of the "entire" experiment including the subharmonic resonance and results from a simulation of the nonlinear disturbance development for the fundamental frequency only (see figures 5.13 and 5.7).

5.5 Summary

Transition in a supersonic flat-plate boundary layer at $Ma = 2.0$ has been investigated using DNS following the experimental studies by Kosinov *et al.* (1994). In both, simulation and experiment, transition has been initiated by a wave train triggered by localized forcing. While the forcing method in the experiment was a glow discharge, in the DNS, the flow has been forced by perturbing the v-velocity in a blowing and suction slot in the flat plate. A receptivity study has been performed to adjust the forcing through the slot in order to match the flow response to the glow discharge. In the experimental studies, Kosinov et al. discovered a new breakdown mechanism, which they called asymmetric subharmonic resonance, where oblique waves with the frequency of $20kHz$ resonate with two oblique subharmonic waves of different spanwise wave numbers. Scrutinizing the experimental data, however, also suggests the presence of a different breakdown mechanism. Understanding this mechanism has been one focus of the present numerical study. Therefore, the subharmonic resonance mechanism was deliberately excluded by only forcing the fundamental frequency of $20kHz$. Despite the absence of a subharmonic resonance, the disturbance development in the simulations agrees very well with the experimental findings for the fundamental frequency for both, the linear and the nonlinear stages. Further, these simulations show that the nonlinear development is caused by an oblique breakdown mechanism. This breakdown mechanism was first discovered in simulations (Fasel *et al.*, 1993) and has not yet been confirmed in any experimental study.

Moreover, asymmetric subharmonic resonance has been studied in detail. Using LST, it is possible to identify various possible asymmetric, subharmonic resonance triads for the physical flow conditions of Kosinov's experiments. DNS with small forcing amplitudes have been conducted in order to study the linear disturbance development including nonparallel effects resulting from the streamwise growth of the boundary layer. The primary wave from all subharmonic resonance triads identified by LST experience strong exponential streamwise amplitude growth. The streamwise wavenumbers of all triad components are only weakly affected by nonparallel effects, leading to the conclusion that the same resonance triads discovered using LST are also present in the DNS with large forcing amplitudes. The results obtained from several DNS with large forcing amplitudes revealed that the amplitude ratio between disturbances with both frequencies does not affect the resonance triad, which is in contrast to the experimental findings. Furthermore, in the simulations, the phase difference between disturbances of both frequencies plays a more important role since it influences the absolute value of the maximum generated by the resonance and its spanwise wavenumber. By changing the phase difference to a certain value, similar resonance triad as in the experiments and in the theoretical investigation by Tumin (1996) was observed in the simulations.

5.6 Hypersonic Flow

For later comparison with the cylindrical and conical geometries, flat-plate simulations are carried out in order to investigate the influence of cone opening angle and spanwise curvature. In this chapter, simulations are performed with the after-shock conditions of the conical experiments (c.f. Stetson *et al.* (1983)). A direct comparison is still difficult based on the variation of the boundary-layer values (see Figure 5.29) and the resulting different unstable frequencies. Relative to the boundary-layer thickness, the location of the generalized inflection point, which is a criterion for the inviscid instability of the boundary layer, collapses for the flat plate and the sharp cone (Figure 5.30). Therefore one could conclude that it might be possible to capture similar stability behavior once the parameters are adjusted. However, the amplification rates of second-mode waves are much stronger for the cone than they are for the flat plate. Hence, the downstream development of second-mode disturbance waves with small amplitude levels (linear behavior) results in five times smaller amplitude levels for the flat plate than for the cone. For the transition investigations over the flat plate, disturbance amplitude levels are therefore quintupled in order to (almost) compensate this effect.

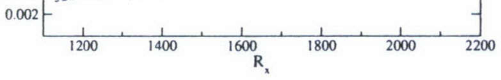

Figure 5.29: Boundary-layer properties. $Ma = 6.8$, $Re = 4,790,000$, $T_\infty = 71K$.

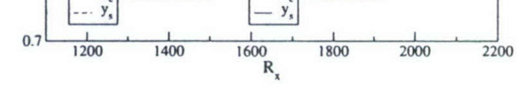

Figure 5.30: Boundary-layer properties (normalized with boundary layer thickness). $Ma = 6.8$, $Re = 4,790,000$, $T_\infty = 71K$.

As mentioned in the introduction (1.4.2.2), the findings by Seddougui & Bassom (1997) over a circular sharp cone indicated a stronger amplification of first-mode waves with increasing radius of the conical cross section, i.e. far downstream, first-mode waves become important during the boundary-layer transition process over the cone. Extrapolating these findings lead to the conclusion that for flat plates, where the cross-sectional radius tends to infinity, first-mode waves might play a role in the hypersonic boundary-layer transition.

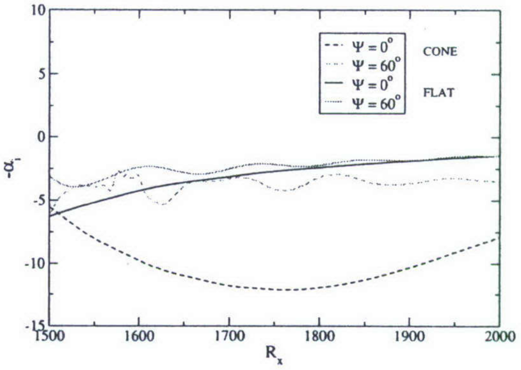

Figure 5.31: Linear amplification rates. *Sharp cone:* $Ma = 8$, $Re = 3,333,333$, $T_\infty = 53.35K$, $F_{1,0} = 1.17 \cdot 10^{-4}$, $A_{1,0} = 1 \cdot 10^{-3}\%$, $F_{1,1} = 5.85 \cdot 10^{-5}$, $A_{1,1} = 1 \cdot 10^{-3}\%$, $\Psi_{1,1} = 60°$. *Flat plate:* $Ma = 6.8$, $Re = 4,790,000$, $T_\infty = 71K$, $F_{1,0} = 8 \cdot 10^{-5}$, $A_{1,0} = 1 \cdot 10^{-3}\%$, $F_{1,1} = 4 \cdot 10^{-5}$, $A_{1,1} = 1 \cdot 10^{-3}\%$, $\Psi_{1,1} = 60°$.

But Figure 5.6, where linear amplification rates of first-mode oblique and second-mode two-dimensional waves are plotted over downstream distance, shows that first-mode waves are not more amplified for the flat plate than they are for the circular cone. In fact, the first-mode three-dimensional waves are more amplified for the cone than for the flat plate. In relation to the second-mode waves, the opposite becomes true. While first-mode oblique waves are just as amplified as second-mode two-dimensional waves for the flat plate, the second-mode two-dimensional waves for the circular cone are much more amplified than the first-mode oblique waves. Hence, not (only) the overall amplification rate might be important in the transition process (as used in the $e^N - method$) but also waves with amplification rates close to the best possible amplification rates should be considered.

5.6.1 Oblique Breakdown

The oblique breakdown played an important role in earlier investigations of supersonic flat-plate boundary-layer transition investigations (see e.g. Thumm (1991), Chang & Malik (1993*a*), and Eißler (1995)). With regard to those supersonic investigations, the hypersonic flat-plate boundary layer is more stable calling for increased disturbance amplitude levels beyond 1%. Figure 5.32 shows the amplitude distribution of selected modes for the oblique breakdown of a second-mode wave at a frequency of $F = 8 \cdot 10^{-5}$ and a wave angle of $\Psi = 20°$. These values are chosen based on the good performance of linear computations of the primary wave. With a disturbance amplitude of 1%, weak nonlinear interactions are present. For an equivalent comparison over the conical geometries, the amplitude level of the primary disturbance is increased to 5% in Figure 5.33. Higher modes rapidly emerge which are amplified in such a manner that primary disturbance wave amplitudes are surpassed downstream of $R_x = 1,800$. This simulation would call for a higher resolution to resolve evolving small-scale structures, but is omitted at this point for the sake of the main focus of this report–the boundary-layer transition for circular cones.

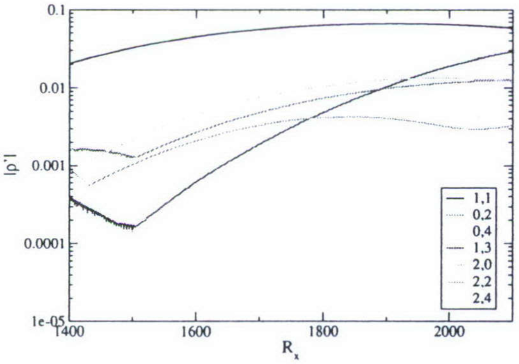

Figure 5.32: Oblique breakdown. $Ma = 6.8$, $Re = 4,790,000$, $T_\infty = 71K$, $F = 8 \cdot 10^{-5}$, $A_{1,1} = 1\%$, $\Psi = 20°$.

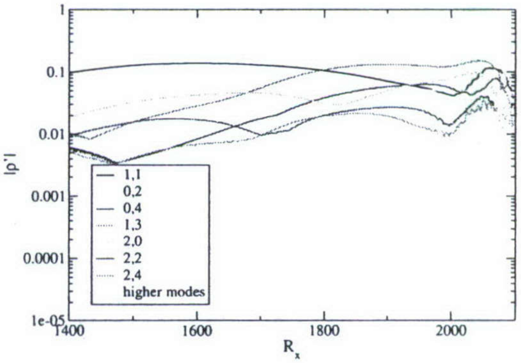

Figure 5.33: Oblique breakdown. $Ma = 6.8$, $Re = 4,790,000$, $T_\infty = 71K$, $F = 8 \cdot 10^{-5}$, $A_{1,1} = 5\%$, $\Psi = 20°$.

In the case of comparable disturbance amplitude levels for both the flat plate and the cone, the oblique breakdown is a stronger mechanism for the flat plate than for the sharp and blunt cones (c.f. section 7.2 and section 8.2).

5.6.2 Oblique Subharmonic Resonance

First discovered by Kosinov *et al.* (1994) in their experimental investigations of a flat-plate boundary layer at $Ma = 2$, this breakdown mechanism is also important for flat-plate flows at hypersonic speeds. Figure 5.34 shows strong nonlinear interactions shortly downstream of the disturbance slot. Remarkable is the strong amplification of two-dimensional waves with the subharmonic frequency and its higher harmonics (i.e. (1,0)-mode, (2,0)-mode, and (3,0)-mode).Although the primary wave amplitudes are exceeded by higher modes around $R_x = 1,700$, which is slightly upstream than for the oblique breakdown, it is hard to evaluate if the oblique subharmonic resonance is a stronger mechanism due to the higher disturbance energy input (two wave pairs are perturbed for this mechanism instead of one pair for the oblique breakdown). Therefore, the only conclusion is that the oblique subharmonic resonance is also a viable candidate for hypersonic boundary layer transition.

If, additionally, a steady streamwise vortex mode is disturbed, the disturbance amplitude has to be reduced to 2% in order to achieve convergence on the same computational grid used for the earlier investigations. Therefore, the steady vortex mode (0,1) enhances the nonlinear interactions of the oblique subharmonic resonance despite the fact that the forced steady vortex mode (0,1) is neutral throughout the computational domain (see Figure 5.35). Unfortunately, no conclusions on which specific modes are influenced by the steady vortex mode can be drawn from this comparison because of the different forcing amplitudes. Nonetheless, steady streamwise vortices enhance the performance of the oblique subharmonic resonance leading to the conclusion that steady vortices have to be considered for hypersonic the transition process.

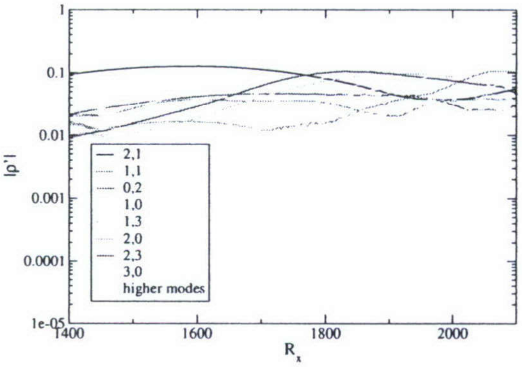

Figure 5.34: Oblique subharmonic resonance. $Ma = 6.8$, $Re = 4,790,000$, $T_\infty = 71K$, $F = 8 \cdot 10^{-5}$, $A_{2,1} = 5\%$, $A_{1,1} = 5\%$, $\Psi_{2,1} = 20°$.

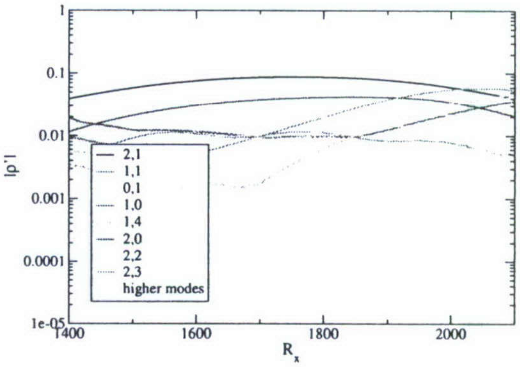

Figure 5.35: Oblique subharmonic resonance. $Ma = 6.8$, $Re = 4,790,000$, $T_\infty = 71K$, $F = 8 \cdot 10^{-5}$, $A_{2,1} = 2\%$, $A_{1,1} = 2\%$, $A_{0,1} = 1\%$, $\Psi_{2,1} = 20°$.

5.6.3 Oblique Fundamental Resonance

Husmeier *et al.* (2005) discussed this breakdown mechanism for a flat-plate boundary layer at Mach 3. In their investigations, the oblique breakdown of the primary wave was stronger than any other mechanism and therefore, the oblique fundamental resonance was a possible but inferior mechanism. For hypersonic speeds, this resonance is a viable path to transition. Figure 5.6.3 shows that higher modes rapidly emerge. Especially the strong amplification of the two-dimensional wave at the fundamental frequency, which reaches primary disturbance wave amplitude levels shortly downstream of the disturbance slot, is remarkable. Different to

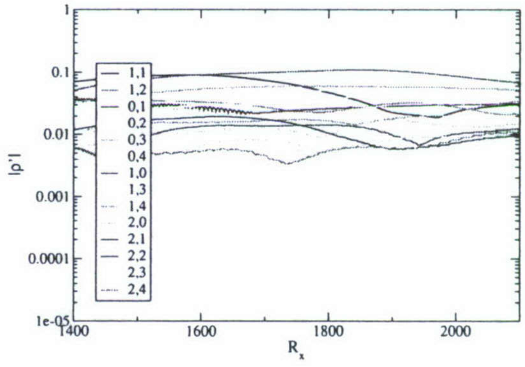

Figure 5.36: Oblique fundamental resonance. $Ma = 6.8$, $Re = 4,790,000$, $T_\infty = 71K$, $F = 8 \cdot 10^{-5}$, $A_{1,1} = 5\%$, $A_{1,2} = 5\%$, $\Psi_{1,1} = 20°$.

the breakdown scenarios discussed earlier, steady vortex modes with different spanwise spacings develop at high amplitudes and are weakly amplified underlining their important part in the transition process. To further substantiate this observation, a steady vortex mode (0,1) is forced in Figure 5.37. Again, the overall disturbance amplitudes had to be even further reduced than for the oblique subharmonic resonance with a steady vortex mode in order to converge a solution on the used grid. Comparing Figure 5.37 with Figure 5.38 reveals that this increase in strength of the nonlinear interactions cannot only be linked to the higher amplitude level of the forced vortex mode (0,1) but also to the stronger amplification of the two-dimensional wave at the fundamental frequency. While downstream development of other higher modes are similar for both cases, the two-dimensional wave (1,0) reaches 2.5 times higher amplitudes than without the steady streamwise vortex mode forced.

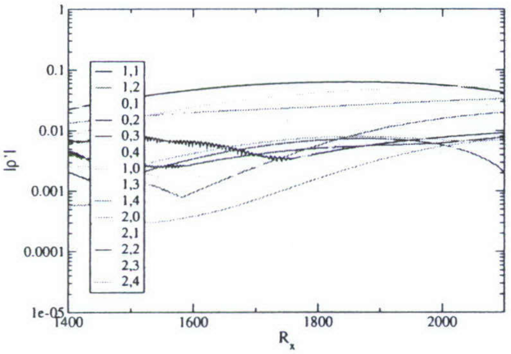

Figure 5.37: Oblique fundamental resonance. $Ma = 6.8$, $Re = 4,790,000$, $T_\infty = 71K$, $F = 8 \cdot 10^{-5}$, $A_{1,1} = 1\%$, $A_{1,2} = 1\%$, $A_{0,1} = 1\%$, $\Psi_{1,1} = 20°$.

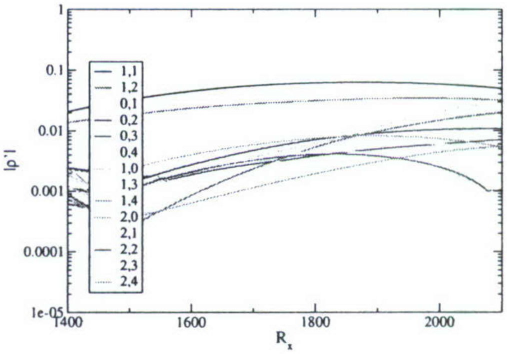

Figure 5.38: Oblique fundamental resonance. $Ma = 6.8$, $Re = 4,790,000$, $T_\infty = 71K$, $F = 8 \cdot 10^{-5}$, $A_{1,1} = 1\%$, $A_{1,2} = 1\%$, $\Psi_{1,1} = 20°$.

5.6.4 Fundamental Breakdown (K-Type)

Before the discovery of the subharmonic breakdown (N-/H-type) in 1984, the fundamental breakdown or so-called Klebanoff breakdown was believed to be the driving mechanism for incompressible flat-plate boundary layer transition. For compressible boundary layers at supersonic speeds ($Ma \leq 5$), this breakdown did not seem to play an important role (c.f., for example, Thumm (1991), Eißler (1995), or Chang & Malik (1994)).

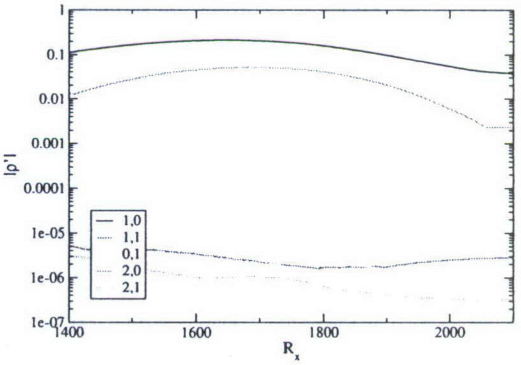

Figure 5.39: Fundamental breakdown. $Ma = 6.8$, $Re = 4,790,000$, $T_\infty = 71K$, $F = 8 \cdot 10^{-5}$, $A_{1,0} = 5\%$, $A_{1,1} = 1 \cdot 10^{-3}\%$, $\Psi_{1,1} = 60°$.

At hypersonic speeds, where the second-mode two-dimensional waves are governing the linear stability behavior (Mack (1984)), the fundamental breakdown might be a suitable candidate for boundary layer transition. Although the primary two-dimensional waves in Figure 5.39 are disturbed at 5% of the free-stream velocity, the secondary oblique waves (1,1) show no signs of a resonance. The amplitude dip around $R_x = 1,800$ is due to the change in location where the maximum amplitude is taken and therefore a relict of the post-processing tool. Klebanoff *et al.* (1962) used spanwise spacer in their experimental investigations and found the fundamental breakdown through interactions of a streamwise vortex (generated by the spacers) and a two-dimensional wave. In our simulations, the forcing of steady vortex modes is not exactly comparable to spanwise spacers because of the local mass addition into the flow—but can still be seen as a first step towards modeling vortex generators. Figure 5.40, in which a steady streamwise vortex mode is forced with 1%, reveals a possible fundamental resonance around $R_x = 1,900$. Stronger amplification than the linear eigenbehavior is experienced downstream of that location. Although disturbance amplitudes for the primary and secondary waves equal the latter case, the overall amplitude level of the secondary wave (1,1) is increased by a factor of 1,000 and thus nonlinear interactions are enhanced. Since this has already been discussed in the proceeding breakdown scenarios, one can conclude that a steady streamwise vortex mode has a strong influence on the nonlinear stability behavior independent of the underlying mechanisms. Differences to these earlier findings are observed once the disturbance amplitude of the primary waves and the steady vortex mode are increased to 5% (Figure 5.41). When comparing Figure 5.41 with Figure 5.40 the amplitude level of the primary waves decrease because emerging higher modes deplete energy from them. Since the primary waves are amplified throughout the computational domain so that amplitude levels towards the end of the domain reach comparable values as for the lower disturbance amplitude (1%). Additionally, the amplitude level of the first higher harmonic of the primary wave, the (2,0)-mode, is strongly reduced by a combination of the influence of the lower primary wave amplitudes and the presence of the steady vortex. Also worth mentioning is that when forcing a steady streamwise vortex mode in combination with a fundamental breakdown the amplitude level of the secondary waves (1,1) is elevated to the amplitude level of the steady vortex mode—a phenomenon, which has not been observed in the investigations before.

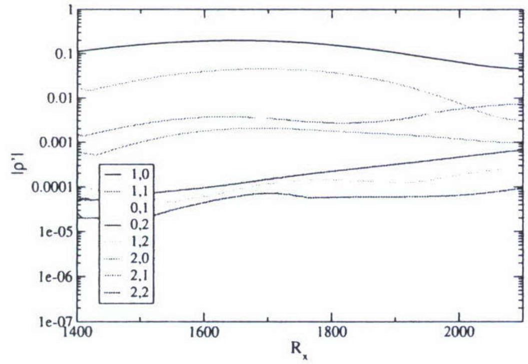

Figure 5.40: Fundamental breakdown. $Ma = 6.8$, $Re = 4,790,000$, $T_\infty = 71K$, $F = 8 \cdot 10^{-5}$, $A_{1,0} = 5\%$, $A_{1,1} = 1 \cdot 10^{-3}\%$, $A_{0,1} = 1\%$, $\Psi_{1,1} = 60°$.

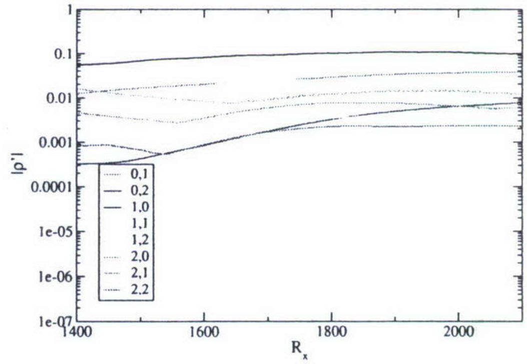

Figure 5.41: Fundamental breakdown. $Ma = 6.8$, $Re = 4,790,000$, $T_\infty = 71K$, $F = 8 \cdot 10^{-5}$, $A_{1,0} = 5\%$, $A_{1,1} = 1 \cdot 10^{-3}\%$, $A_{0,1} = 5\%$, $\Psi_{1,1} = 60°$.

5.6.5 Subharmonic Breakdown (N-/H-Type)

For incompressible boundary layers where the two-dimensional waves are more amplified than three-dimensional waves according to the Squire's Theorem, the subharmonic breakdown is a strong mechanism governing the transition process for many applications. Note, that exceptions of Squire's Theorem exist depending on frequency and downstream location. The hypersonic flat-plate boundary layer, although two-dimensional waves are most amplified, seems to be stable with respect to the subharmonic breakdown. In Figure 5.42, the secondary wave amplitude is increased by a factor of 10 in comparison to the fundamental breakdown discussed in the preceding section. The typical dip in amplitude distribution following a sudden increase in amplification rates associated with the presence of a resonance cannot be observed. Usually, this behavior is an indication of a possible resonance caused by the locking of the phase speeds of primary and secondary waves enabling energy transfer between them. Instead, Figure 5.42 compares the amplitude distribution of the secondary wave in presence of the primary wave and its linear eigenbehavior (scaled to fit amplitude distribution of the secondary wave). Nonlinear growth of the secondary wave

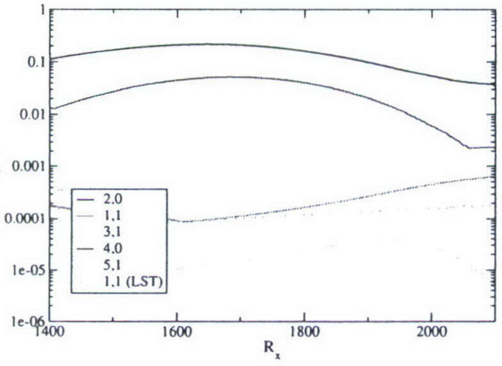

Figure 5.42: Subharmonic breakdown. $Ma = 6.8$, $Re = 4,790,000$, $T_\infty = 71K$, $F_{2,0} = 8 \cdot 10^{-5}$, $A_{2,0} = 5\%$, $A_{1,1} = 1 \cdot 10^{-2}\%$, $\Psi_{1,1} = 60°$.

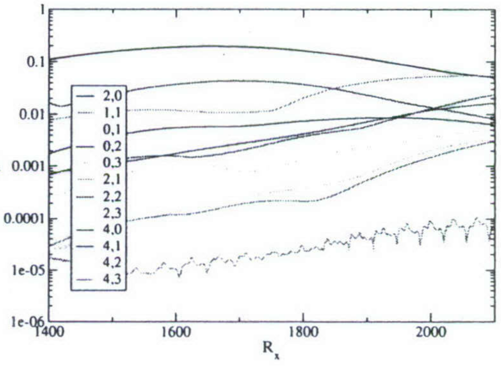

Figure 5.43: Subharmonic breakdown. $Ma = 6.8$, $Re = 4,790,000$, $T_\infty = 71K$, $F_{2,0} = 8 \cdot 10^{-5}$, $A_{2,0} = 5\%$, $A_{1,1} = 1 \cdot 10^{-2}\%$, $A_{0,1} = 1\%$, $\Psi_{1,1} = 60°$.

is present throughout the domain, but emerging higher modes are stabilized towards the end of the domain. With a forced steady vortex mode (0,1) the secondary wave might inherit different frequency components and is therefore randomly oscillating (see Figure 5.43). Moreover, a fundamental resonance between the (2,0)- and (2,1)-modes is clearly present at $R_x = 1,800$. Although the existence and the location of the resonance is independent of the secondary wave amplitude, the increase in secondary wave amplitude level might be responsible for the enhanced fundamental breakdown when comparing Figure 5.40 with Figure 5.43.

5.7 Summary

For a hypersonic flat-plate boundary layer, two-dimensional second-mode waves are most amplified according to LST. Their nonlinear amplification rate in the investigated breakdown scenarios is smaller than for the cone investigations discussed in section 7 and thereafter. Hence, the disturbance amplitude levels are increased to approximate the amplitude magnitude of the simulations over a cone for later comparison.

With primary disturbance amplitude levels of 5% of the free-stream velocity, breakdown mechanisms involving second-mode two-dimensional primary waves (K- and N-/H- Type) do not show strong nonlinear interactions with rapid development of higher modes which would to some degree indicate the initialization of the transition process. With a forced steady streamwise vortex mode, nonlinear interactions are enhanced mainly due to the higher amplitude level of the secondary waves but still no transition on-set is observed.

Looking at the breakdown mechanisms of oblique waves, i.e the oblique breakdown and the subharmonic and fundamental oblique resonances, strong nonlinear interactions are present such that generated higher modes reach primary wave amplitude levels. The wave angle of the primary oblique waves is chosen to be small in order to take advantage of the waves' eigenbehavior. At small wave angles, amplification rates of the oblique waves are almost as strong as the amplification rates of second-mode two-dimensional waves, i.e. they are strongly amplified. A ranking of these mechanisms is omitted at this point because on the one hand further investigations would be necessary requiring finer computational grids and on the other hand these simulations fulfill their purpose for comparison with cylindrical and conical flow investigations in order to draw conclusions on how spanwise curvature influences the stability behavior.

6. Transition Investigations of a Boundary Layer on a Cylinder

To better investigate the influence of spanwise curvature, investigations of a cylindrical geometry are discussed in this section. The cylindrical simulations are set-up in correlation to the conical investigations discussed in section 7. Figure 6.1 illustrates how the simulations for the cylindrical investigations are constituted in comparison to the sharp cone investigations. The conical transition investigations are started at $x_0 \approx 0.27$ downstream of the (virtual) origin. At that location the radius of the cone (R_{in}) is chosen for the radius of the cylinder. Because the boundary layer thickness develops along the conical surface, the same downstream distance from the origin is chosen for the cylindrical investigations resulting in a small downstream shift (see zoom-in of Figure 6.1). The ratio of the boundary layer thickness δ to the radius of the cylinder R is an important parameter for this study. The downstream development of this ratio for the sharp cone investigated in section 7 in comparison to the development over the cylinder is depicted in Figure 6.2. Based on the increasing radius of the cone in downstream direction the ratio δ/R is decreasing because the boundary layer thickness stays almost constant. Hence, spanwise curvature influences become less important advancing in the downstream direction. The insert of Figure 6.2 shows the radius and boundary layer thickness (radius added) over the downstream distance R_x. Because R_x is the square root of the local Reynolds number, the radius of the cone develops nonlinearly which explains the nonlinear decrease of the ratio δ/R for the cone. For the cylinder, however, this ratio increases in downstream direction because of the growth of the boundary-layer thickness (and the constant radius R). Furthermore, the cylinder develops a larger boundary-layer thickness which is comparable to the flat-plate boundary-layer thickness (Figure 6.3) and starts therefore at a larger δ/R-ratio. Due to the similar boundary layer properties in Figure 6.3, the same disturbance frequencies as for the flat-plate investigations are chosen. Because linear amplification rates in Figure 6.4 are similar throughout the computational domain, differences in the stability behavior of different breakdown scenarios can be directly linked to the *nonlinear* influences of spanwise curvature.

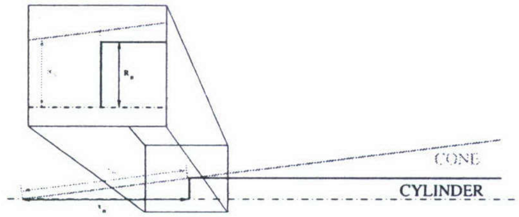

Figure 6.1: Numerical set-up for the cylindrical investigations in comparison to the sharp cone set-up.

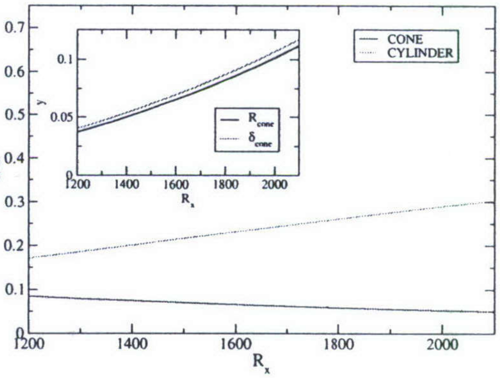

Figure 6.2: Boundary-layer thickness ratio based on radius for the cone and the cylinder. *Cone:* $Ma = 8$, $Re = 3,333,333$, $T_\infty = 53.35K$. *Cylinder:* $Ma = 6.8$, $Re = 4,790,000$, $T_\infty = 71K$.

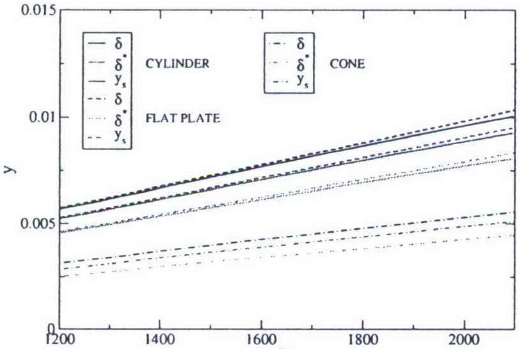

Figure 6.3: Boundary-layer properties for the flat plate, cylinder, and cone. *Flat Plate/Cylinder:* $Ma = 6.8$, $Re = 4,790,000$, $T_\infty = 71K$. *Cone:* $Ma = 8$, $Re = 3,333,333$, $T_\infty = 53.35K$.

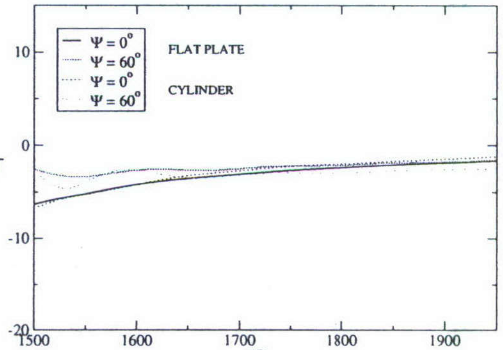

Figure 6.4: Comparison of linear amplification rate for the flat plate and the cylinder. $Ma = 6.8$, $Re = 4,790,000$, $T_\infty = 71K$, $F_{1,0} = 8 \cdot 10^{-5}$, $F_{1,1} = 4 \cdot 10^{-5}$, $\Psi_{1,1} = 60°$.

6.1 Oblique Breakdown

The oblique breakdown was proven to be a strong mechanism for the flat-plate geometries. For the cylinder, Figure 6.5 graphs the amplitude development in downstream direction for an oblique breakdown of a second-mode wave forced with a disturbance amplitude of 1% and a wave angle of $\Psi = 20°$. Higher modes typically associated with the oblique breakdown (e.g. (0,2)- and (1,3)-mode) are emerging. Comparison with Figure 5.32 reveals no significant differences to the flat-plate simulations. As for the flat-plate simulations, the disturbance amplitude is increased to 5% in Figure 6.6. Not surprisingly, stronger nonlinear actions arise developing higher modes which reach primary wave amplitude levels. When compared with the equivalent flat-plate investigations (c.f. Figure 5.33), nonlinear actions are weakened. The resolution limits are not exceeded as for the flat-plate simulations despite the fact that primary wave and waves generated through first/second-level interactions (e.g. mode (0,2), (1,3), and (2,0)) reach comparable amplitude levels. Because linear amplification rates are not altered by the presence of spanwise curvature (see Figure 6.4), the spanwise curvature of the cylinder is obstructing the emerging of higher modes (nonlinear interactions).

To better investigate the influence of spanwise curvature, the computational domain is pushed downstream in Figure 6.7 to increase the δ/R-ratio, i.e. increasing the influence of spanwise curvature. Amplitude growth and overall disturbance amplitude level of the primary wave are lower than for the previous case (c.f. Figure 6.6). Although some higher modes are generated, they are not strongly amplified

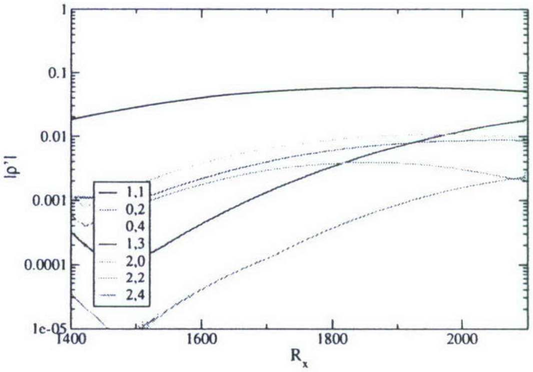

Figure 6.5: Oblique breakdown. $Ma = 6.8$, $Re = 4,790,000$, $T_\infty = 71K$, $F = 8 \cdot 10^{-5}$, $A_{1,1} = 1\%$, $\Psi = 20°$.

so that the development of higher modes is limited. Because the shift in the downstream direction stabilizes the primary disturbance waves, it is difficult to distinguish between a further stabilization through augmented curvature effects or a stabilization through reduced amplification rates (eigenbehavior of the disturbed waves).

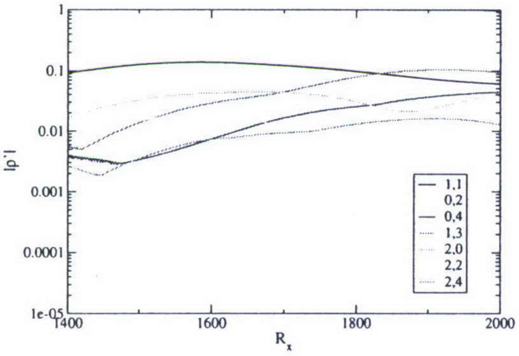

Figure 6.6: Oblique breakdown. $Ma = 6.8$, $Re = 4,790,000$, $T_\infty = 71K$, $F = 8 \cdot 10^{-5}$, $A_{1,1} = 5\%$, $\Psi = 20°$.

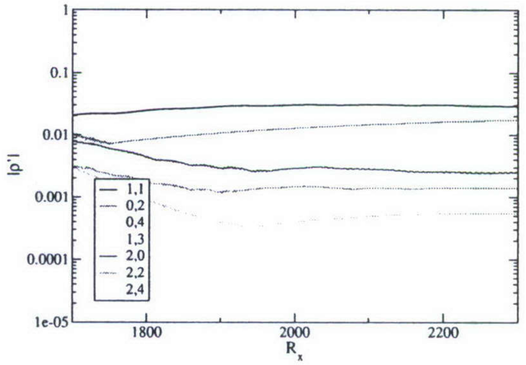

Figure 6.7: Oblique breakdown. $Ma = 6.8$, $Re = 4,790,000$, $T_\infty = 71K$, $F = 8 \cdot 10^{-5}$, $A_{1,1} = 5\%$, $\Psi = 20°$.

6.2 Oblique Subharmonic Resonance

As stated in the proceeding section for the oblique breakdown, the spanwise curvature has also stabilizing effects on the oblique subharmonic resonance. Although numerous higher modes emerge, Figure 6.8 only shows little amplitude growth for these developing higher modes. Since the oblique subharmonic resonance was a strong mechanism for the flat-plate (c.f. section 5.6.2), the disturbance amplitude for the cylindrical investigation is decreased to 2% to allow comparison of the two cases. There might be still the possibility of an oblique subharmonic resonance with increased disturbance wave amplitude levels, but further investigation is omitted since the cylindrical investigations serve only as a reference case for conical flows.

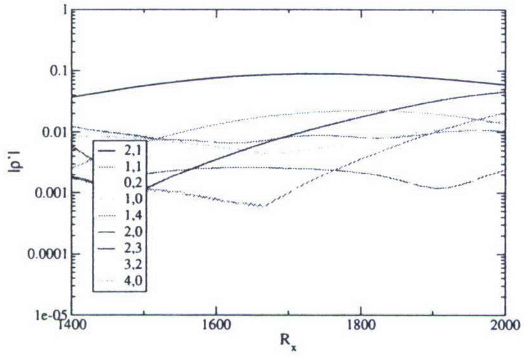

Figure 6.8: Oblique subharmonic resonance. $Ma = 6.8$, $Re = 4,790,000$, $T_\infty = 71K$, $F = 8 \cdot 10^{-5}$, $A_{2,1} = 2\%$, $A_{1,1} = 2\%$, $\Psi_{2,1} = 20°$.

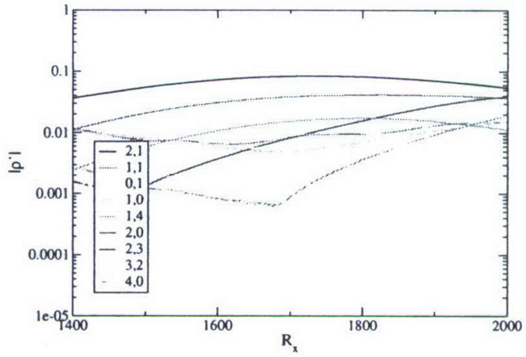

Figure 6.9: Oblique subharmonic resonance. $Ma = 6.8$, $Re = 4,790,000$, $T_\infty = 71K$, $F = 8 \cdot 10^{-5}$, $A_{2,1} = 2\%$, $A_{1,1} = 2\%$, $A_{0,1} = 1\%$, $\Psi_{2,1} = 20°$.

6.3 Oblique Fundamental Resonance

The oblique fundamental resonance over a cylinder behaves differently than expected. Comparing Figure 6.10 with Figure 6.11 show virtually no influence of a forced steady streamwise vortex mode on the nonlinear interactions. This clearly contradicts knowledge gained from other scenarios and geometries. Note, that the disturbance amplitude levels are also reduced to 2%, as in the oblique subharmonic resonance, to allow

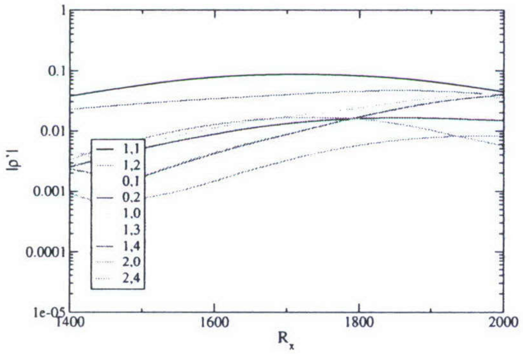

Figure 6.10: Oblique fundamental resonance. $Ma = 6.8$, $Re = 4,790,000$, $T_\infty = 71K$, $F_{1,1} = 8 \cdot 10^{-5}$, $A_{1,1} = 2\%$, $A_{1,2} = 2\%$, $\Psi_{1,1} = 20°$.

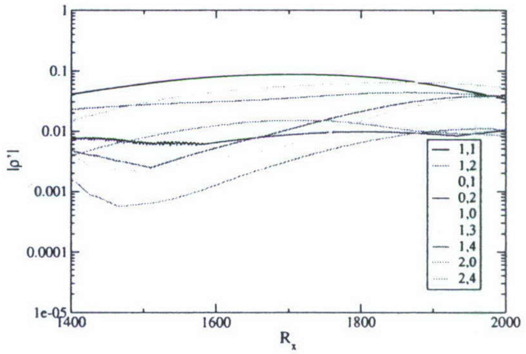

Figure 6.11: Oblique fundamental resonance. $Ma = 6.8$, $Re = 4,790,000$, $T_\infty = 71K$, $F_{1,1} = 8 \cdot 10^{-5}$, $A_{1,1} = 2\%$, $A_{1,2} = 2\%$, $A_{0,1} = 1\%$, $\Psi_{1,1} = 20°$.

for comparison with the flat-plate simulations. By comparing Figure 6.11 with Figure 5.37, it can be concluded that the oblique fundamental resonance is also stabilized by spanwise curvature. It is worth remarking that the oblique fundamental resonance itself may not be turned off by spanwise curvature, but the disturbance amplitude levels would have to be increased significantly for the flow to transition. Thus, the reduced amplitude levels in presence of spanwise curvature seems to be the underlying stabilizing mechanism.

6.4 Fundamental Breakdown (K-Type)

A weak fundamental resonance around $R_x = 1,800$ exists for the cylinder (see Figure 6.12). The few developing waves are weakly damped downstream of that location so that the fundamental breakdown is not a viable mechanism. With a forced steady vortex mode (0,1), the amplitude level and the amplification rate of the secondary waves are raised in Figure 6.13. But still no rapid amplification of generated higher modes further advance the transition process. Therefore, it is questionable if this scenario is an important mechanism for the high-speed transition process over cylinders.

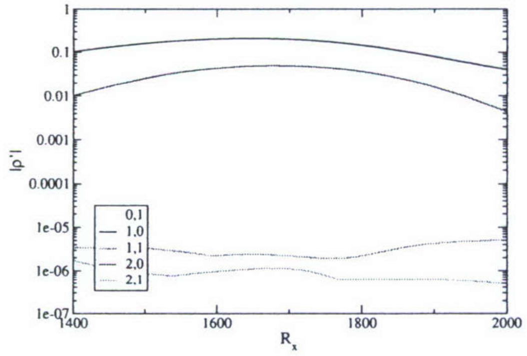

Figure 6.12: Fundamental breakdown. $Ma = 6.8$, $Re = 4,790,000$, $T_\infty = 71K$, $F = 8 \cdot 10^{-5}$, $A_{1,0} = 5\%$, $A_{1,1} = 1 \cdot 10^{-3}\%$, $\Psi_{1,1} = 60°$.

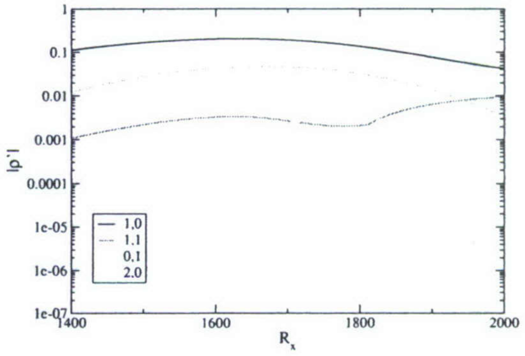

Figure 6.13: Fundamental breakdown. $Ma = 6.8$, $Re = 4,790,000$, $T_\infty = 71K$, $F = 8 \cdot 10^{-5}$, $A_{1,0} = 5\%$, $A_{1,1} = 1 \cdot 10^{-3}\%$, $A_{0,1} = 1\%$, $\Psi_{1,1} = 60°$.

6.5 Subharmonic Breakdown (N-/H-Type)

In contrast to the fundamental breakdown, there is no resonance between the second-mode two-dimensional primary wave and an oblique wave at half the frequency taking place in Figure 6.14. Instead, the secondary wave shows modulations of lower and higher frequencies. In contrast to the mechanism for the flat plate, the higher harmonic of the primary wave evolves as well as the two-dimensional wave at half the frequency (subharmonic). In Figure 6.15 and Figure 6.16, the subharmonic breakdown with forced steady vortex modes at different spanwise spacings are graphed. Still, there is no subharmonic resonance apparent. But with the presence of the steady vortex mode at the same wave angle as the secondary wave (Figure 6.15), a fundamental resonance of the emerging (2,1)-mode with the primary (2,0)-mode is present. This could have already been observed for the flat plate (c.f. section 5.6.5). When comparing the subharmonic breakdown with a forced steady vortex mode with the fundamental breakdown and a forced steady vortex mode (Figure 6.13) emerging higher modes are weakly more amplified.

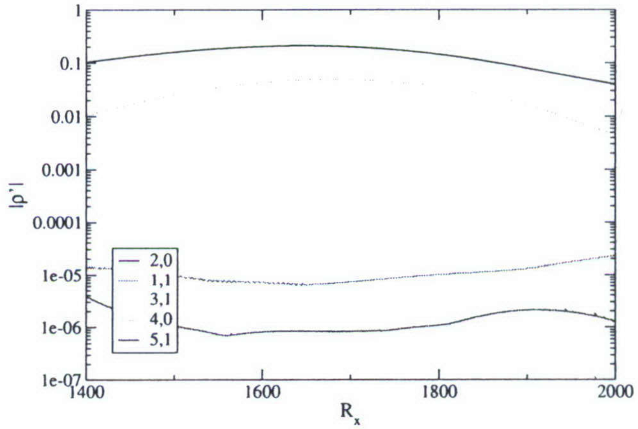

Figure 6.14: Subharmonic breakdown. $Ma = 6.8$, $Re = 4,790,000$, $T_\infty = 71K$, $F_{2,0} = 8 \cdot 10^{-5}$, $A_{2,0} = 5\%$, $A_{1,1} = 1 \cdot 10^{-3}\%$, $\Psi_{1,1} = 60°$.

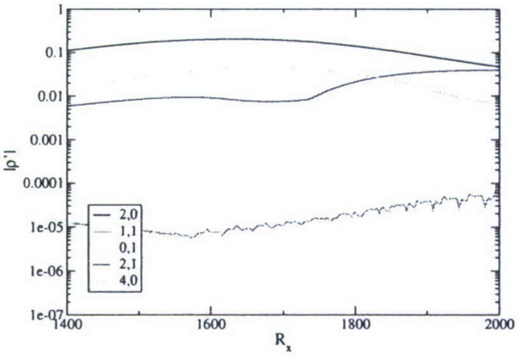

Figure 6.15: Subharmonic breakdown. $Ma = 6.8$, $Re = 4,790,000$, $T_\infty = 71K$, $F_{2,0} = 8 \cdot 10^{-5}$, $A_{2,0} = 5\%$, $A_{1,1} = 1 \cdot 10^{-3}\%$, $A_{0,1} = 1\%$, $\Psi_{1,1} = 60°$.

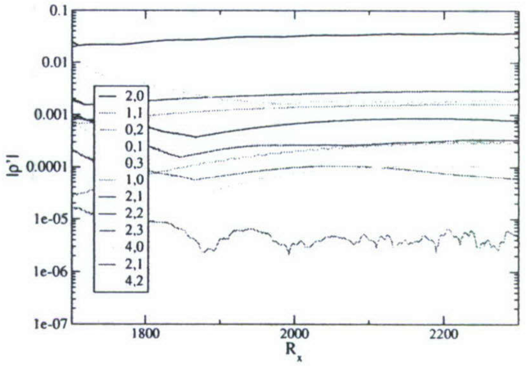

Figure 6.16: Subharmonic breakdown. $Ma = 6.8$, $Re = 4,790,000$, $T_\infty = 71K$, $F_{2,0} = 8 \cdot 10^{-5}$, $A_{2,0} = 5\%$, $A_{1,1} = 1 \cdot 10^{-3}\%$, $A_{0,2} = 1\%$, $\Psi_{1,1} = 60°$.

6.6 Summary

The cylindrical stability investigations demonstrate the benefits of DNS, because a specific parameter, such as the spanwise curvature, can be singled out and its influence on the stability behavior investigated. Experimentally, this is almost impossible because effects of the fore body (e.g. attached/detached shock wave) would change the flow properties eliminating the foundation of an exact comparison.

With DNS, it was possible to construct flow conditions as present in the flat-plate and cone investigations. It became apparent that the ratio of the boundary layer thickness to the radius is an important parameter. Values above 20% have a strong stabilizing effect independent of the studied breakdown scenarios. Because the boundary-layer thickness is thinner for the conical investigations (starting in section 7) and the radius is linearly increasing in downstream direction, the ratio of boundary-layer thickness to radius stays below 20%. Therefore, spanwise curvature effects are weakened for flows over cones so that the geometries under investigation can be ranked according to their stability behavior from unstable to stable: FLAT PLATE, SHARP CONE, CYLINDER.

7. Transition Investigations of a Boundary Layer on a Sharp Cone

The wind-tunnel conditions of Stetson *et al.* (1983) are used as flow conditions for the numerical stability investigations. These flow conditions (before and after the shock) are summarized in Table 7.1.

flow property	Mach number	Temperature	Pressure	Reynolds number	cone angle	shock angle
before the shock	8	53.35 K	165.5 Pa	3,333,333	7°	10.4°
after the shock	6.8	71 K	415.6 Pa	4,790,000		

Table 7.1: Flow parameters before and after the shock.

According to *LST*, second-mode two-dimensional waves are most strongly amplified under these conditions. This fact could have been confirmed in the *DNS*. Also, oblique waves at small wave angles show a similarly strong amplification. Figure 7.1 compares downstream amplitude distribution for a second-mode two-dimensional and second-mode oblique wave at $\Psi = 20°$. Although two-dimensional amplitudes exceed amplitude levels of the oblique wave by a factor of 2, amplification rate of the oblique waves are still strong enough to have second-mode oblique waves considered for transition investigations. Figure 7.2 has already been discussed in section 4.2 for code validation purposes but is repeated here to elaborate the possibility

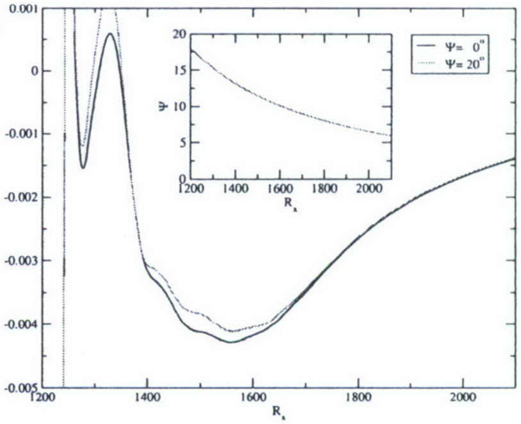

Figure 7.1: Comparison of amplification rates at $\Psi = 0°$ and $\Psi = 20°$. $Ma = 7.95$, $Re = 3,333,333$, $T_\infty = 53.35K$, $F = 1.17 \cdot 10^{-4}$.

of the presence of second-mode oblique waves in the experiments (c.f. Stetson *et al.* (1983)). The experimental measurements of wall pressure stagnates downstream of $R_x = 1,800$. When two-dimensional amplitude levels above 0.1% are being considered, amplitude levels in the simulations drop due to upcoming higher harmonics (see Figure 7.3). Once disturbance amplitude levels have reached 1%, these higher harmonics draw enough energy from the fundamental waves that they become stable. Looking at the wall pressure of the second-mode oblique wave reveals a slightly different amplitude development in downstream direction. The amplitude starts to level off shortly after $R_x = 1,600$ but is not decreasing as strongly at its two-dimensional counterpart. Nonetheless, amplitude levels lie within the experimental uncertainties so that large-amplitude second-mode three-dimensional waves might also be present in the natural transition scenarios of the experiments by Stetson *et al.* (1983).

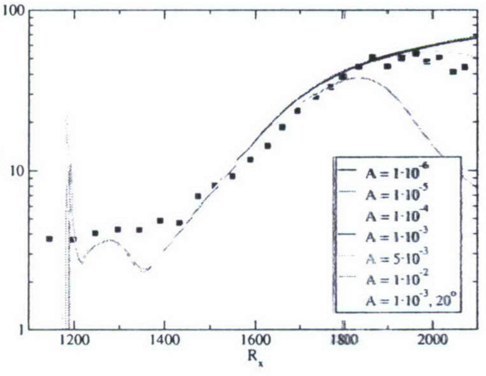

Figure 7.2: Wall-pressure distribution in downstream direction of different disturbance waves. $Ma = 7.95$, $Re = 3,333,333$, $T_\infty = 53.35K$, $F = 1.17 \cdot 10^{-4}$.

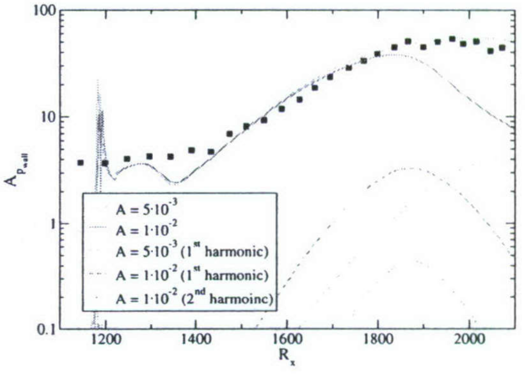

Figure 7.3: Wall-pressure distribution in downstream direction of different disturbance waves and their higher harmonics. $Ma = 7.95$, $Re = 3,333,333$, $T_\infty = 53.35K$, $F = 1.17 \cdot 10^{-4}$.

7.1 Pulsed Disturbance

The linear instability of the flow is investigated with simulations where a small-amplitude pulsed disturbance is introduced into the flow. Because of memory and compute power restriction only discrete spanwise modes are disturbed covering wave angles between $\Psi = 0°$ and $\Psi = 80°$. This leads to the development of a linear wave packet (in time) containing a broad spectrum of frequencies. The time-dependent signal, its spectrum, and the response of the flow (receptivity spectrum) is graphed in Figure 7.4. The flow is most responsive to disturbances around $100kHz$ which includes the most dominant frequency ($f = 102kHz$) reported in the experiments by Stetson *et al.* (1983). Due to the linear superposition principle, the amplification (or decay) of waves with a specific frequency within the wave packet can be extracted using a Fourier transformation in time. Figure 7.5 depicts the downstream development of amplification rates for selected frequencies. The wavy character of the amplification rate distribution for lower frequencies results from the fact that those waves are still developing downstream of the disturbance slot. Confirming Stetson's experimental findings, the frequency $f = 102kHz$ reaches the highest amplification rate within the computational domain. Also, in accordance with the boundary layer thickness (c.f Figure 4.2a), high frequency disturbances are more amplified at the beginning of the domain while lower frequency disturbances become increasingly important advancing in downstream direction. This results in larger instability regions for waves with lower frequencies. Therefore, looking at the amplitude distribution of the disturbance waves in Figure 7.6 shows that the amplitude of the waves with frequency $f = 102kHz$ starts to level off around $R_x = 1,800$ and lower frequencies reach higher amplitudes farther downstream. Plotting the amplification rates over disturbance frequency for two different downstream location confirms the shift to lower frequencies in downstream direction (see Figure 7.7). Because of the large downstream extent of the hypersonic transition region in experiments, most of the simulations are performed at a frequency of $f = 88kHz$ to have strong amplification over a wide range of local Reynolds numbers. This in turn supports breakdown mechanisms through stronger nonlinear wave interactions.

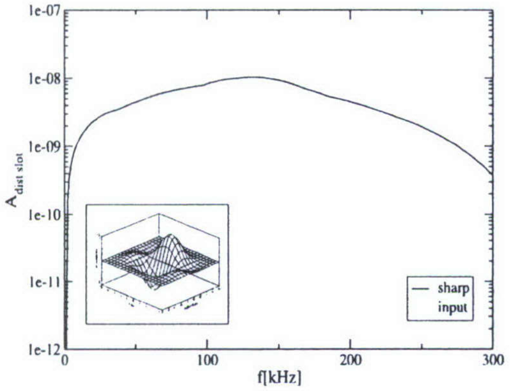

Figure 7.4: Spectral input signal of pulsed disturbance. $Ma = 7.95$, $Re = 3,333,333$, $T_\infty = 53.35K$, $\Psi = 20°$.

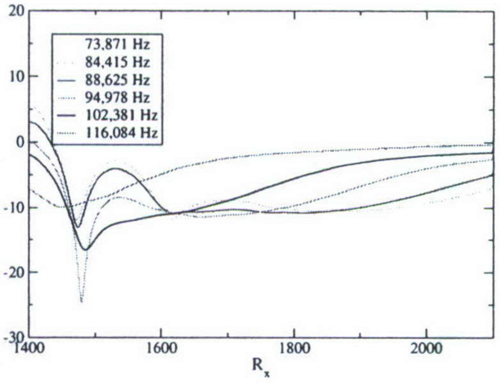

Figure 7.5: Linear amplification rate for selected frequencies. $Ma = 7.95$, $Re = 3,333,333$, $T_\infty = 53.35K$, $\Psi = 20°$.

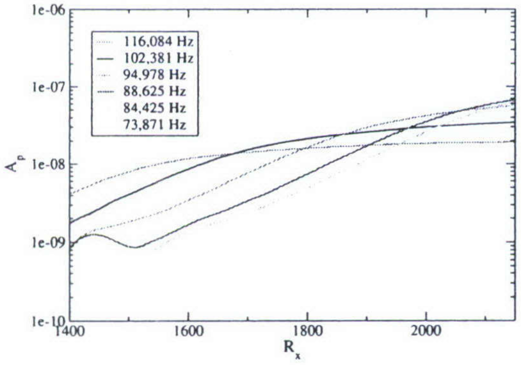

Figure 7.6: Amplitude distribution based on wall pressure for selected frequencies. $Ma = 7.95$, $Re = 3,333,333$, $T_\infty = 53.35K$, $\Psi = 20°$.

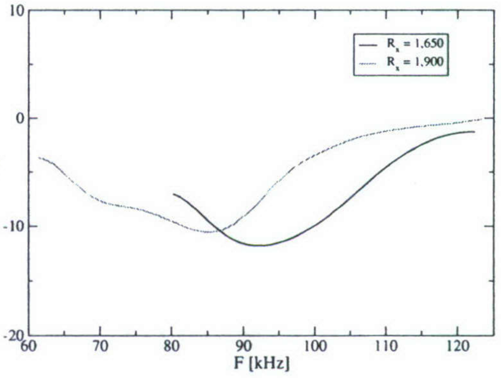

Figure 7.7: Linear amplification rate plotted over frequency at different downstream locations. $Ma = 7.95$, $Re = 3,333,333$, $T_\infty = 53.35K$, $\Psi = 20°$.

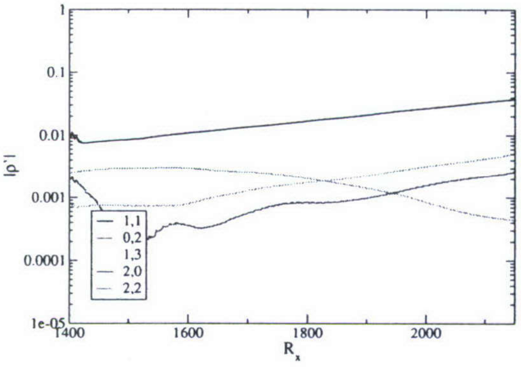

Figure 7.8: Oblique breakdown. ρ'-amplitude distribution. $Ma = 7.95$, $Re = 3,333,333$, $T_\infty = 53.35K$, $F = 4.9 \cdot 10^{-5}$, $A_{1,1} = 1\%$, $\Psi = 60°$.

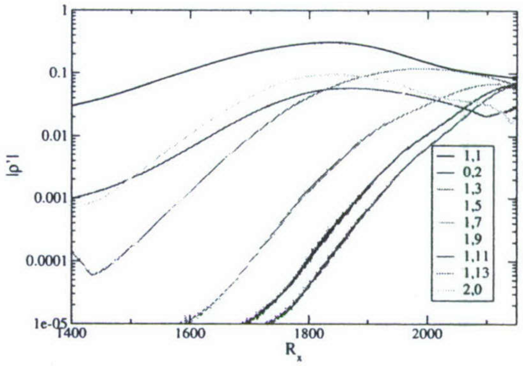

Figure 7.9: Oblique breakdown. ρ'-amplitude distribution. $Ma = 7.95$, $Re = 3,333,333$, $T_\infty = 53.35K$, $F = 1.17 \cdot 10^{-4}$, $A_{1,1} = 1\%$, $\Psi = 20°$.

7.2 Oblique Breakdown

Numerical simulations have shown that the oblique breakdown is a dominant mechanism at lower supersonic Mach numbers smaller than five (c.f. Fasel *et al.* (1993); Chang & Malik (1994); Husmeier *et al.* (2005)). However, for flow over cones at higher Mach numbers ($M \geq 6$), simulations show that second-mode two-dimensional waves are stronger amplified than first-mode oblique waves and the oblique breakdown of first-mode waves (see Figure 7.8) is therefore an unlikely breakdown scenario. On the other hand, according to LST, second-mode oblique waves at small wave angles are almost as strongly amplified as two-dimensional waves (see Figure 7.1). Therefore, the oblique breakdown of second-mode waves, as suggested by Pruett & Chang (1995), might also be a viable mechanism. In contrast to the simulations performed by Pruett & Chang (1995), the wave angle for the present DNS is reduced to $\Psi = 20°$ at the inflow which further reduces to $\Psi = 7°$ at the outflow because of the increasing spanwise extent of the computational domain, as graphed in the insert of Figure 7.1. This results in a higher amplification of instability waves than in the case of Pruett & Chang (1995). As seen from the amplitude distribution of ρ' in Figure 7.9

strongly amplified higher modes initiate the transition process towards the end of the computational domain. The flow structures in Figure 7.10 are different from the X-patterned structures observed at lower supersonic speeds (c.f Husmeier *et al.* (2005)). Instead, the structures show an off-set in azimuthal direction in correlation with the spanwise wave angle over the first half of the computational domain. Farther downstream, these regular flow patterns break up into smaller structures which align in two azimuthally confined areas associated with the large amplitude of the (0,2)-mode (see Figure 7.11). In addition, two-dimensional waves are nonlinearly generated and are highly amplified so that these two-dimensional waves reach comparable amplitude values than the primary oblique disturbance waves. Stetson & Kimmel (1993) observed in their experiments that breakdown to turbulence occurs downstream of the largest fluctuation of two-dimensional waves.

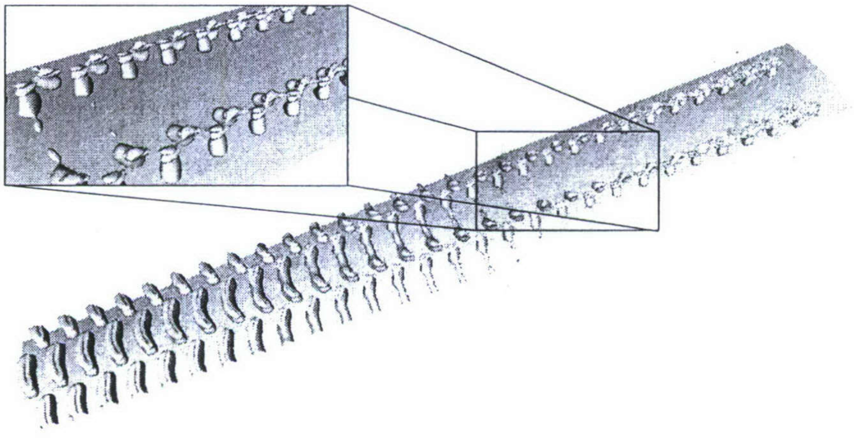

Figure 7.10: Oblique breakdown. Vortical structures identified by the Q-criterion (Q = 500). Ma = 7.95, Re = 3,333,333, $T_\infty = 53.35K$, $F = 1.17 \cdot 10^{-4}$, $A_{1,1} = 1\%$, $\Psi = 20°$.

As reported in section 7.1, disturbance waves at a 15% lower frequency than the dominant frequency in the Stetson experiments experience stronger amplitude growth. Looking at the ρ'-amplitude distribution in the downstream direction in Figure 7.12

confirms this enhanced instability behavior also for nonlinear interactions. As stated for the flat-plate simulations in section 5.6.1, emerging disturbances at the fundamental frequency but larger wave angles (e.g. mode (1,3), mode (1,5)) reach or even surpass amplitude levels of the primary disturbance wave (mode (1,1)). Emanating flow structures identified by the Q-criterion (Figure 7.13) show an agglomeration of vortical structures along the afore-mentioned 'streaks.' In Figure 7.14, flow structures at a higher value of $Q = 1,500$ are graphed. Within the merging of flow structures, a zig-zag pattern located close to the boundary-layer edge prevails. Although these connections of flow structures appear close to the boundary-layer edge, they leave an imprint on the wall heat flux as graphed in Figure 7.15a. Figure 7.15b plots the heat flux distribution close to the boundary-layer edge ($y = \delta$). Despite the highest magnitude in heat flux occurring close to the boundary-layer edge, its spatial extent is too confined in order to influence the overall heat flux significantly.

To get an estimate on how far the transition process is advanced, an oblique breakdown over the flat plate is re-visited with a high-resolution simulation. Due to the larger boundary-layer thickness and the absence of any additional source terms, the computational efforts are decreased by an order of magnitude—hence enabling the computation into the 'fully' turbulent regime. The length of the computational

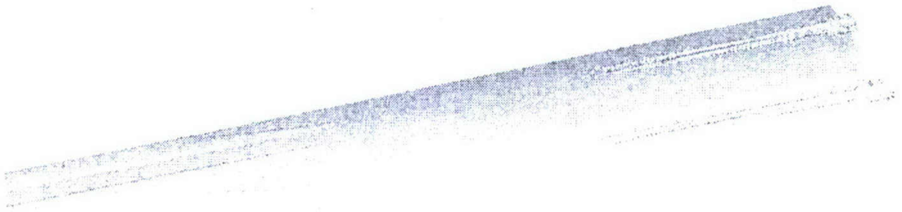

Figure 7.11: Oblique breakdown. Steady vortical structures identified by the Q-criterion (Q = 100). $Ma = 7.95$, $Re = 3,333,333$, $T_\infty = 53.35K$, $F = 1.17 \cdot 10^{-4}$, $A_{1,1} = 1\%$, $\Psi = 20°$.

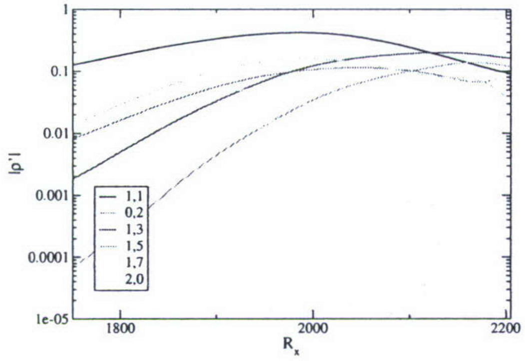

Figure 7.12: Oblique breakdown. ρ'-amplitude distribution. $Ma = 7.95$, $Re = 3,333,333$, $T_\infty = 53.35K$, $F = 9.8 \cdot 10^{-5}$, $A_{1,1} = 1\%$, $\Psi = 26°$.

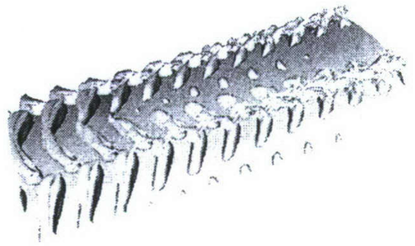

Figure 7.13: Oblique breakdown. Vortical structures identified by the Q-criterion (Q = 500). $Ma = 7.95$, $Re = 3,333,333$, $T_\infty = 53.35K$, $F = 9.8 \cdot 10^{-5}$, $A_{1,1} = 1\%$, $\Psi = 26°$.

domain in Figure 7.16 has been double compared to the conical investigations in order to observe breakdown. The emerging of disturbance waves at the fundamental frequency at higher wave angles, i.e. mode (1,3) and mode (1,5), resemble the stability behavior for the sharp cone. The zig-zag pattern of the flow structures followed by their merging are very similar to the behavior of the circular cone. Farther downstream, it is a striking feature that two-dimensional waves prevail close to the wall despite the chaotic flow structures close to the boundary-layer thickness (see Figure 7.17).

In the simulations for the sharp, the oblique breakdown shows signs of reaching the later stages of the transition process downstream of the largest two-dimensional amplitudes. Additionally, it is believed that the oblique breakdown over a cone will also fully break down as the flat plate. Thus the oblique breakdown of second-mode waves cannot be ruled out as a possible path to transition over circular cones at hypersonic speeds (even in the Stetson experiments). Because no random small-scale structures can be observed within the computational domain, breakdown to fully turbulent flow is still not achieved in this simulation. Hence, larger disturbance

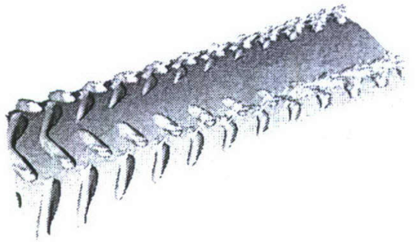

Figure 7.14: Oblique breakdown. Vortical structures identified by the Q-criterion (Q = 1,500). Ma = 7.95, Re = $3,333,333$, $T_\infty = 53.35K$, $F = 9.8 \cdot 10^{-5}$, $A_{1,1} = 1\%$, $\Psi = 26°$.

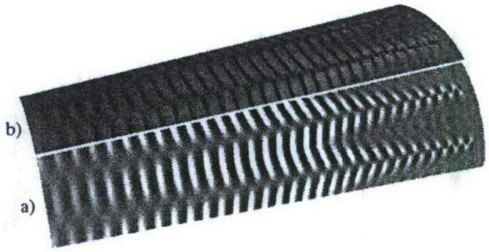

Figure 7.15: Oblique breakdown. Wall-normal heat flux. a) at the wall. b) at the boundary-layer edge. Ma = 7.95, Re = $3,333,333$, $T_\infty = 53.35K$, $F = 9.8 \cdot 10^{-5}$, $A_{1,1} = 1\%$, $\Psi = 26°$.

amplitudes are necessary for the flow to break down within the computational domain. For this, however, a significant increase in resolution is required resulting in a much larger computational grid than the currently afforded 381 million collocation points.

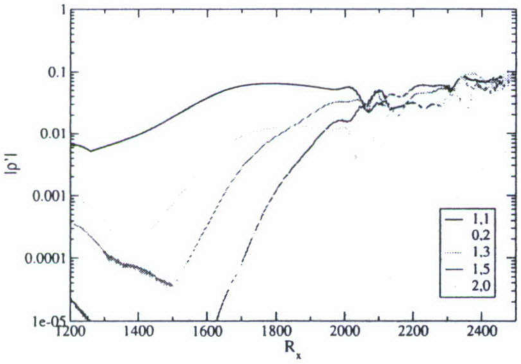

Figure 7.16: Oblique breakdown. Flat Plate. ρ'-amplitude distribution. Ma = 6.8, Re = $4,790,000$, $T_\infty = 71K$, $F = 8 \cdot 10^{-5}$, $A_{1,1} = 2\%$, $\Psi = 20°$.

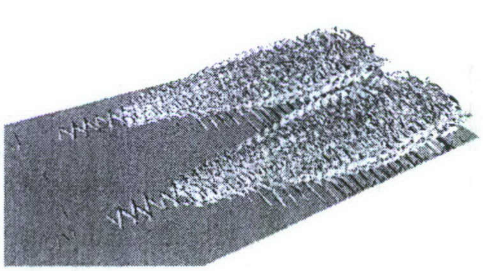

Figure 7.17: Oblique breakdown. Flat Plate. Vortical structures identified by the Q-criterion (Q = 500). Ma = 6.8, Re = $4,790,000$, $T_\infty = 71K$, $F = 8 \cdot 10^{-5}$, $A_{1,1} = 2\%$, $\Psi = 20°$.

7.3 Oblique Subharmonic Resonance

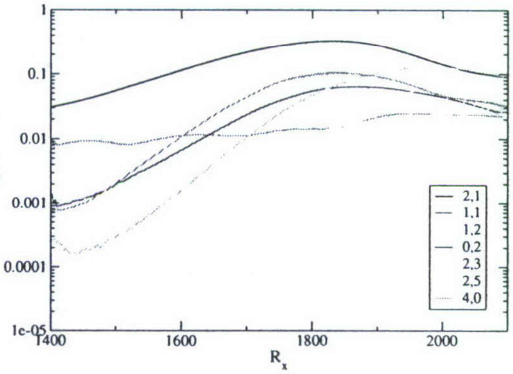

Figure 7.18: Oblique subharmonic resonance. ρ'-amplitude distribution. $Ma = 7.95$, $Re = 3,333,333$, $T_\infty = 53.35K$, $F_{2,1} = 1.17 \cdot 10^{-4}$, $A_{2,1} = 1\%$, $\Psi_{2,1} = 20°$, $F_{1,1} = 5.85 \cdot 10^{-5}$, $A_{1,1} = 1\%$, $\Psi_{1,1} = 36°$.

This mechanism has been investigated experimentally by Kosinov *et al.* (1994) for a flat-plate boundary layer at Mach 2. A wave triad is formed similar to the breakdown scenario described by Craik (1971). In order to fulfill the resonance condition for an oblique subharmonic resonance, the wave number of the secondary waves have to add up to the fundamental wave number. The same is true for the frequencies so that, combining both criteria, three waves at different wave angles Ψ must all travel at the same phase speed. Detailed numerical investigations by Zengl (2005) have shown that this type of breakdown works best when the fundamental and subharmonic waves are disturbed in the same spanwise mode with the same amplitude. The third wave closing the wave triad is then generated through nonlinear interactions. In our simulations, the amplitude distribution in Figure 7.18 shows that the nonlinearly generated modes are less amplified than for the oblique breakdown (see Figure 7.9). Although the primary waves amplitude reaches about twice the amplitude levels of the oblique breakdown (due to the difference in disturbance frequency), nonlinear interactions in Figure 7.18 are not as strong as for the oblique breakdown (c.f. Figure 7.9). Note, that developing higher modes which reach primary wave amplitude levels are associated with the oblique breakdown and not with the oblique subharmonic resonance. Therefore, the conclusion that can be drawn from this comparison is that the secondary waves might be responsible for preventing the strong amplifications of the higher modes for the oblique breakdown—hence reducing nonlinear interactions. Also looking at the phase speeds and streamwise wave numbers in Figure 7.19 reveals that the oblique subharmonic resonance is not a strong mechanism for the sharp cone. Although there is no wave which fulfills the resonance condition better than the nonlinearly generated wave to close the triad, i.e. mode (1,2), the resonance condition is still not met perfectly. Therefore, nonlinear interactions are weakened because the phase speeds only approach each other but do not lock onto each other. There are no other restrictions on the nonlinearly generated secondary wave except the spanwise resolution. Because the chosen resolution allows waves to emerge with a difference in wave angle of 1.5°, it is unlikely that a better combination for this primary wave exist—making the oblique subharmonic resonance an inferior mechanism for the sharp cone geometry. This statement stays valid even when steady streamwise vortices are perturbed. The selected modes in Figure 7.20 do not give rise to the assumption that the stability behavior of this resonance is altered by the presence of steady vortices (even when the disturbance frequency is optimized). Because of the underlying oblique breakdown, flow structures identified by the Q-criterion do not show any significant difference for this breakdown (Figure 7.21) in comparison with the oblique breakdown (Figure7.10). Investigations with larger nose radii will lead to different conclusions so that the oblique subharmonic resonance is not generally weakened for hypersonic boundary layer flows but only for the sharp cone geometry.

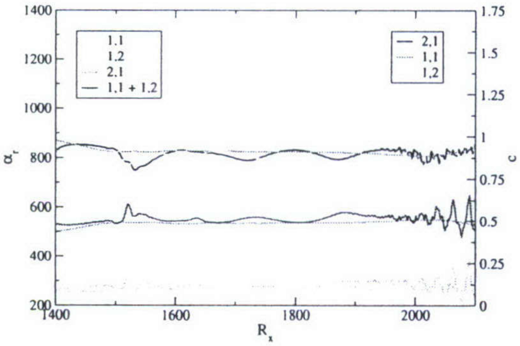

Figure 7.19: Oblique subharmonic resonance. Streamwise wave number and phase velocity. $Ma = 7.95$, $Re = 3,333,333$, $T_\infty = 53.35K$, $F_{2,1} = 1.17 \cdot 10^{-4}$, $A_{2,1} = 1\%$, $\Psi_{2,1} = 20°$, $F_{1,1} = 5.85 \cdot 10^{-5}$, $A_{1,1} = 1\%$, $\Psi_{1,1} = 36°$.

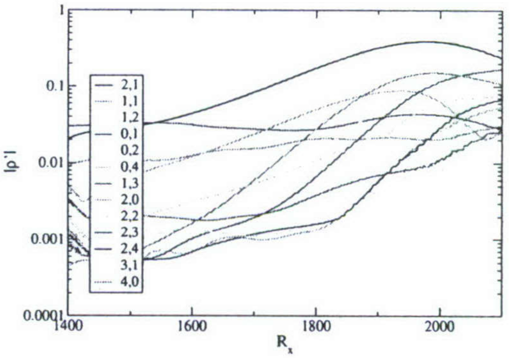

Figure 7.20: Oblique subharmonic resonance. ρ'-amplitude distribution. $Ma = 7.95$, $Re = 3,333,333$, $T_\infty = 53.35K$, $F_{2,1} = 9.8 \cdot 10^{-5}$, $A_{2,1} = 1\%$, $\Psi_{2,1} = 20°$, $F_{1,1} = 4.9 \cdot 10^{-5}$, $A_{1,1} = 1\%$, $A_{0,1} = 1\%$, $\Psi_{1,1} = 36°$.

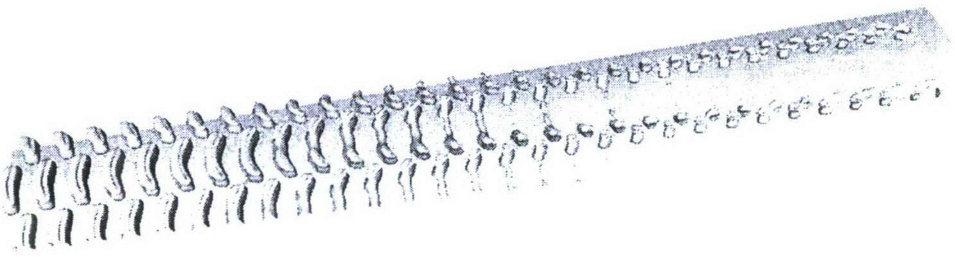

Figure 7.21: Oblique subharmonic resonance. Vortical structures identified by the Q-criterion (Q = 500). $Ma = 7.95$, $Re = 3,333,333$, $T_\infty = 53.35K$, $F_{2,1} = 9.8 \cdot 10^{-5}$, $A_{2,1} = 1\%$, $\Psi_{2,1} = 20°$, $F_{1,1} = 4.9 \cdot 10^{-5}$, $A_{1,1} = 1\%$, $A_{0,1} = 1\%$, $\Psi_{1,1} = 36°$.

7.4 Oblique Fundamental Resonance

Instead of a resonance triad as in the oblique subharmonic breakdown, two waves at the same frequency but traveling at different wave angles Ψ are perturbed. In our simulations, the primary waves are disturbed at $\Psi_{1,1} = 20°$ while the secondary waves, i.e. the (1,2)-mode, travel at a higher wave wangle of $\Psi_{1,2} = 36°$.

When the secondary waves are disturbed at a small amplitude level, the influence of the steady vortex on the second-mode two-dimensional can be observed. Figure 7.22 shows that with increasing amplitude of the secondary waves, the nonlinearly generated steady vortex (0,1) is increasingly more amplified. As a consequence of the higher amplification of this steady mode, the second-mode two-dimensional wave becomes more unstable between $R_x = 1500$ and $R_x = 1800$. Thus, breakdown mechanisms involving steady vortices and their impact on the two-dimensional waves are investigated in the following section.

Once the secondary waves are perturbed with the same amplitude as the primary waves, strong nonlinear interactions occur resulting in the amplification of higher modes. Through first-level wave interactions the (0,1)-mode is generated closing a "triad". One can argue if it is a resonance triad since the steady vortex mode does not possess any phase speed and therefore the phase speeds of the three involving

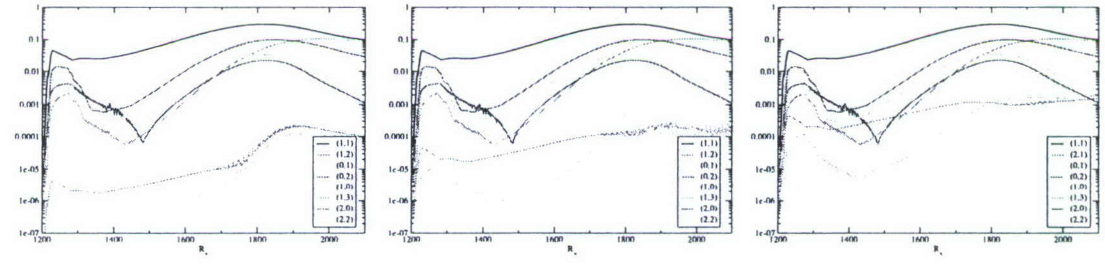

(a) $A_{1,2} = 0.0001\%$. (b) $A_{1,2} = 0.001\%$. (c) $A_{1,2} = 0.01\%$.

Figure 7.22: Oblique fundamental resonance. ρ'-amplitude distribution. $Ma = 7.95$, $Re = 3,333,333$, $T_\infty = 53.35K$, $F = 1.17 \cdot 10^{-4}$, $A_{1,1} = 1\%$, $\Psi_{1,1} = 20°$, $\Psi_{1,2} = 36°$.

waves cannot match. Nonetheless, the forcing of this steady vortex mode influences the stability behavior significantly as graphed in Figure 7.23. The reason for this very good performance lies in the phase speed. Figure 7.24 reveals that the resonance condition is exactly fulfilled throughout the computational domain. It should be mentioned that the oblique subharmonic resonance without forcing of the steady streamwise vortex mode is still a viable breakdown mechanism, but it is the presence of the steady vortices which makes the oblique fundamental resonance a stronger mechanism than the oblique breakdown for the sharp cone.

Evolving flow structures, graphed in Figure 7.25, reveal commonalities and differences to previously discussed cases. A main difference is the distortion of flow structures along the centerline of the computational domain. The steady streamwise vortex mode seems to be responsible for this behavior although it could not have been observed for the oblique subharmonic resonance with a forced steady vortex mode. Additionally, vortex structures travel farther downstream along the centerline so that not all structures are confined in two regions towards the end of the computational domain as seen e.g. for the oblique breakdown. Nonetheless, this splitting of flow structures in two confined regions towards the end of the computational domain is a general characteristic of the breakdown mechanisms involving three-dimensional primary waves. Also, transition occurs within both of these areas—the structures along the centerline seem to be more stable. The detailed view (insert in Figure 7.25) shows rapid development of small-scale structures. Although the spanwise resolution is increased to 129 modes resulting in over 473 million collocation points, a higher resolution is necessary in order ro resolve all emerging structures. Despite the enormous computational power available through the National Leadership Computer Systems ($NLCS$) initiative this simulation pushes the limits of the SGI Altix 4700 system with 2048 CPUs—the simulation ran 3 months on 600 CPUs continually. Hence, this case will hopefully re-visited at a later point in time when even bigger computer systems become available.

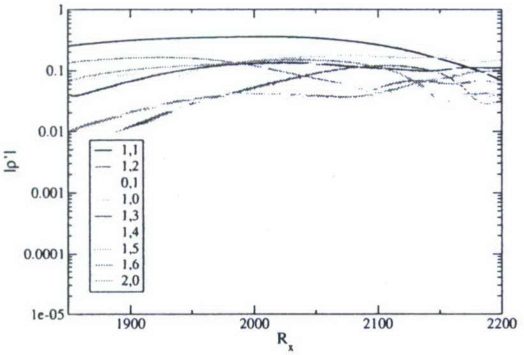

Figure 7.23: Oblique fundamental resonance. ρ'-amplitude distribution. $Ma = 7.95$, $Re = 3,333,333$, $T_\infty = 53.35K$, $F_{1,1} = 9.8 \cdot 10^{-5}$, $A_{1,1} = 1\%$, $A_{1,2} = 1\%$, $A_{0,1} = 1\%$, $\Psi_{1,1} = 20°$, $\Psi_{1,2} = 36°$.

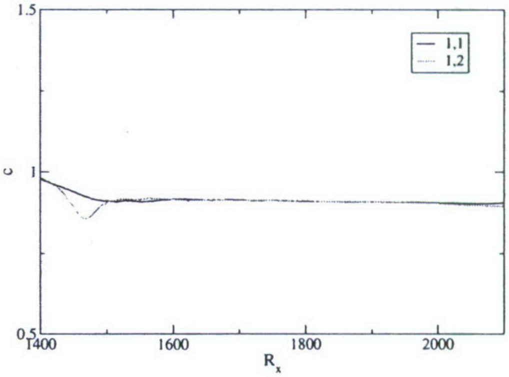

Figure 7.24: Oblique fundamental resonance. Phase speed. $Ma = 7.95$, $Re = 3,333,333$, $T_\infty = 53.35K$, $F_{1,1} = 9.8 \cdot 10^{-5}$, $A_{1,1} = 1\%$, $A_{1,2} = 1\%$, $A_{0,1} = 1\%$, $\Psi_{1,1} = 20°$, $\Psi_{1,2} = 36°$.

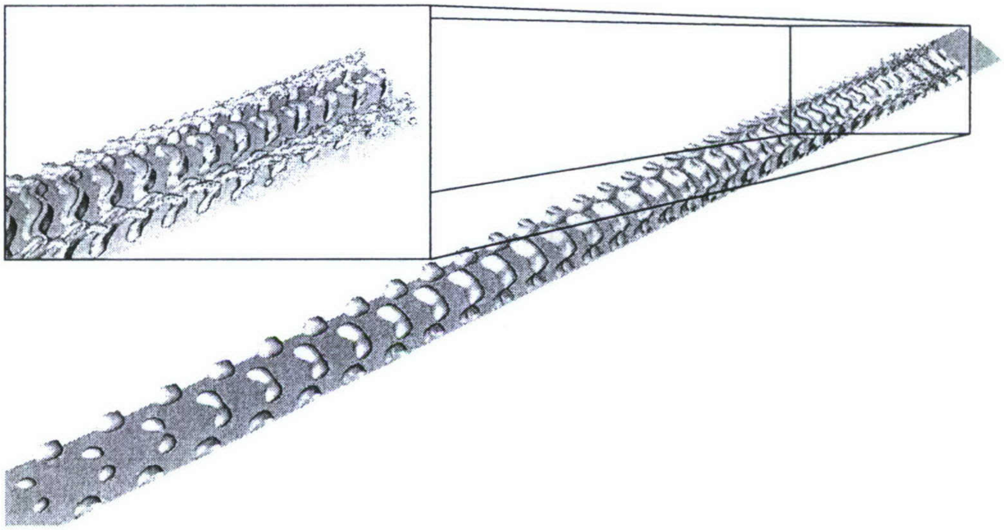

Figure 7.25: Oblique fundamental resonance. Vortical structures identified by the Q-criterion (Q = 500). $Ma = 7.95$, $Re = 3,333,333$, $T_\infty = 53.35K$, $F_{1,1} = 9.8 \cdot 10^{-5}$, $A_{1,1} = 1\%$, $A_{1,2} = 1\%$, $A_{0,1} = 1\%$, $\Psi_{1,1} = 20°$, $\Psi_{1,2} = 36°$.

7.5 Breakdown Mechanisms involving steady vortices

To further investigate the influence of the steady vortex mode on the second-mode two-dimensional wave, we performed simulations at two different wave angles—$\Psi = 20°$ and $\Psi = 60°$. For $\Psi = 20°$, Figure 7.26 shows that the strength of the nonlinear interactions are dependent on the disturbance amplitude of the steady mode. But even for the high amplitude of $A_{0,1} = 1\%$, the two-dimensional primary wave is unaffected by the presence of the steady vortex mode. This result contradicts the findings in the the previous section where the generated (0,1)-mode has an angle of $\Psi = 20°$ and did have an influence of the generated two-dimensional wave. At this point it is hypothesized that the discrepancies arise from the fact that both waves are nonlinearly generated and not specifically disturbed (as in this section).

For $\Psi = 60°$, the steady vortex (0,1) and the oblique fundamental waves (1,1) indicate a possible fundamental resonance with the second-mode primary waves (1,0) around $R_x = 1,900$ (see Figure 7.27). Because this disturbance set-up simulates the experimental disturbance method used by Klebanoff *et al.* (1962), the fundamental (K-type) breakdown mechanism may be a possible participant in the transition process.

The presence of steady oblique vortex modes increase the amplitude level of first-mode waves even more than for second-mode waves—thus further enhancing nonlinear interactions. This in turn accelerates the transition process through stronger amplification of higher modes. Nonetheless, the resonance mechanisms, if present, are not strongly affected by the steady vortices. Hence, increasing the threshold of the disturbance wave amplitudes may results in a similar effect as the presence of steady vortices.

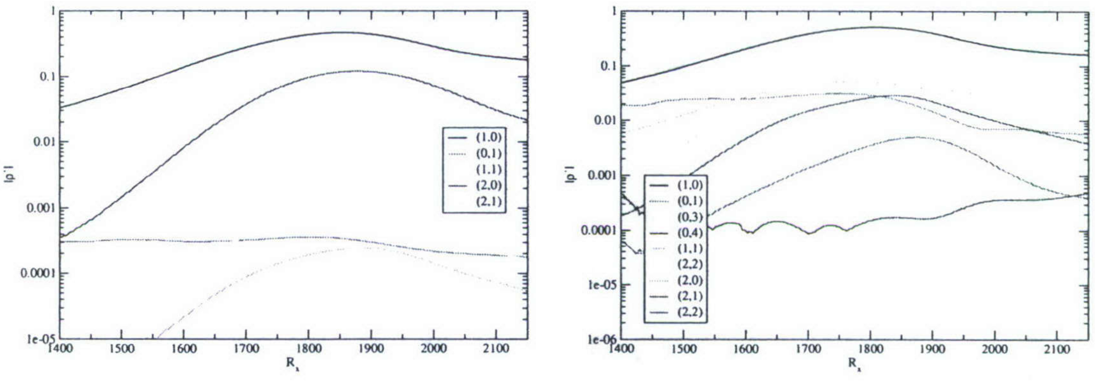

(a) $A_{0,1} = 0.001\%$.

(b) $A_{0,1} = 1\%$.

Figure 7.26: Steady vortex mode. ρ'-amplitude distribution. $Ma = 7.95$, $Re = 3,333,333$, $T_\infty = 53.35K$, $F = 1.17 \cdot 10^{-4}$, $A_{1,0} = 1\%$, $\Psi_{0,1} = 20°$.

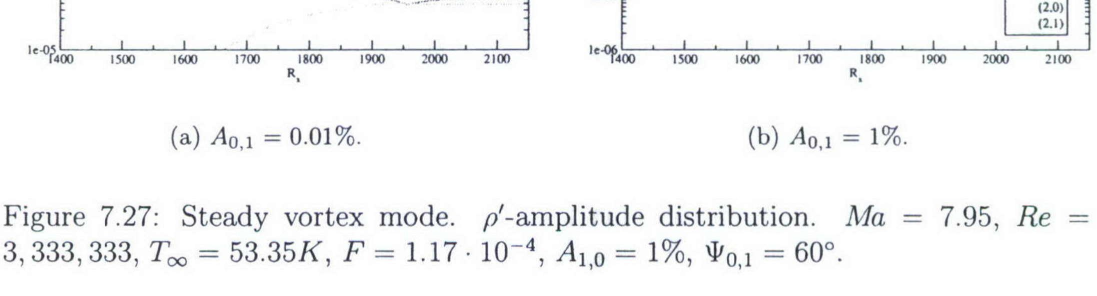

(a) $A_{0,1} = 0.01\%$.

(b) $A_{0,1} = 1\%$.

Figure 7.27: Steady vortex mode. ρ'-amplitude distribution. $Ma = 7.95$, $Re = 3,333,333$, $T_\infty = 53.35K$, $F = 1.17 \cdot 10^{-4}$, $A_{1,0} = 1\%$, $\Psi_{0,1} = 60°$.

7.6 Fundamental Breakdown (K-type)

Based on the knowledge gained in the previous section, the fundamental resonance between a primary two-dimensional wave and a small amplitude oblique wave might play a role in the transition process of hypersonic boundary layers over circular cones. Figure 7.28 shows a departure in the amplitude growth of the secondary waves (mode (1,1)) from linear behavior beginning at $R_x = 2,000$. Because this location is close to the outflow and the resonance is weak, amplification of higher modes is marginal in the present investigations. If, additionally, a steady vortex mode (0,1) is disturbed at a large amplitude, the secondary wave amplitude and amplification is augmented and nonlinear interactions are enhanced (see Figure 7.29). Although the phase speed of the primary and secondary waves in Figure 7.30a agree well throughout the domain, the resonance with and without a perturbed steady vortex mode is weak. But forcing of a steady streamwise vortex mode enhances the resonance itself since the phase speeds at the location of the resonance ($R_x = 2,000$) match exactly (Figure 7.30b), while without a forced steady streamwise vortex the phase speeds diverge at the

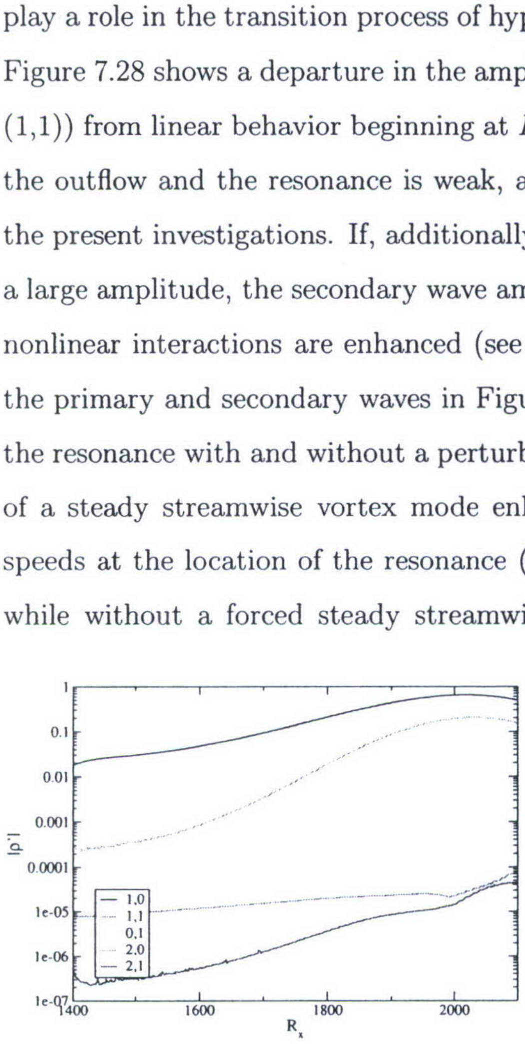

Figure 7.28: Fundamental breakdown. ρ'-amplitude distribution. $Ma = 7.95$, $Re = 3,333,333$, $T_\infty = 53.35K$, $F = 9.8 \cdot 10^{-5}$, $A_{1,0} = 1\%$, $A_{1,1} = 0.001\%$,$\Psi_{1,1} = 60°$.

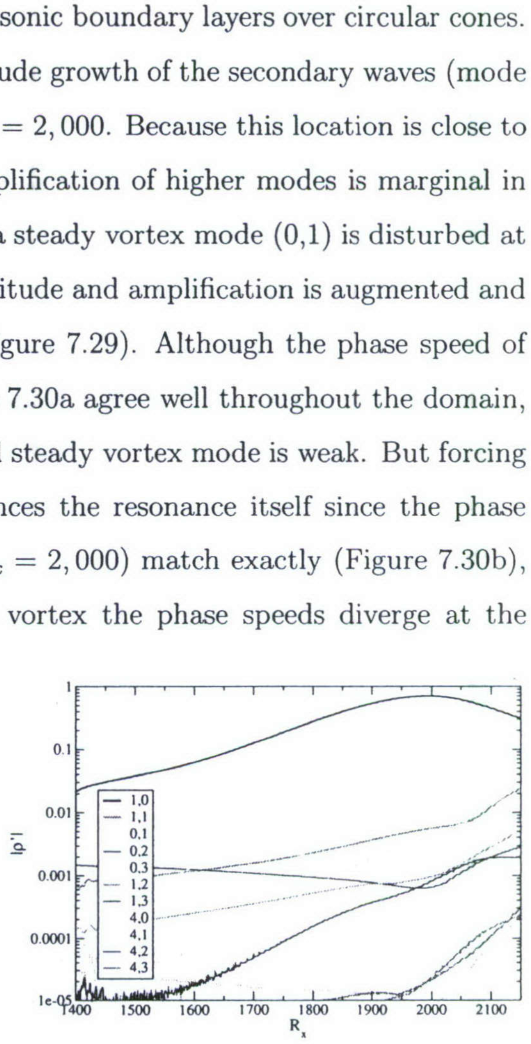

Figure 7.29: Fundamental breakdown. ρ'-amplitude distribution. $Ma = 7.95$, $Re = 3,333,333$, $T_\infty = 53.35K$, $F = 9.8 \cdot 10^{-5}$, $A_{1,0} = 1\%$, $A_{1,1} = 0.001\%$, $A_{0,1} = 1\%$, $\Psi_{1,1} = 60°$.

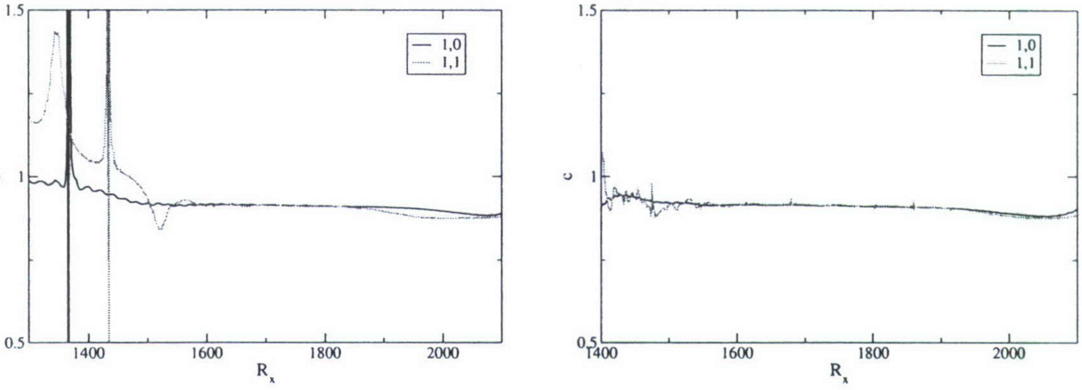

(a) $A_{0,1} = 0\%$

(b) $A_{0,1} = 1\%$

Figure 7.30: Fundamental breakdown. Phase speed. $Ma = 7.95$, $Re = 3,333,333$, $T_\infty = 53.35K$, $F = 9.8 \cdot 10^{-5}$, $A_{1,0} = 1\%$, $A_{1,1} = 0.001\%$, $\Psi_{1,1} = 60°$.

resonance location to approach each other again downstream of $R_x = 2,000$ (Figure 7.30a). Despite the positive effect of the steady vortex mode on the secondary oblique waves, the steady vortex mode does not significantly alter the amplification rate of the two-dimensional primary waves.

As mentioned in the introduction (c.f. section 1.3.1), a phase shift of π in the wall-normal phase distribution for the pressure indicates a second-mode wave. Figure 7.31 graphs the wall-normal phase distribution of the pressure eigenfunction for two different downstream locations with and without the forcing of a steady streamwise vortex mode. It is apparent that upstream of the location of the resonance the secondary waves are of a first-mode character independent if a steady vortex mode is forced or not. Downstream of the resonance location, the secondary wave transforms into a second-mode wave. Therefore, second-mode secondary waves are investigated to see if they result in a stronger resonance. But, in Figure 7.32 amplitude levels of the secondary waves decrease downstream of $R_x = 2,000$ so that second-mode secondary waves seem to have no important role in the transition process.

Because not only is the equality of phase speeds important but also the rela-

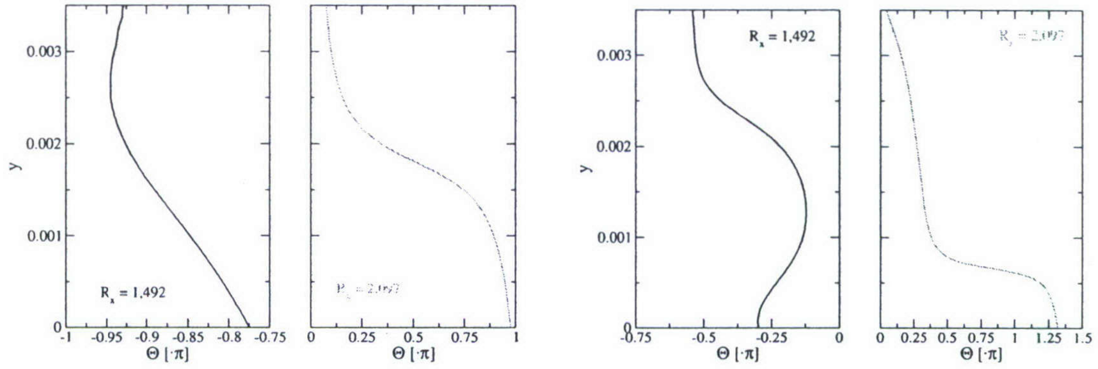

(a) $A_{0,1} = 0\%$

(b) $A_{0,1} = 1\%$

Figure 7.31: Fundamental breakdown. Wall-normal phase distribution. $Ma = 7.95$, $Re = 3,333,333$, $T_\infty = 53.35K$, $F = 9.8 \cdot 10^{-5}$, $A_{1,0} = 1\%$, $A_{1,1} = 0.001\%$, $\Psi_{1,1} = 60°$.

tive phase between disturbance waves, the forcing signal of the secondary waves has been adjusted. To assure that the generated disturbance waves travel in phase with each other, a phase shift of $\Delta\phi = 1.93511$ has been introduced. Amplification of the secondary waves is stronger upstream of the resonance location in Figure 7.33 when compared with Figure 7.28. Therefore, more energy is transferred to the secondary waves when they are synchronized with the primary waves. Unfortunately, the resonance is not enhanced so that the fundamental breakdown is still an inferior mechanism to breakdown scenarios involving second-mode three-dimensional waves.

Instead of disturbing with the phase difference, increasing the disturbance amplitude of the primary waves to 5% has shown a more promising result. The maximum primary wave amplitude reaches about 40% of the corresponding free-stream value. Because primary amplitude levels impact the resonance behavior, the resonance location moved upstream to $R_x = 1,800$ and the nonlinear amplification thereafter is significantly enhanced (Figure 7.34). Figure 7.35 shows the 'classical' steps to transition as described in section 1.2. The increasingly three-dimensional variation of the two-dimensional rollers in downstream direction results in λ-vortices which are then

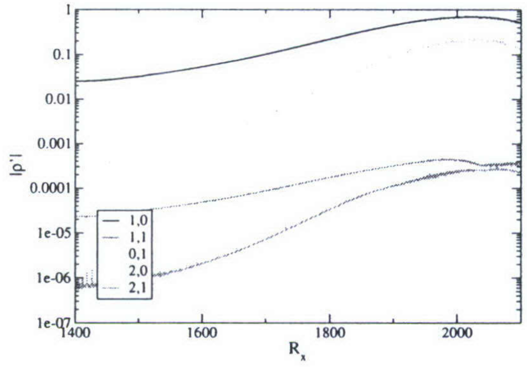

Figure 7.32: Fundamental breakdown. ρ'-amplitude distribution. $Ma = 7.95$, $Re = 3,333,333$, $T_\infty = 53.35K$, $F = 9.8 \cdot 10^{-5}$, $A_{1,0} = 1\%$, $A_{1,1} = 0.001\%$, $\Psi_{1,1} = 20°$.

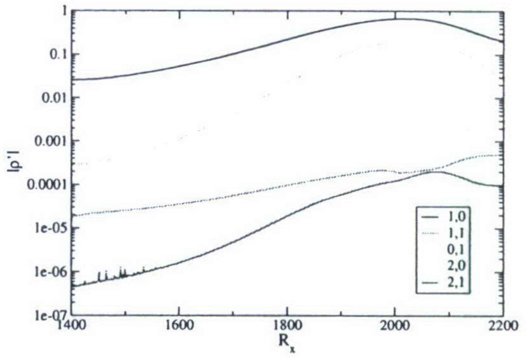

Figure 7.33: Fundamental breakdown. ρ'-amplitude distribution. $Ma = 7.95$, $Re = 3,333,333$, $T_\infty = 53.35K$, $F = 9.8 \cdot 10^{-5}$, $A_{1,0} = 1\%$, $A_{1,1} = 0.001\%$, $\Psi_{1,1} = 60°$, $\Delta\phi = 1.93511$.

stretched by the different amplification rates of the peak and valley stations. Based on these findings it is concluded that the compressible fundamental breakdown incorporates the same physical mechanisms as the incompressible counterpart. Hence, the massively stabilizing effect of compressibility, which can be mainly attributed to the high wall temperature, causes no change in flow physics but calls for a very high disturbance energy input.

Temporal Direct Numerical Simulations ($TDNS$) are performed to confirm the possibility of a fundamental resonance. To this end, base-flow profiles from a spatial simulation at $R_x = 2,000$ are chosen for the base flow of the $TDNS$. Figure 7.36 shows the amplitude development over time for the secondary waves (mode (1,1)). After $t = 8.0$, amplification higher than exponential growth can be observed proofing the possibility of a fundamental resonance. The base-flow profile in Figure 7.37 at $t = 8.0$ incorporates a steeper wall-normal gradient than the initial base-flow profile causing the strong amplification. This change of the base-flow profile can be linked to the arising steady streamwise vortex mode (0,1). The amplitude decrease after $t = 14.1$, can be attributed to the temporal base-flow treatment. Although the

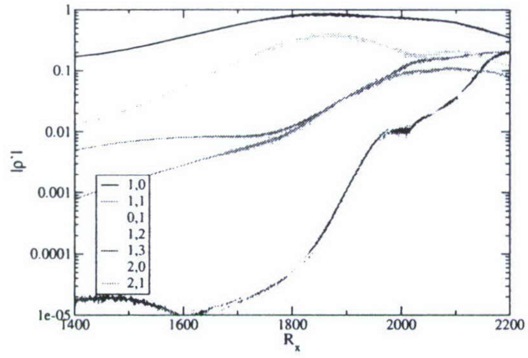

Figure 7.34: Fundamental breakdown. ρ'-amplitude distribution. $Ma = 7.95$, $Re = 3,333,333$, $T_\infty = 53.35K$, $F = 9.8 \cdot 10^{-5}$, $A_{1,0} = 5\%$, $A_{1,1} = 0.001\%$, $A_{0,1} = 1\%$, $\Psi_{1,1} = 60°$.

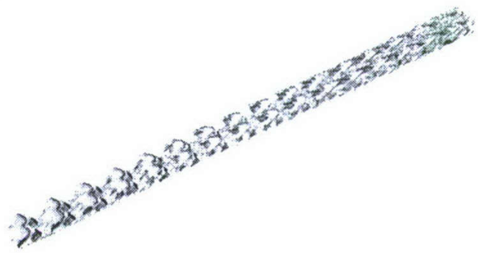

Figure 7.35: Fundamental breakdown. Vortical structures identified by the Q-criterion (Q = 500). $Ma = 7.95$, $Re = 3,333,333$, $T_\infty = 53.35K$, $F = 9.8 \cdot 10^{-5}$, $A_{1,0} = 1\%$, $A_{1,1} = 0.001\%$, $\Psi_{1,1} = 60°$.

growing steady streamwise vortex mode (0,1) further changes the base-flow profiles, the upward movement of the boundary-layer edge is unphysical and therefore the stabilization can be linked to be an artifact of the temporal approach.

Thus, although second-mode two-dimensional waves are most strongly amplified and the possibility of a fundamental resonance exists, the significance of the funda-

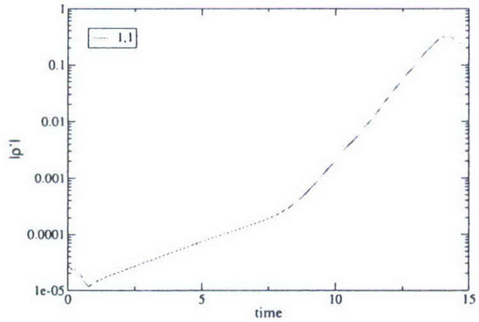

Figure 7.36: Fundamental breakdown. Temporal DNS. ρ'-amplitude development in time. $Ma = 7.95$, $Re = 3,333,333$, $T_\infty = 53.35K$, $F = 9.8 \cdot 10^{-5}$, $A_{1,0} = 1\%$, $A_{1,1} = 0.001\%$, $\Psi_{1,1} = 60°$.

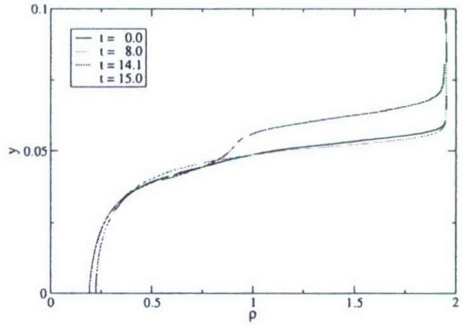

Figure 7.37: Fundamental breakdown. Temporal DNS. ρ'-base-flow profiles at different times. $Ma = 7.95$, $Re = 3,333,333$, $T_\infty = 53.35K$, $F = 9.8 \cdot 10^{-5}$, $A_{1,0} = 1\%$, $A_{1,1} = 0.001\%$, $\Psi_{1,1} = 60°$.

mental breakdown in the nonlinear stages of the transition process is less pronounced. Nonetheless, in an environment with strong steady vortices (e.g. isolated roughness) or under conditions where large two-dimensional amplitude levels could be reached (e.g. cooled walls), the fundamental breakdown (K-type) might become an important breakdown mechanism.

7.7 Subharmonic Breakdown (N-/H-type)

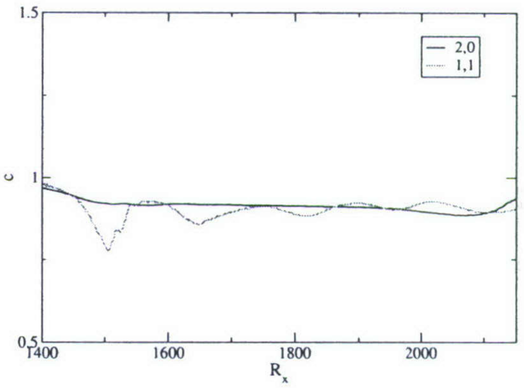

Figure 7.38: Subharmonic breakdown. Phase speed. $Ma = 7.95$, $Re = 3,333,333$, $T_\infty = 53.35K$, $F = 9.8 \cdot 10^{-5}$, $A_{2,0} = 1\%$, $A_{1,1} = 0.001\%, \Psi_{1,1} = 60°$.

In their temporal DNS over sharp circular cones under conditions of the Stetson experiments, Pruett & Zang (1992) claimed to have found a subharmonic resonance of second-mode primary waves with oblique secondary waves. Stetson & Kimmel (1993) revisited their experimental data and were unable to confirm the existence of a subharmonic breakdown. Performed *DNS* only show a very small departure from the linear eigenbehavior of the secondary wave downstream of $R_x = 1,900$ concluding that a subharmonic resonance is possible but so weak that it is practically untraceable in the (noisy) experiments. Figure 7.38 plots the phase speed for the subharmonic breakdown and in comparison with the fundamental breakdown (c.f. Figure 7.30), the phase speeds are farther apart making the subharmonic breakdown a weaker mechanism than the fundamental breakdown. Therefore it is questionable if the subharmonic breakdown may play a role in the transition process for conical geometries.

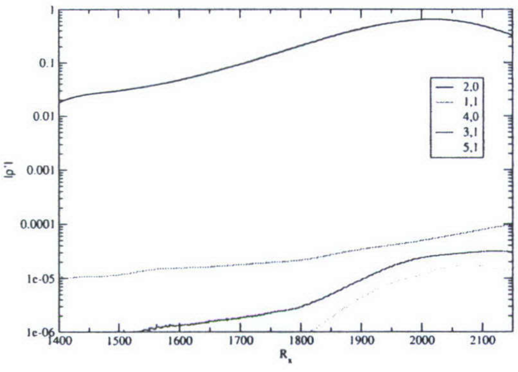

Figure 7.39: Subharmonic breakdown. ρ'-amplitude distribution. $Ma = 7.95$, $Re = 3,333,333$, $T_\infty = 53.35K$, $F = 9.8 \cdot 10^{-5}$, $A_{2,0} = 1\%$, $A_{1,1} = 0.001\%, \Psi_{1,1} = 60°$.

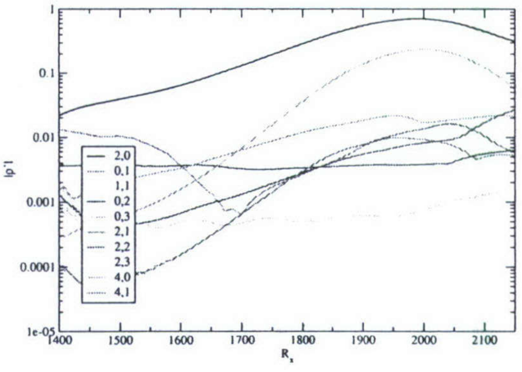

Figure 7.40: Subharmonic breakdown. ρ'-amplitude distribution. $Ma = 7.95$, $Re = 3,333,333$, $T_\infty = 53.35K$, $F = 9.8 \cdot 10^{-5}$, $A_{2,0} = 1\%$, $A_{1,1} = 0.001\%$, $A_{0,1} = 1\%$, $\Psi_{1,1} = 60°$.

More importantly, if the steady vortex mode (0,1) is forced in addition to the primary (2,0) and the secondary waves (1,1), nonlinear interactions are more pronounced (Figure 7.40). This leads to the conclusion that in the presence of large amplitude steady vortices, oblique waves (first-mode waves upstream of the resonance location) play a crucial role in hypersonic breakdown scenarios. The forcing of mode (0,1) also affects the subharmonic resonance. Nonlinear amplitude growth of the secondary wave increases downstream of the resonance location but stays below significant values. The reason for the better performance of the subharmonic resonance when a steady streamwise vortex mode is additionally forced might not be due to a better matching of phase speeds (see Figure 7.42) as observed for the

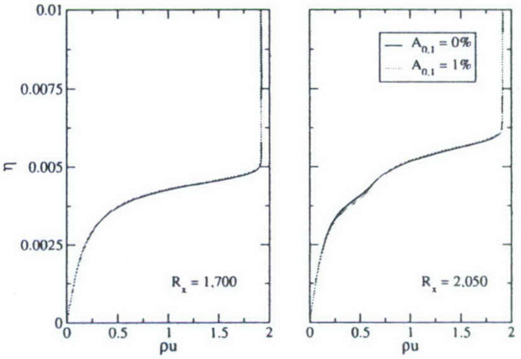

Figure 7.41: Comparison of mean-flow profiles with and without steady vortex mode. $Ma = 7.95$, $Re = 3,333,333$, $T_\infty = 53.35K$, $F = 1.17 \cdot 10^{-4}$.

fundamental breakdown (c.f. section 7.6). Because the steady vortex mode worsen the quality of the signal so that the phase speeds become unusable, the phase speeds are not conclusive for this case. Instead, the change in mean-flow profiles (Figure 7.41) might be responsible for the higher amplification of the subharmonic secondary waves. The deviation in the base-flow profiles around $y = 0.004$ with and without a steady vortex mode forced is likely linked to the emerging of stronger amplified higher modes. Because Figure 7.40 also indicates the presence of a fundamental resonance between the (2,0)- and the (2,1)-mode which occurs at higher amplitude levels than the subharmonic resonance, the change in base-flow profiles might be caused by this fundamental resonance. Thus, the fundamental breakdown might enhance the subharmonic breakdown, although the amplitude level of the secondary waves with fundamental frequency (2,1) decrease downstream of the resonance location ($R_x = 2,000$). Even with the better performance when a steady streamwise vortex mode is forced the subharmonic resonance is still an unlikely candidate for conical boundary-layer transition at hypersonic speeds.

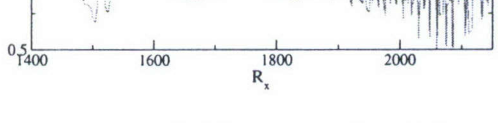

Figure 7.42: Subharmonic breakdown. Phase speed. $Ma = 7.95$, $Re = 3,333,333$, $T_\infty = 53.35K$, $F = 9.8 \cdot 10^{-5}$, $A_{2,0} = 1\%$, $A_{1,1} = 0.001\%$, $A_{0,1} = 1\%$, $\Psi_{1,1} = 60°$.

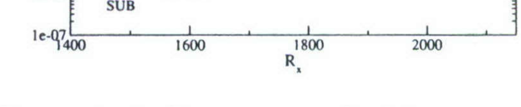

Figure 7.43: Comparison of subharmonic breakdown with fundamental breakdown. ρ'-amplitude distribution. $Ma = 7.95$, $Re = 3,333,333$, $T_\infty = 53.35K$, $F = 9.8 \cdot 10^{-5}$, $A_{primary} = 1\%$, $A_{secondary} = 0.001\%, \Psi_{secondary} = 60°$.

For a direct comparison of the fundamental and subharmonic resonance, the fundamental breakdown (from the previous section) and the subharmonic breakdown, both with a forced steady streamwise vortex mode, are plotted in the same graph (Figure 7.43). In Figure 7.43, the nonlinearly generated fundamental secondary wave (2,1) is higher amplified than the specifically disturbed wave from the fundamental breakdown. This stronger amplification can be explained by the fact that the secondary waves (2,1) are in phase with the primary waves (2,0). This is not the case, when the secondary wave is explicitly forced without specifying a phase shift (c.f. section 7.6). But towards the end of the computational domain amplitude levels of both fundamental secondary waves reach similar values.

If the subharmonic secondary waves (mode (1,1)) are disturbed in phase with the primary waves, the instability of the secondary waves is increased until the subharmonic waves are damped downstream of the resonance location. As for the fundamental breakdown, the weak resonance is not stronger amplified by the phase shift in the disturbance signal.

Temporal DNS confirm the very weak resonance behavior of a subharmonic breakdown in Figure 7.44 which shows the secondary-wave amplitude distribution over time. Doubling the disturbance frequency (specifying half the streamwise wavelength) result in amplitude levels of the secondary wave which are comparable with the primary wave amplitudes. The linear behavior in the logarithmic plot (Figure 7.45) shows that the high amplitude levels are reached by exponential growth, i.e. the eigenbehavior of the wave and thus no subharmonic resonance is present. This leads to the conclusion that the subharmonic breakdown (N-/H-type) is even less important than the fundamental breakdown (K-type).

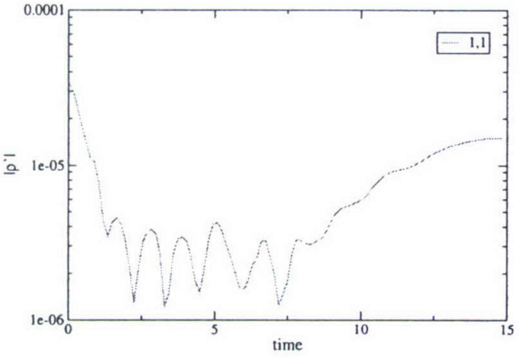

Figure 7.44: Subharmonic breakdown. Temporal DNS. ρ'-amplitude development in time. $Ma = 7.95$, $Re = 3,333,333$, $T_\infty = 53.35K$, $F = 9.8 \cdot 10^{-5}$, $A_{2,0} = 1\%$, $A_{1,1} = 0.001\%$, $\Psi_{1,1} = 60°$.

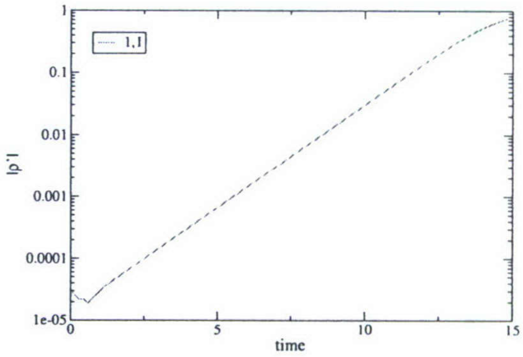

Figure 7.45: Subharmonic breakdown. ρ'-amplitude distribution. ρ'-amplitude development in time. $Ma = 7.95$, $Re = 3,333,333$, $T_\infty = 53.35K$, $F = 1.96 \cdot 10^{-4}$, $A_{2,0} = 1\%$, $A_{1,1} = 0.001\%, \Psi_{1,1} = 60°$.

7.8 Summary

Second-mode waves are essential for hypersonic boundary layer transition for the sharp cone. Thus low-frequency waves and/or waves with large wave angles do not contribute to the general stability behavior. Although Stetson *et al.* (1983) stated that first-mode waves become increasingly important for the later stages of breakdown, first-mode waves in the simulations are only generated through nonlinear interactions late in the transition process and always stay far below primary amplitude disturbance levels. Therefore, three-dimensional and two-dimensional second-mode waves control boundary layer transition for this configuration. Simulations with a pulsed disturbance reveal that a lower frequency as reported in the experimental findings by Stetson *et al.* (1983) experience an overall stronger amplification. The oblique breakdown of second-mode waves at a small wave angle is a strong mechanism under investigation. For this breakdown, steady streamwise vortices and two-dimensional waves typically rise up to primary disturbance levels. Transition is initiated downstream of the maximal amplitude levels as Stetson *et al.* (1983) has observed it in their experiments. Because Stetson *et al.* (1983) did not perform any three-dimensional measurements and the wave angle in the simulation drops below $\Psi = 10°$, it might be possible that an oblique breakdown is present in the experiments.

When a steady streamwise vortex mode is disturbed at high amplitude, nonlinear interactions are generally enhanced. The oblique fundamental resonance experiences the largest improvement making this type of breakdown the strongest mechanism for high-speed boundary layers over sharp circular cones.

Although a fundamental resonance of a second-mode two-dimensional wave with an oblique first-mode wave is possible, this resonance is too weak to play an important role for the sharp circular cone. The subharmonic breakdown performs even worse. Further fine-tuning of the mechanisms involving two-dimensional primary waves (e.g. wave angle, phase shift, etc.) does not result in a significant stability change. Therefore, the fundamental and subharmonic breakdown are inferior mechanisms for "cold“ wind-tunnel conditions. But they might become important when steady streamwise vortices or cooled walls are present.

8. Transition Investigations of a Boundary Layer on a Blunt Cone ($R_N = 0.15$")

The nose radius is chosen according to the experiments by Stetson *et al.* (1984). The nose radius of $R_N = 0.15$", which is a 100 times larger than the sharp cone radius, is the smallest radius under consideration for the investigation of the effects of nose bluntness. Resulting after-shock conditions are summarized in Table 8.1. Base-flow profiles of different quantities are plotted in Figure 8.1 for three downstream locations in comparison with profiles for the sharp cone. The profiles for the blunt cone approach the profiles for the sharp in downstream direction so that the influence of the nose radius mainly affects the front section of the cone. Maxima in Figure 8.2 determine the location of the generalized inflection point which also approaches the location for the sharp cone in the downstream direction. Although the generalized inflection point is a main criterion in determining second-mode instability, the stability behavior of the blunt cone does not recover to the sharp cone behavior as discussed in the following section. Stetson *et al.* (1984) claim the entropy layer responsible for this change in stability behavior. The entropy layer results from a detached shock wave for blunt geometries. While over a small region in the vicinity of the nose tip a normal shock with high entropy generation exist, there is an oblique shock wave away from the nose section with a weaker entropy generation. This results in a layer of higher entropy flow after shock (entropy layer), which is usually higher than the boundary layer thickness in the vicinity of the nose. Because the height of the entropy

flow property	Mach number	Temperature	Pressure	Reynolds number	cone angle	shock angle
before the shock	8	53.35 K	165.5 Pa	3,333,333	7°	12°
after the shock	6.85	69.3 K	387.2 Pa	4,730,000		

Table 8.1: Flow parameters before and after the shock.

layer is decreasing in downstream direction and the boundary-layer thickness is increasing, there is a possibility that the boundary layer merges with the entropy layer somewhere over the frustum of the cone—the so-called swallowing length. Stetson & Kimmel (1992) report for this nose bluntness that as long as the entropy layer is not swallowed by the boundary layer, amplification rates drop below values for the sharp cone and therefore stabilize the flow.

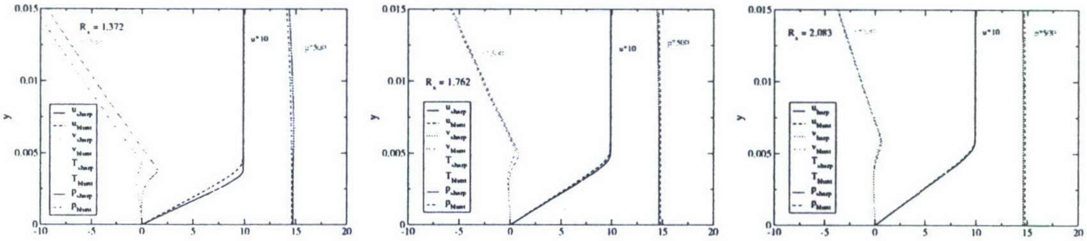

(a) $R_x = 1,372$.

(b) $R_x = 1,763$.

(c) $R_x = 2,083$.

Figure 8.1: Base-flow profiles. Comparison of blunt cone with sharp cone for three different downstream locations. $Ma = 7.95$, $Re = 3,333,333$, $T_\infty = 53.35K$.

It is our opinion that there might be another explanation for this altered stability behavior for the blunt cone. According to LST, the wall temperature influences second-mode instability waves—cooling the wall destabilizes the second-mode waves (c.f. section 1.3.1). Because the total temperature is conserved for the shock but velocities after a normal shock are slower than after an oblique shock, the static temperature after a normal shock is higher than after an oblique shock wave. Figure 8.3 compares wall temperatures for the blunt and the sharp cone with the wall temperature for the blunt cone being $5K$ to $20K$ higher than for the sharp cone. Therefore, the second mode, which governs the stability behavior of hypersonic boundary layer flows, is more unstable for the sharp cone than for the blunt geometry. However, this seems to contradict the statement made in the introduction (c.f. 1.1) that large nose radii reduce the heat flux into the wall. This is true under the assumption of isothermal walls. But in case of the adiabatic wall considered in the simulations, the heat flux is zero and therefore a rise in wall temperature is the logical consequence.

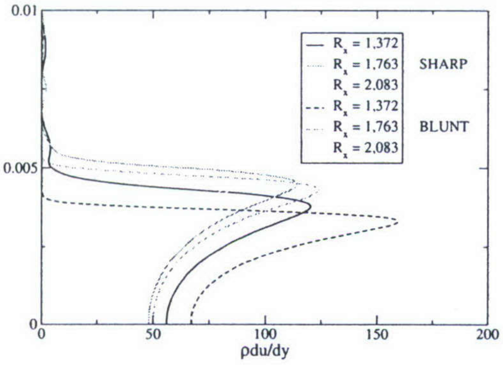

Figure 8.2: Simplified generalized inflection point criterion for three different location in comparison with sharp cone results. $Ma = 7.95$, $Re = 3,333,333$, $T_\infty = 53.35K$.

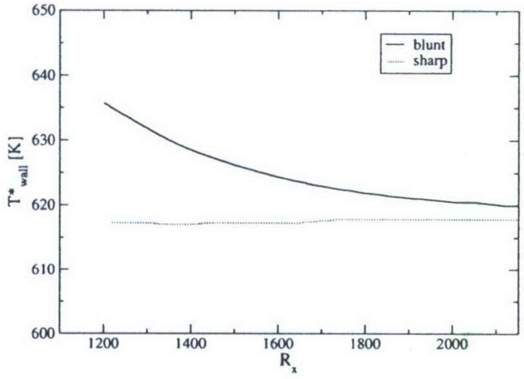

Figure 8.3: Linear amplification rate for different frequencies. $Ma = 7.95$, $Re = 3,333,333$, $T_\infty = 53.35K$, $\Psi = 20°$.

8.1 Pulsed Disturbance

As for the sharp cone, a small-amplitude pulsed disturbance is introduced into the flow to investigate the linear stability behavior for a circular cone with a small nose radius. Figure 8.4 shows that, with an equivalent input signal for the pulse, the flow responses in the same way over the disturbance slot for the blunt and the sharp cone. Hence, the receptivity of the flow seems not to be altered by the nose bluntness. But the downstream development of the disturbances are different. Figure 8.5 shows resulting amplification rates for selected frequencies. In comparison with Figure 7.4 the maximal amplification rate is reached at a farther downstream location than for the sharp cone. Thus, a cone with a small nose bluntness is stabilized as reported in the experiments by Stetson *et al.* (1984), although the maximum amplification rate in both cases (for the sharp and the blunt cone) reaches comparable values.

For a better comparison of the stability behavior of a sharp and a blunt cone, amplitude distribution are plotted in Figure 8.6 for the sharp (solid) and the blunt

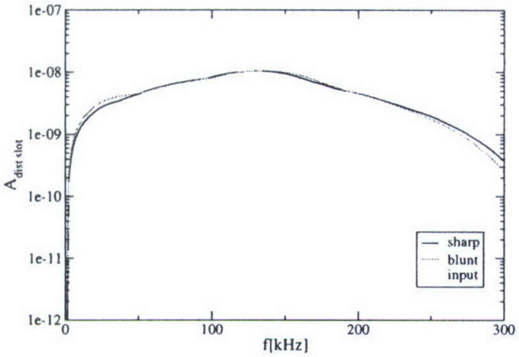

Figure 8.4: Spectral input signal of pulsed disturbance. Ma = 7.95, Re = 3,333,333, $T_\infty = 53.35K$, $\Psi = 20°$.

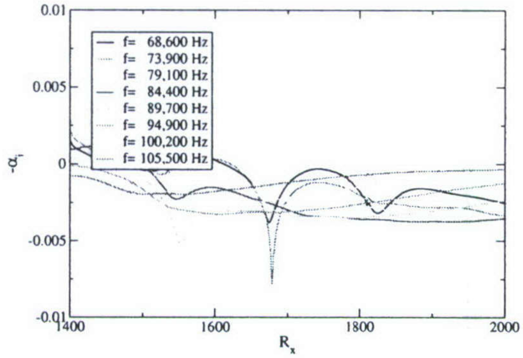

Figure 8.5: Linear amplification rate for selected frequencies. Ma = 7.95, Re = 3,333,333, $T_\infty = 53.35K$, $\Psi = 20°$.

cone (dashed). For each frequency, the blunt cone amplitude levels are lower than for the sharp cone—the higher the frequency the larger the difference in amplitude. This shift of high amplification to lower frequencies can be explained by the increase in boundary-layer thickness (see Figure 8.7). Figure 8.7 graphs boundary-layer values for the blunt (dashed) and the sharp cone (solid). The integral properties of the boundary layer (e.g. the displacement thickness) in Figure 8.7 are not as strongly influenced as the boundary layer thickness, mainly due to the presence of the entropy layer up to about $R_x = 1,700$.

Figure 8.8 plots the amplification rates over frequency at two different downstream locations for the blunt and the sharp cone. For both locations in Figure 8.8, the sharp cone is unstable to higher frequencies than the blunt cone. For the upstream location ($R_x = 1,600$) in Figure 8.8a, the blunt cone is only unstable to a small frequency band between $75kHz$ and

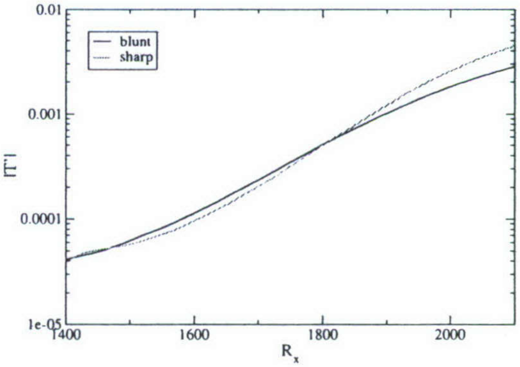

Figure 8.9: Comparison of T'-amplitude distribution. Ma = 7.95, Re = 3,333,333, $T_\infty = 53.35K$, $F = 9.8 \cdot 10^{-5}$, $\Psi = 0°$.

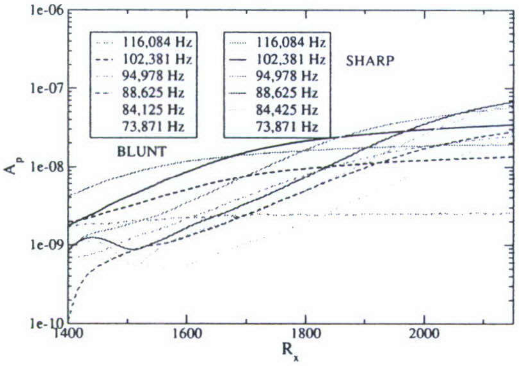

Figure 8.6: Amplitude distribution based on wall pressure for different frequencies. $Ma = 7.95$, $Re = 3,333,333$, $T_\infty = 53.35K$, $\Psi = 20°$.

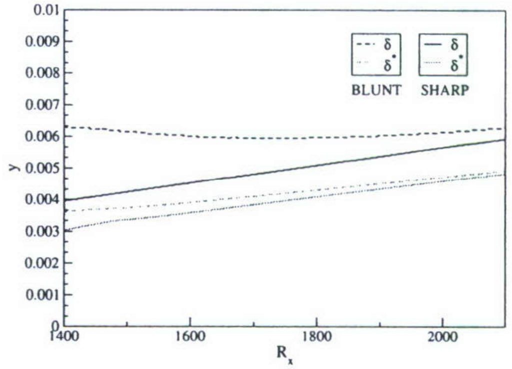

Figure 8.7: Base-flow properties of the blunt cone (dashed) compared to the sharp cone (solid).

$95kHz$. High frequency noise penetrating into the boundary layer (as in wind-tunnel experiments) would decay, further contributing to a more stable configuration for the blunt cone. Farther downstream, at $R_x = 1,900$, the blunt cone and the sharp cone experience their maximal amplification at the same frequency with the amplification rate for the blunt cone only slightly lower than for the sharp cone. Therefore, most breakdown scenarios are investigated at a frequency of $f = 88kHz$, the same frequency as for the sharp cone, to take advantage of the waves' eigenbehaviors and in order to allow a direct comparison with sharp cone results. Figure 8.9 compares the amplitude distribution for disturbance waves at $F = 9.8 \cdot 10^{-5}$ ($f = 88kHz$) over the blunt and the sharp cone. From their similar linear amplitude distribution follows that significant differences in the investigated breakdown scenarios are *nonlinear* effects of the nose bluntness.

8.2 Oblique Breakdown

Because the higher boundary-layer thickness for the blunt cone decreases the unstable frequency range when compared with the sharp cone, first-mode disturbance

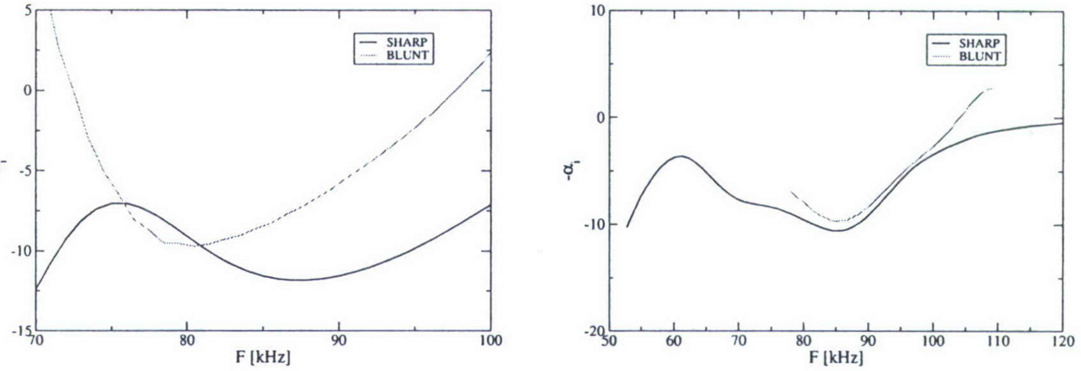

(a) $R_x = 1,600$.

(b) $R_x = 1,900$.

Figure 8.8: Linear amplification rate plotted over frequency for different downstream locations. $Ma = 7.95$, $Re = 3,333,333$, $T_\infty = 53.35K$, $\Psi = 20°$.

waves may become important in breakdown scenarios for the blunt cone. Although the oblique breakdown mechanism of first-mode disturbances (Figure 8.10) involves stronger interactions than for the sharp cone (c.f. Figure 7.8), the amplitude levels are still too low for breakdown to occur. With the low degree of nonlinear actions present in the oblique breakdown of first-mode waves, the emerging two-dimensional wave at twice the disturbance frequency is remarkably amplified. This wave constitutes a second-mode wave so that the oblique breakdown of a second-mode oblique wave at a small wave angle is investigated next.

In contrast to the sharp cone, finite-amplitude second-mode oblique waves (Figure 8.11) result in weaker nonlinear interactions confirming the stabilizing effects of small nose radii observed in the experiments (c.f. Stetson *et al.* (1984)). For comparison, the waves in the simulations for the blunt and the sharp cone are disturbed with the same amplitude and frequency (as reported in the experiments by Stetson *et al.* (1983)). The resulting lower amplitude levels for the blunt cone weaken nonlinear interactions and hence also reduce the amplitude levels of the generated higher modes. The larger boundary-layer thickness of the blunt cone with resulting lower unstable frequencies

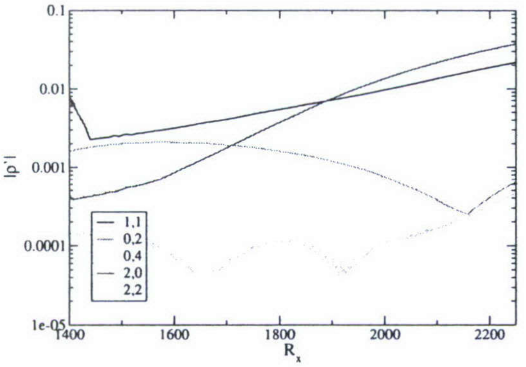

Figure 8.10: Oblique breakdown. ρ'-amplitude distribution. $Ma = 7.95$, $Re = 3,333,333$, $T_\infty = 53.35K$, $F = 4.9 \cdot 10^{-5}$, $A_{1,1} = 1\%$, $\Psi = 70°$.

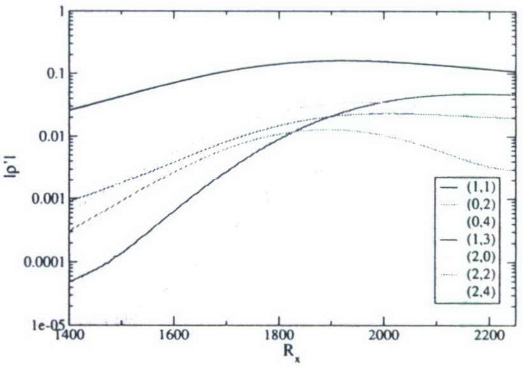

Figure 8.11: Oblique breakdown. ρ'-amplitude distribution. $Ma = 7.95$, $Re = 3,333,333$, $T_\infty = 53.35K$, $F = 1.17 \cdot 10^{-4}$, $A_{1,1} = 1\%$, $\Psi = 20°$.

is the main stabilizing factor in this comparison. Other parameters influencing the stability behavior include (but are not limited to) the shock location (longer distance between wall and shock stabilizes), entropy layer (as suggested by Stetson *et al.* (1984)), and the wall temperature.

8.3 Oblique Subharmonic Resonance

Due to the observed increase in the amplification of first-mode oblique waves in the previous section, investigations of breakdown mechanisms involving first-mode waves are also considered in order to clarify if these waves play a role for this breakdown mechanism.

The oblique subharmonic resonance of a first-mode wave triad shows some nonlinear interactions as seen in Figure 8.12. However, as mentioned before in case of the oblique breakdown, the amplitude levels remain low and it is questionable if the oblique subharmonic resonance of first-mode waves is strong enough to lead to breakdown of the flow. If, in addition to the wave triad, a steady vortex mode (0,1) is perturbed (Figure 8.13), nonlinear interactions of first-mode waves are more pronounced

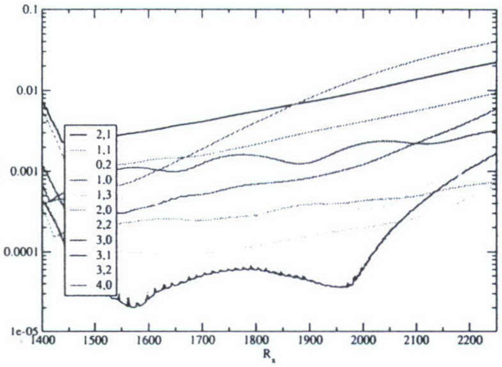

Figure 8.12: Oblique subharmonic resonance. ρ'-amplitude distribution. $Ma = 7.95$, $Re = 3,333,333$, $T_\infty = 53.35K$, $F = 4.9 \cdot 10^{-5}$, $A_{2,1} = 1\%$, $A_{1,1} = 1\%$, $\Psi_{2,1} = 70°$, $\Psi_{1,1} = 80°$.

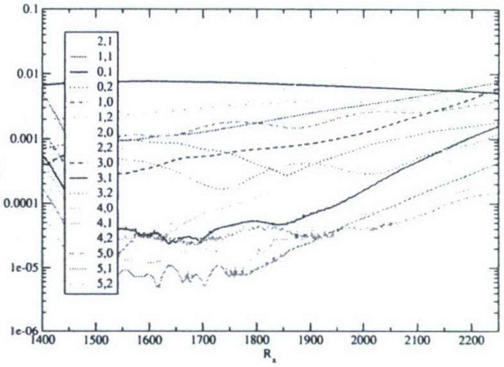

Figure 8.13: Oblique subharmonic resonance. ρ'-amplitude distribution. $Ma = 7.95$, $Re = 3,333,333$, $T_\infty = 53.35K$, $F = 4.9 \cdot 10^{-5}$, $A_{2,1} = 1\%$, $A_{1,1} = 1\%$, $A_{0,1} = 1\%$, $\Psi_{2,1} = 70°$, $\Psi_{1,1} = 80°$.

as already discussed for the sharp cone in section 7.6. The strong amplification of the (4,0)-mode in Figure 8.13, which even exceeds the primary wave amplitude levels by a factor of three, is associated with a second-mode two-dimensional wave. Thus, the oblique subharmonic resonance of second-mode waves with small wave angles, which are known to be almost as amplified as second-mode two-dimensional waves, is investigated in Figure 8.14. In comparison with the equivalent breakdown scenario for the sharp cone (c.f. Figure 7.18), the impact of the nose radius on the nonlinear interactions is only minor. Therefore, the oblique subharmonic resonance of second-mode waves gains in importance for the blunt cone relative to the oblique breakdown which is stabilized by the small nose radius (c.f. section 8.2). As can be seen in Figure 8.15, the forcing of the steady streamwise vortex mode (0,1) in addition to the subharmonic wave triad results in even stronger nonlinear interactions. Based on the comparison of Figure 8.14 with Figure 8.15, the steady vortices rise the primary waves ((2,1)-mode) amplitude levels. This observation stands in contrast to the stability behavior of the sharp cone where the second-mode waves were mostly unaffected by the presence of steady vortices. Also, the forcing of the steady vortex mode (0,1) results

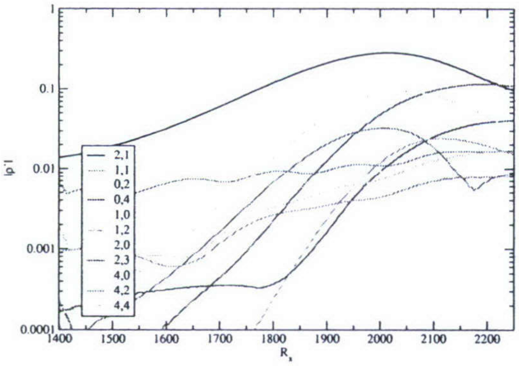

Figure 8.14: Oblique subharmonic resonance. ρ'-amplitude distribution. $Ma = 7.95$, $Re = 3,333,333$, $T_\infty = 53.35K$, $F = 9.8 \cdot 10^{-5}$, $A_{2,1} = 1\%$, $A_{1,1} = 1\%$, $\Psi_{2,1} = 20°$, $\Psi_{1,1} = 36°$.

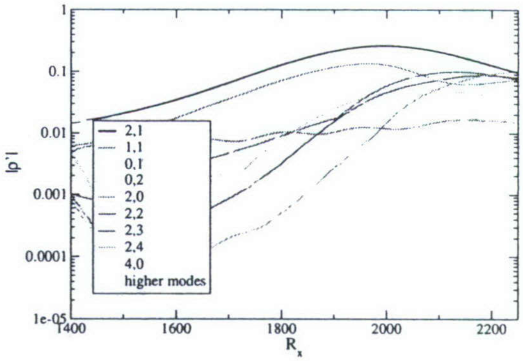

Figure 8.15: Oblique subharmonic resonance. ρ'-amplitude distribution. $Ma = 7.95$, $Re = 3,333,333$, $T_\infty = 53.35K$, $F = 9.8 \cdot 10^{-5}$, $A_{2,1} = 1\%$, $A_{1,1} = 1\%$, $A_{0,1} = 1\%$, $\Psi_{2,1} = 20°$, $\Psi_{1,1} = 36°$.

in a stronger resonance triad. Although phase speeds in Figure 8.16 and Figure 8.17 are not exactly matching, the phase speed of the nonlinearly generated secondary wave (1,2) agrees better with a forced steady vortex mode (Figure 8.17) than without its presence (Figure 8.16). Looking at the resulting flow structures in Figure 8.18 and

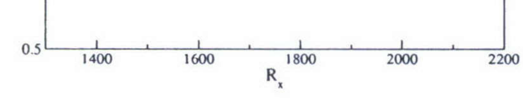

Figure 8.16: Oblique subharmonic resonance. Phase velocity. $Ma = 7.95$, $Re = 3,333,333$, $T_\infty = 53.35K$, $F = 9.8 \cdot 10^{-5}$, $A_{2,1} = 1\%$, $A_{1,1} = 1\%$, $\Psi_{2,1} = 20°$, $\Psi_{1,1} = 36°$.

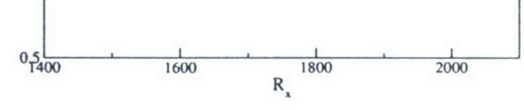

Figure 8.17: Oblique subharmonic resonance. Phase velocity. $Ma = 7.95$, $Re = 3,333,333$, $T_\infty = 53.35K$, $F = 9.8 \cdot 10^{-5}$, $A_{2,1} = 1\%$, $A_{1,1} = 1\%$, $A_{0,1} = 1\%$, $\Psi_{2,1} = 20°$, $\Psi_{1,1} = 36°$.

Figure 8.19 shows that forcing of a steady vortex mode moves the splitting of the flow structures upstream. Based on the enhanced nonlinear interactions in presence of a forced steady streamwise vortex mode, the resulting flow structures in Figure 8.19 breakdown in smaller scales than without the explicit forcing of the steady vortex mode (Figure 8.18). Once breakdown is initiated over the blunt cone, developing flow structures resemble the results for the sharp cone results in Figure 7.21.

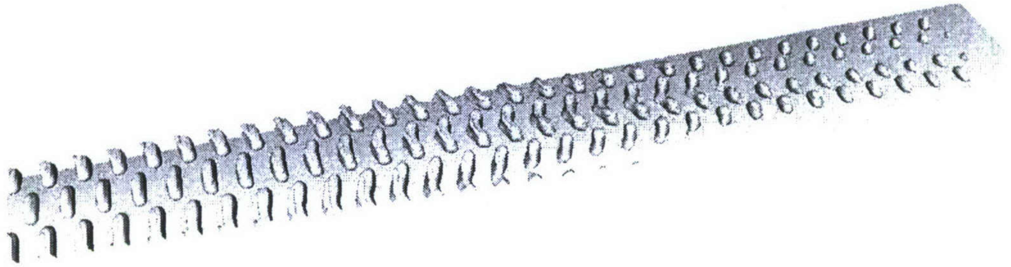

Figure 8.18: Oblique subharmonic resonance. Vortical structures identified by the Q-criterion (Q = 500). $Ma = 7.95$, $Re = 3,333,333$, $T_\infty = 53.35K$, $F_{2,1} = 9.8 \cdot 10^{-5}$, $A_{2,1} = 1\%$, $\Psi_{2,1} = 20°$, $F_{1,1} = 4.9 \cdot 10^{-5}$, $A_{1,1} = 1\%$, $\Psi_{1,1} = 36°$.

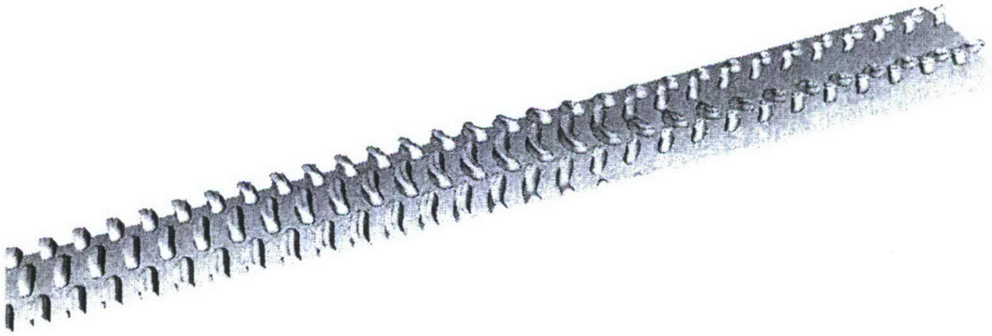

Figure 8.19: Oblique subharmonic resonance. Vortical structures identified by the Q-criterion (Q = 500). $Ma = 7.95$, $Re = 3,333,333$, $T_\infty = 53.35K$, $F_{2,1} = 9.8 \cdot 10^{-5}$, $A_{2,1} = 1\%$, $\Psi_{2,1} = 20°$, $F_{1,1} = 4.9 \cdot 10^{-5}$, $A_{1,1} = 1\%$, $A_{0,1} = 1\%$, $\Psi_{1,1} = 36°$.

8.4 Oblique Fundamental Resonance

The investigation of an oblique fundamental resonance of first-mode waves in Figure 8.20 and Figure 8.21 does not conclude any new findings. Therefore, second-mode waves govern the stability behavior of a hypersonic boundary layer over a circular cone with small nose bluntness.

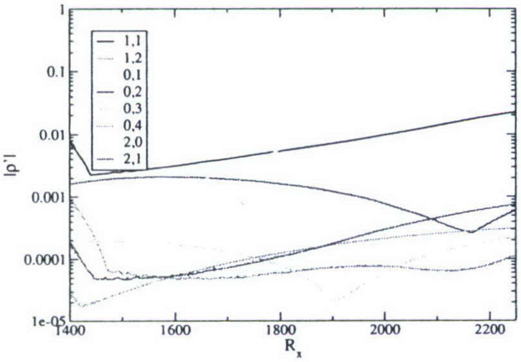

Figure 8.20: Oblique fundamental resonance. ρ'-amplitude distribution. $Ma = 7.95$, $Re = 3,333,333$, $T_\infty = 53.35K$, $F = 4.9 \cdot 10^{-5}$, $A_{1,1} = 1\%$, $A_{1,2} = 1\%$, $\Psi_{1,1} = 70°$, $\Psi_{1,2} = 80°$.

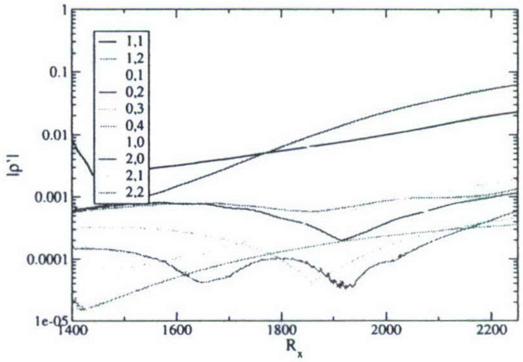

Figure 8.21: Oblique fundamental resonance. ρ'-amplitude distribution. $Ma = 7.95$, $Re = 3,333,333$, $T_\infty = 53.35K$, $F = 4.9 \cdot 10^{-5}$, $A_{1,1} = 1\%$, $A_{1,2} = 1\%$, $A_{0,1} = 1\%$, $\Psi_{1,1} = 70°$, $\Psi_{1,2} = 80°$.

For the sharp cone, the oblique fundamental resonance of second-mode waves is a very strong mechanism. The small nose radius of the blunt cone has also stabilizing effects for this breakdown mechanism. Because the phase speeds of primary and secondary waves in Figure 8.22 agree even better than for the oblique subharmonic resonance (c.f. Figure 8.16), stronger nonlinear interactions and more rapid development of emerging higher modes can be observed in Figure 8.23 when compared with Figure 8.14. For the blunt cone, the main difference of the oblique fundamental resonance to other mechanisms under investigation is that a forcing of a steady streamwise vortex mode does not improve nonlinear interactions. Although phase speeds of disturbed waves agree at least as well as without the presence of a perturbed steady vortex mode (compare Figure 8.22 with Figure 8.24), developing higher modes (e.g.

the (1,4)-mode) do not reach as high amplitude levels in Figure 8.25 as without the forced steady streamwise vortex (see Figure 8.23).

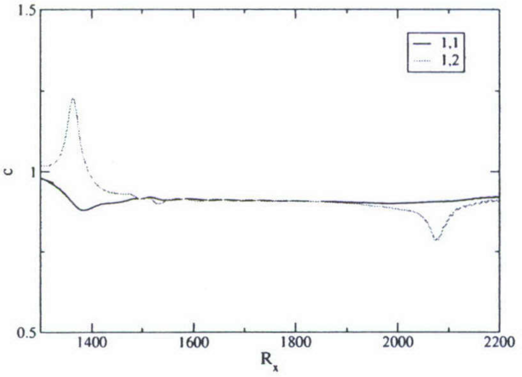

Figure 8.22: Oblique fundamental resonance. Phase velocity. $Ma = 7.95$, $Re = 3,333,333$, $T_\infty = 53.35K$, $F = 9.8 \cdot 10^{-5}$, $A_{1,1} = 1\%$, $A_{1,2} = 1\%$, $\Psi_{1,1} = 20°$, $\Psi_{1,2} = 36°$.

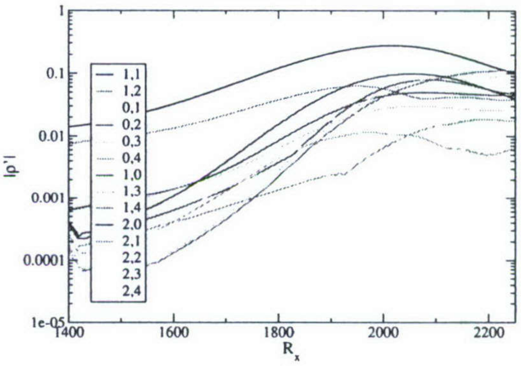

Figure 8.23: Oblique fundamental resonance. ρ'-amplitude. $Ma = 7.95$, $Re = 3,333,333$, $T_\infty = 53.35K$, $F = 9.8 \cdot 10^{-5}$, $A_{1,1} = 1\%$, $A_{1,2} = 1\%$, $A_{0,1} = 1\%$, $\Psi_{1,1} = 20°$, $\Psi_{1,2} = 36°$.

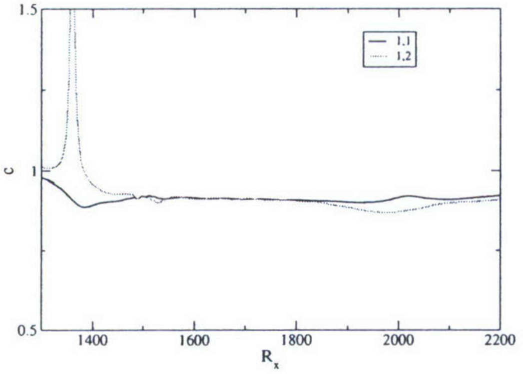

Figure 8.24: Oblique fundamental resonance. Phase velocity. $Ma = 7.95$, $Re = 3,333,333$, $T_\infty = 53.35K$, $F = 9.8 \cdot 10^{-5}$, $A_{1,1} = 1\%$, $A_{1,2} = 1\%$, $A_{0,1} = 1\%$, $\Psi_{1,1} = 20°$, $\Psi_{1,2} = 36°$.

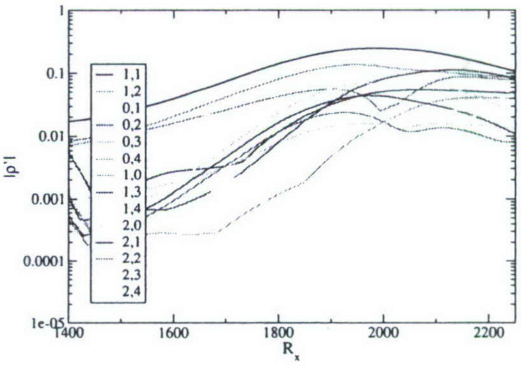

Figure 8.25: Oblique fundamental resonance. ρ'-amplitude. $Ma = 7.95$, $Re = 3,333,333$, $T_\infty = 53.35K$, $F = 9.8 \cdot 10^{-5}$, $A_{1,1} = 1\%$, $A_{1,2} = 1\%$, $A_{0,1} = 1\%$, $\Psi_{1,1} = 20°$, $\Psi_{1,2} = 36°$.

8.5 Fundamental Breakdown (K-type)

Because second-mode two-dimensional waves are far stronger amplified than first-mode two-dimensional waves, further investigation of breakdown scenarios of primary first-mode waves is omitted.

As known from investigations on the sharp cone geometry, the fundamental breakdown involving second-mode waves might be a viable mechanism. Figure 8.26 and Figure 8.27 both illustrate the possibility of a fundamental resonance at $R_x \approx 2,000$. While Figure 8.26 reveals only weak nonlinear interactions, Figure 8.27 shows amplified higher modes if the steady vortex mode (0,1) is disturbed at a high amplitude. For the wave angle of $\Psi = 41°$, most of the higher modes saturate and decay along with the primary disturbance wave (1,0). If the secondary wave angle is increased to $\Psi = 60°$, a resonance in Figure 8.28 exists only very weakly around $R_x \approx 2,000$. But if the steady streamwise vortex mode (0,1) is also disturbed (Figure 8.29), nonlinear interactions are greatly enhanced. The secondary (1,1)-wave is stronger amplified and the resonance at $R_x = 2,000$ is more pronounced. Towards the end of the computational domain, emerging higher modes are amplified so that the forcing of the steady streamwise vortex mode has a bigger impact on the fundamental (K-type) breakdown than it has on other mechanisms discussed for the blunt cone. Although no strong resonance is visible and amplitude levels of the different higher modes range over several orders of magnitude, the fundamental breakdown (K-type) is a candidate for further considerations in the investigation of breakdown scenarios for the blunt cone.

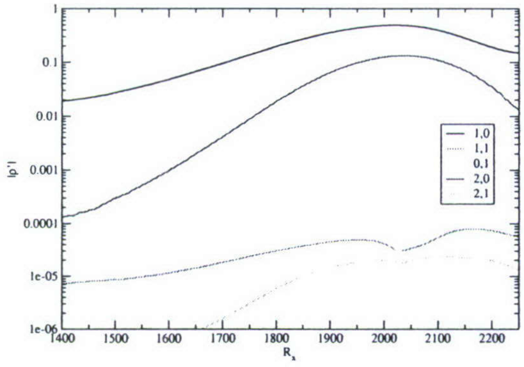

Figure 8.26: Fundamental breakdown. ρ'-amplitude distribution. $Ma = 7.95$, $Re = 3,333,333$, $T_\infty = 53.35K$, $F = 9.8 \cdot 10^{-5}$, $A_{1,0} = 1\%$, $A_{1,1} = 1 \cdot 10^{-3}\%$, $\Psi = 41°$.

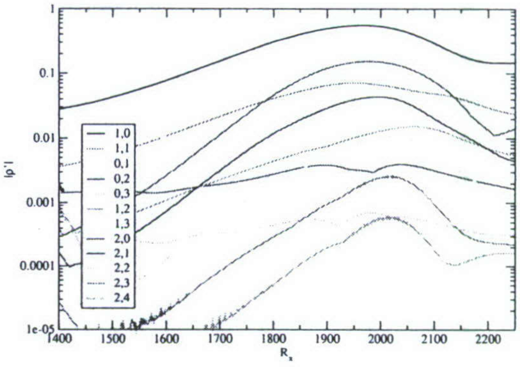

Figure 8.27: Fundamental breakdown. ρ'-amplitude distribution. $Ma = 7.95$, $Re = 3,333,333$, $T_\infty = 53.35K$, $F = 9.8 \cdot 10^{-5}$, $A_{1,0} = 1\%$, $A_{1,1} = 1 \cdot 10^{-3}\%$, $A_{0,1} = 1\%$, $\Psi = 41°$.

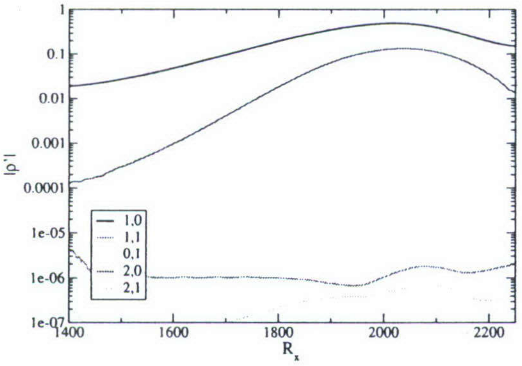

Figure 8.28: Fundamental breakdown. ρ'-amplitude distribution. $Ma = 7.95$, $Re = 3,333,333$, $T_\infty = 53.35K$, $F = 9.8 \cdot 10^{-5}$, $A_{1,0} = 1\%$, $A_{1,1} = 1 \cdot 10^{-3}\%$, $\Psi = 60°$.

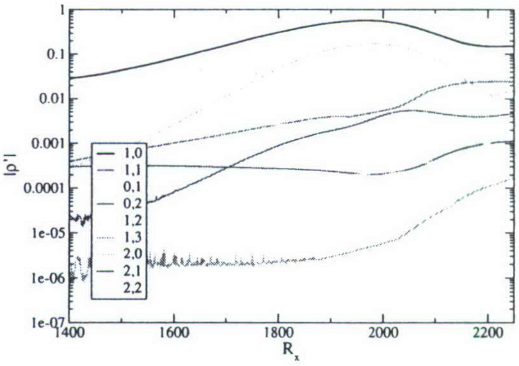

Figure 8.29: Fundamental breakdown. ρ'-amplitude distribution. $Ma = 7.95$, $Re = 3,333,333$, $T_\infty = 53.35K$, $F = 9.8 \cdot 10^{-5}$, $A_{1,0} = 1\%$, $A_{1,1} = 1 \cdot 10^{-3}\%$, $A_{0,1} = 1\%$, $\Psi = 60°$.

8.6 Subharmonic Breakdown (N-/H-type)

In experiments on a flared cone, researchers like Chokani (1999) or Shiplyuk *et al.* (2003) reportedly found a subharmonic resonance of a second-mode two-dimensional wave with a secondary oblique wave at half the frequency. So far, a subharmonic resonance of two-dimensional primary waves with oblique secondary waves has not been discovered within the parameter space of experimental and computational investigations for a circular cone. Simulations are performed with the most amplified frequency for the primary disturbance wave. Although the secondary wave amplitude in Figure 8.30 dips around $R_x = 2,000$, linear amplification rates are recovered thereafter. Therefore, a resonance is not present. This fact stays true even when a steady streamwise vortex mode (0,1) is forced. As for the sharp cone, Figure 8.31 shows a possible fundamental resonance, but amplification of the subharmonic secondary waves is not altered. Hence, even the destabilization of second-mode two-dimensional waves in the presence of a steady vortex mode does not lead to a subharmonic breakdown. Therefore, it is speculated that other parameters like adverse pressure gradients or the presence of Görtler vortices favors the subharmonic breakdown on flared cones.

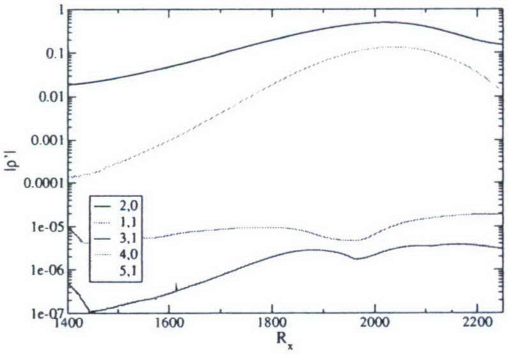

Figure 8.30: Subharmonic breakdown. ρ'-amplitude distribution. $Ma = 7.95$, $Re = 3,333,333$, $T_\infty = 53.35K$, $F = 9.8 \cdot 10^{-5}$, $A_{2,0} = 1\%$, $A_{1,1} = 1 \cdot 10^{-3}\%$, $\Psi = 60°$.

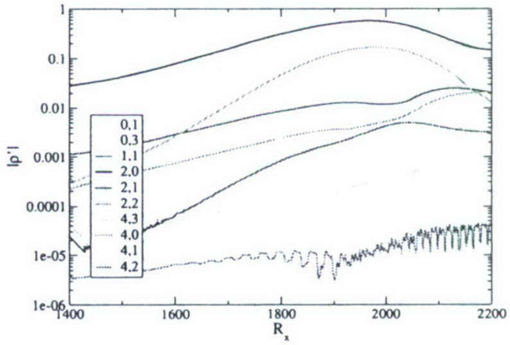

Figure 8.31: Subharmonic breakdown. ρ'-amplitude distribution. $Ma = 7.95$, $Re = 3,333,333$, $T_\infty = 53.35K$, $F = 9.8 \cdot 10^{-5}$, $A_{2,0} = 1\%$, $A_{1,1} = 1 \cdot 10^{-3}\%$, $A_{0,1} = 1\%$, $\Psi = 60°$.

8.7 Summary

The overall stabilizing effects of a small nose radius reported by Stetson *et al.* (1984) could have been confirmed in the DNS. Especially, the amplification of high frequency waves is greatly reduced because of the larger boundary layer thickness. Interestingly, the frequency with the highest amplification rate along the computational domain seems not be influences by this increase in boundary-layer thickness and does therefore not significantly differ from the frequency for the sharp cone.

Based on the stabilizing effects of the nose bluntness nonlinear interaction are weakening independent of the breakdown mechanism under investigation. As already observed for the sharp cone, nonlinear interactions are enhanced through of forcing steady streamwise vortex modes. Their impact on the stability behavior is more pronounced than for the sharp cone. Therefore, it is essential for a steady streamwise vortex to be present in order to see strong nonlinear behavior with the computational domain. Compared to the results, the steady streamwise vortex modes gain in importance for the blunt cone. The oblique subharmonic and fundamental resonances seem to be least influenced by the stabilizing effects of the nose radius. Hence, the strongest mechanism within the scope of the investigations is the oblique fundamental resonance, although forcing of a steady streamwise vortex mode does not further enhance this mechanism.

9. Transition Investigations of a Boundary Layer on a Blunt Cone ($R_N = 0.7$")

The largest nose radius studied in this investigation is also the largest nose radius in the experimental effort by Stetson *et al.* (1984). Stetson *et al.* (1984) observed a transition reversal, i.e. when compared with the transition on-set for the sharp cone, transition for the blunt cone with a large nose radius moved upstream. Numerical efforts by e.g. Rosenboom *et al.* (1999) or Zhong (2005) did not reveal this trend. In their simulations, transition moved downstream with increasing nose radius. While experimental and other numerical efforts used a unit Reynolds number of $Re/ft = 2.5 \cdot 10^6$, the unit Reynolds number in this investigation is reduced to $Re/ft = 1 \cdot 10^6$ ($Re = 3,333,333$) to allow for a direct comparison of results obtained in chapter 7 and chapter 8. Resulting after-shock conditions at the inflow of the computational domain are summarized in table 9.1.

flow property	Mach number	Temperature	Pressure	Reynolds number	cone angle	shock angle
before the shock	8	53.35 K	165.5 Pa	3,333,333	7°	10°
after the shock	6.0	81.6 K	590.2 Pa	4,350,000		

Table 9.1: Flow parameters before and after the shock.

To elaborate differences in the stability behavior for the cone with a large nose radius in comparison to cones with sharp nose tips and small nose radii a discussion of the flow conditions after the shock and their downstream development follows. Figure 9.1 compares the edge Mach number along the computational domain for all three nose radii. Up to the location $R_X = 1,700$, the edge Mach number is below the Mach numbers of the other two configurations which should slightly increase the amplification rates of second-mode waves. Remember that according to LST, the amplification rates of second-mode waves are highest when they are generated around $Ma = 4$ and then drop with increasing Mach number. The comparison of boundary-layer properties in Figure 9.2 shows a dramatic increase in boundary-layer thickness. As mentioned for the small nose radius, it is hard to distinguish between entropy-layer and boundary-layer thickness so that this increase can be partly attributed to the higher entropy-layer thickness. In fact, Figure 9.3 gives rise to the assumption that the entropy layer is not being swallowed by the boundary layer over the downstream extent of the computational domain. Despite this discovery, the frequency of (unstable) disturbance waves should decrease significantly over the unstable frequencies for the other two nose radii.

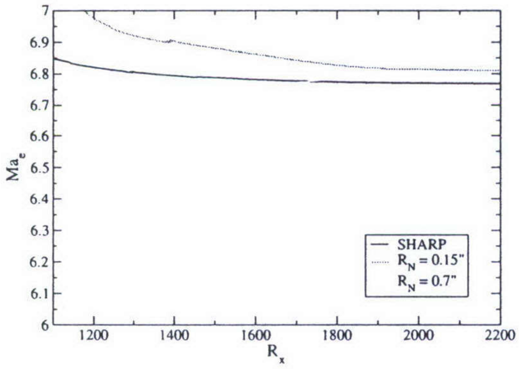

Figure 9.1: Edge Mach number comparison. $Ma = 7.95$, $Re = 3,333,333$, $T_\infty = 53.35K$.

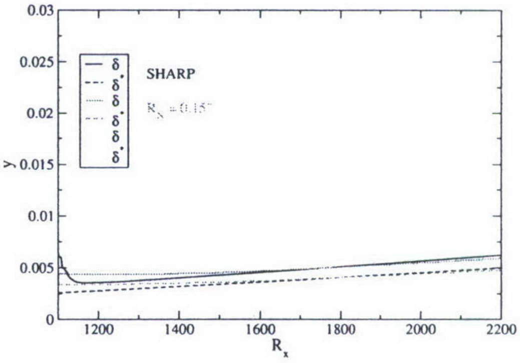

Figure 9.2: Comparison of boundary-layer thickness and displacement thickness for different nose radii. $Ma = 7.95$, $Re = 3,333,333$, $T_\infty = 53.35K$.

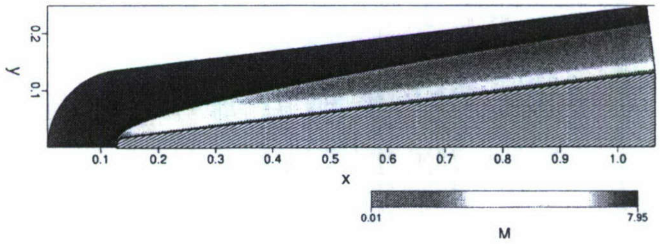

Figure 9.3: Flow field around the blunt cone with a nose radius of $R_N = 0.7$". $Ma = 7.95$, $Re = 3,333,333$, $T_\infty = 53.35K$.

9.1 Pulsed Disturbance

When the same pulsed disturbance used for earlier investigations is introduced into the wall through a blowing and suction slot, not a single amplified disturbance wave could be observed. Varying the wave angle Ψ and pulse duration to favor first-mode waves did not result in any different discoveries. This seems to confirm findings of other numerical efforts and does not explain the transition reversal as seen in experiments (c.f. Stetson *et al.* (1984)). Looking at the wall temperature distribution in Figure 9.4 shows a strong increase over the entire computational domain which stabilizes the flow. But the wall temperature is unlikely to have such a strong impact. Moreover, the strong stabilization of the boundary layer over the cone with a large nose radius can be explained by Figure 9.5. In Figure 9.5, the wall-normal location of the generalized inflection point and of the critical layer are plotted for all conical geometries investigated. While for the sharp cone and the cone with small nose bluntness, the generalized inflection point lies on top of the critical layer, the opposite is true for the cone with a large nose bluntness. According to LST, it is a sufficient condition for an *unstable* subsonic disturbance wave to exist that the location of the generalized inflection point is above the location of the critical layer ($y_s > y_0$). Because wall blowing and suction will only result in waves traveling with a phase speed less than the free-stream velocity, subsonic waves are generated through the disturbance slot at the wall. Hence, all waves are stable. For such a scenario, that the critical layer is above the generalized inflection point, so-called regular or non-inflectional waves traveling with a phase speed between $1 < c < 1 - \frac{1}{Ma}$, i.e. a subsonic disturbance which is faster than the free stream, might be unstable according to LST. If these waves are actually amplified for the cone with a large nose bluntness, the observed transition reversal in experiments will be logical because only natural disturbances, i.e. noise radiated from the environment onto the cone, were considered. Investigations involving regular disturbances can be found in section 9.3.

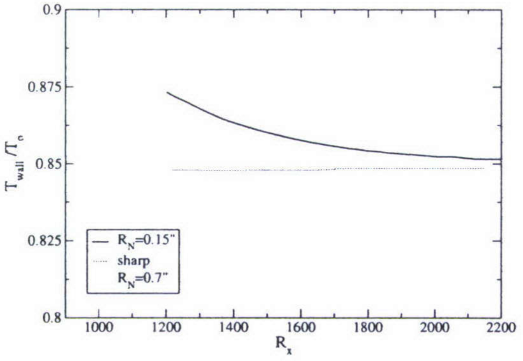

Figure 9.4: Wall-temperature distribution for different nose radii. $Ma = 7.95$, $Re = 3,333,333$, $T_\infty = 53.35K$.

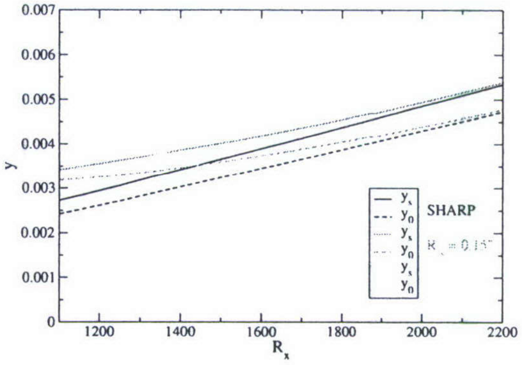

Figure 9.5: Wall-normal location of the generalized inflection point and the critical layer. $Ma = 7.95$, $Re = 3,333,333$, $T_\infty = 53.35K$.

9.2 Breakdown Mechanisms of Slow Subsonic Disturbance Waves

Results described in this section are comparable to the breakdown mechanisms discussed for the sharp cone in section 7 and for the cone with a small nose radius in section 8. The lack of linear amplification of primary waves (as discussed in the previous section) might not necessarily result in an absence possible resonances. Since no strong interactions are observed, detailed discussions of each breakdown scenario is omitted. Instead, special features and differences to the investigations for the cone with the sharp nose tip and the small nose radius are shortly summarized on the basis of the oblique breakdown and the oblique fundamental resonance.

9.2.1 Oblique Breakdown

Disturbance amplitude levels are increased to 5% of the free-stream velocity in order to compensate for the non-existing instability mechanisms and nonlinear interactions to occur. Despite this large disturbance amplitude no resonances are observed within the scope of the investigations. But Figure 9.6 for the oblique breakdown at $\Psi = 55°$ reveals a strong amplification of two-dimensional waves at the subharmonic frequency with its higher harmonics emerging. Due the high-amplitude levels of the (0,2)-mode, nonlinear interactions produce the unsteady oblique disturbance waves at the frequency of the two-dimensional waves (1/2,2), (1,2), (3/2,2), etc. When combinations of these modes are disturbed individually in a fundamental (K-type) or a subharmonic (N-/H-type) breakdown, neither a resonance nor the strong amplification of involved waves can be observed. This fact stays true even when the steady streamwise vortex mode (0,2) is additionally forced at high amplitudes. Reducing the disturbance frequency and the wave angle results in overall higher amplitude levels in Figure 9.7. No breakdown occurs but steady streamwise vortex modes at large wave angles are amplified. For the breakdown scenarios with a small nose radius, we know that steady streamwise vortex modes have a stronger impact on the instability of the flow than for the sharp cone. Hence, with increasing nose radius steady vortex modes become more unstable and their wave angles, at which the vortex modes are amplified, also seem to increase with respect to the nose radius.

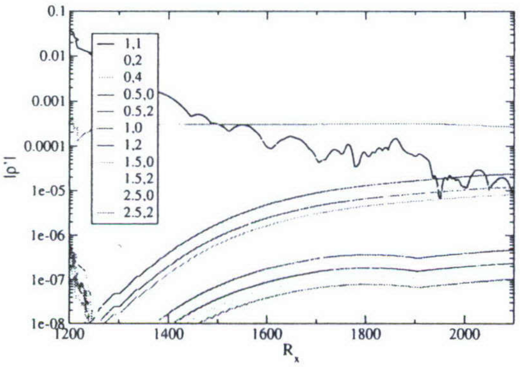

Figure 9.6: Oblique breakdown. ρ'-amplitude distribution. $Ma = 7.95$, $Re = 3,333,333$, $T_\infty = 53.35K$, $F = 8.7 \cdot 10^{-5}$, $A_{1,1} = 5\%$, $\Psi = 55°$.

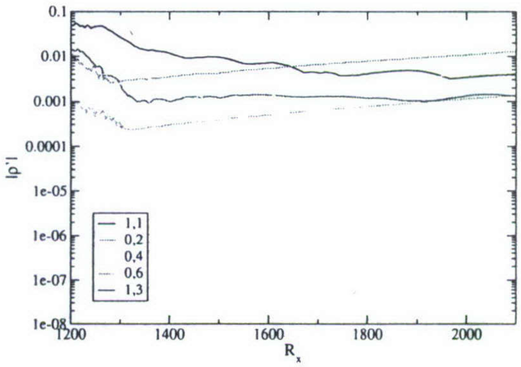

Figure 9.7: Oblique breakdown. ρ'-amplitude distribution. $Ma = 7.95$, $Re = 3,333,333$, $T_\infty = 53.35K$, $F = 3.625 \cdot 10^{-5}$, $A_{1,1} = 5\%$, $\Psi = 20°$.

9.2.2 Oblique Fundamental Resonance

The oblique fundamental resonance reaches the highest amplitudes levels within the scope of the transition investigation of slow subsonic disturbance waves. Again, steady streamwise vortex modes at various wave angles are strongly amplified in Figure 9.8. Here, strongly is in relation to the amplification rate of the steady vortex modes in case of the sharp and the small-nose bluntness cones where the steady vortex modes were mainly neutral or weakly amplified. Compared to second-mode amplification rates experienced for the other two geometries, the steady vortex modes in the presence of the large nose bluntness are less amplified. As observed for the oblique breakdown in Figure 9.6, two-dimensional waves at half the frequency and their higher harmonics are strongly nonlinearly amplified. When a steady streamwise vortex mode is also disturbed amplitude levels are raised although the forced (0,1)-mode is stable throughout the domain (see Figure 9.9). Note, that forcing steady streamwise vortex modes at higher wave angles results in a poorer performance of the oblique fundamental resonance because the amplification rates of those steady modes decrease when they are

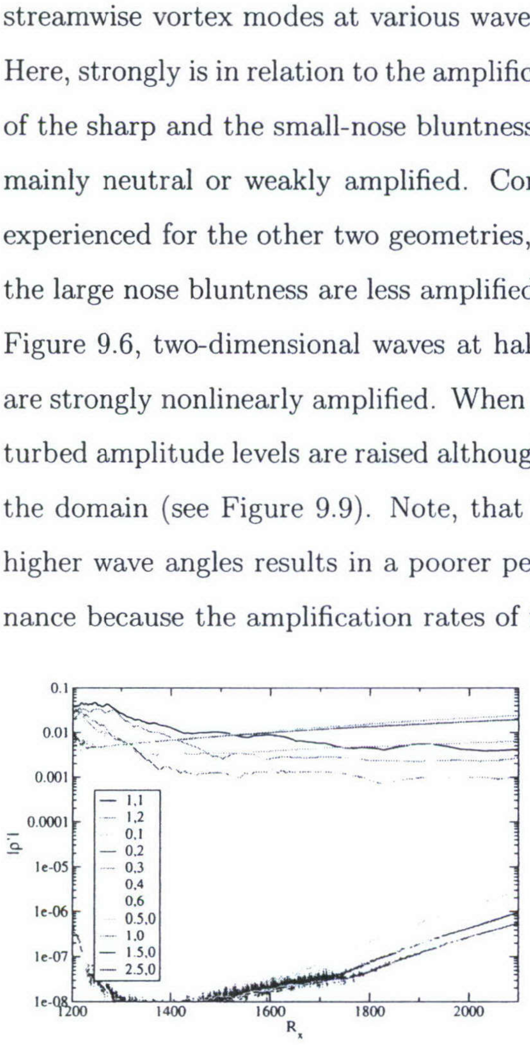

Figure 9.8: Oblique fundamental resonance. ρ'-amplitude distribution. $Ma = 7.95$, $Re = 3,333,333$, $T_\infty = 53.35K$, $F = 3.625 \cdot 10^{-5}$, $A_{1,1} = 5\%$, $A_{1,2} = 5\%$, $\Psi_{1,1} = 20°$.

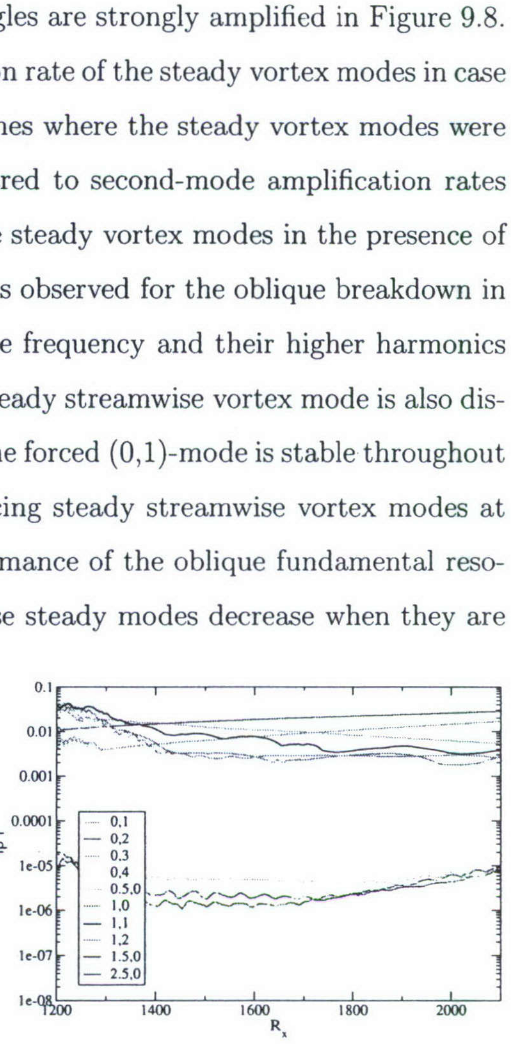

Figure 9.9: Oblique fundamental resonance. ρ'-amplitude distribution. $Ma = 7.95$, $Re = 3,333,333$, $T_\infty = 53.35K$, $F = 3.625 \cdot 10^{-5}$, $A_{1,1} = 4\%$, $A_{1,2} = 4\%$, $A_{0,1} = 2\%$, $\Psi_{1,1} = 20°$.

explicitly forced. It is also noted that in presence of the steady streamwise vortex mode (0,1), the amplification rates of the two-dimensional waves (e.g. mode (1/2,0), mode (3/2,0),...) drop in comparison to the case without the perturbed steady vortex mode.

9.3 Breakdown Mechanisms of Regular Disturbance Waves

As mentioned in the introduction (see section 1.3.1.1) a regular disturbance travels faster than the free stream. In comparison with subsonic waves, the regular disturbance waves do not require the generalized inflection point to be present and are therefore also called non-inflectional waves. The regular disturbance waves cannot be generated with a wall blowing and suction slot, which mainly excites vortical modes. Therefore, disturbances are generated in the free stream between the boundary and the entropy layer (see Figure 9.10).

Simulations show an unstable region downstream of the disturbance generation. The downstream extent of this instability region is influenced by the height where the disturbances are introduced (see Figure 9.11). A farther distance to the boundary-

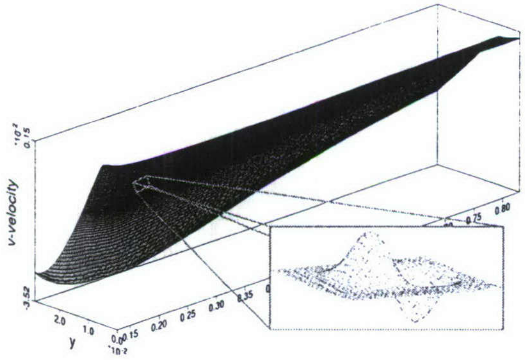

Figure 9.10: Schematic of introducing free-stream disturbances.

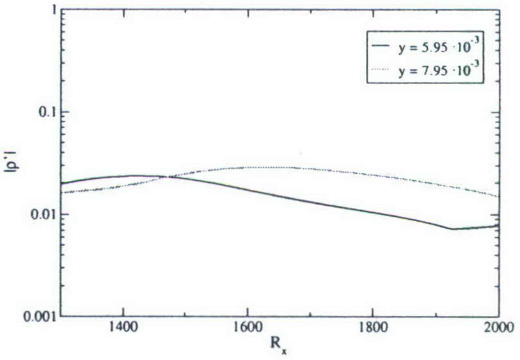

Figure 9.11: Regular disturbance. ρ'-amplitude distribution for two different heights. $Ma = 7.95$, $Re = 3,333,333$, $T_\infty = 53.35K$, $F = 3.625 \cdot 10^{-5}$, $A_{1,1} = 0.01\%$, $\Psi_{1,1} = 20°$.

layer edge results in a longer instability region in the downstream direction. Note, that since the entropy layer is not swallowed by the boundary layer, disturbances penetrating into the boundary layer are not amplified. Thus, the entropy layer is solely responsible for the stability behavior of the blunt cone with a large nose radius.

The simulation of an oblique breakdown with a disturbance amplitude of 1% (Figure 9.12) shows that waves of the fundamental frequency at higher wave angles are amplified farther downstream and thus extending the instability region. Because of the relatively short downstream extent of the instability region, even for high disturbance locations, the amplitude levels are further increased to 3% in Figure 9.13. An interesting fact is that the frequency of the most unstable subsonic disturbance wave (c.f. section 9.1) also results in the most unstable regular disturbance wave. Due to the poor receptivity behavior of the entropy layer to the introduced disturbances, amplitude levels of the primary wave are initiated at 0.5% resulting in a maximum amplitude of about 1.5%. Transition on-set for the sharp and blunt cone with a small nose radius could be observed for maximum amplitude levels of about 20% (c.f. chapter 7 and 8). Hence, the flow of the blunt cone with a large nose radius is drastically destabilized to regular disturbances. Although transition is initiated for in

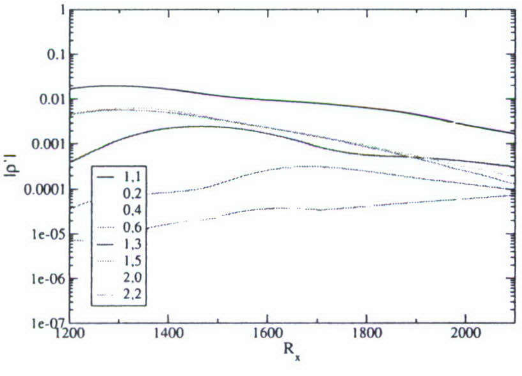

Figure 9.12: Oblique breakdown. ρ'-amplitude. $Ma = 7.95$, $Re = 3,333,333$, $T_\infty = 53.35K$, $F = 3.625 \cdot 10^{-5}$, $A_{1,1} = 1\%$, $\Psi_{1,1} = 20°$.

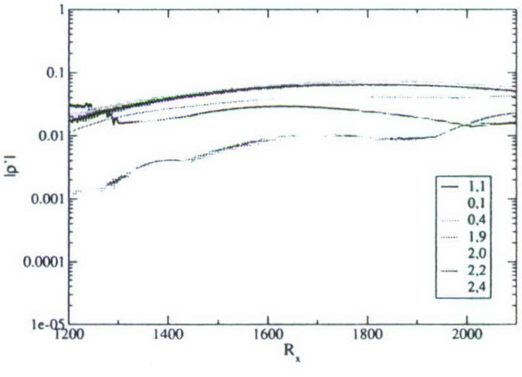

Figure 9.13: Oblique breakdown. ρ'-amplitude. $Ma = 7.95$, $Re = 3,333,333$, $T_\infty = 53.35K$, $F = 3.625 \cdot 10^{-5}$, $A_{1,1} = 3\%$, $\Psi_{1,1} = 20°$.

Figure 9.13, a transition reversal however cannot be observed yet—mainly due to the low disturbance amplitude levels. Despite the strong amplification of two-dimensional waves, no fundamental nor subharmonic resonance could be discovered. Hence, it is concluded that oblique waves govern the stability behavior at hypersonic speeds.

9.4 Summary

For the first time, the discrepancy between experimental findings and numerical efforts for a circular cone with a large nose bluntness could be explained. Due to the change of the location of the critical layer with respect to the location of the generalized inflection point, unsteady subsonic disturbances excited by wall blowing and suction are completely stable along the computational domain. Based on that discovery, results from other numerical efforts could be confirmed. The transition reversal as observed in experiments (c.f. Stetson *et al.* (1984)) is most likely caused by the natural disturbance environment where sound radiated from the turbulent wind-tunnel walls penetrates through the shock and entropy layer into the boundary layer. Simulations where disturbances are introduced in the free stream reveal a drastically reduced critical Reynolds number. Due to the poor receptivity behavior of the entropy layer to the introduction of regular disturbance waves, disturbance levels exceeding 3% are necessary to observe the transition reversal present in the experiments.

10. Conclusions

10.1 Supersonic Flow at Mach 2

Transition in a supersonic flat-plate boundary layer at $Ma = 2.0$ has been investigated using DNS following the experimental studies by Kosinov *et al.* (1994). In the experimental studies, Kosinov *et al.* (1994) discovered a new breakdown mechanism, which they called asymmetric subharmonic resonance, where oblique waves with the frequency of $20kHz$ resonate with two oblique subharmonic waves of different spanwise wave numbers. Scrutinizing the experimental data, however, also suggests the presence of a different breakdown mechanism. Understanding both mechanisms has been the focus of our present numerical study. By deliberately excluding the subharmonic resonance mechanism from the transition process it was possible to show in the simulations that this second breakdown mechanism, which was not reported by the experimentalists, has the features of oblique breakdown. If confirmed by the experimentalists, this would be the first experimental evidence of oblique breakdown in a supersonic boundary layer.

Moreover, asymmetric subharmonic resonance has been studied in detail. Using LST, it was possible to identify various asymmetric, subharmonic resonance triads for the physical flow conditions of Kosinov's experiments. The streamwise wave numbers of all triad components are only weakly affected by nonparallel effects, leading to the conclusion that the same resonance triads discovered using LST are also present in the DNS with large forcing amplitudes. The results obtained from several DNS with large forcing amplitudes revealed that the amplitude ratio between disturbances with both frequencies does not affect the resonance triad, which is in contrast to the experimental findings. Furthermore, in the simulations, the phase difference between disturbances of both frequencies plays a more important role since it influences the absolute value of the maximum generated by the resonance and its spanwise wave number. By changing the phase difference to a certain value, a similar resonance triad as in the experiments and in the theoretical investigation by Tumin (1996) could be observed in the DNS.

10.2 Hypersonic Flow at Mach 8

The nonlinear stages of breakdown over a flat plate, a cylinder, and a cone have been studied. The main focus has been on the circular cone geometry and the effects of spanwise curvature and nose bluntness. The simulations are based on the experimental conditions by Stetson *et al.* (1983) to allow for a direct comparison with experimental findings for validation purposes. Additionally, further insight of the underlying physical mechanisms can be extracted from the simulations in order to draw conclusion on the stability behavior present in the natural disturbance environment of the experiments.

To elaborate the effects of spanwise curvature, breakdown mechanisms for the flat-plate and the cylinder geometry are compared. Second-mode primary waves, three-dimensional and two-dimensional, govern the stability behavior for these geometries. First-mode waves only seem to play a minor role in initiating the transition on-set. Independent of the breakdown mechanism under investigation, spanwise convex curvature is reducing nonlinear interactions. Although linear amplification rates for the circular cone exceed amplification rates for the flat plate, the flat plate is nonlinearly the most unstable of these three geometries. Modes generated by nonlinear interactions are more numerous and also more strongly amplified for the flat plate than for the cylinder and the circular cone. Because spanwise curvature effects over the cone with its increasing radius and its almost constant boundary-layer thickness decrease in downstream direction, the front part of the slender cone is responsible for the increased stability. Therefore, the cylinder is the most stable configuration based on the considered ratio of the boundary-layer thickness to the radius.

Independent of geometry, steady streamwise vortex modes are destabilizing. When steady streamwise vortex modes are generated through a first-level interaction, as in the oblique fundamental resonance or fundamental breakdown (K-type), the destabilizing effects are exceptionally pronounced. This may be due to the stronger amplification of first-mode waves. Second-mode two-dimensional waves are virtually unaffected by the presence of the steady vortex mode and second-mode three-dimensional waves are only noticeably altered for the cone with a small nose radius. But the profoundly stronger amplification of first-mode waves, specifically for the fundamental breakdown, did not accelerate the transition process. Transition has to be already initiated as for the oblique subharmonic resonance before the stronger amplification of first-mode wave further pronounce the instability.

Considering the effects of nose bluntness on the stability behavior of a circular cone, three different nose radii following the experiments by Stetson *et al.* (1984), are studied—the sharp cone ($R_N = 0.0015$"), a small nose radius ($R_N = 0.15$") and a large nose radius ($R_N = 0.7$"). For the sharp circular cone and the cone with a small nose radius, second-mode three-dimensional waves, which travel more slowly than the free stream (subsonic disturbance), govern the stability behavior. The flow over the cone with the large nose radius is unstable to regular, non-inflectional disturbance waves. Conclusions for each nose radius are summarized as follows:

SHARP CONE: An oblique breakdown of second-mode waves as reported by Pruett & Chang (1995) shows strong nonlinear interactions and allows for the conclusion of the start-up of the transition process. But the strongest mechanisms within the scope of this investigation is the oblique fundamental resonance when a steady streamwise vortex mode is also present. Without the forced steady vortex mode, high-amplitude secondary waves, for both the oblique subharmonic and the oblique fundamental resonance (thus independent of their frequency), inhibit energy transfer to higher modes which reduces their amplification.

BLUNT CONE ($R_N = 0.15$"): The nose radius mainly affects the stability behavior of the front part of the cone. This in turn confirms the stabilizing effect as reported in the experiments by Stetson *et al.* (1984). The larger boundary-layer thickness reduces the unstable frequency range. Although linear amplification rates for a far downstream location are close to rates for the sharp cone, nonlinear interactions for all investigated breakdown scenarios are weakened. The destabilizing effects of steady streamwise vortex modes become increasingly important for all mechanisms except for the oblique fundamental resonance. As for the sharp cone, the oblique fundamental resonance is characterized by strong amplification of generated higher modes. Despite the fact that the developing higher modes are not quite as strongly amplified as for the sharp cone, the transition on-set will also eventually occur for the cone with a small nose radius—even though the destabilizing effects of a steady streamwise vortex mode are reduced for this breakdown.

BLUNT CONE ($R_N = 0.7$"): For the largest nose radius under investigation the stability characteristics obtained from numerical simulations by other investigators differ from those observed in experiments. The so-called transition reversal observed in experiments by Stetson *et al.* (1984) could not be found in numerical investigations by Rosenboom *et al.* (1999) or Zhong (2005).

In our investigations when disturbances were introduced through a blowing and suction slot at the wall confirmed the above mentioned numerical results, i.e. increasing the nose radius stabilized the flow. Our detailed investigations of the stability of the base-flow profiles revealed the possibility of "fast" instability waves—so-called regular disturbances (c.f. Mack (1984)). Small-amplitude (linear) stability investigations based on these regular disturbances, which are perturbed outside the boundary layer, show a short downstream instability region between $R_x = 1,200$ and $R_x = 1,400$ for these waves. With increasing disturbance amplitude, developing higher modes at larger wave angles are amplified farther downstream, therefore extending the instability region. With a high disturbance amplitude of 3% of the free-stream velocity transition is initiated. Because natural disturbances penetrated into the boundary layer in the experiments by Stetson *et al.* (1984), disturbances traveling faster than the free stream are also present. Based on our numerical results, the transition reversal observed in the experiments is caused by these "fast" disturbance waves explaining the discrepancies between earlier numerical and experimental investigations.

Appendix A: List of Vectors and Coefficients in the Governing Equations

Defining the sum of internal and kinetic energy as the total energy per unit volume in non-dimensional form

$$E_t = \rho \left(\frac{T}{\gamma(\gamma-1)Ma^2} + \frac{u_k u_k}{2} \right) , \tag{A.1}$$

together with the non-dimensional equation of state

$$p = \frac{\rho T}{\gamma Ma^2} \tag{A.2}$$

results in the following vectors for the equation:

$$\frac{\partial \mathbf{U}}{\partial t} + \frac{1}{h_1 h_2 h_3} \left[\frac{\partial h_2 h_3 \mathbf{E}}{\partial \xi} + \frac{\partial h_1 h_3 \mathbf{F}}{\partial \eta} + \frac{\partial h_1 h_2 \mathbf{G}}{\partial \varphi} + \mathbf{H} \right] = 0\,. \tag{A.3}$$

with

$$\mathbf{U} = \begin{bmatrix} \rho \\ \rho u \\ \rho v \\ \rho w \\ E_t \end{bmatrix} \tag{A.4}$$

$$\mathbf{E} = \begin{bmatrix} \rho u \\ \rho u^2 + p - \tau_{\xi\xi} \\ \rho u v - \tau_{\xi\eta} \\ \rho u w - \tau_{\xi\varphi} \\ (E_t + p)u - u\tau_{\xi\xi} - v\tau_{\xi\eta} - w\tau_{\xi\varphi} + q_\xi \end{bmatrix} \tag{A.5}$$

$$\mathbf{F} = \begin{bmatrix} \rho v \\ \rho u v - \tau_{\xi\eta} \\ \rho v^2 + p - \tau_{\eta\eta} \\ \rho v w - \tau_{\eta\varphi} \\ (E_t + p)v - u\tau_{\xi\eta} - v\tau_{\eta\eta} - w\tau_{\eta\varphi} + q_\eta \end{bmatrix} \tag{A.6}$$

$$\mathbf{G} = \begin{bmatrix} \rho w \\ \rho u w - \tau_{\xi\varphi} \\ \rho v w - \tau_{\eta\varphi} \\ \rho w^2 + p - \tau_{\varphi\varphi} \\ (E_t + p)w - u\tau_{\xi\varphi} - v\tau_{\eta\varphi} - w\tau_{\varphi\varphi} + q_\varphi \end{bmatrix} \tag{A.7}$$

$$\mathbf{H} = \mathbf{H_1} - \mathbf{H_2}\,, \tag{A.8}$$

where

$$\mathbf{H_1} = \begin{bmatrix} 0 \\ h_3\frac{\partial h_1}{\partial \eta}\left(\rho uv - \tau_{\xi\eta}\right) + h_2\frac{\partial h_1}{\partial \varphi}\left(\rho uw - \tau\xi\varphi\right) \\ h_3\frac{\partial h_2}{\partial \xi}\left(\rho uv - \tau_{\xi\eta}\right) + h_1\frac{\partial h_2}{\partial \varphi}\left(\rho vw - \tau_{\eta\varphi}\right) \\ h_2\frac{\partial h_3}{\partial \xi}\left(\rho uw - \tau\xi\varphi\right) + h_1\frac{\partial h_3}{\partial \eta}\left(\rho vw - \tau_{\eta\varphi}\right) \\ 0 \end{bmatrix} \tag{A.9}$$

and

$$\mathbf{H_2} = \begin{bmatrix} 0 \\ h_3\frac{\partial h_2}{\partial \xi}\left(\rho v^2 + p - \tau_{\eta\eta}\right) + h_2\frac{\partial h_3}{\partial \xi}\left(\rho w^2 + p - \tau_{\varphi\varphi}\right) \\ h_3\frac{\partial h_1}{\partial \eta}\left(\rho u^2 + p - \tau_{\xi\xi}\right) + h_1\frac{\partial h_3}{\partial \eta}\left(\rho w^2 + p - \tau_{\varphi\varphi}\right) \\ h_2\frac{\partial h_1}{\partial \varphi}\left(\rho u^2 + p - \tau_{\xi\xi}\right) + h_1\frac{\partial h_2}{\partial \varphi}\left(\rho v^2 + p - \tau_{\eta\eta}\right) \\ 0 \end{bmatrix}. \tag{A.10}$$

The normal stresses are computed with

$$\begin{aligned} \tau_{\xi\xi} &= \tfrac{2}{3}\tfrac{\mu}{Re}\left(2e_{\xi\xi} - e_{\eta\eta} - e_{\varphi\varphi}\right) \\ \tau_{\eta\eta} &= \tfrac{2}{3}\tfrac{\mu}{Re}\left(2e_{\eta\eta} - e_{\xi\xi} - e_{\varphi\varphi}\right) \\ \tau_{\varphi\varphi} &= \tfrac{2}{3}\tfrac{\mu}{Re}\left(2e_{\varphi\varphi} - e_{\xi\xi} - e_{\eta\eta}\right)\,, \end{aligned} \tag{A.11}$$

where

$$\begin{aligned} e_{\xi\xi} &= \tfrac{1}{h_1}\tfrac{\partial u}{\partial \xi} + \tfrac{v}{h_1 h_2}\tfrac{\partial h_1}{\partial \eta} + \tfrac{w}{h_1 h_3}\tfrac{\partial h_1}{\partial \varphi} \\ e_{\eta\eta} &= \tfrac{1}{h_2}\tfrac{\partial v}{\partial \eta} + \tfrac{w}{h_2 h_3}\tfrac{\partial h_2}{\partial \varphi} + \tfrac{u}{h_1 h_2}\tfrac{\partial h_2}{\partial \xi} \\ e_{\varphi\varphi} &= \tfrac{1}{h_3}\tfrac{\partial w}{\partial \varphi} + \tfrac{u}{h_1 h_3}\tfrac{\partial h_3}{\partial \xi} + \tfrac{v}{h_2 h_3}\tfrac{\partial h_3}{\partial \eta}\,. \end{aligned} \tag{A.12}$$

The shear stresses become

$$\begin{aligned} \tau_{\xi\eta} &= \tfrac{\mu}{Re}\left(\tfrac{h_2}{h_1}\tfrac{\partial}{\partial \xi}\left(\tfrac{v}{h_2}\right) + \tfrac{h_1}{h_2}\tfrac{\partial}{\partial \eta}\left(\tfrac{u}{h_1}\right)\right) \\ \tau_{\xi\varphi} &= \tfrac{\mu}{Re}\left(\tfrac{h_1}{h_3}\tfrac{\partial}{\partial \varphi}\left(\tfrac{u}{h_1}\right) + \tfrac{h_3}{h_1}\tfrac{\partial}{\partial \xi}\left(\tfrac{w}{h_3}\right)\right) \\ \tau_{\eta\varphi} &= \tfrac{\mu}{Re}\left(\tfrac{h_3}{h_2}\tfrac{\partial}{\partial \eta}\left(\tfrac{w}{h_3}\right) + \tfrac{h_2}{h_3}\tfrac{\partial}{\partial \varphi}\left(\tfrac{v}{h_2}\right)\right)\,, \end{aligned} \tag{A.13}$$

and the heat fluxes result in

$$\begin{aligned} q_\xi &= -\tfrac{\mu}{(\gamma-1)Ma^2 Re Pr}\tfrac{1}{h_1}\tfrac{\partial T}{\partial \xi} \\ q_\eta &= -\tfrac{\mu}{(\gamma-1)Ma^2 Re Pr}\tfrac{1}{h_2}\tfrac{\partial T}{\partial \eta} \\ q_\varphi &= -\tfrac{\mu}{(\gamma-1)Ma^2 Re Pr}\tfrac{1}{h_3}\tfrac{\partial T}{\partial \varphi}\,. \end{aligned} \tag{A.14}$$

The radius r is defined as $r = \xi \cdot sin\alpha + \eta \cdot cos\alpha$ and therefore the h_i-factors are:

Circular Cone

$$\begin{aligned} h_1 &= 1 \\ h_2 &= 1 \\ h_3 &= r \end{aligned} \tag{A.15}$$

Elliptical Cone

$$\begin{aligned} h_1 &= \sqrt{cos^2\alpha + \tfrac{sin^2\alpha}{1-e^2 sin^2\varphi}} \\ h_2 &= \sqrt{sin^2\alpha + \tfrac{cos^2\alpha}{1-e^2 sin^2\varphi}} \\ h_3 &= r\sqrt{\tfrac{cos^2\varphi+(e^2-1)^2 sin^2\varphi}{(1-e^2 sin^2\varphi)^3}}, \end{aligned} \tag{A.16}$$

with the eccentricity

$$e = \sqrt{1 - \frac{b^2}{a^2}}. \tag{A.17}$$

where a and b are the major and minor axis of the ellipse, respectively.

Appendix B: Postprocessing of Simulation Results

B.1 Amplitude Distribution Plots

Whenever amplitude plots are presented in this work, they are based on the maximal density amplitude within the flow field. Figure B.1 in which amplification curves of different flow quantities are graphed, reveals that the curves computed from the u- and v-velocity deviate significantly from those computed from other (mostly conservative) quantities and may therefore not be representative of the overall stability behavior.

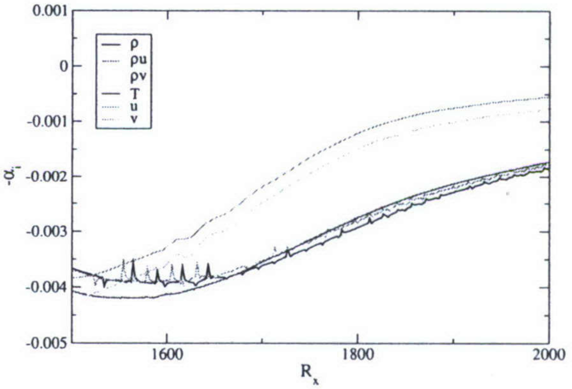

Figure B.1: Two-dimensional amplification rate based on various flow quantities. $Ma = 7.95$, $Re = 3,333,333$, $T_\infty = 53.35K$, $F = 1.17 \cdot 10^{-4}$, $A_{1,0} = 0.001\%$.

To obtain the density amplitude distribution, a Fourier transformation in time, the maximum in wall-normal direction of the density amplitude is taken for each downstream location. Because simulations for the flat-plate and the cylinder are computed with the flow conditions after the conical shock, amplitude levels also represent the relative magnitude of the disturbance waves in relation to the free stream of the mean flow. For the cone simulations, flow quantities are normalized with pre-shock conditions so that plotted values have to be divided by the density of the mean flow after the shock in order to obtain the relative magnitude of the disturbance wave to the mean flow (after the shock).

B.2 Vorticity

Although the vorticity does not appear explicitly in our formulation of the governing equations, equation (2.6), it is often calculated to aid identifying vortical structures. For the present work, the vorticity is defined as the negative curl of velocity.

$$\boldsymbol{\omega} = -\nabla \times \mathbf{u} \tag{B.1}$$

or, in scalar form,

$$\begin{aligned}
\omega_x &= \frac{1}{h_2 h_3}\frac{\partial h_2 v}{\partial \varphi} - \frac{\partial h_3 w}{\partial \eta} \\
\omega_y &= \frac{1}{h_1 h_3}\frac{\partial h_3 w}{\partial \xi} - \frac{\partial h_1 u}{\partial \varphi} \\
\omega_z &= \frac{1}{h_1 h_2}\frac{\partial h_1 u}{\partial \eta} - \frac{\partial h_2 v}{\partial \xi}\,.
\end{aligned}$$

The total vorticity is defined as the absolute value

$$\omega_t = \sqrt{\omega_x^2 + \omega_y^2 + \omega_z^2}\,.$$

B.3 Q-criterion

This so-called Q-criterion is the second invariant of the velocity gradient $\nabla \mathbf{u}$. It can be interpreted as the balance between strain and rotation. If rotation prevails strain, the Q-criterion is positive and per definition of Jeong & Hussain (1995) a vortex core is identified. A more thorough derivation for compressible (conical) flows with application of the Einstein summation convention follows:

$$Q = \frac{1}{2}\left(P^2 + W_{ij}W_{ij} - S_{ij}S_{ij}\right)\,, \tag{B.2}$$

with

$$P = -\frac{\partial u_i}{\partial x_j}\,,\; S_{ij} = \frac{1}{2}\left(\frac{\partial u_i}{\partial x_j} + \frac{\partial u_j}{\partial x_i}\right)\,,\; W_{ij} = \frac{1}{2}\left(\frac{\partial u_i}{\partial x_j} - \frac{\partial u_j}{\partial x_i}\right)\,.$$

In the incompressible case, P incorporates the continuity equation and is therefore zero. In the compressible case, P^2 cancels with terms of $S_{ij}S_{ij}$ so that the equation for the Q-criterion simplifies to

$$Q = \frac{1}{2}\left(W_{12}^2 + W_{13}^2 + W_{23}^2 - \left(S_{12}^2 + S_{13}^2 + S_{23}^2\right)\right) \tag{B.3}$$

with $W_{ii} = 0$.

In curvilinear coordinates the individual terms of the equation (B.3) are computed with:

$$\begin{aligned}
S_{12} = S_{21} &= \frac{h_2}{2h_1}\frac{\partial}{\partial \xi}\left(\frac{v}{h_2}\right) + \frac{h_1}{2h_2}\frac{\partial}{\partial \eta}\left(\frac{u}{h_1}\right)\\
S_{13} = S_{31} &= \frac{h_3}{2h_1}\frac{\partial}{\partial \xi}\left(\frac{w}{h_3}\right) + \frac{h_1}{2h_3}\frac{\partial}{\partial \varphi}\left(\frac{u}{h_1}\right)\\
S_{23} = S_{32} &= \frac{h_3}{2h_2}\frac{\partial}{\partial \eta}\left(\frac{w}{h_3}\right) + \frac{h_2}{2h_3}\frac{\partial}{\partial \varphi}\left(\frac{v}{h_2}\right)\\
W_{12} = -W_{21} &= \frac{h_2}{2h_1}\frac{\partial}{\partial \xi}\left(\frac{v}{h_2}\right) - \frac{h_1}{2h_2}\frac{\partial}{\partial \eta}\left(\frac{u}{h_1}\right)\\
W_{13} = -W_{31} &= \frac{h_3}{2h_1}\frac{\partial}{\partial \xi}\left(\frac{w}{h_3}\right) - \frac{h_1}{2h_3}\frac{\partial}{\partial \varphi}\left(\frac{u}{h_1}\right)\\
W_{23} = -W_{32} &= \frac{h_3}{2h_2}\frac{\partial}{\partial \eta}\left(\frac{w}{h_3}\right) - \frac{h_2}{2h_3}\frac{\partial}{\partial \varphi}\left(\frac{v}{h_2}\right)
\end{aligned}$$

For the flat plate, where $h_1 = h_2 = h_3 = 1$, the compressible formulation of the Q-criterion reduces to the incompressible equivalent. For the circular cone, Q is computed with

$$Q = -\left(\frac{\partial v}{\partial \xi}\frac{\partial u}{\partial \eta} + \frac{\partial v}{\partial \varphi}\frac{\partial}{\partial \eta}\left(\frac{w}{r}\right) + \frac{\partial u}{\partial \varphi}\frac{\partial}{\partial \xi}\left(\frac{w}{r}\right)\right) . \tag{B.4}$$

With this helpful tool at hand, it is still important to scan interesting amplitude levels during post-processing. Exemplary, Figure B.2 illustrates the difference of different iso-surfaces identified with the Q-criterion. Based on the contour level different conclusions about the flow stability behavior can be drawn—while in Figure B.2a the flow does not appear to have any significant vortex interactions, Figure B.2b shows

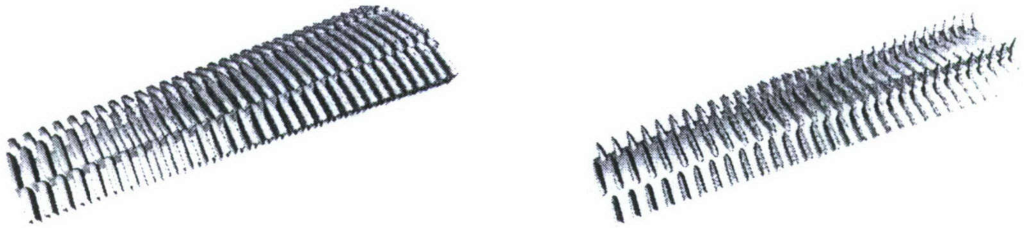

(a) $Q = 10$. (b) $Q = 500$.

Figure B.2: Example of flow structures identified by the Q-criterion for flow over a cone. $Ma = 7.95$, $Re = 3,333,333$, $T_\infty = 53.35K$.

a confinement of vortical structures which is an indication for a strong nonlinear behavior.

The advantages of vortex identification through the Q-criterion in comparison with vorticity becomes obvious when looking at Figure B.3. Here, the Q-criterion is compared with streamwise vorticity (ω_x), wall-normal vorticity (ω_y), spanwise vorticity (ω_z), and total vorticity (ω_t). All iso-surfaces are built at the same level. The streamwise vorticity mainly identifies the shear layer in between the vortical structures identified by the Q-criterion. The vorticity contours of spanwise and total vorticity incorporate both shear and rotation making it harder to identify vortical structures through vorticity due to a present shear layer in vicinity of the boundary layer edge. The wall-normal vorticity ($\omega_y = 10$) in Figure B.3b resembles more structures identified at a higher Q-iso-surface far downstream ($Q = 500$ in Figure B.2b). Comparing the terms for calculating both quantities allows for the conclusion that both, the change of the w-velocity in streamwise direction and the spanwise change in u-velocity gain importance far downstream. Because their difference is small (small ω_y) but their product large (high Q), it is assumed that both terms are in the same order of magnitude and therefore equally important.

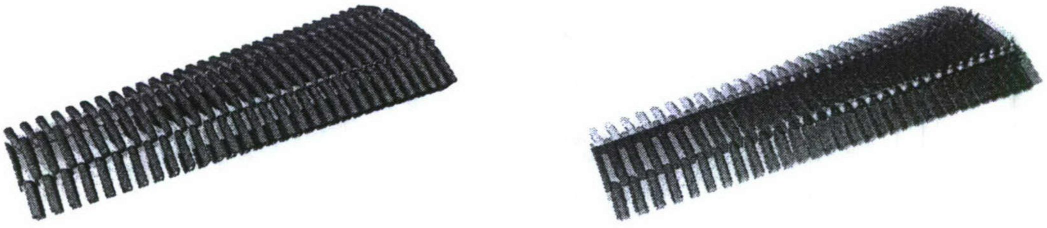

(a) streamwise vorticity ω_x.

(b) wall-normal vorticity ω_y.

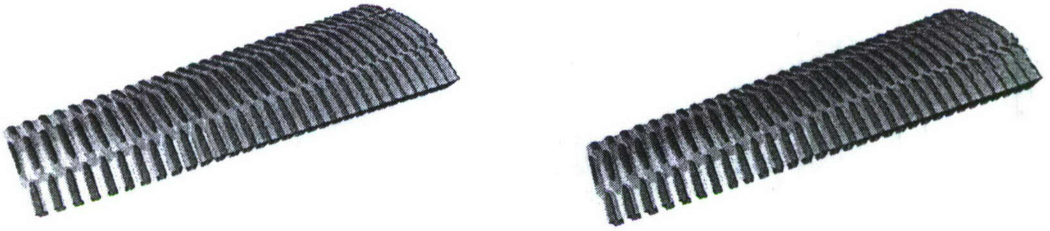

(c) spanwise vorticity ω_z.

(d) total vorticity ω_t.

Figure B.3: Comparison of flow structures identified by the Q-criterion ($Q = 10$) and by vorticity ($\omega_i = 10$). $Ma = 7.95$, $Re = 3,333,333$, $T_\infty = 53.35K$.

B.4 Displacement thickness

Pruett (1993) derives a formula for the displacement thickness of axisymmetric bodies. It is our understanding that when taking the limit of R to infinity, the compressible formulation for a flat-plate geometry is recovered. Therefore, the compressible displacement thickness as in Schlichting & Gersten (2001) instead of the formulation suggested by Pruett (1993) is used.

Appendix C: Computational Parameters

The acronyms to identify the different simulations are composed in Table C.1.

Validation	Simulation to compare base-flow properties
LST	Small-amplitude simulation to compare with *LST*
PULSE	simulation of a pulsed disturbance
OB1	Oblique breakdown of first-mode waves
OB2	Oblique breakdown of second-mode waves
OS1	Oblique subharmonic resonance of first-mode waves
OS1S	Oblique subharmonic resonance of first-mode waves with a forced steady streamwise vortex mode
OS2	Oblique subharmonic resonance of second-mode waves
OS2S	Oblique subharmonic resonance of second-mode waves with a forced steady streamwise vortex mode
OF1	Oblique fundamental resonance of first-mode waves
OF1S	Oblique fundamental resonance of first-mode waves with a forced steady streamwise vortex mode
OF2	Oblique fundamental resonance of second-mode waves
OF2S	Oblique fundamental resonance of second-mode waves with a forced steady streamwise vortex mode
2DSV	simulation of two-dimensional waves with a steady streamwise vortex mode forced
FB1	Fundamental breakdown (K-type) of first-mode secondary waves
FB1S	Fundamental breakdown (K-type) involving first-mode secondary waves and a perturbed steady streamwise vortex mode
FB2	Fundamental breakdown (K-type) involving second-mode secondary waves
SB1	Subharmonic breakdown (N-/H-type) of first-mode secondary waves
SB1S	Subharmonic breakdown (N-/H-type) involving first-mode secondary waves and a perturbed steady streamwise vortex mode
RLST	simulation of small-amplitude regular disturbance waves
ROB	Oblique breakdown of regular disturbance waves

Table C.1: Acronyms.

	Validation	LST	OB2	OB2
$dx \cdot 10^4$	6.38828	6.38828	6.38828	6.38828
$dy \cdot 10^5$	9	9	9	9
$dz \cdot 10^3$	-	4.425923	2.623749	2.623749
$dt \cdot 10^5$	1.12340208	1.12340208	1.12340208	1.12340208
n_x	1130	1130	1130	1130
n_y	300	300	300	300
n_z	-	3	9	9
x_{in}	0.2724355	0.2724355	0.2724355	0.2724355
x_{out}	0.993673	0.993673	0.993673	0.993673
y_{equi}	0.011	0.011	0.011	0.011
domain height	0.10125	0.10125	0.10125	0.10125
Re	4,790,000	4,790,000	4,790,000	4,790,000
Ma	6.8	6.8	6.8	6.8
$T_\infty[K]$	71	71	71	71
$F_{prim} \cdot 10^5$	8	4	8	8
Ψ_{prim}	-	60	20	20
$F_{sec} \cdot 10^5$	-	-	-	-
Ψ_{sec}	-	-	-	-
$A_{prim}[\%]$	0.001	0.001	1	5
$A_{sec}[\%]$	-	-	-	-
$A_{steady}[\%]$	-	-	-	-

Table C.2: Computational parameter. Flat plate.

	OS2	OS2S	OF2	OF2S	OF2
$dx \cdot 10^4$	6.38828	6.38828	6.38828	6.38828	6.38828
$dy \cdot 10^5$	9	9	9	9	9
$dz \cdot 10^3$	2.632749	2.632749	2.623749	2.623749	2.632749
$dt \cdot 10^5$	1.12340208	1.12340208	1.12340208	1.12340208	1.12340208
n_x	1130	1130	1130	1130	1130
n_y	300	300	300	300	300
n_z	9	9	9	9	9
x_{in}	0.2724355	0.2724355	0.2724355	0.2724355	0.2724355
x_{out}	0.993673	0.993673	0.993673	0.993673	0.993673
y_{equi}	0.011	0.011	0.011	0.011	0.011
domain height	0.10125	0.10125	0.10125	0.10125	0.10125
Re	4,790,000	4,790,000	4,790,000	4,790,000	4,790,000
Ma	6.8	6.8	6.8	6.8	6.8
$T_\infty[K]$	71	71	71	71	71
$F_{prim} \cdot 10^5$	8	8	8	8	8
Ψ_{prim}	20	20	20	20	20
$F_{sec} \cdot 10^5$	4	4	8	8	8
Ψ_{sec}	36	36	36	36	36
$A_{prim}[\%]$	5	2	5	1	1
$A_{sec}[\%]$	5	2	5	1	1
$A_{steady}[\%]$	-	1	-	1	-

Table C.3: Computational parameter. Flat plate.

	FB1	FB1S	FB1S	SB1	SB1S
$dx \cdot 10^4$	6.38828	6.38828	6.38828	6.38828	6.38828
$dy \cdot 10^5$	9	9	9	9	9
$dz \cdot 10^3$	0.5532221	0.5532221	0.5532221	1.105355	1.105355
$dt \cdot 10^5$	1.12340208	1.12340208	1.12340208	1.12340208	1.12340208
n_x	1130	1130	1130	1130	1130
n_y	300	300	300	300	300
n_z	9	9	9	9	9
x_{in}	0.2724355	0.2724355	0.2724355	0.2724355	0.2724355
x_{out}	0.993673	0.993673	0.993673	0.993673	0.993673
y_{equi}	0.011	0.011	0.011	0.011	0.011
domain height	0.10125	0.10125	0.10125	0.10125	0.10125
Re	4,790,000	4,790,000	4,790,000	4,790,000	4,790,000
Ma	6.8	6.8	6.8	6.8	6.8
$T_\infty[K]$	71	71	71	71	71
$F_{prim} \cdot 10^5$	8	8	8	8	8
Ψ_{prim}	0	0	0	0	0
$F_{sec} \cdot 10^5$	8	8	8	4	4
Ψ_{sec}	60	60	60	60	60
$A_{prim}[\%]$	5	5	5	5	5
$A_{sec}[\%]$	0.001	0.001	0.001	0.01	0.01
$A_{steady}[\%]$	-	1	5	1	1

Table C.4: Computational parameter. Flat plate.

	LST	LST	OB2	OB2	OB2
$dx \cdot 10^4$	6.38828	6.38828	6.38828	6.38828	6.38828
$dy \cdot 10^5$	3	3	3	3	3
$d\varphi \cdot 10^2$	-	13.33305	7.9296	7.9296	7.9296
$dt \cdot 10^5$	1.12340208	1.12340208	1.12340208	1.12340208	1.12340208
n_x	1130	1130	1130	1130	1130
n_y	600	600	600	600	600
n_z	-	3	9	9	9
$R_{in} \cdot 10^2$	3.32	3.32	3.32	3.32	3.32
x_{in}	0.2724355	0.2724355	0.2724355	0.2724355	0.501136
x_{out}	0.993673	0.993673	0.993673	0.993673	1.222373
y_{equi}	0.012	0.012	0.012	0.012	0.012
domain height	0.09558	0.09558	0.09558	0.09558	0.09558
Re	4,790,000	4,790,000	4,790,000	4,790,000	4,790,000
Ma	6.8	6.8	6.8	6.8	6.8
$T_\infty[K]$	71	71	71	71	71
$F_{prim} \cdot 10^5$	8	4	8	8	8
Ψ_{prim}	0	60	20	20	20
$F_{sec} \cdot 10^5$	-	-	-	-	-
Ψ_{sec}	-	-	-	-	-
$A_{prim}[\%]$	0.001	0.001	1	5	5
$A_{sec}[\%]$	-	-	-	-	-
$A_{steady}[\%]$	-	-	-	-	-

Table C.5: Computational parameter. Cylinder.

	OS2	OS2S	OF2	OF2S
$dx \cdot 10^4$	6.38828	6.38828	6.38828	6.38828
$dy \cdot 10^5$	3	3	3	3
$d\varphi \cdot 10^2$	7.9296	7.9296	7.9296	7.9296
$dt \cdot 10^5$	1.12340208	1.12340208	1.12340208	1.12340208
n_x	1130	1130	1130	1130
n_y	600	600	600	600
n_z	9	9	9	9
$R_{in} \cdot 10^2$	3.32	3.32	3.32	3.32
x_{in}	0.501136	0.501136	0.2724355	0.2724355
x_{out}	1.222373	1.222373	0.993673	0.993673
y_{equi}	0.012	0.012	0.012	0.012
domain height	0.09558	0.09558	0.09558	0.09558
Re	4,790,000	4,790,000	4,790,000	4,790,000
Ma	6.8	6.8	6.8	6.8
$T_\infty[K]$	71	71	71	71
$F_{prim} \cdot 10^5$	8	8	8	8
Ψ_{prim}	20	20	20	20
$F_{sec} \cdot 10^5$	4	4	8	8
Ψ_{sec}	36	36	36	36
$A_{prim}[\%]$	2	2	2	2
$A_{sec}[\%]$	2	2	2	2
$A_{steady}[\%]$	-	1	-	1

Table C.6: Computational parameter. Cylinder.

	FB1	FB1S	SB1	SB1S
$dx \cdot 10^4$	6.38828	6.38828	6.38828	6.38828
$dy \cdot 10^5$	3	3	3	3
$d\varphi \cdot 10^2$	1.6663	1.6663	3.332625	3.332625
$dt \cdot 10^5$	1.12340208	1.12340208	1.12340208	1.12340208
n_x	1130	1130	1130	1130
n_y	600	600	600	600
n_z	9	9	9	9
$R_{in} \cdot 10^2$	3.32	3.32	3.32	3.32
x_{in}	0.501136	0.501136	0.2724355	0.2724355
x_{out}	1.222373	1.222373	0.993673	0.993673
y_{equi}	0.012	0.012	0.012	0.012
domain height	0.09558	0.09558	0.09558	0.09558
Re	4,790,000	4,790,000	4,790,000	4,790,000
Ma	6.8	6.8	6.8	6.8
$T_\infty[K]$	71	71	71	71
$F_{prim} \cdot 10^5$	8	8	8	8
Ψ_{prim}	0	0	0	0
$F_{sec} \cdot 10^5$	8	8	4	4
Ψ_{sec}	60	60	60	60
$A_{prim}[\%]$	5	5	5	5
$A_{sec}[\%]$	0.001	0.001	0.001	0.001
$A_{steady}[\%]$	-	1	-	1

Table C.7: Computational parameter. Cylinder.

	LST	LST/PULSE	OB1	OB2
$dx \cdot 10^4$	6.38828	6.38828	6.38828	1.59707
$dy \cdot 10^5$	3	3	3	2
$d\varphi \cdot 10^2$	-	various	3.332624	0.6871746
$dt \cdot 10^5$	1.12340208	1.12340208	1.12340208	0.561701
n_x	1130	1130	1130	2925
n_y	261	261	261	385
n_z	-	various	9	65
x_{in}	0.2724355	0.2724355	0.2724355	0.2724355
x_{out}	0.993673	0.993673	0.993673	0.993673
y_{equi}	0.005864	0.005864	0.005864	0.005864
domain height	0.015925	0.015925	0.015925	0.015925
Re	3,333,333	3,333,333	3,333,333	3,333,333
Ma	7.95	7.95	7.95	7.95
$T_\infty[K]$	53.35	53.35	53.35	53.35
$F_{prim} \cdot 10^5$	11.7	11.7	4.9	11.7
Ψ_{prim}	0	various	60	20
$F_{sec} \cdot 10^5$	-	-	-	-
Ψ_{sec}	-	-	-	-
$A_{prim}[\%]$	various	various	1	1
$A_{sec}[\%]$	-	-	-	-
$A_{steady}[\%]$	-	-	-	-

Table C.8: Computational parameter. Sharp cone.

	OS2	OS2S	OF2	OF2S
$dx \cdot 10^4$	6.38828	6.38828	6.38828	1.59707
$dy \cdot 10^5$	3	3	3	2
$d\varphi \cdot 10^2$	1.465972	1.465972	5.497396	0.6225228
$dt \cdot 10^5$	1.12340208	1.12340208	1.12340208	0.561701
n_x	1130	1130	1130	2925
n_y	261	261	261	385
n_z	31	31	9	65
x_{in}	0.2724355	0.2724355	0.2724355	0.2724355
x_{out}	0.993673	0.993673	0.993673	0.993673
y_{equi}	0.005864	0.005864	0.005864	0.005864
domain height	0.015925	0.015925	0.015925	0.015925
Re	3,333,333	3,333,333	3,333,333	3,333,333
Ma	7.95	7.95	7.95	7.95
$T_\infty[K]$	53.35	53.35	53.35	53.35
$F_{prim} \cdot 10^5$	11.7	9.8	1.17	9.8
Ψ_{prim}	20	20	20	20
$F_{sec} \cdot 10^5$	5.85	4.9	1.17	9.8
Ψ_{sec}	36	36	36	36
$A_{prim}[\%]$	1	1	1	0.3
$A_{sec}[\%]$	1	1	various	0.3
$A_{steady}[\%]$	-	1	-	0.3

Table C.9: Computational parameter. Sharp cone.

	2DSV	2DSV	FB1	FB1S
$dx \cdot 10^4$	6.38828	6.38828	6.38828	6.38828
$dy \cdot 10^5$	3	3	3	3
$d\varphi \cdot 10^2$	5.497396	1.110864	1.249612	0.3332298
$dt \cdot 10^5$	1.12340208	1.12340208	1.12340208	1.12340208
n_x	1130	1130	1130	1130
n_y	261	261	261	261
n_z	9	9	9	31
x_{in}	0.2724355	0.2724355	0.2724355	0.2724355
x_{out}	0.993673	0.993673	0.993673	0.993673
y_{equi}	0.005864	0.005864	0.005864	0.005864
domain height	0.015925	0.015925	0.015925	0.015925
Re	3,333,333	3,333,333	3,333,333	3,333,333
Ma	7.95	7.95	7.95	7.95
$T_\infty[K]$	53.35	53.35	53.35	53.35
$F_{prim} \cdot 10^5$	11.7	11.7	9.8	9.8
Ψ_{prim}	0	0	0	0
$F_{sec} \cdot 10^5$	0	0	9.8	9.8
Ψ_{sec}	20	60	60	60
$A_{prim}[\%]$	1	1	1	1
$A_{sec}[\%]$	-	-	0.001	0.001
$A_{steady}[\%]$	various	various	-	1

Table C.10: Computational parameter. Sharp cone.

	FB2	FB1	SB1	SB1S
$dx \cdot 10^4$	2.129427	2.129427	6.38828	6.38828
$dy \cdot 10^5$	2	2	3	3
$d\varphi \cdot 10^2$	4.980182	2.310435	3.332625	3.332625
$dt \cdot 10^5$	0.3229781	0.3229781	1.12340208	1.12340208
n_x	3745	3745	1130	1130
n_y	440	440	261	261
n_z	9	9	9	9
x_{in}	0.2724355	0.2724355	0.2724355	0.2724355
x_{out}	0.993673	0.993673	0.993673	0.993673
y_{equi}	0.005864	0.005864	0.005864	0.005864
domain height	0.015925	0.015925	0.015925	0.015925
Re	3,333,333	3,333,333	3,333,333	3,333,333
Ma	7.95	7.95	7.95	7.95
$T_\infty[K]$	53.35	53.35	53.35	53.35
$F_{prim} \cdot 10^5$	9.8	9.8	9.8	9.8
Ψ_{prim}	0	0	0	0
$F_{sec} \cdot 10^5$	9.8	9.8	4.9	4.9
Ψ_{sec}	20	43	60	60
$A_{prim}[\%]$	1	1	1	1
$A_{sec}[\%]$	0.001	0.001	0.001	0.001
$A_{steady}[\%]$	-	-	-	1

Table C.11: Computational parameter. Sharp cone.

	Validation	Validation	PULSE	OB1	OB2
$dx \cdot 10^4$	6.38828	6.38828	6.38828	6.38828	6.38828
$dy \cdot 10^5$	2	3	3	3	3
$d\varphi \cdot 10^2$	-	-	5.497396	1.575702	5.497396
$dt \cdot 10^5$	1.12340208	1.12340208	1.12340208	1.12340208	1.12340208
n_x	1330	1330	1330	1330	1330
n_y	340	296	296	296	296
n_z	-	-	9	9	9
x_{in}	0.1672013	0.271137	0.271137	0.271137	0.271137
x_{out}	1.016203	1.100975	1.100975	1.100975	1.100975
y_{equi}	0.0036	0.0065	0.0065	0.0065	0.0065
domain height	0.01638	0.015924	0.015924	0.015924	0.015924
Re	8,566,826	3,333,333	3,333,333	3,333,333	3,333,333
Ma	7.99	7.95	7.95	7.95	7.95
$T_\infty[K]$	54.47	53.35	53.35	53.35	53.35
$F_{prim} \cdot 10^5$	-	-	11.7	4.9	11.7
Ψ_{prim}	-	-	various	70	20
$F_{sec} \cdot 10^5$	-	-	-	-	-
Ψ_{sec}	-	-	-	-	-
$A_{prim}[\%]$	-	-	0.001	1	1
$A_{sec}[\%]$	-	-	-	-	-
$A_{steady}[\%]$	-	-	-	-	-

Table C.12: Computational parameter. Blunt cone ($R_N = 0.15"$).

	OS1	OS1S	OS2	OS2S
$dx \cdot 10^4$	6.38828	6.38828	6.38828	6.38828
$dy \cdot 10^5$	3	3	3	3
$d\varphi \cdot 10^2$	1.575702	1.575702	4.980182	4.980182
$dt \cdot 10^5$	1.12340208	1.12340208	1.12340208	1.12340208
n_x	1330	1330	1330	1130
n_y	296	296	296	261
n_z	9	9	9	9
x_{in}	0.271137	0.271137	0.271137	0.271137
x_{out}	1.100975	1.100975	1.100975	1.100975
y_{equi}	0.0065	0.0065	0.0065	0.0065
domain height	0.015924	0.015924	0.015924	0.015924
Re	3,333,333	3,333,333	3,333,333	3,333,333
Ma	7.95	7.95	7.95	7.95
$T_\infty[K]$	53.35	53.35	53.35	53.35
$F_{prim} \cdot 10^5$	4.9	4.9	9.8	9.8
Ψ_{prim}	70	70	20	20
$F_{sec} \cdot 10^5$	2.45	2.45	4.9	4.9
Ψ_{sec}	80	80	36	36
$A_{prim}[\%]$	1	1	1	1
$A_{sec}[\%]$	1	1	1	1
$A_{steady}[\%]$	-	-	-	1

Table C.13: Computational parameter. Blunt cone ($R_N = 0.15$").

	OF1	OF1S	OF2	OF2S	FB1
$dx \cdot 10^4$	6.38828	6.38828	6.38828	6.38828	6.38828
$dy \cdot 10^5$	3	3	3	3	3
$d\varphi \cdot 10^2$	1.575702	1.575702	4.980182	4.980182	2.319367
$dt \cdot 10^5$	1.12340208	1.12340208	1.12340208	1.12340208	1.12340208
n_x	1330	1330	1330	1330	1330
n_y	296	296	296	296	296
n_z	9	9	9	9	9
x_{in}	0.271137	0.271137	0.271137	0.271137	0.271137
x_{out}	1.100975	1.100975	1.100975	1.100975	1.100975
y_{equi}	0.0065	0.0065	0.0065	0.0065	0.0065
domain height	0.015924	0.015924	0.015924	0.015924	0.015924
Re	3,333,333	3,333,333	3,333,333	3,333,333	3,333,333
Ma	7.95	7.95	7.95	7.95	7.95
$T_\infty[K]$	53.35	53.35	53.35	53.35	53.35
$F_{prim} \cdot 10^5$	4.9	4.9	9.8	9.8	9.8
Ψ_{prim}	70	70	20	20	0
$F_{sec} \cdot 10^5$	4.9	4.9	9.8	9.8	9.8
Ψ_{sec}	80	80	36	36	41
$A_{prim}[\%]$	1	1	1	1	1
$A_{sec}[\%]$	1	1	1	1	0.001
$A_{steady}[\%]$	-	1	-	1	-

Table C.14: Computational parameter. Blunt cone ($R_N = 0.15$").

	FB1S	FB1	FB1S	SB1	SB1S
$dx \cdot 10^4$	6.38828	6.38828	6.38828	6.38828	6.38828
$dy \cdot 10^5$	3	3	3	3	3
$d\varphi \cdot 10^2$	1.236996	1.164051	1.164051	1.332919	1.332919
$dt \cdot 10^5$	1.12340208	1.12340208	1.12340208	1.12340208	1.12340208
n_x	1330	1330	1330	1330	1330
n_y	296	296	296	296	296
n_z	16	9	9	16	16
x_{in}	0.271137	0.271137	0.271137	0.271137	0.271137
x_{out}	1.100975	1.100975	1.100975	1.100975	1.100975
y_{equi}	0.0065	0.0065	0.0065	0.0065	0.0065
domain height	0.015924	0.015924	0.015924	0.015924	0.015924
Re	3,333,333	3,333,333	3,333,333	3,333,333	3,333,333
Ma	7.95	7.95	7.95	7.95	7.95
$T_\infty[K]$	53.35	53.35	53.35	53.35	53.35
$F_{prim} \cdot 10^5$	9.8	9.8	9.8	9.8	9.8
Ψ_{prim}	0	0	0	0	0
$F_{sec} \cdot 10^5$	9.8	9.8	9.8	4.9	4.9
Ψ_{sec}	41	60	60	60	60
$A_{prim}[\%]$	1	1	1	1	1
$A_{sec}[\%]$	0.001	0.001	0.001	0.001	0.001
$A_{steady}[\%]$	1	-	1	-	1

Table C.15: Computational parameter. Blunt cone ($R_N = 0.15$").

	Validation	PULSE	OB1	OB1
$dx \cdot 10^4$	6.38828	12.77656	6.38828	12.77656
$dy \cdot 10^4$	1	1	1	1
$d\varphi \cdot 10^2$	-	5.497396	2.383072	5.55732
$dt \cdot 10^5$	3.370206	3.370206	1.12340208	1.12340208
n_x	827	599	1200	599
n_y	125	157	157	157
n_z	-	9	9	9
x_{in}	0.193904	0.2947638	0.2947638	0.2947638
x_{out}	0.721575	1.058801	1.058801	1.058801
y_{equi}	0.0	0.0	0.0	0.0
domain height	0.023977	0.038948	0.038948	0.038948
Re	3,333,333	3,333,333	3,333,333	3,333,333
Ma	7.95	7.95	7.95	7.95
$T_\infty[K]$	53.35	53.35	53.35	53.35
$F_{prim} \cdot 10^5$	-	various	4.9	3.625
Ψ_{prim}	-	various	55	52
$F_{sec} \cdot 10^5$	-	-	-	-
Ψ_{sec}	-	-	-	-
$A_{prim}[\%]$	-	0.001	5	5
$A_{sec}[\%]$	-	-	-	-
$A_{steady}[\%]$	-	-	-	-

Table C.16: Computational parameter. Blunt cone ($R_N = 0.7$").

	LST	ROB
$dx \cdot 10^4$	6.38828	6.38828
$dy \cdot 10^5$	5	5
$d\varphi \cdot 10^2$	4.980182	various
$dt \cdot 10^5$	1.12340208	1.12340208
n_x	1300	1300
n_y	325	325
n_z	9	various
x_{in}	0.2362447	0.2362447
x_{out}	1.066082	1.066082
y_{equi}	0.012	0.012
domain height	0.028702	0.028702
Re	3,333,333	3,333,333
Ma	7.95	7.95
$T_\infty[K]$	53.35	53.35
$F_{prim} \cdot 10^5$	3.625	3.625
Ψ_{prim}	60	60
$F_{sec} \cdot 10^5$	-	-
Ψ_{sec}	-	-
$A_{prim}[\%]$	-	various
$A_{sec}[\%]$	-	-
$A_{steady}[\%]$	-	-

Table C.17: Computational parameter. Blunt cone ($R_N = 0.7$").

		CFUND 1	CFUND 2	CFUND 3
Flow properties:				
Re_1	[1/m]	$6.6E6$	$6.6E6$	$6.6E6$
Ma	[-]	2.00	2.00	2.00
T^*_∞	[K]	160.00	160.00	160.00
Pr	[-]	0.71	0.71	0.71
κ	[-]	1.40	1.40	1.40
Forcing properties:				
f^*	[kHz]	20.00	20.00	20.00
$\tilde{A}(\beta)$	[-]	$1.0E-7$	Mayer *et al.* (2007)	Mayer *et al.* (2007)
$\tilde{\theta}(\beta)$	[-]	0.00	figure 5.7b	figure 5.7b
Domain size:				
x_0	[-]	0.020	0.020	0.020
x_L	[-]	0.097	0.172	0.172
y_H	[-]	0.035	0.035	0.035
z_W	[-]	0.063	0.063	0.063
Forcing location:				
x_1	[-]	0.029	0.029	0.029
x_2	[-]	0.038	0.038	0.038
Buffer domain:				
x_3	[-]	0.069	0.142	0.142
Grid size:				
n_x	[-]	163	318	318
n_y	[-]	651	651	651
n_z	[-]	161	161	81
Grid resolution:				
Δt	[-]	$1.25E-5$	$1.25E-5$	$1.25E-5$
Δx (infl.)	[-]	$4.80E-4$	$4.80E-4$	$4.80E-4$
Δx (outfl.)	[-]	$4.80E-4$	$4.80E-4$	$4.80E-4$
Δy (wall)	[-]	$1.25E-5$	$1.25E-5$	$1.25E-5$
Δy (free)	[-]	$1.37E-4$	$1.37E-4$	$1.37E-4$

Table C.18: Parameters used for simulations of a flat-plate boundary layer at Mach 2.

		CFUND 4	CFUND 5
Flow properties:			
Re_1	[1/m]	$6.6E6$	$6.6E6$
Ma	[-]	2.00	2.00
T^*_∞	[K]	160.00	160.00
Pr	[-]	0.71	0.71
κ	[-]	1.40	1.40
Forcing properties:			
f^*	[kHz]	20.00	20.00
$\tilde{A}(\beta)$	[-]	Mayer *et al.* (2007)	Mayer *et al.* (2007)
$\tilde{\theta}(\beta)$	[-]	figure 5.7b	figure 5.7b
Domain size:			
x_0	[-]	0.020	0.020
x_L	[-]	0.172	0.181
y_H	[-]	0.035	0.035
z_W	[-]	0.063	0.063
Forcing location:			
x_1	[-]	0.029	0.029
x_2	[-]	0.038	0.038
Buffer domain:			
x_3	[-]	0.142	0.155
Grid size:			
n_x	[-]	318	651
n_y	[-]	651	651
n_z	[-]	81	161
Grid resolution:			
Δt	[-]	$1.25E-5$	$1.25E-5$
Δx (infl.)	[-]	$4.80E-4$	$4.80E-4$
Δx (outfl.)	[-]	$4.80E-4$	$1.20E-4$
Δy (wall)	[-]	$1.25E-5$	$1.25E-5$
Δy (free)	[-]	$1.37E-4$	$1.37E-4$

Table C.19: Parameters used for simulations of a flat-plate boundary layer at Mach 2.

		CSUB 1	CSUB 10
Flow properties:			
Re_1	[1/m]	$6.6E6$	$6.6E6$
Ma	[-]	2.00	2.00
T^*_∞	[K]	160.00	160.00
Pr	[-]	0.71	0.71
κ	[-]	1.40	1.40
Forcing properties:			
f_1^*	[kHz]	20.00	20.00
$\tilde{A}_1$	[-]	Mayer & Fasel (2008)	Mayer & Fasel (2008)
θ_p	[-]	figure 5.7b	figure 5.7b
f_2^*	[kHz]	10.00	10.00
$\tilde{A}_2$	[-]	$5.0E-6$	$5.0E-6$
$\Delta\theta_p^{2D}/\pi$	[-]	0.00	-0.30
Domain size:			
x_0	[-]	0.020	0.020
x_L	[-]	0.106	0.172
y_H	[-]	0.024	0.035
z_W	[-]	0.063	0.063
Forcing location:			
x_1	[-]	0.029	0.029
x_2	[-]	0.038	0.038
Buffer domain:			
x_3	[-]	-	0.142
Grid size:			
n_x	[-]	181	318
n_y	[-]	451	651
n_z	[-]	161	161
Grid resolution:			
Δt	[-]	$1.25E-5$	$1.25E-5$
Δx (infl.)	[-]	$4.80E-4$	$4.80E-4$
Δx (outfl.)	[-]	$4.80E-4$	$4.80E-4$
Δy (wall)	[-]	$1.25E-5$	$1.25E-5$
Δy (free)	[-]	$1.37E-4$	$1.37E-4$

Table C.20: Parameters used for simulations of a flat-plate boundary layer at Mach 2. See table 5.2 and table 5.3 for CSUB 2-9.

References

ADAMS, N. A. & SANDHAM, N. A. 1993 Numerical simulation of boundary-layer transition at Mach two. *Appl. Sci. Res.* **51**, 371–375.

BALZER, W. 2003 Investigation of supersonic wakes using temporal direct numerical siumulations. Master's thesis, Universität Stuttgart.

BESTEK, H. & EISSLER, W. 1996 Direct numerical simulation of transition in Mach 4.8 boundary layers at flight conditions. Engineering turbulence modelling and experiments 3(Rodi and Bergeles, eds). Elsevier Science B.V.

BOUNTIN, D. A., SHIPLYUK, A. N., MASLOV, A. A. & CHOKANI, N. 2004 Nonlinear aspects of hypersonic boundary layer stability on a porous surface. *AIAA Paper* **04-0255**, 42nd aerospace sciences meeting, Reno NV, Jan. 2004.

BROWN, G. L. & FAN, X. 2003 Private Communication.

BROWN, G. L. & GRAZIOSI, P. 2002 Experiments on stability and transition at Mach 3. *J. Fluid Mech.* **472**, 83–124.

CHANG, C.-L. & MALIK, M. R. 1993*a* Linear and nonlinear PSE for compressible boundary layers. NASA-CR 191537. National Advisory Committee for Aeronautics.

CHANG, C.-L. & MALIK, M. R. 1993*b* Non-parallel stability of compressible boundary layers. *AIAA Paper* **93-2912**.

CHANG, C.-L. & MALIK, M. R. 1994 Oblique-mode breakdown and secondary instability in supersonic boundary layers. *J. Fluid Mech.* **273**, 323–360.

CHANG, C.-L., MALIK, M. R. & VINH, H. 1995 Linear and nonlinear stability of compressible swept-wing boundary layers. *AIAA Paper* **95-2278**.

CHOKANI, N. 1999 Nonlinear spectral dynamics of hypersonic laminar boundary layer flow. *Phys. Fluids* **11** (12), 3846–3851.

CHOKANI, N. 2000*a* Wave modulation in the transition of a hypersonic boundary layer flow. *AIAA Paper* **00-2653**.

CHOKANI, N. 2000*b* Wavelet analysis of a hypersonic laminar boundary layer flow. *AIAA Paper* **00-0535**.

CORKE, T. C., CAVALIERI, D. A. & MATLIS, E. 2002 Boundary-layer instability on sharp cone at Mach 3.5 with controlled input. *AIAA J.* **40** (5), 1015–1018.

CRAIK, A. D. D. 1971 Nonlinear resonant instability in boundary layers. *J. Fluid Mech.* **50**, 393–413.

DOGGETT, G. P., CHOKANI, N. & WILKINSON, S. P. 1997 Effect of angle of attack on hypersonic boundary-layer stability. *AIAA J.* **35** (3), 464–470.

EISSLER, W. 1995 Numerische Untersuchungen zum laminar-turbulenten Strömungsumschlag in Überschallgrenzschichten. PhD thesis, Universität Stuttgart.

ERMOLAEV, Y. G., KOSINOV, A. D. & SEMIONOV, N. V. 1996 Experimental investigation of laminar-turbulent transition in supersonic boundary layer using controlled disturbances. *Nonlinear Instability and Transition in Three-Dimensional Boundary Layers, IUTAM Symposium, Manchester, U.K., 1995.* Kluwer Academic Publishers.

FASEL, H. F., THUMM, A. & BESTEK, H. 1993 Direct numerical simulation of transition in supersonic boundary layer: Oblique breakdown. Transitional and turbulent compressible flows(L.D. Kral and T.A. Zang, eds). ASME, New York.

FEZER, A. & KLOKER, M. 1999 Spatial direct numerical simulation of transition phenomena in supersonic flat-plate boundary layers. In *Laminar-Turbulent Transition* (ed. H. F. Fasel & W. S. Saric), pp. 415–420. Springer.

FEZER, A. & KLOKER, M. 2004 Grenzschichtumschlag bei Überschallströmungen. *Sonderforschungsbericht 259* **Teilprojekt C4**, 391–419.

GASTER, M. 1962 A note on the relation between temporally-increasing and spatially-increasing disturbances in hydrodynamic stability. *J. Fluid Mech.* **138**, 222–224.

GRAZIOSI, P. 1999 An experimental investigation on stability and transition at Mach 3. PhD thesis, Princeton University.

HARRIS, P. J. 1995 Numerical investigation of the supersonic plane wake using the compressible Navier-Stokes equations. Master's report, The University of Arizona.

HARRIS, P. J. 1997 Numerical investigation of transitional compressible plane wakes. PhD thesis, The University of Arizona.

HERBERT, T. 1984 Analysis of the subharmonic route to transition in boundary layers. *AIAA Paper* **84-0009**.

HERBERT, T. 1988 Secondary instability of boundary layers. *Ann. Rev. Fluid Mech.* **20**, 487–526.

HORVATH, T. 2002 Boundary layer transition on slender cones in conventional and low disturbance Mach 6 wind tunnels. *AIAA Paper* **02-2743**.

HUSMEIER, F. 2002 Stability investigation of a flat-plate boundary layer at mach 3. Master's thesis, University of Arizona.

HUSMEIER, F., MAYER, C. S. & FASEL, H. F. 2005 Investigation of transition of supersonic boundary layers at Mach 3 using DNS. *AIAA Paper* **2005-0095**.

JEONG, J. & HUSSAIN, F. 1995 On the identification of a vortex. *J. Fluid Mech.* **285**, 69–94.

KACHANOV, Y. S. & LEVCHENKO, V. Y. 1984 The resonant interaction of disturbances at laminar-turbulent transition in a boundary layer. *J. Fluid Mech.* **138**, 209–247.

KIM, J. W. & DUCK, J. L. 2000 Generalized characteristic boundary conditions for computational aeroacoustics. *AIAA J.* **38** (11), 2040–2049.

KIMMEL, R. L., KLEIN, M. A. & SCHWOERKE, S. N. 1997 Laminar-turbulent transition in a Mach 8 elliptic cone flow. *Journal of Spacecraft and Rockets* **34** (4), 409–415.

KIMMEL, R. L., POGGIE, J. & SCHWOERKE, S. N. 1999 Laminar-turbulent transition in a Mach 8 elliptic cone flow. *AIAA J.* **37**, 1080–1087.

KLEBANOFF, P. S., TIDSTROM, K. D. & SARGENT, L. 1962 The three-dimensional nature of boundary-layer instability. *J. Fluid Mech.* **12**, 1–34.

KLOKER, M. J. 2002 DNS of transitional boundary-layer flows at sub- and hypersonic speeds. Proc. DGLR Congress, Stuttgart.

KOSINOV, A. 2006 Private Communication.

KOSINOV, A., SEMINONOV, N., SHEVELKOV, S. & ZININ, O. 1994 Experiments on the nonlinear instability of supersonic boundary layers. *Nonlinear Instability of Nonparallel Flows, IUTAM Symposium, Potsdam, N.Y., 1993.* Springer.

KOSINOV, A. & TUMIN, A. 1996 Resonance interaction of wave trains in supersonic boundary layer. *Nonlinear Instability and Transition in Three-Dimensional Boundary Layers, IUTAM Symposium, Manchester, U.K., 1995.* Kluwer Academic Publishers.

KOSINOV, A. D., MASLOV, A. A. & SHEVELKOV, S. G. 1990 Experiments on the stability of supersonic laminar boundary layers. *J. Fluid Mech.* **219**, 621–633.

LACHOWICZ, J. T., CHOKANI, N. & WILKINSON, S. P. 1996 Boundary-layer stability measurements in a hypersonic quiet tunnel. *AIAA J.* **34** (12), 2496–2500.

LADDON, D. W. & SCHNEIDER, S. P. 1998 Measurements of controlled wave packets at Mach 4 on a cone at angle of attack. *AIAA Paper* **98-0436**, 36th aerospace sciences meeting and exhibit, Reno NV, Jan 1998.

LEES, L. & RESHOTKO, E. 1962 Stability of the compressible laminar boundary layer. *J. Fluid Mech.* **12**, 555–590.

LEVCHENKO, V. Y., KOSINOV, A. D., SEMIONOV, N. V. & ERMOLAEV, Y. G. 1996 Instability of a three-dimensional supersonic boundary layer. *Nonlinear Instability and Transition in Three-Dimensional Boundary Layers, IUTAM Symposium, Manchester, U.K., 1995.* Kluwer Academic Publishers.

MACK, L. M. 1965 Stability of the compressible laminar boundary layer according to a direct numerical solution. *AGARDograph* **97**, 329–362.

MACK, L. M. 1984 Boundary-layer linear stability theory. *AGARD Report* **709**, 3.1–3.81.

MARTIN, M. P., WEIRS, G., PIOMELLI, U., HEATH, J., NOMPELIS, I. & CANDLER, G. V. 2000 Toward the large-eddy simulation over a hypersonic elliptical cross-section cone. *AIAA Paper* **2000-2311**, Fluids 2000 Meeting and Exhibit.

MARTIN, M. P., WRIGHT, M., CANDLER, G. V., PIOMELLI, U., WEIRS, G. & JOHNSON, H. 2001 Prelimenary LES over a hypersonic elliptical cross-section cone. In *Annual Research Briefs 2001*. Center for Turbulence Research.

MARXEN, O. 1998 Temporal direct numerical simulation of a flat plate boundary layer. Master's thesis, Universität Stuttgart.

MAYER, C. S. J. 2004 Stability investigation of a flat plate boundary layer with adverse pressure gradient at Mach 3. Master's thesis, University of Arizona.

MAYER, C. S. J. & FASEL, H. F. 2008 Investigation of asymmetric subharmonic resonance in a supersonic boundary layer at Mach 2 using DNS. *AIAA Paper* **2008-0591**, 46th AIAA Aerospace and Sciences Meeting and Exhibit.

MAYER, C. S. J., WERNZ, S. & FASEL, H. F. 2007 Investigation of oblique breakdown in a supersonic boundary layer at Mach 2 using DNS. *AIAA Paper* **2007-949**, 45th AIAA Aerospace and Sciences Meeting and Exhibit.

MEITZ, H. 1996 Numerical investigation of suction in a transitional flat-plate boundary layer. PhD thesis, The University of Arizona.

Norris, J. D. & Chokani, N. 2001 Identification of nonlinear interactions in hypersonic boundary layers using STFT. *AIAA Paper* **01-0207**.

Norris, J. D. & Chokani, N. 2002 Transient nonlinear interactions in a hypersonic boundary layer. *AIAA Paper* **02-0154**.

Poggie, J., Kimmel, R. L. & Schwoerke, S. N. 2000 Traveling instability waves in a Mach 8 flow over an elliptical cone. *AIAA J.* **38**, 251–258.

Pruett, C. D. 1993 On the accurate prediction of the wall-normal velocity in compressible boundary-layer flow. *Intern. J. for Num. Methods in Fluids* **16**, 133–152.

Pruett, C. D. & Chang, C.-L. 1995 Spatial direct numerical simulation of high-speed boundary-layer flows. Part II: Transition on a cone in Mach 8 flow. *Theoret. Comput. Fluid Dynamics* **7**, 397–424.

Pruett, C. D. & Chang, C.-L. 1998 Direct numerical simulation of high-speed boundary-layer flow on a flared cone. *Theoret. Comput. Fluid Dynamics* **11**, 49–67.

Pruett, C. D. & Zang, T. A. 1992 Direct numerical simulation of laminar breakdown in high-speed axisymmetric boundary layers. *AIAA Paper* **92-0742**.

Pruett, C. D., Zang, T. A., Chang, C.-L. & Carpenter, M. H. 1995 Spatial direct numerical simulation of high-speed boundary-layer flows. Part I: Algorithmic considerations and validation. *Theoret. Comput. Fluid Dynamics* **7**, 49–76.

Robarge, T. W. & Schneider, S. P. 2005 Laminar boundary-layer instabilities on hypersonic cones: Computations for benchmark experiments. *AIAA Paper* **2005-5024**, 35th AIAA Fluid Dynamics Conference.

Rosenboom, I., Hein, S. & Dallmann, U. 1999 Influence of nose bluntness on boundary-layer instabilities in hypersonic cone flows. *AIAA Paper* **99-3591**, 30th AIAA fluid dynamics conference, Norfolk, VA.

Saric, W. & Reed, H. 2002 Supersonic laminar flow control on swept wings using distributed roughness. *AIAA Paper* **2002-0147**, 40th Aerospace sciences meeting and exhibit, Reno, NV, Jan 2002.

Schlichting, H. & Gersten, K. 2001 In *Boundary Layer Theory*. Springer Verlag, New York.

Schmisseur, J. D., Schneider, S. P. & Collicott, S. H. 2002 Supersonic boundary-layer response to optically generated freestream disturbances. *Experiments in Fluids* **33**, 225–231.

SEDDOUGUI, S. O. & BASSOM, A. P. 1997 Instability of hypersonic flow over a cone. *J. Fluid Mech.* **345**, 383–411.

SHIPLYUK, A. N., BOUNTIN, D. A., MASLOV, A. A. & CHOKANI, N. 2003 Nonlinear mechanisms of the initial stage of the laminar-turbulent transition at hypersonic velocities. *J. Appl. Mech. and Techn. Phys.* **44** (5), 654–659.

STETSON, K. F. 1979 Effect of bluntness and angle of attack on boundary layer transition on cones and biconic configurations. *AIAA Paper* **79-0269**, 17th Aerospace Science Meeting, New Orleans LA, January 1979.

STETSON, K. F. & KIMMEL, R. L. 1992 On hypersonic boundary-layer stability. *AIAA Paper* **92-0737**, 30th aerospace sciences meeting and exhibit, Reno NV, Jan 1992.

STETSON, K. F. & KIMMEL, R. L. 1993 On the breakdown of a hypersonic boundary layer. *AIAA Paper* **93-0896**, 31st aerospace sciences meeting and exhibit, Reno NV, Jan 1993.

STETSON, K. F., THOMPSON, E. R., DONALDSON, J. C. & SILER, L. G. 1983 Laminar boundary layer stability experiments on a cone at Mach 8. Part I: Sharp cone. *AIAA Paper* **83-1761**, 16th fluid and plasma dynamics conference, Danvers MA, July 1983.

STETSON, K. F., THOMPSON, E. R., DONALDSON, J. C. & SILER, L. G. 1984 Laminar boundary layer stability experiments on a cone at Mach 8. Part II: Blunt cone. *AIAA Paper* **84-0006**, 22nd aerospace sciences meeting, Reno, NV, January 1984.

TANNEHILL, J., ANDERSON, D. & PLETCHER, R. 1997 *Computational Fluid Mechanics and Heat Transfer*. Taylor and Francis.

TEREKHOVA, N. M. 2003 Three-wave interactions of disturbances in a supersonic boundary layer. *J. Appl. Mech. and Techn. Phys.* **44** (4), 532–537.

TERZI, D. A. V. 2004 Numerical investigation of transitional and turbulent backward-facing step flows. PhD thesis, The University of Arizona.

THOMPSON, K. W. 1987 Time dependent boundary conditions for hyperbolic systems. *J. Comp. Phys.* **68**, 1–24.

THOMPSON, K. W. 1990 Time-dependent boundary conditions for hyperbolic systems, II. *J. Comp. Phys.* **89**, 439–461.

THUMM, A. 1991 Numerische Untersuchungen zum laminar-turbulenten Strömungsumschlag in transsonischen Grenzschichtströmungen. PhD thesis, Universität Stuttgart.

THUMM, A., WOLZ, W. & FASEL, H. 1989 Numerical simulation of Tollmien-Schlichting waves in compressible transsonic boundary layers on plates. *Z. Angew. Math. Mech.* **69**, 598–600.

THUMM, A., WOLZ, W. & FASEL, H. 1990 Numerical simulation of spatially growing three-dimensional disturbance waves in compressible boundary layers. In *Proceedings 3rd IUTAM Symposium on Laminar–Turbulent Transition* (ed. H. F. Fasel & W. S. Saric). Springer.

TUMIN, A. 1996 Nonlinear interaction of wave trains in a supersonic boundary layer. *Phys. Fluids* **8** (9), 2252–2254.

ZELMAN, M. B. & MASLENNIKOVA, I. I. 1993 Tollmien-schlichting-wave resonant mechanism for subharmonic-type transition. *J. Fluid Mech.* **252**, 449–478.

ZENGL, M. 2005 Direct numerical simulations of oblique-subharmonic wave interactions in a flat-plate boundary layer at Mach 3. Master's thesis, Universität Stuttgart.

ZHONG, X. 2005 Effect of nose bluntness on hypersonic boundary layer receptivity over a blunt cone. *AIAA Paper* **2005-5022**, 35th AIAA Fluid Dynamics Conference and Exhibit.